THE UNIVERSITY *of* EDINBURGH

This thesis has been submitted in fulfilment of the requirements for a postgraduate degree (e. g. PhD, MPhil, DClinPsychol) at the University of Edinburgh. Please note the following terms and conditions of use:

- This work is protected by copyright and other intellectual property rights, which are retained by the thesis author, unless otherwise stated.
- A copy can be downloaded for personal non-commercial research or study, without prior permission or charge.
- This thesis cannot be reproduced or quoted extensively from without first obtaining permission in writing from the author.
- The content must not be changed in any way or sold commercially in any format or medium without the formal permission of the author.
- When referring to this work, full bibliographic details including the author, title, awarding institution and date of the thesis must be given.

THE UNIVERSITY
of EDINBURGH

Application of Optical Flow for High-Resolution Velocity Measurements in Wall-bounded Turbulence

Alexander Nicolas

A thesis submitted for the degree of
Doctor of Philosophy

The University of Edinburgh
2023

Abstract

This thesis assesses the performance of an advanced wavelet-based optical flow (wOF) algorithm in extracting high accuracy and high-resolution velocity vector fields from tracer particle images in wall-bounded turbulent flows. wOF is first evaluated using synthetic particle images generated from a channel flow DNS of a turbulent boundary layer. The sensitivity of wOF to the regularization parameter (λ) is quantified and results are compared to state-of-the-art cross-correlation-based PIV. Results on synthetic particle images indicated different sensitivity to under-regularization or over-regularization depending on which region of the boundary layer is being analysed. Nonetheless, tests on synthetic data revealed that wOF can modestly outperform PIV in vector accuracy across a broad λ range. wOF showed clear advantages over PIV in resolving the viscous sublayer and obtaining highly accurate estimates of the wall shear stress and thus normalising boundary layer variables.

Following the validation of the wOF algorithm using synthetic PIV images rendered from the DNS simulation, wOF is subsequently applied to an experimental data acquired in a well-established flow facility referred to as a side-wall quenching burner (SWQ) facility. This experimental facility is designed for reacting flows, but wOF is first applied to data acquired under non-reacting flow conditions, where a jet flow impinges onto a parallel wall, creating a developing turbulent boundary layer. Overall, wOF revealed good agreement with results from both PIV and a combined PIV + PTV (particle tracking velocimetry) method. However, wOF was able to successfully resolve the wall shear stress and correctly normalise the boundary layer streamwise velocity to wall units where PIV and PIV + PTV showed larger deviations. The enhanced vector resolution of wOF enabled improved estimation of instantaneous derivative quantities and intricate flow structure both closer to the wall and more accurately than the other velocimetry methods.

In the final investigation of the thesis, both wOF and PIV are applied to experimental PIV images from the same SWQ facility, now operated under reacting conditions to investigate the coupling between flame-wall interaction (FWI) and wall-turbulence. Characteristic vortex types were identified and a conditional analysis is performed to characterise the vortex dynamics and hydrodynamic influences affecting flame quenching. The action of a dominant vortex, known as a Type 3 vortex, is predominantly to push the flame deeper into the shear layer at the wall, leading to increased strains and heat loss which result in quenching. A flame vortex interaction mechanism, which has only been postulated previously in the literature, is revealed explicitly for the first time. The turbulent flow field facilitating the transport process due to this flame vortex interaction is analysed through a quadrant analysis of the turbulent fluctuations, explicitly revealing the role of the T3 vortex in entraining burnt gases into the reactants leading to unique thermochemical states.

Lay abstract

In this thesis, a method of determining motion from images, known as optical flow, is used to investigate flow physics in flows that are constrained by physical boundaries. The motivation is to overcome limitations from traditional methods used in the engineering community that uses techniques known as cross-correlation-based particle image velocimetry (PIV). A specific implementation of optical flow, known as wavelet-based optical flow (wOF), is used to achieve high resolution and high accuracy measurements that outperform traditional cross-correlation methods. wOF is benchmarked on wall-bounded scenarios using both computer simulated and real experimental data. The final part of this thesis uses wOF to study novel flow physics in a wall-bounded flow featuring combustion and investigates practically relevant flame wall interactions. Phenomena that have been previously hypothesised in literature are explicitly revealed for the first time and investigated at a level of detail never possible previously with traditional PIV correlation-based methods.

Acknowledgements

I would like to express my sincere gratitude to my supervisor Brian. Being Brian's first PhD student to submit their thesis, I can certainly say it has been an interesting journey over the last four years and Brian's guidance and support have been invaluable throughout. Brian provided me with many opportunities to engage with the research community throughout multiple conferences during my PhD. Brian was also there for me not just as my supervisor, but as a friend.

I would also like to extend my sincere gratitude to my second supervisor Professor Mark Linne, who was my primary supervisor during my master's thesis where the precursor optical flow algorithm to the present work was developed. Mark's interest and faith in my (often overly ambitious) approach were a strong motivator for me pursuing research to postgraduate level.

Thank you to Dr Florian Zentgraf and Professor Andreas Dreizler at the Technical University of Darmstadt for providing the quality experimental data analysed in this thesis, as well as their expertise, efficiency and numerous insightful discussions.

Lastly, and most of all, I would like to express my gratitude to my mother and my grandmother for their constant love and support. My family is the biggest blessing in my life and they have always been there for me. I thank them for everything.

Declarations

I declare that the thesis has been composed by myself and that the work has not be submitted for any other degree or professional qualification. I confirm that the work submitted is my own, except where work which has formed part of jointly-authored publications has been included. My contribution and those of the other authors to this work have been explicitly indicated below. I confirm that appropriate credit has been given within this thesis where reference has been made to the work of others.

The work presented in Chapter 4 was previously published in the journal Experiments in Fluids as Assessment and application of wavelet-based optical flow velocimetry (wOFV) for turbulent wall-bounded Flows by Alexander Nicolas (author), Florian Zentgraf, Mark Linne, Andreas Dreizler, Brian Peterson (supervisor). I implemented the wavelet-based optical flow code, designed the synthetic test case and performed data analysis. The experimental PIV image data used in this thesis was acquired by Florian Zentgraf at the Institute of Reactive Flows and Diagnostics at the Technical University of Darmstadt.

Contents

List of Figures

Chapter 1

Introduction

Few physical phenomena in the world are as complex, intricate and technologically-relevant as the turbulent motion of fluids. The fascinating character of turbulence is matched with formidable difficulties in achieving a thorough understanding, such that three dimensional turbulence remains one of the most complex known and poorly understood problems in classical physics. By elucidating the intrinsic dynamics of turbulent flows, researchers unlock profound insights into phenomena present in both natural and engineered systems. The advancement of such knowledge furthers design optimisation and control systems in a myriad of practical applications. The complexity attracts a multifaceted scientific approach involving the intersection of theoretical, computational and experimental paradigms, each with their own strengths and limitations.

The interaction between turbulent fluid flow and physical boundaries is of particular importance in a variety of engineering applications. Detailed knowledge of the momentum transport processes in these wall-bounded turbulent flows underpins the success of many industrial, aerodynamic and medical designs and their relevant applications. In particular, the dynamics of the 'boundary layer' region in close proximity to the wall are of major interest and have been the subject of extensive research since the fundamental work of (Prandtl, 1905). Obtaining accurate velocity measurements across the extent of the boundary layer flow is key to developing a sound understanding of the complex multi-scale mass and energy transport phenomena present in wall-bounded turbulence.

Particle image velocimetry (PIV) is a well-known diagnostic tool used for obtaining velocity measurements in fluid flows and is applicable across a broad range of flow experiments (Raffel et al., 2018). The operative principle behind calculating velocity from PIV images involves cross-correlating image subregions between an image pair to determine a statistically averaged velocity of tracer particles advected by the flow within the subregion. Many advancements to this cross-correlation-based approach have been incorporated, making PIV a reliable, well-established tool for laser diagnostics in fluid dynamics (Raffel et al., 2018).

A well-known and fundamental limitation exists in PIV, however, being that the velocity vector field is of a significantly lower resolution than the image itself. This low-resolution limitation of PIV is fundamentally a by-product of using a window-based cross-correlation approach for estimating the image plane motion. This drawback has detrimental consequences for velocity measurements in wall-bounded turbulent flows, where strong velocity gradients induced by physical boundaries often

lead to inaccuracies from PIV when estimating derivative quantities and small-scale turbulent fluctuations which are key in characterising the structure of the boundary layer and the turbulence dynamics.

In order, to compensate for the low-resolution restriction of PIV, experimental images have to be taken at a higher magnification which compromises the field of view. This is particularly undesirable for boundary layer studies where resolving velocity in close proximity of the wall is important, as well as larger scale motion occurring in the outer boundary layer regions that is key in the organisation of wall-turbulence (Adrian, Meinhart, & Tomkins, 2000) as well as energy and mass transfer processes in boundary layers. It is possible to use multiple camera setups simultaneously at different magnifications (Jainski et al., 2013), but this complicates the experimental setup and subsequent data processing. Other approaches attempting to overcome the spatial resolution limitations of PIV have been proposed, such as particle tracking velocimetry (PTV) (Stitou & Riethmuller, 2001) and single-pixel ensemble correlation (Westerweel et al., 2004). These methods come with their own distinct disadvantages and are discussed in detail in Chapter 2 of this thesis.

The goal of determining velocity from the image plane has been the motivation of multiple research efforts across different communities and is part of a fundamental overarching task known more generally as motion estimation. Despite a confluence of interests, there has been relatively little interaction between the fields of engineering and computer vision, where an alternative method known as optical flow (OF) was originally proposed in the seminal work of (Horn & Schunck, 1981) for application in machine vision. OF presents an alternative approach to extracting velocity from the image plane as opposed to cross-correlation analysis used in PIV. The basis of OF methods is to solve the transport equation for the image intensity brightness patterns. The OF motion field estimates the transformation that leads one image to evolve into the subsequent in order to conserve the total image intensity. It can be proven that the image transformation represented by this optical flow velocity vector field is physically related to the projected two-dimensional transport equation of a passive scalar (T. Liu & Shen, 2008).

The resulting velocity field from OF is dense, i.e., has one vector per pixel. Therefore, application of OF for fluid flow velocimetry has the potential to surpass the resolution limitations of traditional cross-correlation methods used in PIV. Indeed, previous studies using OF have previously demonstrated increased accuracy and resolution over conventional correlation-based PIV methods (S. Cai et al., 2018; Corpetti et al., 2006; Dérian et al., 2013; Héas et al., 2012; Yuan et al., 2007), to name a few. Interestingly, the very earliest application of OF velocimetry can be traced back to (Fitzpatrick & Pederson, 1988). The impressive spatial resolution and accuracy available from OF make it an attractive tool to resolve velocity in wall-turbulence, including key quantities such as the wall shear stress τ_w which is fundamental in accurate normalisation and evaluation of boundary layer quantities. At the same time, OF can improve estimation of small-scale turbulent fluctuations in proximity of the wall, as well as computation of derivative quantities which yield insight on near-wall vortical structures that are believed to play an important role in the organisation of turbulence and mixing processes within the boundary layer (Adrian, 2007; Herpin et al., 2010; Robinson, 1991). High fidelity near-wall velocity measurements are particularly important in studying phenomena occurring in practical combustion systems such as engines (Drake & Haworth, 2007; L JONES, 1997)

and gas turbines (Huang & Yang, 2004; Stopper et al., 2013), where flames interact with a turbulent boundary layer as part of *flame-wall interaction* (FWI).

1.1 Flame-wall interaction

The interaction between the wall, flame and turbulence as part of FWI features complex and mutually coupled processes involving chemical and hydrodynamic processes. Flames in proximity to a wall come into contact with the hydrodynamic boundary layer from the wall. This affects flame characteristics including the propagation speed and combustion reaction rate. A turbulent flow field wrinkles the flame surface while the flame modifies the turbulence dynamics with effects of thermal expansion and density changes. The wall modifies turbulent length scales and experiences high heat fluxes from the flame, which result in strong thermal stresses and affects material durability.

Excessive heat loss from the flame to the wall, which acts as a heat sink, can lead to flame quenching if the reaction rate falls below the limit needed sustain the combustion process. Understanding the influences leading to flame quenching is key in improving energy efficiency by reducing unburnt fuel that is wasted when the flame is quenched. Additional concerns from incomplete combustion including the formation of carbon monoxide (CO), nitrogen oxides (NOx) and unburnt hydrocarbons (depending on the fuel) which cause severe environmental and health consequences (Luo & Liu, 2018). In fuel-rich environments, the deposition of soot resulting from incomplete combustion can coat surfaces, altering surface morphology and promoting mechanical abrasion (Hasse et al., 2000). In the case of laminar wall-bounded flames, the quenching distance has been reported as being in range of 0.17 - 0.43mm depending on thermochemical conditions (Kosaka et al., 2018a).

Improved understanding of FWI is key in the successful development of high efficiency engines that are downsized (Sroka, 2012) where the surface-to-volume ratio is increased such that effects of FWI become increasingly prominent. There is a need to study FWI to minimise environmental damage and design cleaner engine systems and next generation powertrains that operate under new strategies such as dilute combustion, higher power densities to produce improved emissions profiles (Huang & Yang, 2004; Stopper et al., 2013).

Predictive modelling of combustion phenomena remains difficult due to the complex interaction between combustion chemistry and turbulence dynamics. The full solution of the generalised Navier-Stokes equations including variable density and viscosity through direct numerical simulation (DNS) are often limited to simplified cases (Baritaud et al., 1996; T. Poinsot, 1996). Therefore, large eddy simulation (LES) and Reynolds Averaged Navier-Stokes (RANS) modelling approaches are used, a thorough description of which is too vast to summarise here, but is available in (T. Poinsot & Veynante, 2005).

Approaching FWI using experimental laser diagnostics such as PIV is challenging due to the range of time and lengthscales involved, requiring the need for high resolution measurements close to the wall surface. The practical complexity of the experimental setup becomes increasingly difficult for high fidelity multiparameter measurements. Given the complexity of practical combustion devices, experimental studies typically use simplified geometries to study isolated features of FWI phenomena in a side-wall quenching (SWQ) or head-on quenching (HOQ) configuration.

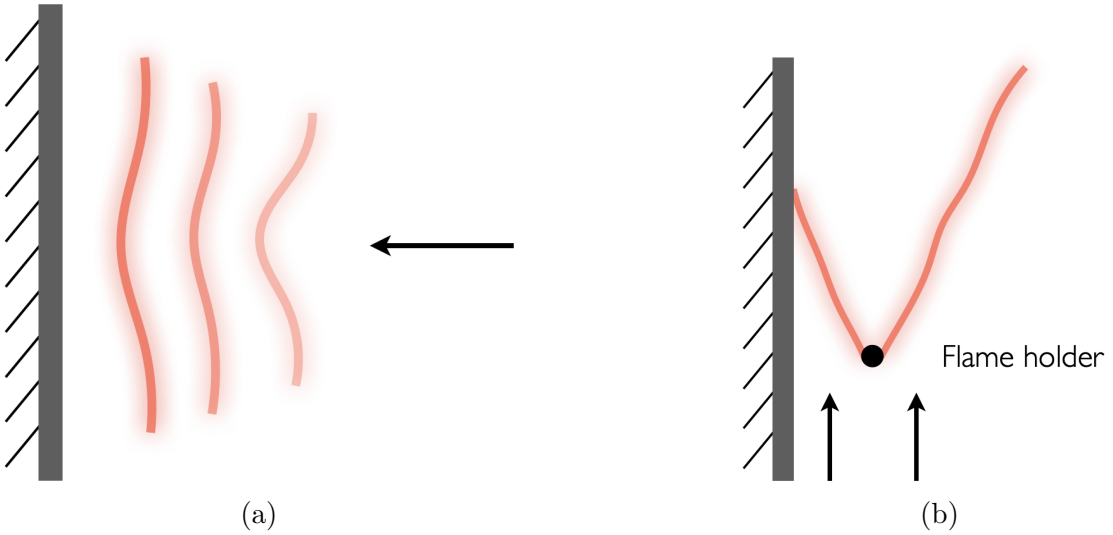

Figure 1.1: a) Head-on quenching (HOQ) of a flame propagating normal to a wall. b) Side-wall quenching (SWQ) where a flame, stabilised by a flame holder, is propagating parallel to the wall and impinges at an angle.

These simplifications also enable greater optical access in experiments and improved investigation of relevant boundary conditions that can be used in numerical studies. The two configurations are shown in Figure 1.1. HOQ is the case when the flame front propagates normal towards the wall. SWQ is the case of a flame front propagating at an angle parallel to a wall.

In both SWQ and HOQ scenarios, as the flame approaches the wall it interacts with a hydrodynamic boundary layer which is typically turbulent in practical combustion systems. The unique flame flow interaction will modify the mass and energy transfer transfer processes in wall-turbulence, as well as have implications on flame behaviour. Thus, resolving the underlying turbulent flow dynamics is a fundamental component in developing understanding of the very complex set of physical processes involved in FWI. The following literature review summarises both experimental and numerical studies considering flow dynamics in reacting turbulent boundary layers, followed by a summary of the open questions in this area. Studies that are not directly related to flow dynamics and focus predominantly on chemical kinetics or heat transfer are not included in the following. Relevant literature on these aspects can be found in references of the FWI review articles of (Dreizler & Böhm, 2015; Luo & Liu, 2018).

1.2 Literature review of flow dynamics in flame-wall interaction

Among the first FWI investigations can be traced back to the work of (Cheng et al., 1981). The experimental setup involved a premixed hydrogen air that was ignited in a channel flow using heating strips. Rayleigh scattering was used for density measurements combined with velocity measurements from laser doppler velocimetry (LDV). Even from these early experiments, the influence of combustion on the velocity was notable as a significant decrease in the intensity of velocity fluctuations

observed in the presence of the flame front. This was attributed to the decreased density of the burnt gas and thus a lower effective Reynolds number.

A similar reacting channel flow setup was investigated in (Ng et al., 1982) using LDV and high-speed schlieren photography. Results indicated that the presence of combustion greatly reduced the magnitude of the Reynolds stresses and kinetic energy production. The authors noted however that both density fluctuations and other terms in the turbulent kinetic energy (TKE) transport equation that were not measurable in the study are likely to play a role. An additional contribution of (Ng et al., 1982) was the visualisation of the large scale flame structures in the boundary layer from schlieren imaging. These large scale structures were observed to be linked to the combustion process with reaction zones occurring in the structures themselves.

The DNS study of (T. J. Poinsot et al., 1993) accounted for variable density and viscosity but was limited to 2D. This work investigated FWI using both laminar and turbulent simulations, with the turbulent test case using a 'shear-free' boundary layer. This is equivalent a frame of reference that is moving with the mean flow. Concentrated regions of positive vorticity were observed to attract regions of the flame closer to the wall, while negative vorticity would repel the flame away from the wall.

Fully three dimensional evidence of the importance of these interactions between the flame and the flow dynamics became available in the 3D DNS of (Bruneaux et al., 1996), which assumed constant density and variable viscosity. Large-scale horse-shoe vortices, which are characteristic feature in non-reacting boundary layers, were identified through the local pressure field topology and observed to push the flame closer to the wall, increasing the local heat flux. On the opposite side of the vortex the fresh gases were lifted up into protruding 'tongue' or 'finger' like structures. similar structures have been observed in experiments of (Richard & Escudie, 1999). Interestingly, the existence of these protrusions showed a high indication that a local quenching event is present nearby. Downstream of the quenching point, the burnt gases feature higher viscosity that damps turbulence to the extent that a new laminar boundary layer forms.

The interaction between the flow dynamics and flame front was investigated more directly in the DNS study of (T. Alshaalan & Rutland, 2002) with variable density and constant viscosity. Downward fluctuation of the flame front towards the wall would either cause a low speed velocity streak or moderate a high speed streak in the flow. Low speed velocity streaks decrease flame stretch and increase the wall heat flux, while high speed streaks would create the opposite effect. Sufficiently strong vortices, with strength defined as the vortex circulation, were able to push the flame towards the wall, while weak vortices were found to have little effect. Using an indirect measure of vortex presence based on the fluctuation of the vertical velocity component, this study found that vortices were key in modifying the heat flux to the wall through the action of pushing the flame.

The study of (T. Alshaalan & Rutland, 2002) also reported that the flame had a significant effect on the Reynolds stresses. Using the quadrant analysis scheme of (Wallace et al., 1972), the flame was found to have a strong influence of the directional distribution of the velocity fluctuation, and therefore the sign of the Reynolds stress term. It was found that the probability for Q1 and Q3 events (where both fluctuating velocity components have the same sign, either positive or

negative) increased significantly in the reaction zone. Conversely, the probability of Q2 and Q4 events decreased in the reaction zone but were more likely closer to the wall in the unburnt gases. Quadrant analysis will be described in detail in Chapter 2. However, the change from Q2 and Q4 processes, which are dominant in a non-reacting boundary layer (Spalart, 1988), to Q1 and Q3 is indicative of a very different set of momentum transfer processes occurring in the reacting case. The increased probability of Q1 and Q3 events makes the production term $\mathcal{P}$ from the TKE transport equation become negative. This change results in TKE being removed, thus heat release from the flame was suppressing turbulence.

The detailed work of (Gruber et al., 2010) used a much larger domain and more detailed chemical kinetics to more accurately model flame quenching distances and local wall heat flux. Variable density and viscosity are assumed. The larger domain enabled a more comprehensive characterisation of the flame, vortex and heat transfer interactions. Using a method of vortex detection known as the Q criterion (Hunt et al., 1988), a variety of vortical structures were identified both in the burnt and unburnt gas regions. The effect of the flame was to cause an increase in the characteristic lengthscale of these vortical structures in the burnt gas region. The length and timescales were observed to decrease with decreasing distance from the wall, confirming prior observations from (T. M. Alshaalan & Rutland, 1998; Bruneaux et al., 1997). The fluctuations in heat flux at the wall were also discovered to be highly correlated with the action of these vortical structures which push the flame either toward or away from the wall inducing large gradients in heat flux.

The experimental investigation of (Jainski et al., 2018) was a pivotal experimental work in FWI flow research. A key contribution was the application of quadrant analysis at different downstream locations of a side-wall quenching (SWQ) burner setup. The flame front was found to cause a significant increase of the Reynolds stresses in Q1 and Q3 quadrants. This trend is in agreement with the analysis of quadrant probability (T. Alshaalan & Rutland, 2002), where the influence of the flame causes a change from Q2/Q4 quadrants to Q1/Q3 quadrants indicating that a typical source term in non-reacting turbulent boundary layers becomes a sink of turbulent kinetic energy in the reacting case.

Experimental studies investigating vortex dynamics in FWI first appeared in a recent experimental work from (Zentgraf et al., 2021). By identifying vortical structures using the 2D form of the Q criterion, this work was the first experimental study to observe the presence of vortical structures interacting with the flame producing changes in flame topology. Vortical structures were observed to induce a change in flame topology from HOQ to SWQ states prior to quenching. The flame was found to exist approximately 50% of the time in either an HOQ or SWQ state, alternately quickly between the two.

Based on measurements using dual-pump coherent anti-stoke raman spectroscopy (DP-CARS), an interesting conclusion was the existence of unique thermochemical states involving burnt gas products (CO_2) at low temperatures (<450 K) existing near the wall. This state is not present under laminar conditions (Zentgraf et al., 2022). The authors of (Zentgraf et al., 2021) postulated that a flame-vortex interaction mechanism, illustrated in Figure 1.2, is responsible for this effect. A vortex is hypothesised to transport burnt gas, initially downstream of the flame quenching point, through gap between the flame tip and the wall. During this passage, the burnt gas fluid would cool due to heat loss at the wall and would mix with fresh

reactant gases upstream of the quenching location.

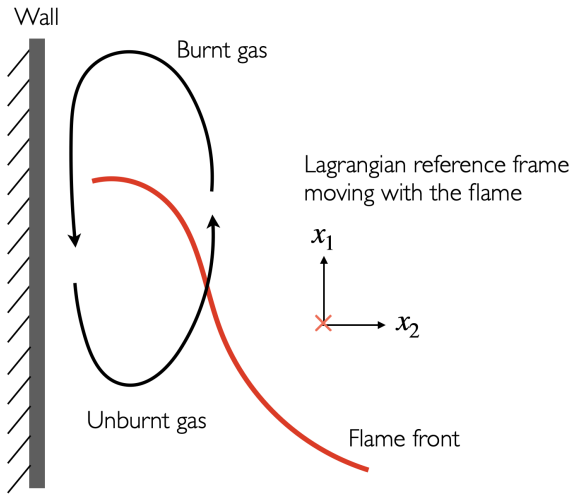

Figure 1.2: Schematic of the transport phenomenon proposed by (Zentgraf et al., 2021).

This flame-vortex interaction mechanism was investigated in a recent simulation study from (Steinhausen et al., 2023). A vortical structure, identified from elevated regions of the Q criterion, was found to be present downstream of the flame tip. This vortical structure was seen to move with the flame downstream in close proximity of the flame tip. This was observed very frequently (>80% of the time) and results from the numerical study support an entrainment mechanism of the hot exhaust gases to the colder unburnt gas region upstream of the flame tip. Based on this mechanism, an extension to previous Quenching Flamelet-Generated manifolds (QFM) (Efimov et al., 2020; Steinhausen et al., 2021) was proposed to include this mixing effect, termed QFM with exhaust gas recirculation (QFM-EGR). A priori validation of this improved manifold showed significant improvements in the prediction of thermochemical states near the wall over previous models, demonstrating the importance of resolving the flow dynamics that facilitate the transport processes occurring in FWI.

1.2.1 Open questions

It is evident in the existing literature that there is a general deficiency of detailed experimental investigation of the turbulent flow dynamics involved in FWI beyond the works of (Jainski et al., 2018; Zentgraf et al., 2021). Several open scientific questions of immediate relevance are:

- **Vortex dynamics** The existence of vortices involved in FWI is based on elevated regions of Q criterion. While this criterion can indicate vortical motion in the flow, the actual vortex vector field of the flame-vortex interaction postulated by (Zentgraf et al., 2021) has never actually been proven or explicitly revealed. Directly analysing the vortical flow field by adopting a Lagrangian-like perspective moving with the flow is key in furthering understanding of flame-wall-vortex interactions. Analysis of the explicit vortex flow field itself is needed to investigate whether the vortical flow topology is indeed capable

of facilitating transport of the burnt gases to the unburnt gas region. General properties of the hypothesised flame-tip vortex such as its strength, or time-history remain completely unknown.

- **Quenching phenomena** The contribution of possible mechanisms leading to flame quenching in FWI is unknown. Hydrodynamic strain in particular has been known to quench flames (T. Poinsot et al., 1991) by stretching the flame front beyond the limits needed sustain combustion. While species and heat flux measurements are beyond the scope of this work, understanding the transport process involving expected species such as CO and uncombusted hydrocarbons (dimethyl ether in the present case) will aid future investigations focusing on thermochemical aspects. The proximity of the flame front in the high shear region close to wall may support straining the flame sufficiently to support quenching. Investigating the potential of the vortex to push the flame towards the wall, leading quenching through excessive heat loss is additionally important in developing understanding of the complex multiphysics phenomena present in FWI. The action of vortices pushing the flame has been qualitatively reported in the studies discussed in the literature review, however a direct assessment of this correlation in experimental data is missing.

Satisfactorily answering these questions in their entirety is a formidable challenge that will take the collaboration of several research efforts beyond the scope of the current work. Highly resolved velocity measurements of the hydrodynamic phenomena occurring close to the wall during FWI can be achieved using OF. Despite its capabilities, only a few applications of OF for velocimetry in wall-bounded flows exist in the literature (S. Cai et al., 2019; Gevelber et al., 2022; Kähler et al., 2016; Kapulla et al., 2011; Ruhnau & Schnörr, 2006; Stanislas et al., 2005; Stark, 2013). Such studies primarily use wall-bounded environments as test cases for other aspects of the specific OF algorithms and limit investigations to velocity profiles. A thorough evaluation of OF to resolve a turbulent boundary layer is missing. Furthermore, analysis of derived quantities such as the wall shear stress as well as evaluation of the accuracy and effect on resolution of the inner-scaled turbulent boundary layer quantities in a canonical non-reacting boundary layer is absent in the literature.

Variational OF techniques involve selection of a scalar regularization parameter that is typically determined empirically. Regularization imparts a degree of spatial regularity to the estimated flow field that suppresses non-physical noise and provides closure to the optical flow problem. Correct selection of the regularization parameter λ is key in obtaining accurate velocity fields that accurately resolve fine-scale motion without excessive damping or smoothing of velocity gradients. This is especially important in measuring gradient quantities near the wall, where the discontinuity in motion at the wall can be particularly susceptible to the smoothing effect inherent in regularization (Aubert et al., 1999; Black & Anandan, 1996; Kalmoun, 2018; Weickert & Schnörr, 2001). To the best of the authors' knowledge, other works exploring or discussing this parameter in the context of fluid velocimetry are limited to those of (S. Cai et al., 2018; Corpetti et al., 2002; Heas et al., 2013; Kapulla et al., 2011; B. E. Schmidt & Sutton, 2020; Stark, 2013). None of these, however, have investigated the sensitivity of λ specifically in relation to near-wall measurements in wall-bounded flows. Thus, validation of the applicability of OF for velocimetry in traditional wall-turbulence is a necessary prerequisite to its application in a reacting

turbulent boundary layer.

1.3 Objectives of current work

The aim of this thesis is to advance the measurement of velocities in turbulent wall-bounded flows using optical flow and use its unique attributes to shed light on some of open questions in FWI phenomena described in the previous section. A description of the relevant theory behind turbulent boundary layers, PIV and generic optical flow is presented in Chapter 2. Chapter 3 describes the specifics of an advanced *wavelet-based* optical flow (wOF) method dedicated to highly accurate measurements in turbulent flows.

The results of the thesis are then organised into two main themes, starting with validation in Chapter 4. The performance of wOF in obtaining highly resolved and accurate measurements of velocity and derived quantities such as the wall shear stress in turbulent wall-bounded flows is compared with industry state-of-the-art PIV cross-correlation algorithms. wOF is first evaluated using synthetic particle images generated from a channel flow DNS of a turbulent boundary layer. The influence of regularization on velocity results and normalised boundary layer quantities is investigated to understand the effect of this parameter. wOF is subsequently applied to experimental data acquired in the well-established SWQ burner flow facility that was used in the experimental work of (Jainski et al., 2018; Zentgraf et al., 2021). This experimental facility is designed for reacting flows, but wOF is first applied to data acquired under non-reacting flow conditions, where a jet flow impinges onto a parallel wall, creating a developing turbulent boundary layer. Results are compared to correlation-based PIV processing to validate the use of wOF as an alternative technique in the study of turbulent wall-bounded flows.

Following validation, both cross-correlation PIV and wOF are applied to experimental PIV images from the same SWQ facility, now operated under reacting conditions to investigate the described research questions in FWI. The role of vortices in mechanisms of flame-quenching is investigated, together with contributing effects from hydrodynamic strain that is present due to the shear layer from the wall. Quadrant analysis of the velocity fluctuations is applied to investigate the dominant momentum transport processes associated with the hypothesised tip vortex transport mechanism postulated by (Zentgraf et al., 2021) and supported by (Steinhausen et al., 2023). Conclusions of the thesis are presented in Chapter 6.

Chapter 2

Theory

2.1 Wall-bounded turbulent flow

The canonical case of a turbulent boundary layer developing across an infinite flat plate is shown in Figure 2.1. An initially laminar flow travelling at U_∞ in the x_1 direction impinges on the leading edge of a flat plate at $(x_1, x_2) = (0, 0)$. A boundary layer region forms where large viscous shearing forces act on the flow due strong velocity gradient created by the no-slip condition $\mathbf{U} = (U_1, U_2, U_3)^{\mathrm{T}} = 0$ at the wall. The boundary layer thickness $\eta(x_1)$ grows in the x_1 direction. An average boundary layer thickness for a given streamwise location is often defined using the mean streamwise velocity $\langle U_1 \rangle$ based on the wall-normal location (x_2) where $\langle U_1 \rangle = 0.99 U_\infty$. This gives a common metric known as the δ_{99} boundary layer thickness. Other integral measures based on the boundary layer displacement or momentum thickness are also similarly common. As such, different Reynolds numbers in wall-bounded flows can be defined depending on the choice of length and velocity scales. One possible option is:

$$Re_{x_1} = \frac{U_\infty x_1}{\nu} \tag{2.1}$$

where ν is the kinematic viscosity and x_1 is the downstream distance from the leading edge.

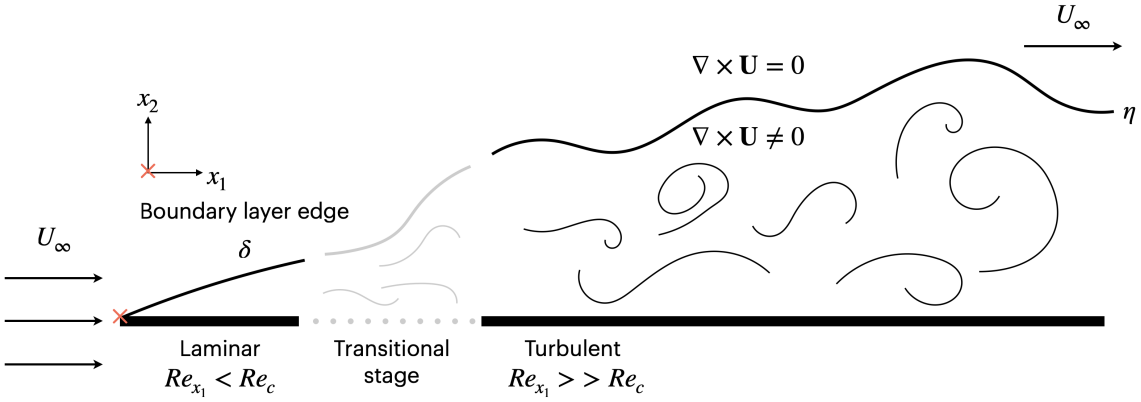

Figure 2.1: Schematic of a turbulent boundary layer over a flat plate.

Immediately downstream from the leading edge the boundary layer flow field is

laminar. The boundary layer continues to develop downstream of the leading edge, eventually beginning a transition to turbulence at a critical Reynolds number Re_c. The exact value of Re_c is highly dependent on the degree of flow disturbances in the free stream (Schlichting & Gersten, 2016) but is in the range of $Re_c \approx 10^6$ (Pope, 2000). Beyond the transitional stage $Re_{x_1} >> Re_c$ the boundary layer reaches its fully developed turbulent state. In experimental investigations, various methods such as wires placed across the flow can be used to trip the initially laminar boundary layer and promote transition to turbulence sooner than in a naturally developing boundary layer (Arnal & Michel, 2012; Kachanov, 1994). Alternatively, the incoming flow field U_∞ over the wall can already be prior made turbulent using a turbulence grid (Jainski et al., 2018; Zentgraf et al., 2021). The turbulent boundary layer edge η defines a spatiotemporally evolving intermittent interface between the turbulence contained within the boundary layer and the outside region where the flow travelling at U_∞ is laminar. Outside the boundary layer region delineated by η, the influence of viscosity near the wall can be largely neglected and thus inviscid flow theory approximations are suitable.

Assuming a constant density ρ and kinematic viscosity ν with negligible body forces, the instantaneous momentum transport equation of a flow is given by the following form of the Navier-Stokes equations:

$$\frac{\partial U_i}{\partial t} + U_j \frac{\partial U_i}{\partial x_j} = -\frac{1}{\rho}\frac{\partial p}{\partial x_i} + \nu \frac{\partial U_i}{\partial x_j \partial x_j} \tag{2.2}$$

where $U_i,\ i = 1, 2, 3$ is the instantaneous velocity component associated to spatial direction x_i. Turbulent flows are frequently modelled using the Reynolds decomposition:

$$U_i = \langle U_i \rangle + u_i \tag{2.3}$$

where $\langle \cdot \rangle$ represents the ensemble averaging operator. This decomposition separates an instantaneous velocity U_i into an averaged mean $\langle U_i \rangle$ component, which is time-constant if the flow is steady, together with the fluctuating velocity u_i, where $\langle u_i \rangle = 0$ necessarily. Substituting equation 2.3 into 2.2 produces the well-known Reynolds-Averaged Navier-Stokes (RANS) equation:

$$\frac{\partial \langle U_i \rangle}{\partial t} + \langle U_j \rangle \frac{\partial \langle U_i \rangle}{\partial x_j} = -\frac{1}{\rho}\frac{\partial p}{\partial x_i} + \nu \frac{\partial \langle U_i \rangle}{\partial x_j \partial x_j} - \frac{\partial \langle u_i u_j \rangle}{\partial x_j} \tag{2.4}$$

The additional term $\langle u_i u_j \rangle$ requires closure or modelling to solve the above. Equation 2.4 can be alternatively arranged to produce this term in the form $-\rho\langle u_i u_j \rangle$, which is interpretable as a stress, hence the name *Reynolds stresses*.

Assuming the flow is statistically two-dimensional and bounded by quiescent flow ($\partial p / \partial x_i = 0$), together with the assumptions in equation 2.2, the streamwise momentum transport equation is given by (Pope, 2000):

$$\langle U_1 \rangle \frac{\partial \langle U_1 \rangle}{\partial x_1} + \langle U_2 \rangle \frac{\partial \langle U_1 \rangle}{\partial x_2} = \nu \frac{\partial^2 \langle U_1 \rangle}{\partial x_2^2} - \frac{\partial \langle u_1 u_2 \rangle}{\partial x_2} \tag{2.5}$$

This is coupled with the no-slip condition at the wall $\mathbf{U} = 0$ at $x_2 = 0$. In the present work, indices $i = 1, 2, 3$ will always denote the in-plane streamwise ($i = 1$), wall-normal ($i = 2$) and out-of-plane ($i = 3$) directions. The properties of the mean boundary layer flow field $\langle U_i \rangle$ are next presented, followed by the structure of

the turbulent velocity fluctuations (u_i) and the dynamics of the coherent structures present in wall-bounded turbulence.

2.1.1 Properties of the mean flow field

The structure of the turbulent boundary layer is commonly delineated based on regions primarily dominated by either viscous stresses (the viscous sublayer) due to the influence of the wall, turbulent Reynolds stresses (the logarithmic region) or influenced by both (the buffer layer). To evaluate and facilitate comparison of these different regions between theoretical, numerical and experimental results, the boundary layer mean streamwise velocity $\langle U_1 \rangle$ and wall-normal distance coordinate x_2 are typically normalised to the so-called wall units:

$$u^+ = \frac{\langle U_1 \rangle}{u_\tau} \tag{2.6}$$

$$y^+ = x_2 \frac{u_\tau}{\nu} \tag{2.7}$$

The key variable involved in the nondimensionalisation is the friction velocity u_τ, defined as:

$$u_\tau = \sqrt{\frac{\tau_w}{\rho}} \tag{2.8}$$

where τ_w is the mean wall shear stress:

$$\tau_w = \mu \frac{\partial \langle U_1 \rangle}{\partial x_2}|_{x_2=0} = \mu\gamma \tag{2.9}$$

where μ is the dynamic viscosity ($\mu = \nu\rho$). Normalising $\langle U_1 \rangle$ velocity profiles to wall units collapses trends from different wall-turbulence datasets onto a common curve depicted in Figure 2.2 where the abscissa is plotted in semilog scale. The distinct regions of the curve are discussed below.

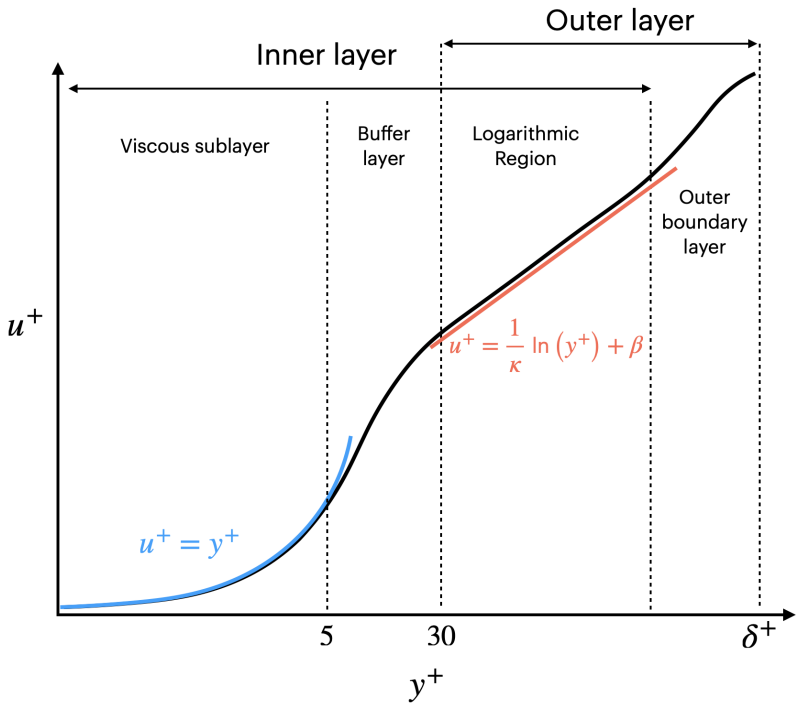

Figure 2.2: Depiction of u^+, y^+ in a canonical turbulent boundary layer.

The viscous sublayer ($y^+ < 5$) is the flow region in closest proximity to the wall where the influence of fluid viscosity dominates over the Reynolds stresses. The variation of u^+ with y^+ in this region can be shown to be linear ($u^+ = y^+$) to first order, until $y^+ = 5$. This result, dating back to (Prandtl, 1925), is part of the result referred to as the *law of the wall* in literature (Pope, 2000; Schlichting & Gersten, 2016) and is generally believed to be universal for wall-bounded flows with constant physical properties. Beyond $y^+ = 5$, higher order terms in the full expansion of the law of the wall begin to have influence (Townsend, 1976).

The buffer layer is a region involving competitive balance of both the viscous shear caused by the strong velocity gradient near the wall, against the Reynolds stresses. Unlike the viscous sublayer and logarithmic law region, there is no known explicit expression for the buffer layer region. Its extent is typically defined from $5 \leq y^+ < 30$ (Pope, 2000). The buffer layer features the highest turbulence intensity together with coherent flow structures affecting momentum transport and redistributing turbulent kinetic energy (TKE) in the boundary layer.

Beyond $y^+ \geq 30$, the Reynolds stresses dominate over the viscous shear stresses. This *logarithmic law* (log-law) region is typically described with the relation $u^+ = \ln(y^+) + \beta$ using constants $\kappa = 0.41$ and $\beta = 5.2$ (Pope, 2000). The upper bound y^+ extent of the logarithmic law region is Reynolds number dependent, with a greater range of the log-law existing at higher Reynolds numbers. The log-law region is generally assumed to be universal in turbulent boundary layer, although the κ and β parameters become modified in the presence of surface roughness effects, pressure gradients and other flow specific features (Smits et al., 2011). Some controversy about the log-law remains in the turbulence community, and arguments have been advanced that the log-law does have a Reynolds number dependence and therefore lacks the previously assumed universality (Barenblatt & Monin, 1979; George &

Castillo, 1997; Long & Chen, 1981). It is generally agreed[1] however that the log-law is still a good description of this boundary layer region for a broad range of wall-bounded flows (George, 2006, 2007).

The combined extent of the viscous sublayer, buffer layer and logarithmic region is part of the *inner layer* of the boundary layer. The extent of the inner layer is Reynolds number dependent but is commonly quoted as $x_2/\delta \approx 0.1$ (Pope, 2000). The outer boundary layer is the region between $y^+ > 50$ and the edge of the boundary layer $\delta^+ = \delta u_\tau/\nu$ where effects of viscosity on the mean velocity $\langle U_1 \rangle$ can be neglected.

The outer layer overlaps with the inner layer in the log-law region. Similarly to how normalisation to u^+, y^+ wall units used u_τ as an inner velocity scale, a different outer scale based on U_∞ for can be used as part of the *velocity defect law* (Coles, 1956). This collapses streamwise profile curves onto a common curve for the outer layer valid for part of the logarithmic region up until the edge of the mean boundary layer thickness δ_{99}. The overlap between the log-law region and the defect law region is sometimes termed the *overlap* region (Millikan & Laboratory, 1938).

2.1.2 Turbulent flow structure

Embedded within the streamwise momentum of the mean boundary layer flow, various distinct persistent flow patterns exist within wall-turbulence. These organised turbulent flow motions or turbulent *coherent structures* (Kline & Robinson, 1990) are central to momentum transport and energy production and dissipation processes in boundary layers. A great deal of research over the last half century has been devoted to studying the organisation of turbulence within boundary layer. Different models attempt to describe phenomena in wall turbulence in terms of more elementary interactions between individual coherent structures. The structural characteristics of these flow features have been detailed in the extensive review articles of (Cantwell, 1981; Kline & Robinson, 1990; Robinson, 1991). These include flow features such as:

- **Ejections** of low-speed streaks of fluids upwards and against the mean flow direction. An unstable lifting and subsequent breakdown of the low-speed ejection region itself can also take place in a process termed *bursting* (Kline et al., 1967). Ejections (known as Q2 events) tend to occur in groups.

- **Sweeps** of high-speed fluid downward towards the wall in the mean flow direction. This can include inrush of fluid from the outer boundary layer region. These sweeps are also known as Q4 events and frequently occur after a Q2 event although have a lower velocity than the Q2 event (Adrian, 2007).

- **Vortical structures of various types.** The swirling axes of the vortical structures can be oriented in the streamwise direction (i.e., parallel to the mean flow) creating a counter-rotating vortex pair or *roll* (Bakewell Jr & Lumley, 1967; Blackwelder & Haritonidis, 1983). Other vortices have their axes in their spanwise direction (normal to the x_1-x_2 plane).

[1] A thorough review of the controversy between proponents of the log-law versus a proposed *power law* can be found in the appendix of (Örlü et al., 2010).

- **Shear layers:** Inclined shear layers near the wall. These are sometimes formed from the intersection of a Q4 event above a Q2 event (Adrian, 2007). The shear layers can also roll-up to form vortices.
- **Large scale motions** on the order of the boundary layer thickness δ. These are also referred to as turbulent bulges (Falco, 1977).

Coherent vortices are of particular importance due to their ability to transport momentum in the boundary layer. Any vortex with its axis not directly perpendicular to the wall will induce transport across the mean streamwise velocity gradient (Robinson, 1991). It will be presented how the induced turbulent flow field from these vortical motions is a major mechanism behind the production of turbulent kinetic energy (TKE) production in the boundary layer.

Although the strict and universally accepted definition of a vortex can be a debatable topic in turbulence research, a commonly adopted definition in boundary layer research was provided by (Robinson et al., 1989): "A vortex exists when instantaneous streamlines mapped onto a plane normal to the vortex core exhibit a roughly circular or spiral pattern, when viewed from a reference frame moving with the centre of the vortex core". Although other definitions are possible (Blackwelder & Swearingen, 1990; Lugt, 1979), this definition is particularly relevant for boundary layers since vortices and other coherent structures are convected by the streamwise momentum of the boundary layer. Therefore, to a stationary observer, the vortices embedded in the flow appear as velocity gradients, while assuming a Lagrangian reference frame of the convecting vortex reveals the full vortex circulation. This aspect is detailed in an example with 2D velocity measurements using Particle Image Velocimetry (PIV) in a non-reacting turbulent boundary layer shown below.

2.1.2.1 Vortices

Figure 2.3 below shows experimental planar velocity measurements from PIV in a non-reacting turbulent boundary layer experiment presented in detail later in this thesis. Briefly, the turbulent boundary layer flow is in the upward direction and the wall is at the left side at $x_2 = 0$mm and the FOV is of size: $(\Delta x_1, \Delta x_2) =$ (10.9,10.6)mm. The FOV begins at $x_1 =$42.4mm from the leading edge of a flat plate which is placed at the outlet of a turbulent jet. The figure shows the velocity field magnitude $|\mathbf{U}| = \sqrt{U_1^2 + U_2^2}$ with streamlines of the instantaneous velocity field $\mathbf{U} = (U_1, U_2)^{\mathrm{T}}$.

A low velocity region is expectedly present in the vicinity of the wall. Some velocity gradients separate this region from the freestream at ≈3m/s. Above $x_2 >$ 8mm, there is a slight wake region from a ceramic rod used as a flame holder in the reacting operation experiment. The flow field represents that viewed in a stationary reference frame, such as the camera or laboratory reference frame. Velocity gradients are present but no vortical pattern is apparent in the streamlines.

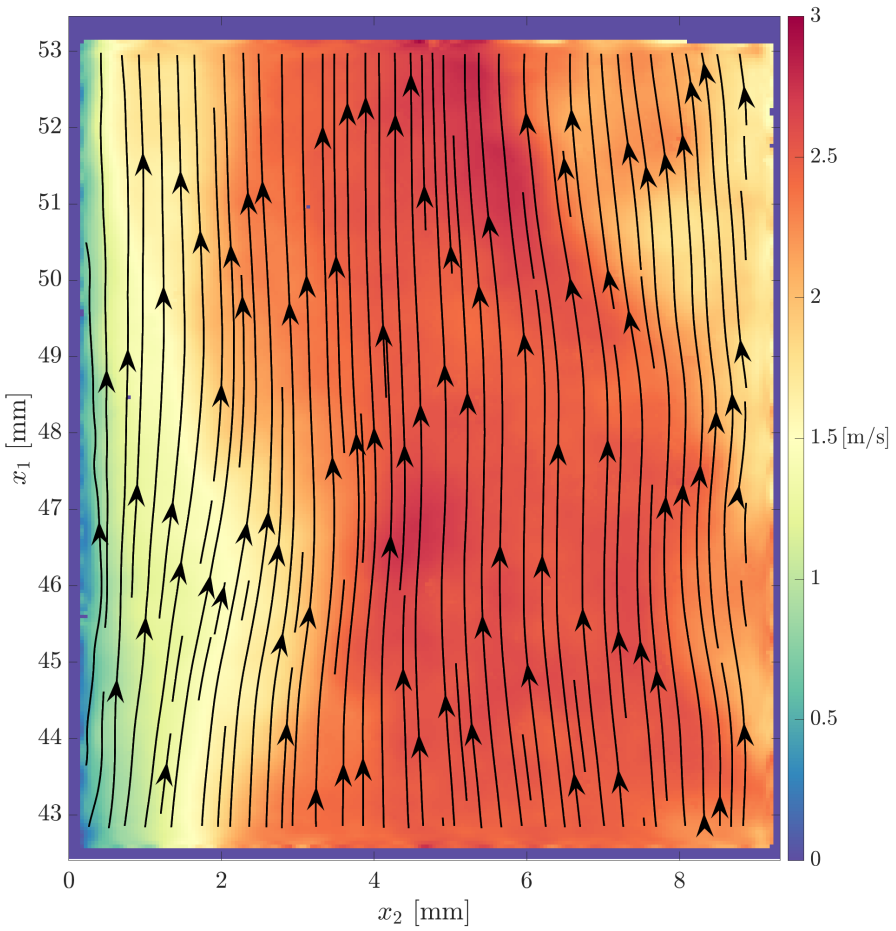

Figure 2.3: Instantaneous flow field magnitude $|\mathbf{U}|$ from a non-reacting turbulent boundary layer.

An observer linearly translating in the streamwise direction with the flow at a speed $U_{1,g}$ would observe a different velocity field given by $\mathbf{U_G} = (U_1 - U_{1,G}, U_2)$. Subtraction of the constant velocity value $U_{1,G}$ changes the reference frame from one of stationary observer to a Lagrangian point of reference moving with the flow. This is exampled in Figure 2.4 where different streamwise values of $U_{1,G} = [1.5, 2, 3]$m/s are subtracted from the flow field in Figure 2.3.

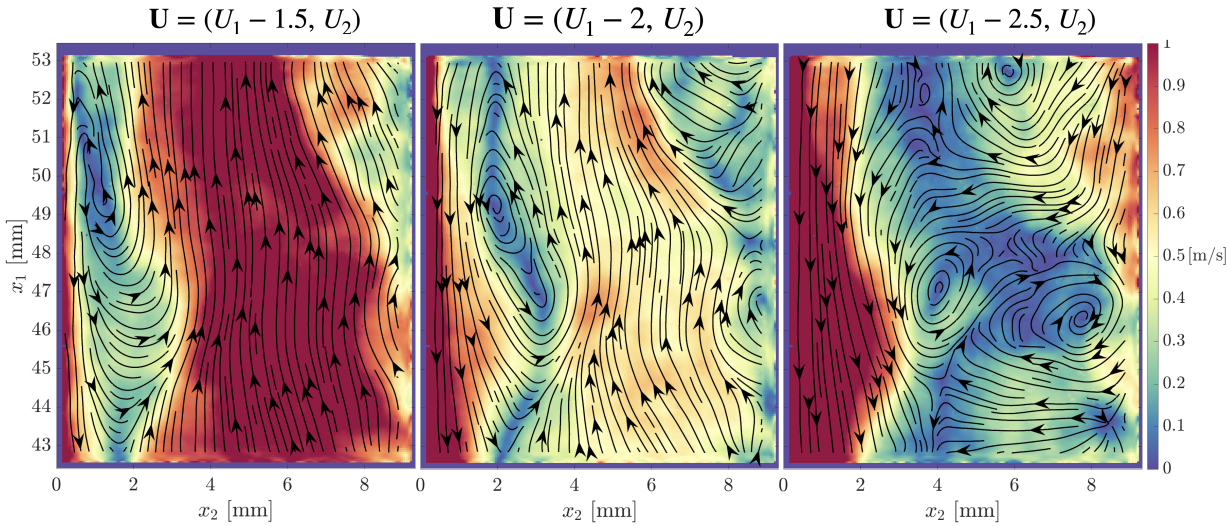

Figure 2.4: Vortices visualised by Galilean decomposition using different convection velocities $U_{1,G}$. Colour scale denotes the respective velocity magnitude $|\mathbf{U}|$.

Subtraction of $U_{1,G}$ in Figure 2.4 (left) produces a distorted vortical pattern in proximity of the wall. This structure has partially closed streamlines and does not resemble a full vortex circulation. Subtraction of the correct vortex convection velocity at $U_{1,G} = 2\text{m/s}$, i.e., the velocity at or near the vortex core centre, produces the closed-streamline flow field in Figure 2.4 (middle) confirming a vortex as per the definition of (Kline & Robinson, 1990). The vortex in Figure 2.4 left and Figure 2.4 middle is actually the same dynamic phenomenon, however, it is observed differently depending on the frame of reference. The closed-streamline pattern of Figure 2.4 middle confirms that $U_{1,G}$ is at or at least very near the convection velocity of the vortex core. This results in the vanishing velocity magnitude $\mathbf{U_G} \approx 0$ at the vortex centre. Increasing $U_{1,G}$ further to 2.5m/s in Figure 2.4 (right) reveals several different vortices further away from the wall. The region of the FOV where a vortex was visualised with $U_{1,G} = 1.5, 2\text{m/s}$ has disappeared.

This method of subtracting a constant flow field value is termed *Galilean* decomposition (Adrian, Christensen, & Liu, 2000) and is commonly exampled in boundary layer studies to verify if a true vortex is present (Adrian, Meinhart, & Tomkins, 2000; Jodai & Elsinga, 2016; Natrajan et al., 2007; Y. Wu & Christensen, 2006). Since one convection velocity $U_{1,G}$ is selected, only vortices advecting at or sufficiently near that convection velocity are revealed. Therefore, to reveal every vortex present a range of convection velocities must be tested and the resulting vortical flow fields detected cannot all simultaneously observed in a common frame of reference. The Navier-Stokes equations are Galilean invariant (Pope, 2000) therefore there is no immediate advantage of preferring one reference frame over another.

Decomposition methods in general seek to separate the flow field into the component including the vortex itself, and a background component that is advecting the vortex. The superposition of the two fields; the vortical flow, together with the underlying convective flow recovers the full instantaneous flow field viewed by a stationary observer. Other decomposition methods to subtract the background component include frequency filtering schemes (Clark & Kook, 2018), proper orthogonal decomposition (POD) or its variations such as spectral POD, and Large Eddy Simulation filtering schemes (Adrian et al., 2000) for example. The classical

Reynolds decomposition is another method of revealing the flow field as observed in a reference frame moving with the mean flow. This has been shown to reveal a broad range of vortices in non-reacting boundary layers (Adrian, Christensen, & Liu, 2000), since many vortices have a convection velocity broadly similar to the local mean (Elsinga et al., 2012). The resulting fluctuating field u_i also has the advantage of producing directly interpretable turbulence quantities such as the Reynolds stress $-\rho\langle u_i u_j \rangle$.

2.1.2.2 Galilean invariant vortex detection

Rather than relying on the vector field topology, kinematic flow quantities can be used to identify local regions of vortical motions embedded within the flow. The use of vorticity $\Omega = \partial U_1/\partial x_2 - \partial U_2/\partial x_1$ has been widely used to detect vortex cores in free shear flows (Bisset et al., 1990; Metcalfe et al., 1987). However, in the case of many wall-bounded flows, the background shear due to the wall ($\partial U_1/\partial x_2$) can be comparable to the vorticity magnitude in the vortex, resulting in it being masked (Jeong & Hussain, 1995). Thus, the vortex core, may not always be sufficiently detectable from the instantaneous vorticity Ω alone. The relationship between strong vorticity and actual vortices convected by the boundary layer flow has therefore been described as being rather weak, particularly in the near-wall region (Robinson et al., 1989). Vorticity can also assume increased values and not indicate a vortex. This effect is clearly evident in solutions of the so-called 'blasius' laminar boundary layer (Blasius, 1907), where the wall-normal Ω distribution peaks at the wall but no coherent structure or vortex is ever present.

Galilean invariant vortex identification methods, such as the well-known Q criterion (Hunt et al., 1988), λ_2 criterion (Jeong & Hussain, 1995), Δ criterion (Cucitore et al., 1999) and swirling strength (λ_{ci} criterion) (Zhou et al., 1999), are therefore preferred to detect vortical structures being advected by the flow. These techniques detect regions of vortical motion in a manner which, in principle, is independent of the reference frame the method is used in. With the exception of the λ_2 criterion, the other criteria can in fact all be expressed in terms of the components available from the swirling strength λ_{ci} (P. Chakraborty et al., 2005) which has been used extensively in pioneering wall turbulence studies including (Adrian, Meinhart, & Tomkins, 2000; Christensen & Adrian, 2001; Gao et al., 2011; Natrajan et al., 2007; Y. Wu & Christensen, 2006; Zhou et al., 1999).

The swirling strength is derived from the eigenvalue decomposition of the velocity gradient tensor $\nabla\mathbf{U}$:

$$\nabla\mathbf{U} = \begin{bmatrix} \dfrac{\partial U_1}{\partial x_1} & \dfrac{\partial U_1}{\partial x_2} & \dfrac{\partial U_1}{\partial x_3} \\ \dfrac{\partial U_2}{\partial x_1} & \dfrac{\partial U_2}{\partial x_2} & \dfrac{\partial U_2}{\partial x_3} \\ \dfrac{\partial U_3}{\partial x_1} & \dfrac{\partial U_3}{\partial x_2} & \dfrac{\partial U_3}{\partial x_3} \end{bmatrix} \tag{2.10}$$

If the flow contains a locally spiralling motion, this corresponds to the characteristic equation of the velocity gradient tensor $\nabla\mathbf{U}$ having a real eigenvalue λ_r and complex conjugate pair $\lambda_{cr} + i\lambda_{ci}$, where i is the imaginary number. The imaginary component of the complex conjugate pair is the swirling strength λ_{ci} with $\lambda_{ci} > 0$,

representing the strength of local swirling motion inside the vortex. The orbital period of one revolution following a streamline around the vortex is given by $2\pi/\lambda_{ci}$. Therefore, the higher the value of λ_{ci}, the faster a massless tracer completes a revolution around the vortex axis and the stronger the vortex. This has the advantage of giving the swirling strength a clear kinematic interpretation. Additionally, it is possible to optionally determine further properties of the vortex from the ratio $\lambda_{cr}/\lambda_{ci}$ termed the *inverse spiralling compactness* (P. Chakraborty et al., 2005) which is a measure of the radial distance traversed by a massless tracer during one revolution around the vortex. A visual interpretation of these quantities is available in (P. Chakraborty et al., 2005; Haimes & Kenwright, 1999). In full 3D measurements where $\nabla\mathbf{U}$ is a 3×3 matrix, it is possible to determine the swirling axis of the vortex from the eigenvector $\mathbf{v}_r$ associated to the real eigenvalue λ_r. In 2D planar data, only a 2×2 matrix subset of $\nabla\mathbf{U}$ is available therefore determining the true orientation of the vortex swirling axis in 3D space is not possible.

In 2D, some minor differences between the Q, Δ and λ_{ci} criteria result due to slightly different weightings of divergence ($\partial U_i/\partial x_i$) terms when the 2D form of each is derived. In general, very similar results are obtained in 2D from any of the mentioned derivative-based vortex detection methods because of the similarity of their respective 2D equations as discussed in (Q. Chen et al., 2015). Generally, swirling strength can be considered the most lenient in 2D, i.e., accepts more vortices while the Q criterion is the strictest and rejects weaker vortices.

The swirling strength λ_{ci}, calculated from the instantaneous velocity field $\mathbf{U}$, is shown for the example from Figure 2.4. The 3 vortices revealed in the two previous Galilean decompositions ($U_{1,G} = 2, 2.5$ m/s) are overlaid. The vortex centres (regions of vanishing velocity magnitude) closely coincide with local maxima of the swirling strength field. As demonstrated in Figure 2.4, varying the the translation velocity $U_{1,G}$ changes the observed vortex position slightly. If $U_{1,G}$ was selected based on the pointwise instantaneous velocity at local maxima of the swirling strength field, the overlap of the vortex cores with swirlings strength patches would be in direct alignment, as also exampled in studies such as (Adrian, Christensen, & Liu, 2000; Adrian, Meinhart, & Tomkins, 2000). Note however, that only 2 of the 3 vortices can be visualised in the same frame of reference but all three are overlaid simultaneously in Figure 2.4.

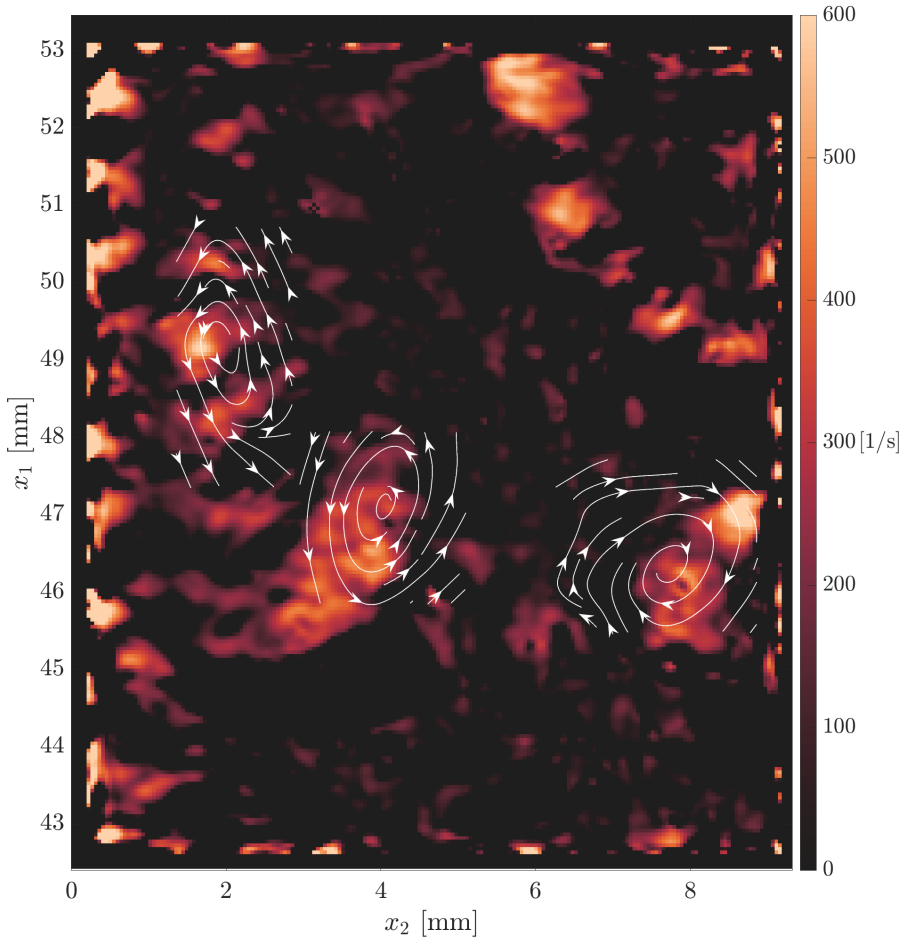

Figure 2.5: The swirling strength λ_{ci} calculated for the previous velocity field in Figure 2.4). A local Galilean decomposition is visualised around three regions of λ_{ci}.

Aside from the vortex core itself, the surrounding flow motions organised around and induced by a vortex are key in the energy transport processes in the boundary layer. Several conceptual models of elementary vortex structures such as the attached eddy hypothesis (Townsend, 1976) and hairpin or horsehoe vortex model (Adrian, 2007; Adrian, Meinhart, & Tomkins, 2000). A thorough review of these models is presented in (Robinson et al., 1989) and (Robinson, 1991). The hairpin vortex model, originally attributable to (Theodorsen, 1952), gained traction due to its ability to potentially explain a wide variety of flow statistics (Perry & Chong, 1982; Perry et al., 1986) and also transient observations (Bandyopadhyay, 1980; Head & Bandyopadhyay, 1981). It should be considered however, that although the existence of low and high speed streaks and quadrant events throughout the turbulent boundary layer is now commonly accepted, some controversy remains in models of vortical structures (Wang et al., 2019).

A depiction of the hairpin vortex model is shown in Figure 2.6. The legs of the hairpin structure are vortices oriented in the streamwise direction. These legs rotate (in either sense), tilting upwards in the streamwise direction and connecting to form an arch at the vortex head. The hairpin vortex induces secondary flow motions such as ejection (Q2) and sweep (Q4) events in the local vicinity of the hairpin. The depiction in Figure 2.6 is highly idealised and the hairpin is rarely, symmetrical or

isolated from the influence of surrounding hairpins. Many observations of hairpins feature incomplete arches, existing in a tilted 'tornado-like' form (Robinson et al., 1989). A hairpin vortex can lead to a complex nonlinear process of *autogeneration* leading to the creation of new *packets* of hairpin vortices (Goudar et al., 2016; Jodai & Elsinga, 2016; Zhou et al., 1999) in streamwise succession. These hairpin packets can work cooperatively to increase the Reynolds stress (Adrian, Meinhart, & Tomkins, 2000; Dennis & Nickels, 2011; Ganapathisubramani et al., 2003). In the following section, the in-plane projection of the turbulent flow field containing the induced sweep (Q4) and ejection (Q2) motions will be analysed and their relationship to energy transport will be presented.

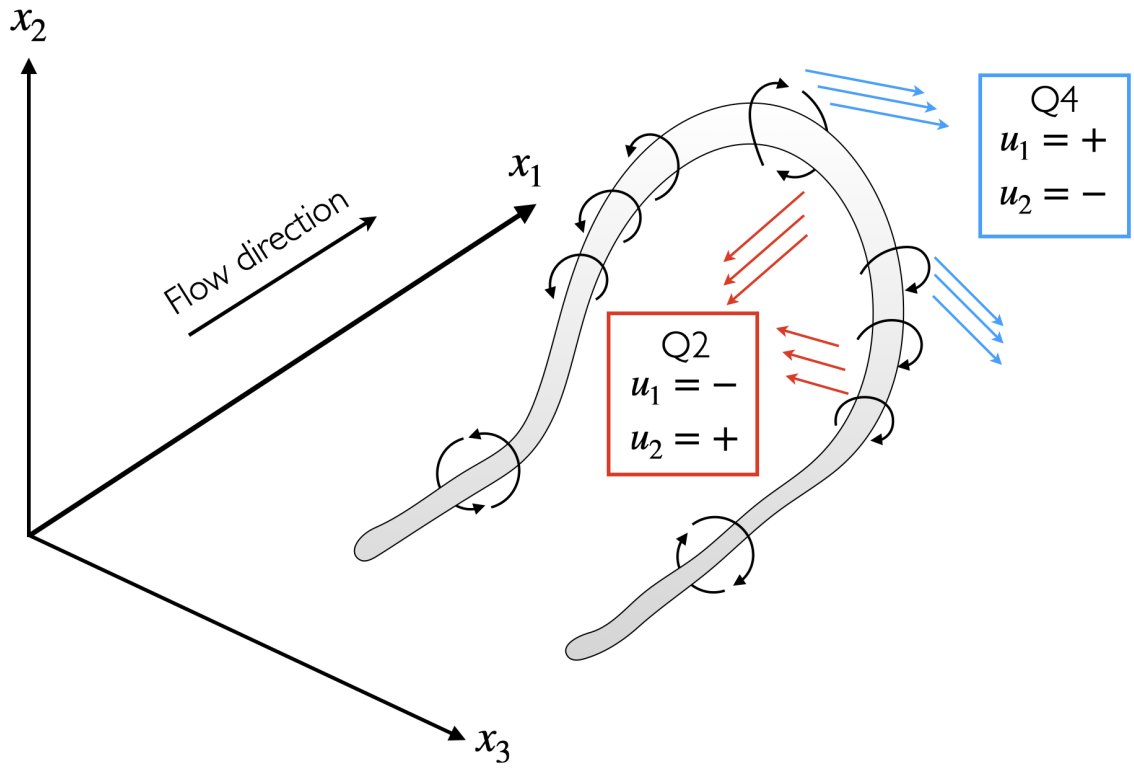

Figure 2.6: Depiction of the hairpin vortex model from (Adrian, 2007; Theodorsen, 1952). Frame of reference is moving with the flow.

2.1.3 Quadrant analysis

The fluctuating velocity field u_i is important in energy and momentum transport, as energy is extracted from the mean flow and converted into the turbulent fluctuations from large to small length scales through an energy cascade, eventually dissipating as thermal energy (Tennekes & Lumley, 1972). The near-wall region in boundary layers is where most of the turbulence activity is located, with the majority of the TKE production occurring in the viscous sublayer and buffer layer (Klebanoff, 1955). The role of the fluctuating velocity field is key in the mixing dynamics of wall-bounded turbulent flows. In particular, the quasi-periodic presence of strong coherent motions such as ejection (Q2) and sweep (Q4) events which are a mechanism of turbulence production, simultaneously transport momentum across the boundary layer (Robinson, 1991).

Quadrant analysis is a methodology originally introduced by (Wallace et al., 1972) to characterise coherent flow motions from the landmark visualisation studies of (Corino & Brodkey, 1969) and (Kline et al., 1967). The principle is to partition the velocity fluctuations based on their location in the Reynolds stress plane u_1u_2 shown in Figure 2.7 below. The relevant quadrant assignment (Q1 - Q4) of a velocity vector is based on the sign of the streamwise u_1 and wall-normal u_2 fluctuating velocity. These quadrant events are termed outward (Q1: $u_1 = +, u_2 = +$) interaction, ejection (Q2: $u_1 = -, u_2 = +$), inward interaction (Q3: $u_1 = -, u_2 = -$) and sweep (Q4: $u_1 = +, u_2 = -$).

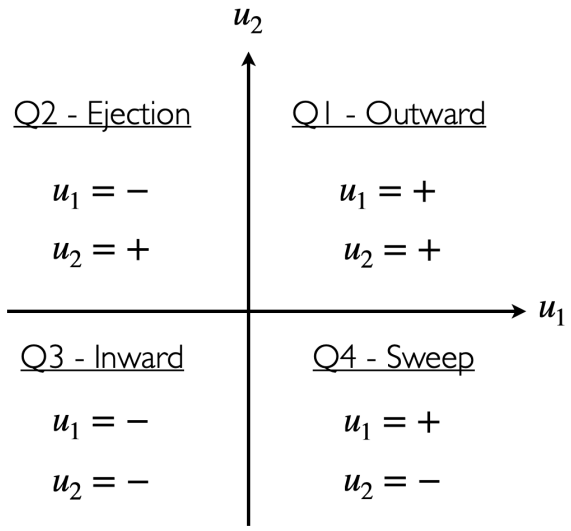

Figure 2.7: The quadrant splitting scheme of (Wallace et al., 1972).

A fluctuating velocity field from PIV demonstrating an ejection event and other features of the structure of wall-bounded turbulence is shown in Figure 2.8. The colour indicates the Reynolds stress u_1u_2. Blue is therefore associated to any regions of Q1 and Q3 while Q2 and Q4 are red. The large dark red region is associated to a strong Q2 event in the buffer layer. A vortex is present above the Q2 region. This is likely the planar projection through a hairpin vortex as shown in Figure 2.6 since, together with shear layer at an angle of $\approx 45^{\circ}$, it satisfies the hairpin signature described in (Adrian, 2007). Regions further from the wall (>8mm) show strong Reynolds stresses. These are from the wake region behind the flame holder and are not boundary layer sweep or ejection events in the canonical sense.

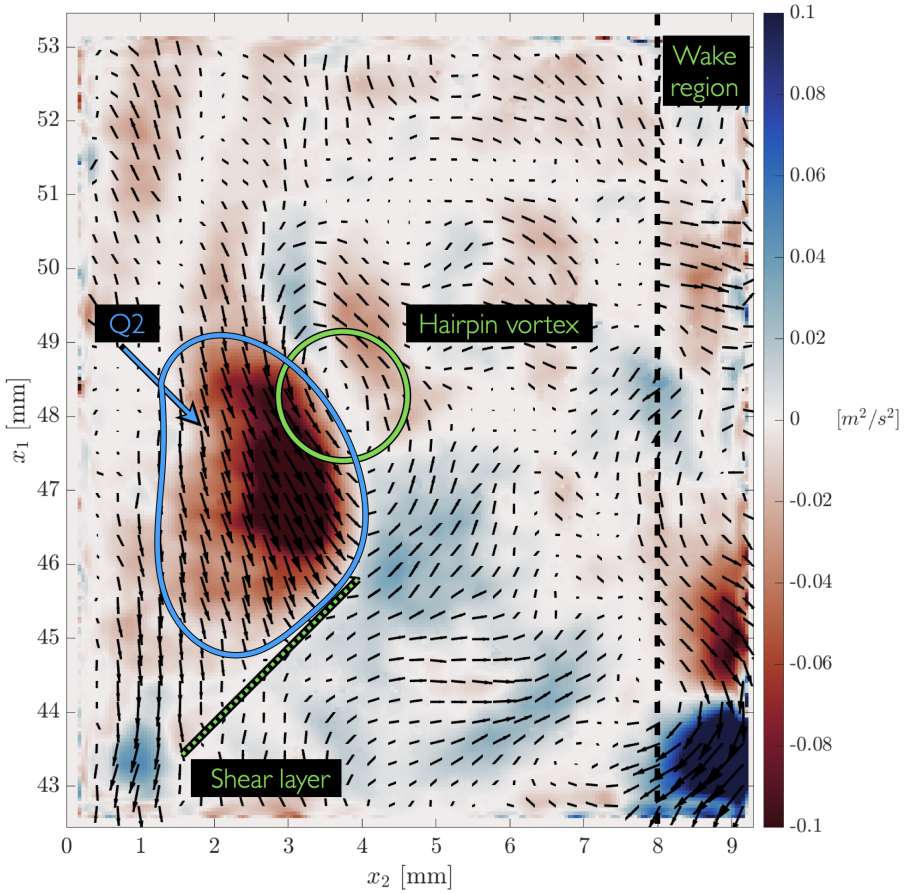

Figure 2.8: Reynolds stress u_1u_2 in a non-reacting boundary layer. The sweep and ejection regions are labelled. Vector field is shown downsampled $\times 6$.

The energetic significance of quadrant events is apparent when considering the transport of turbulent kinetic energy (TKE) equation which features the TKE *production* term:

$$\mathcal{P} = -\langle u_1 u_2 \rangle \frac{\partial \langle U_1 \rangle}{\partial x_2} \tag{2.11}$$

Q2 and Q4 events, which produce a negative u_1u_2 product, will result in positive TKE production $\mathcal{P}$. Conversely, Q1 and Q3 events producing a positive u_1u_2 product result in $\mathcal{P}$ acting as a sink term. It should be remembered that other terms including viscous dissipation, turbulent diffusion, and dissipation transport are also present in the TKE transport equation (Schlichting & Gersten, 2016). $\mathcal{P}$ is a dominant source of streamwise velocity fluctuations $\langle u_1^2 \rangle$ across the boundary layer, with the action of pressure redistribute energy from this component to the others $\langle u_2^2 \rangle$ and $\langle u_3^2 \rangle$ (Pope, 2000; Spalart, 1988). Thus, accurately resolving the transient dynamics within the turbulent fluctuations u_i is key in the energy transport, as well as in mechanisms of mixing and entrainment.

The quadrant distribution of u_1u_2 is shown in Figure 2.9 below. This is also partitioned into the different quadrants. This resembles the well-known canonical case (Wallace, 2016) where the presence of Q2 and Q4 events in the buffer layer peaks the turbulence activity in that region. Conversely, the presence of Q1 and Q3 is minimal.

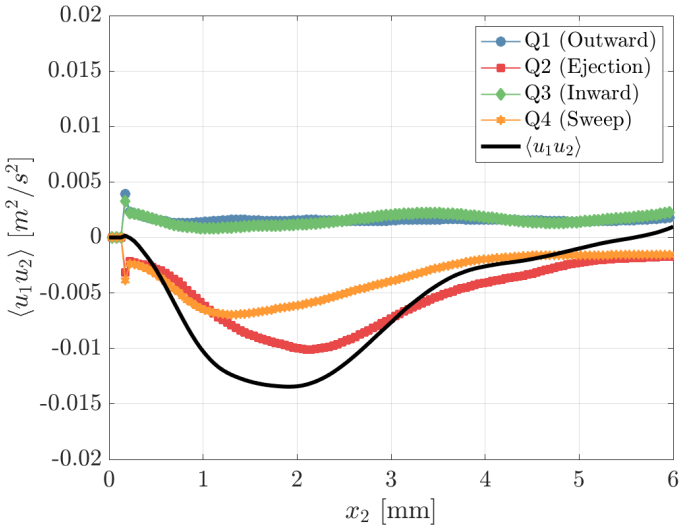

Figure 2.9: Quadrant distribution in a non-reacting boundary layer measured using PIV.

2.2 Particle image velocimetry

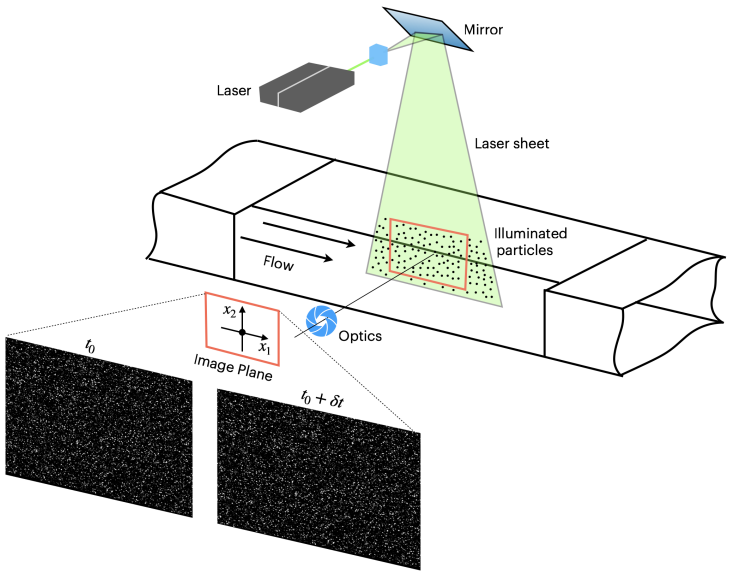

Figure 2.10: A generic PIV setup.

Particle image velocimetry (PIV) has become an established method of obtaining velocity measurements in fluid dynamics (Raffel et al., 2018). A fluid flow is entrained with particles with properties such as size and density selected so as to faithfully follow the flow. A high-intensity laser fires to illuminate a 2D sheet segment within the flow being investigated. The laser pulse frequency is synchronised with a camera shutter to obtain successive pairs of images of particle motion within the laser sheet. A prototypical PIV setup is shown in Figure 2.10.

To determine the velocity in the image plane, each PIV image is subdivided into interrogation windows (IWs), which are cross-correlated between two image frames I_0 and I_1 according to:

$$R(\Delta x_1, \Delta x_2) = \sum_{i=-n}^{n} \sum_{j=-m}^{m} I_0(i,j) \cdot I_1(i + \Delta x_1, j + \Delta x_2) \tag{2.12}$$

where n and m are typically half the IW size and Δx_i is the sample shift of an IW from I_0 in the respective x_1 and x_2 directions. Equation 2.12 is typically normalised by the intensity variance of each IW and computed via fast fourier transform (FFT) to accelerate computation. For each sample shift Δx_i, the respective correlation value $R(\Delta x_1, \Delta x_2)$ between the IWs is calculated. This calculation is repeated across the full image region where the peak value of each correlation map R indicates the statistically averaged velocity of the particles in a given IW. Numerous improvements to the basic method described have been proposed over the years, including overlapping interrogation windows, image deformation, Gaussian fitting of the correlation function, multiple pass correlation and others described in (Raffel et al., 2018). Cross-correlation-based PIV has become a mature diagnostic technique that is robust, efficient and well-understood in terms of its sources of error and theoretical underpinnings.

However, a fundamental limitation still exists in that the spatial resolution of PIV is directly related to the smallest size of the IW (Kähler et al., 2012a). Since the velocity vector represents a spatially averaged velocity of particles within each IW, the estimated velocity is a low-pass filtered version of the true fluid flow, which is problematic if turbulent fluctuations and velocity gradients are present within the IW itself. Particularly in the case of wall-bounded flows, which always feature strong velocity gradients near the wall, obtaining accurate and reliable velocity measurements in the vicinity of the wall can present challenges for cross-correlation-based PIV. The low-pass filtering effect increases uncertainty in regions of high velocity gradients due to an increased spread and biasing of the correlation peak (Kähler et al., 2012a, 2012b; Raffel et al., 2018; Scarano & Riethmuller, 2000).

Particle tracking velocimetry (PTV) is a method which attempts to detect and subsequently match individual tracer particles between frames to determine their velocity. In contrast to PIV, PTV typically requires lower seeding densities to minimise ambiguities in matching the same particle across frames. PTV is sometimes used as a subsequent step following an initial PIV result in hybrid PIV + PTV algorithms (Keane et al., 1995; Stitou & Riethmuller, 2001). Use of PIV + PTV can significantly improve the achievable spatial resolution over PIV alone (Kähler et al., 2012a), without requiring low seeding densities and has been employed to study boundary layer flows previously (Ding et al., 2019; Kähler et al., 2012b; Renaud et al., 2018). However, PTV vector fields often contain higher noise levels in the signal, and sufficient filtering or direct spatial averaging is required to mitigate this noise. Additionally, PTV produces an unstructured grid arrangement of the vector field, requiring interpolation to a structured mesh before calculating derived quantities, such as the wall shear stress γ.

Another velocimetry technique, known as single-pixel ensemble-correlation, is able to extract mean velocity fields with both increased accuracy over cross-correlation-based PIV (Westerweel et al., 2004), and significantly improved spatial resolution that is limited by the particle image size (Kähler et al., 2012a). The image sequence

is first divided into two sets separating the first and second frames of the acquired image pairs. The principle is to correlate the intensity time-history of each pixel from the first image frame with its neighbours in the second frame. The correlation peak can then be used to determine the ensemble averaged mean velocity. This technique requires a sufficiently large number of images, typically thousands, for the correlation peak to become sufficiently distinguishable from background noise. This method, however, is limited to extraction of the ensemble average velocities only, so transient phenomena cannot be recovered and the method's applicability is restricted to periodic and quasi-stationary flows.

An alternative method of determining motion in the image plane, avoiding the limitations of traditional correlation or PTV-based approaches, is to approach the fundamental problem of motion estimation in the image plane from an alternative perspective and directly consider the relationship of the imaged motion to the spatial variations in pixel intensity. Such a method, originating from the field of computer vision, is known as optical flow.

2.3 Optical flow principles

Optical flow is the apparent velocity field associated with the motion of brightness intensity patterns in an image sequence (Horn & Schunck, 1981). Fundamentally, optical flow can be understood as the motion field that leads an image at time t to advance to its state at $t + \delta t$ under the constraint that image intensity is conserved. This assumption of photometric invariance states that pixel intensity is neither created or destroyed, but simply transported between successive images. Expressing this as the total derivative:

$$\frac{DI(\boldsymbol{x}, t)}{Dt} = 0 \tag{2.13}$$

Taking the first-order Taylor expansion of equation 2.13 leads to the *Optical Flow Constraint Equation* (OFCE):

$$\frac{\partial I(\boldsymbol{x}, t)}{\partial t} + \mathbf{U}(\boldsymbol{x}, t) \cdot \nabla I(\boldsymbol{x}, t) = 0 \tag{2.14}$$

where $I(\boldsymbol{x}, t)$ is the brightness intensity at pixel locations $\boldsymbol{x} = (x_1, x_2)^T$ in the image domain Ω and $\mathbf{U}(\boldsymbol{x}, t) = (U_1(\boldsymbol{x}, t), U_2(\boldsymbol{x}, t))^T$ is the two-dimensional image-plane displacement. Equation 2.14 is recognisable as the transport equation of a passive scalar in a divergence-free flow (T. Liu & Shen, 2008).

The geometric interpretation of equation 2.14 is easily visible by rearranging it in the straight line form $U_2 = -(\partial_{x_1} U_1 + \partial_t I)/\partial_{x_2} I$ shown in Figure 2.11. Separating the optical flow vector into normal and tangential components $\mathbf{U} = U_N + U_T$, the displacement in the direction of the brightness gradient vector ∇I can be calculated by:

$$U_N = \frac{\partial_t I}{\sqrt{(\partial_{x_1} I)^2 + (\partial_{x_2} I)^2}} \tag{2.15}$$

The result of of this expression is that motion across contours of image brightness (i.e. along the brightness gradient vector) can be calculated. It is therefore known

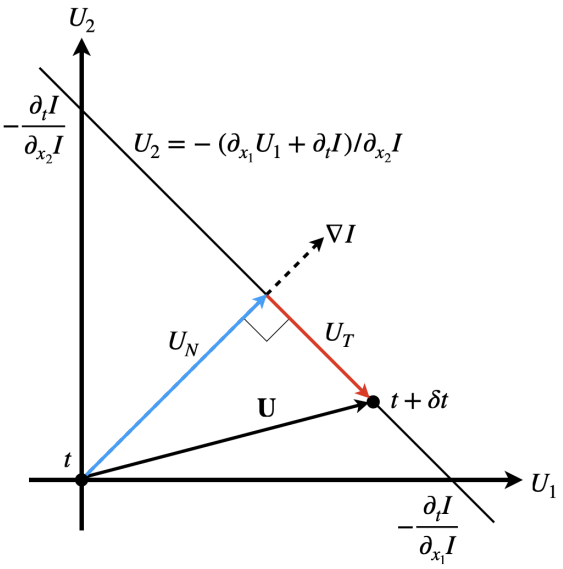

Figure 2.11: The optical flow constraint line. The displacement of a pixel must lie at some point along this line at $t + \delta t$.

that the motion of every pixel in the image lies at some point along their respective OFCE lines, but there is no further information available from the image data alone that can be used to resolve the tangential motion component (U_T) - making equation 2.14 under-constrained. This ambiguity in motion along contours of image brightness is known as *aperture problem* (Beauchemin & Barron, 1995; Ullman, 1979), illustrated below in Figure 2.12. The aperture problem is a fundamental problem initially facing any endeavour to recover motion from 2D images, even in the context of the human visual system (Kane et al., 2011) [2].

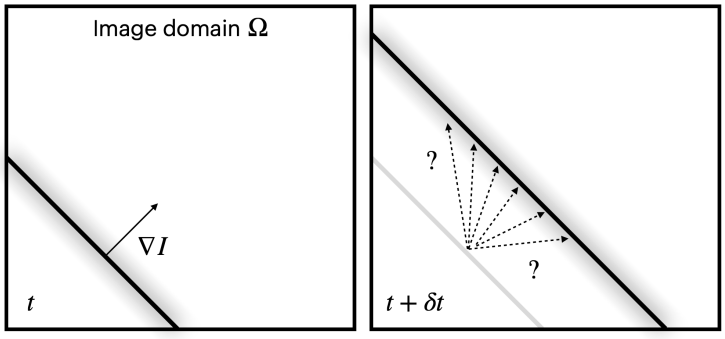

Figure 2.12: Depiction of the aperture problem. Viewed in a finite-sized image or 'aperture', only one motion component in the direction of the brightness gradient vector ∇I of the translating line can be determined. Motion across the brightness gradient vector (i.e., along the pattern line) is ambiguous since it does not result in spatial variation of the local brightness intensity.

The fundamental goal of all motion estimation in general is to overcome this ill-posedness and thus estimate the second tangential component with certainty. For closure of the motion ambiguity created by the aperture, some additional information

[2] The well-known spinning 'barber pole' optical illusion is based on this very principle.

or constraint on the motion $\mathbf{U}$ is needed. Different such methods exist including region-based, frequency-based and phase-based matching techniques (Barron et al., 1994). Cross-correlation of intensity patterns contained in subregions (IWs) as done in PIV can be shown to have an equivalence to the minimisation of equation 2.16 to be presented within individual IWs (Heitz et al., 2010). This reduces the number of variables (i.e., number of velocity vectors) to solve for, reducing spatial resolution but circumventing the aperture problem since there are now more pixels available in the image then velocity vectors. This is essentially a reduction of the dimensionality of the problem, and is also used in *local* OF approaches using window-based methods such as the famous Lukas-Kanade OF algorithm (Lucas & Kanade, 1981). Another family of OF methods achieve a *dense* (i.e. 1 vector per pixel) motion field and are known as *global* or *variational* OF. The seminal work of (Horn & Schunck, 1981) originally proposed such an approach to cast the optical flow problem as a coupled minimisation involving two terms; (1) the data term, which relates the brightness intensity $I(\boldsymbol{x}, t)$ to the image-plane motion $\mathbf{U}(\boldsymbol{x}, t)$, and (2) a regularization term that enforces an assumed spatial coherence or a priori smoothness to the velocity field.

2.3.1 Data term

The data term establishes the relationship between a measurement in the image plane, being the brightness intensity $I(\boldsymbol{x}, t)$, and the pixel displacements in the image plane $\mathbf{U}$ via the OFCE. The differential form of the OFCE in equation 2.14 is only valid for small pixel displacements and smooth image gradients, making it inappropriate for large displacements between images. Assuming a constant velocity between an image pair I_0, I_1 and integrating the OFCE over a unit time interval yields the full, non-linear representation of the optical flow problem known as the *displaced frame difference* (DFD):

$$I_0(\boldsymbol{x}) - I_1(\boldsymbol{x} + \mathbf{U}(\boldsymbol{x})) = 0 \tag{2.16}$$

The term $I_1(\boldsymbol{x}+\mathbf{U}(\boldsymbol{x}))$ is known as the *motion-compensated* image, also referred to as the warped image. It can be understood that the motion field $\mathbf{U}(\boldsymbol{x})$ that warps the second image (I_1) to the first image (I_0) to conserve image intensity describes the positional change of every pixel between the two images. The data term is incorporated into a quadratic penalty function for minimisation:

$$J_D = \frac{1}{2} \int_\Omega \left[I_0(\boldsymbol{x}) - I_1(\boldsymbol{x} + \mathbf{U}(\boldsymbol{x})) \right]^2 d\boldsymbol{x} \tag{2.17}$$

The assumption of photometric invariance is not strictly valid in the presence of image noise, out-of-plane motion, illumination change, or in regions at the edges of the image or in occluded parts. By formulating the solution of the DFD via a minimisation as above, it is possible to solve for the velocity field $\mathbf{U}(\boldsymbol{x})$ that *best* conforms to the conservation of intensity. While the original formulation from (Horn & Schunck, 1981) used the OFCE as the data term and is common in computer vision, use of the DFD is valid for all magnitudes of displacement and is preferable in fluid velocimetry (Corpetti et al., 2002). The DFD alone is also similarly ill-posed as the OFCE and requires some additional information on the motion for the resulting minimisation of equation 2.17 to be convex. Unlike the linear OFCE, the DFD is

highly non-linear in $\mathbf{U}$ and therefore requires a robust optimisation strategy to avoid becoming trapped in local minima and achieving poor solutions. The advantages of the wavelet multiresolution framework for this aspect will be discussed in Chapter 3.

2.3.2 Regularization term

In order to close the ill-posedness of the optical flow problem, an additional *regularization* term is necessary to impose a constraint on the estimated velocity field. The ultimate purpose of regularization is to provide additional information about the velocity field to compensate for image regions where the data term alone cannot recover motion, such as tangentially along image contours, as well regions of constant, uniform image features where spatiotemporal image gradients vanish. In these regions, regularization acts as a type of filtering or diffusion process where information in regions where motion can be determined is diffused to regions of ambiguous motion to assist estimation (Horn & Schunck, 1981). Using a quadratic penalty function ($J_R = |\cdot|^2$) for the regularization term results in this diffusion process being isotropic (Weickert & Schnörr, 2001). It is also possible to make this diffusion process anisotropic using image-driven (Enkelmann & Nagel, 1986) or flow-driven regularization schemes (Zach et al., 2007) Regularization also functions as a type of outlier rejection process during the minimisation process (Heitz et al., 2010) and reduces the susceptibility of the estimated vector field to noise and imaging imperfections.

The regularization term depends solely on the velocity field and introduces a constraint on the spatial continuity of the velocity field. Intuitively, this is understood as the visually perceived 'smoothness' of the flow field and therefore is related to the spatial derivatives of the velocity. The smoothness of a function is a property that can be defined by the number of derivatives it has that are continuous (Seroussi & Barsky, 1991). By incorporating particular velocity derivatives in the regularization term, an a priori assumption is made about the degree of spatial continuity in the velocity field. The original optical flow formulation by Horn and Schunck used a regularization term involving the first-order derivatives of the velocity field:

$$\begin{aligned} J_R &= \int_\Omega |\nabla U_1|^2 + |\nabla U_2|^2 d\boldsymbol{x} \\ &= \int_\Omega \left(\frac{\partial U_1}{\partial x_1}\right)^2 + \left(\frac{\partial U_1}{\partial x_2}\right)^2 + \left(\frac{\partial U_2}{\partial x_1}\right)^2 + \left(\frac{\partial U_2}{\partial x_2}\right)^2 d\boldsymbol{x} \end{aligned} \tag{2.18}$$

This regularization term penalises the first-order derivatives of the velocity field and therefore encourages the velocity field to have weak spatial gradients with groups of pixels all primarily moving in the same direction. This is usually sufficient in OF applications in computer vision, where rigid-body motion primarily features linear translation and therefore mild spatial gradients. In the more complex dynamics of fluid flow, the attenuation of velocity gradients leads to a non-physical smoothing of flow features and underestimates of derived quantities such as vorticity and divergence (Corpetti et al., 2002). This regularization has been successfully used in fluid velocimetry in a few past studies (Khalid et al., 2017; T. Liu & Shen, 2008; T. Liu et al., 2015) primarily due to its simplicity. Significant improvements in accuracy

can be achieved by incorporating higher order derivatives in the regularization term J_R (Heitz et al., 2010). In the literature, multiple different high-order regularization terms have been proposed, such as the second-order regularization (Kadri-Harouna et al., 2013), second-order divergence and curl regularization (Suter, 1994), divergence regularization (X. Chen et al., 2015) and Laplacian regularization, which was in fact proposed in the original work of (Horn & Schunck, 1981) together with equation 2.18. These terms using higher-order derivative are typically evaluated with finite difference schemes which can lead to more complex discretisation methods to avoid numerical instabilities (Corpetti et al., 2006; Yuan et al., 2007). In Chapter 3, efficient evaluation of such schemes by computing velocity derivatives in the wavelet domain will be presented.

2.3.3 Minimisation

The regularization term is added to equation 2.17 with an empirical weighting parameter λ and cast as a minimisation problem to form the full objective function:

$$\hat{\mathbf{U}} = \arg\min_{\mathbf{U}} J_D(I_0, I_1, \mathbf{U}) + \lambda J_R(\mathbf{U}) \tag{2.19}$$

The resulting minimisation is performed via an optimisation algorithm that seeks a per-pixel vector field transformation $\hat{\mathbf{U}}$ that maps one image onto the subsequent to best: (1) conserve pixel brightness intensity and (2) enforce the velocity field regularity defined by J_R. Unlike in traditional cross-correlation PIV, there are no separate ad-hoc smoothing or outlier detection or vector replacement postprocessing steps in dense OF methods. The final per-pixel OF velocity field is all calculated in one coherent single process. The weighting parameter λ in equation 2.19 establishes the relative importance of J_D versus J_R during the minimisation process and determines the extent to which J_R can deviate the estimated velocity field $\hat{\mathbf{U}}$ from the constraint of brightness conservation in J_D. Lower λ values place a stronger emphasis on reducing J_D during minimisation, thus attempting to better match pixel intensities between I_0 and I_1 to reduce the DFD even if the intensity variations do not correspond to the true physical motion. The result is non-physical velocity fluctuations at fine scales visible as noise in $\hat{\mathbf{U}}$. Increasing λ dampens the small-scale motion. However, an overly high λ weighting can lead to excessive smoothing of the velocity field.

Sensitivity analysis of this parameter is a key aspect in understanding the applicability of optical flow methods as an alternative diagnostic technique to studying fluid flows. The canonical form of equation 2.19, involving a data term and a regularization term, is exceedingly common in the resolution of inverse ill-posed problems studied in the image processing community such as for image denoising (Rudin et al., 1992), image inpainting (Xiao, 2017) and tomography reconstruction (Hansen & Jørgensen, 2011) to name a few. For these applications, techniques for automatic parameter selection such as generalised cross-validation (GCV) (Golub et al., 1979) and Stein's unbiased risk estimator (SURE) (Stein, 1981) have been proposed. These however, require an estimate of the noise in the considered data term and therefore their success depends on the noise estimate and also whether this noise is correlated (Hansen, 1992). Parameter selection methods not requiring a noise estimate such as the L-curve (Hansen, 1999) or its variations (Krawczyk-Stańdo & Rudnicki, 2007) and the quasi-optimality criterion (Bauer & Kindermann, 2008) have demonstrated

success in practical problems (Correia et al., 2009). These have also been shown to be provide incorrect estimates and also risk being problem specific (Reichel & Rodriguez, 2013). Furthermore, it can be proven that without knowledge of the true noise level in the data term, it is impossible for any such method to always guarantee an optimal regularization weighting, an infamous mathematical result known as the Bakushinskii veto (Bakushinskii, 1984).

Specifically in the context of OF, empirical attempts at automatic parameter selection include those based on discrepancy between the initial and motion-compensated image in the DFD (Tu et al., 2012), or heuristic methods (Stark, 2013; Zimmer et al., 2011). There has been success when formulating the optical flow problem in a Bayesian setting (Heas et al., 2013) or from dimensional analysis of the optical flow problem considered in a stochastic transport framework (S. Cai et al., 2018). These, however, are highly specific to the exact OF algorithm considered and do not generalise to other methods. Successful selection of the regularization parameter λ has been demonstrated by considering the turbulent kinetic energy (TKE) power spectrum (B. E. Schmidt & Sutton, 2019; B. E. Schmidt et al., 2021) which is directly affected by λ selection, somewhat similarly to effect of IW size in PIV results (J M Foucaut et al., 2004). This method of *a posteriori* justification of suitable λ selection based on physically correct spectrum behaviour of the fluctuating velocity field u_i show promise and is motivated by physical principles of the turbulent energy cascade (Richard & Escudie, 1999). The influence of this parameter on estimating velocity and boundary layer quantities, as well as physically-motivated selection in the context of wall-bounded flows, is a key contribution of the current work to be presented as part of validation in Chapter 4.

2.3.4 Multiresolution schemes

To extend the dynamic range of measurable displacements that can be captured by optical flow, the minimisation of equation 2.19 is often embedded in pyramidal schemes (Heitz et al., 2010), shown in Figure 2.13 below. The multiresolution scheme is created from a series of downsampled and Gaussian filtered forms of the original image pair. The optical flow problem in equation 2.19 is solved for the coarsest resolution image pair first to obtain a per-pixel vector field for the low resolution images. The optimisation process is then repeated for the next finer resolution image pair, using an upsampled form of the coarse resolution velocity field as the initial condition to begin the minimisation. This process repeats until the full resolution image pair is reached. In this manner, the largest scale (and lowest resolution) motion in the image plane is estimated first, before being used to guide the optimisation process and assist determining the progressively smaller magnitude fluid velocity captured in the finer resolution images. These 'classical' multiresolution schemes have some drawbacks, however. Namely, because the estimation of velocity proceeds in a one way manner towards the finest resolution image pair, there is no way of correcting spurious vectors originating from previous coarser scale estimates. Therefore, errors from previous estimates at coarser images propagate down towards the final resolution result with no possibility of posterior correction, an effect known as 'freezing'. Additionally, since the OF problem defined by equation 2.19 is calculated for each different resolution image pair independently, technically a slightly different optimisation problem is being solved each time, with the image

pairs being related only by empirical combinations of downsampling and Gaussian filtering. Although it is possible to formulate a theoretical relationship for the OF between the different image resolutions (Brox et al., 2004), a much more natural multiresolution scheme based on the wavelet decomposition will be described in the context of *wavelet-based optical flow* in Chapter 3.

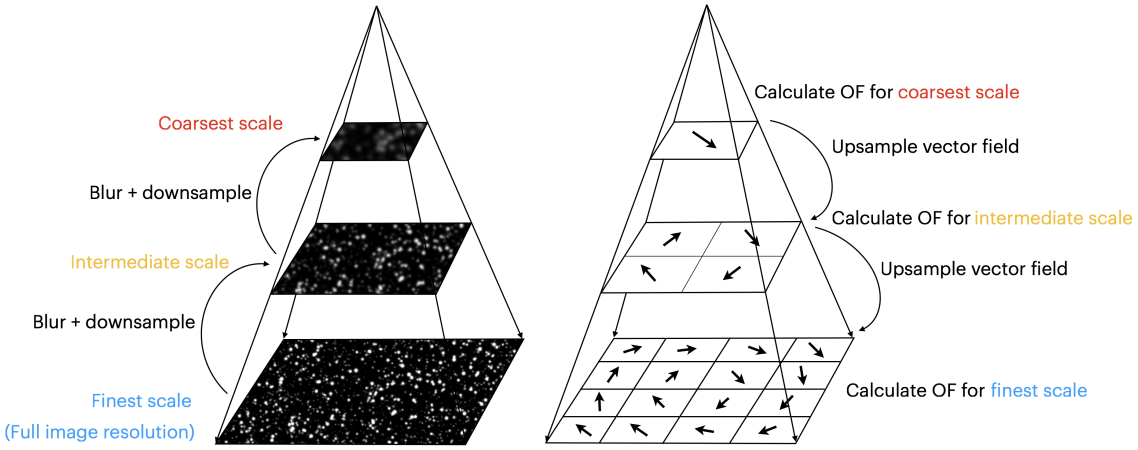

Figure 2.13: Example of classical multiresolution schemes in OF. A 'pyramid' of successfully filtered and downsampled images is first presented. The velocity is first estimated at the lowest resolution or coarsest scale image pair, before upsampling and successively refining this estimate for each higher resolution image until the full resolution or finest scale is reached.

Chapter 3

Wavelet-based Optical Flow

The first use of wavelet basis functions to represent the optical flow field was by (Y. T. Wu et al., 2000) for computer vision applications. This was then furthered by (L. F. Chen et al., 2002) who incorporated wavelets in the computation of the regularization term. The general form of wavelet-based optical flow algorithm for application in fluid velocimetry was initially proposed by (Dérian et al., 2013), significantly improving upon the high computational requirements of the previous approaches and generalising compatibility to more common wavelet families.

Since the introduction of wavelet-based optical flow for fluid velocimetry (Dérian, 2012), advancements such as improved boundary conditions (B. E. Schmidt & Sutton, 2020) and efficient implementation of high-order and physically sound regularization terms (Kadri-Harouna et al., 2013; B. E. Schmidt & Sutton, 2021) have furthered the robustness and accuracy of this technique. Previous studies demonstrated the wavelet-based implementation to be among some of the most accurate existing methods methods at the time, see (S. Cai et al., 2018; Dérian et al., 2013; Kadri-Harouna et al., 2013; B. E. Schmidt & Sutton, 2019). Wavelet analysis is an extensive subject, both in the fields of mathematics and signal processing (Daubechies, 1992; Mallat, 2009). The chapter begins with an introduction of the relevant theoretical framework of wavelet analysis in the *orthogonal* setting. This is followed by practical computation of wavelet transforms. Considerations for the more general biorthogonal setting (Cohen et al., 1993) are next presented and the implementation of the wavelet-based optical flow velocimetry (wOF) algorithm is described.

3.1 Wavelets framework

Time-frequency analysis is the study of a signal in two domains; the physical spatial or temporal domain, and the spectral domain where the signal is represented as frequency components. The motivation for this is to access or manipulate information that is poorly represented or unavailable in the signals' original form. One technique of such analysis, that allows simultaneous access to information in both spatial and frequency domains, is through the use of functions called wavelets.

Broadly speaking, a wavelet representation of a function or signal splits it into a low-pass filtered form represented by wavelet *approximation coefficients*, together with a set of *detail coefficients* representing a high-pass filtered form. This decomposition can be repeated on the approximation coefficients, further decomposing the

signal and separating its spatial information into different levels of detail or *scales* that depend on the frequency content. It is this inherent multiresolution scheme available using wavelet expansion that is a central feature of wavelet-based optical flow.

3.1.1 Basic principles

Considering a generic 1D signal $f(x)$, time-frequency analysis studies the various frequencies present. A well-known such representation in the frequency domain is the Fourier expansion:

$$f(x) = \sum_{k=-\infty}^{\infty} c_k e^{i2\pi kx} \quad x \in \mathbb{R} \tag{3.1}$$

where $i = \sqrt{-1}$ in this equation, c_k are the Fourier coefficients, associated to the k^{th} frequency represented by complex exponentials $e^{i2\pi kx}$ or sine waves. The Fourier coefficients c_k can be calculated by the following inner product:

$$c_k = \int_{\mathbb{R}} f(x) e^{-i2\pi kx} dx = \left\langle f(x) \; ; \; e^{-i2\pi kx} \right\rangle \tag{3.2}$$

The Fourier coefficients c_k represent the average of the frequency content of f, for a given frequency k. The analysing functions $e^{i2\pi kx}$ differ only in their frequency but all cover an infinite domain from $x \in [-\infty; \infty]$. The consequence of this is that while Fourier expansion reveals the harmonic content of the signal, it cannot reveal where the individual frequencies are located in $f(x)$ because the sinusoidal basis functions lack localisation in x, i.e., they lack a property known as *compact support* (Mallat, 2009).

Instead of sinusoids, wavelet expansion decomposes a signal across two different types of basis functions called scaling functions ϕ and wavelet functions ψ. These are also respectively referred to as the father wavelet (ϕ) and mother wavelet (ψ). The wavelet expansion can be expressed:

$$f(x) = \sum_{k=0}^{2^C-1} a_{C,k} \phi_{C,k}(x) + \sum_{j=C}^{F-1} \sum_{k=0}^{2^j-1} d_{j,k} \psi_{j,k}(x) \quad x \in \mathbb{R}, \; C \leq j < F \tag{3.3}$$

where j is a *scale* parameter and k is a shift or *translation* parameter. The parameter j scales the support (width) of the basis functions and k defines the translation of this support interval within a given scale j. The constant C with $C \geq 0$ and F with $F > C$ are non-negative integers indicating the *coarsest* and *finest* scale respectively. These will be discussed further in the context of multiresolution analysis (MRA). The coefficients $a_{C,k}$, associated to scaling functions ϕ are known as the *approximation* coefficients and $d_{j,k}$ associated to wavelet functions ψ are the *detail* coefficients. The approximation coefficients $a_{C,k}$ represent an averaged or low-pass filtered form of the signal $f(x)$. Conversely, the detail coefficients $d_{j,k}$ represent a high-pass filtered form, containing the information lost between the low-pass filtered form in $a_{C,k}$ and the original function $f(x)$. Analogously to the Fourier expansion, these coefficients are given by the following inner products:

$$a_{C,k} = \int_{\mathbb{R}} f(x) \phi_{C,k}(x) dx = \left\langle f(x) \; ; \; \phi_{C,k}(x) \right\rangle \tag{3.4}$$

$$d_{j,k} = \int_{\mathbb{R}} f(x)\psi_{j,k}(x)dx = \left\langle f(x)\ ;\ \ \psi_{j,k}(x) \right\rangle \tag{3.5}$$

Note, that an explicit expression for the functions ϕ, ψ is not given, unlike in the Fourier expansion where the basis functions are sinusoids. Although the function values of ϕ, ψ, are computable, most wavelets do not have an explicit geometric formula. They instead are expressed as scaled and translated forms of themselves between a pair of scales from j to $j+1$ via the following *refinement relations*:

$$\phi_{j,k'}(x) = \sum_{k=-\infty}^{\infty} h(k)\phi_{j+1,k} = \sqrt{2}\sum_{k=-\infty}^{\infty} h(k)\phi(2^{j+1}x - k) \tag{3.6}$$

$$\psi_{j,k'}(x) = \sum_{k=-\infty}^{\infty} g(k)\phi_{j+1,k} = \sqrt{2}\sum_{k=-\infty}^{\infty} g(k)\phi(2^{j+1}x - k) \tag{3.7}$$

Equations 3.6 - 3.7 are also referred to as the *dilation equations* or the *two-scales relations* in wavelet literature (Cohen et al., 1993; Daubechies, 1992; Mallat, 2009). They express how a wavelet or scaling function at a given scale j and given location k' is related to translated forms of other scaling functions along k at the next higher resolution or finer scale $j+1$. The coefficient sets $h(k)$ and $g(k)$ govern the shape of the associated scaling and wavelet functions and act as conjugate mirror filters used in the practical computation of the wavelet transform itself. The wavelet family, comprised of ϕ (scaling function or father wavelet) and ψ (wavelet function or mother wavelet) is entirely defined by the values of the two filters $h(k)$, $g(k)$.

The values of these filters are possible roots to imposed constraints on the properties of the wavelet family. This could include specific forms of orthogonality (e.g. orthonormality, biorthogonality, double-shift orthogonality), normality (e.g. degrees of normalisation such as square normalisation), and the smoothness of the wavelet (e.g. conditions on the number of vanishing moments). It is the choice of these constraints that ultimately designs the wavelet family and its characteristics. There are an infinite number of possible wavelet families. Not any function can be a wavelet, a wavelet must satisfy the admissibility condition (Daubechies, 1992) formally stating that the Fourier transform of the wavelet ψ must vanish at zero frequency in the Fourier domain. Therefore, the mean value of the wavelet function must be zero, and as a consequence, the wavelet has to exhibit oscillatory behaviour. These properties are visible in the the orthogonal Daubechies-7 family shown in Figure 3.1. Note the oscillatory nature of the wavelet function and that it has zero mean.

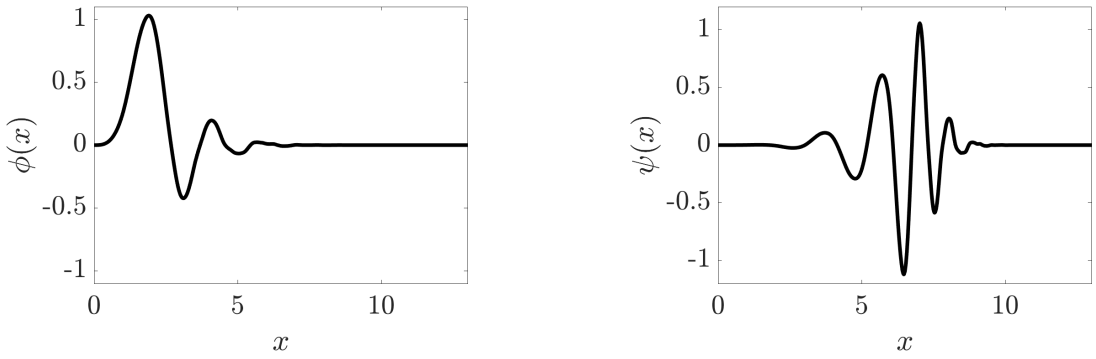

(a) (b)

Figure 3.1: The Daubechies-7 ($db7$) wavelet family. a) Scaling function ϕ b) Wavelet function ψ

3.1.2 Multiresolution analysis

The full possible range of functions that can be represented by the basis functions of the wavelet family is known as the span of the basis. The span of ϕ at a given scale level j is the approximation space $V_j = \text{span}\{\phi_{j,k}\}$ with $\phi_{j,k} = 2^{j/2}\phi(2^j x - k)$. Similarly, the span of ψ covers the detail space $W_j = \text{span}\{\psi_{j,k}\}$ with $\psi_{j,k} = 2^{j/2}\psi(2^j x - k)$ which is complementary to the space V_j. Multiresolution analysis (MRA) is a framework for decomposing a function $f(x)$ across various levels of detail that are contained within an approximation space V_j. The following axioms are necessary for MRA:

$$f(x) \in V_j \quad iff \quad f(2x) \in V_{j+1} \quad \text{- Self similarity in time} \tag{3.8}$$

$$V_j \subset V_{j+1} \quad \forall \in \mathbb{Z} \quad \text{- Self similarity in scale} \tag{3.9}$$

$$\cup_{j=-\infty}^{\infty} V_j(\mathbb{R}) \text{ is dense in } \boldsymbol{L}^2(\mathbb{R}) \quad \text{- Completeness} \tag{3.10}$$

$$\cap_{j=-\infty}^{\infty} V_j = \{0\} = \emptyset \quad \text{- Uniqueness} \tag{3.11}$$

$$\exists \phi_{0,k} \in V_0 \text{ such that } \phi_{0,k} = \phi(x-k) \text{ - forms an orthogonal basis} \tag{3.12}$$

The first property in 3.8 is a statement that any function in a given space can be represented using the bases of the next finer resolution space. The second property in 3.9 describes that the approximation spaces are sequentially nested within each other .. $\subset V_{-1} \subset V_0 \subset V_1 \subset$ .... The third property in 3.10 states that the collection of all spaces V_j entirely defines the Lebesgue space $L^2(\mathbb{R})$. Therefore, any function belonging to the space of square, integrable functions $L^2(\mathbb{R})$ can also be represented fully in the approximation space V_j. Property 3.11 states that these spaces are not redundant or that only the zero vector can be shared in all spaces, therefore information about a function in one space is unique to any other. The final property

in 3.12 formally introduces the existence of ϕ as the scaling function as the basis spanning V_j.

Fundamentally, the MRA framework formally allows a space V_{j+1} to be decomposed into two complimentary spaces:

$$V_{j+1} = V_j \oplus W_j \tag{3.13}$$

where W_j is the detail space that is complementary to the approximation space V_j. The direct sum of these two recovers the approximation space at the next finer scale V_{j+1}. This single step decomposition defined by equation 3.13 is in fact the action of the wavelet transform. For a function $f(x)$ in a given *finest scale* ($j = F$) subspace $f(x) \in V_F$, this decomposition can be applied recursively on V_F down to a *coarsest scale* subspace V_C:

$$\begin{aligned} f(x) \in V_F &= V_C \oplus W_C \oplus W_{C+1} \oplus ... \oplus W_{F-2} \oplus W_{F-1} \\ &= V_C \oplus \left(\bigoplus_{j=C}^{F-1} W_j \right) \end{aligned} \tag{3.14}$$

Therefore, a function $f(x)$ present in the finest scale approximation space V_F can be fully described by the direct sum of its representations in $V_{j<F}$ which are the nested subspaces. In a purely theoretical setting, the coarse scale C and fine scale F with $F > C$ can take any integer value from $[-\infty; \infty]$. In practise, the finest scale F is determined by the number of samples in the signal and is not a selectable parameter in wavelet analysis. A signal consisting of $2^3 = 8$ samples will have $F = \log_2(2^3) = 3$ as its finest scale. The coarsest scale decomposed to, is indicated by C, with $0 \leq C < F$ in a discrete setting. Unlike F, this parameter is selectable in wavelet transforms and is discussed in the computation of the discrete wavelet transform in the following section. The decomposition structure of the MRA in equation 3.14 for a discretised function or signal $f(x)$ with 2^3 samples is shown below in Figure 3.2.

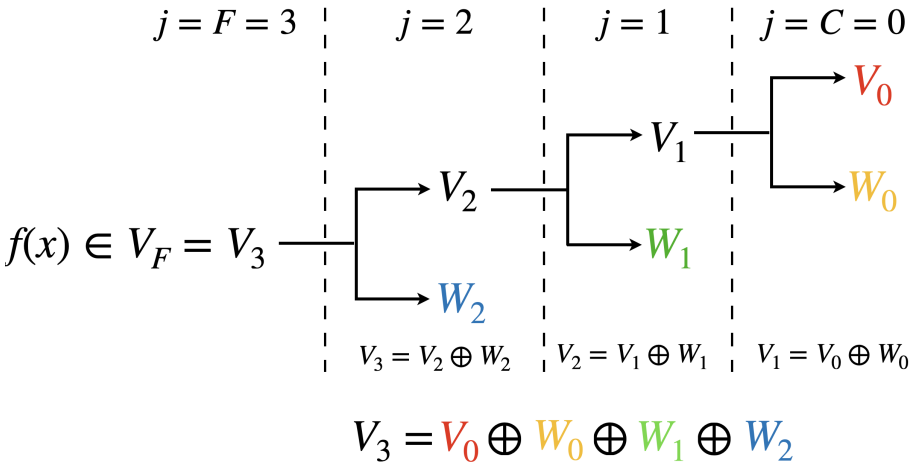

Figure 3.2: Conceptual representation of wavelet MRA on a function $f(x)$.

3.1.3 Discrete wavelet transform

The introduction of the wavelet framework so far has introduced the prerequisite theory, it is now necessary to describe the practical computation of the *discrete*

wavelet transform (DWT) algorithm which computes the projection of a discrete function associated to V_F onto the multiscale wavelet basis spanning the nested subspaces within V_F.

The action of the DWT is equivalent to a filterbank in signal processing (Mallat, 2009) using the $h(k)$ and $g(k)$ coefficients from in the refinement relations (equations 3.6 and 3.7). This is represented in Figure 3.3. The forward DWT consists of convolution of the input signal $f(x)$ with $\bar{h}(k)$ as a low-pass filter and $\bar{g}(k)$ as a high-pass filter. The $\bar{\cdot}$ indicates the time-reverse operator, i.e. $\bar{h}(k) = h(-k)$. This then followed by a downsampling of the separate filter outputs by a factor of 2 to yield the approximation coefficients $a_{j,k}$ and detail coefficients $d_{j,k}$. The input signal $f(x)$ can be reconstructed with no loss of information via the inverse DWT by upsampling of the two coefficient sets by a factor 2 followed by convolution with the original reconstruction filters $h(k)$, $g(k)$ and summation of these products.

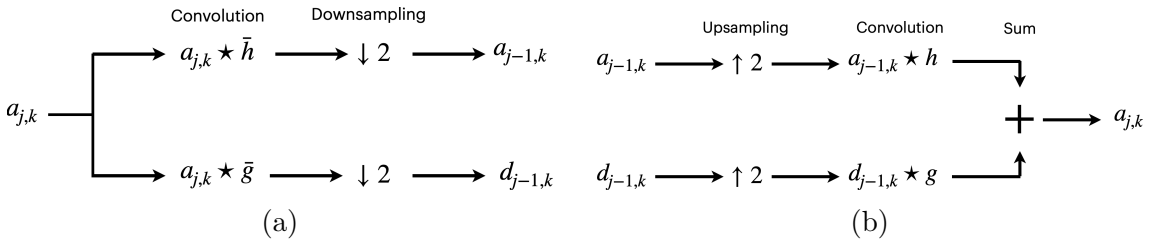

Figure 3.3: Computation of the a) forward DWT and b) inverse DWT.

The DWT described produces the wavelet decomposition across a single scale. The full multiscale decomposition defined by equation 3.14 is performed by recursive application of the DWT onto only the approximation coefficients $a_{j,k}$. The DWT halves the number of approximation coefficients at each stage as a result of the downsampling. The DWT can be repeated until only 1 approximation coefficient remains, therefore further downsampling and application and application of the DWT is not possible. Therefore, the coarsest possible scale $C = 0$ and $0 \leq C < F$ in discrete data. This yields the full scale or full depth decomposition. The combined set of $a_{C,k}$ and $d_{j,k}$ is the wavelet representation of $f(x)$ in the subspace V_F. Multiscale reconstruction proceeds with application of the inverse DWT at coarsest scale $j = C$, before iterating the procedure up to the finest scale $j = F$.

The approximation subspace V_C and each detail subspace W_j contain 2^j respective coefficients in the classical case. Depending on the boundary condition used in the wavelet transform, it is possible to produce $> 2^j$ coefficients per subspace if the boundary condition is *expansive* and therefore produces more coefficients than actual input samples in order to have a reversible wavelet transform. This aspect is discussed further in the forthcoming section but it should be noted that for optical flow purposes only *non-expansive* boundary conditions are used, therefore there are always 2^j coefficients per subspace.

A wavelet decomposition of an example one dimensional signal from (Mallat, 2009) is shown in Figure 3.4. The signal has $2^{10} = 1024$ samples, making the finest scale $F = \log_2(2^{10}) = 10$. The coarse scale is set at $C = 6$ in this example. The signal is therefore decomposed across 5 spaces; 4 detail spaces $W_{6 \leq j \leq 9}$, along with the approximation space V_6. Note the resemblance of the approximation coefficients to the original signal, and how the location of peaks in the detail coefficients coincide directly with the sharp gradients present in the signal. Due of the compact support of

the wavelet basis functions, discontinuities and rapid variations of a signal are easily represented in the wavelet coefficients. This property has made wavelet analysis an attractive tool in applications such as denoising (Abramovich et al., 2006; T. T. Cai, 2002; Donoho & Johnstone, 1995) and edge detection (Mallat & Zhong, 1992).

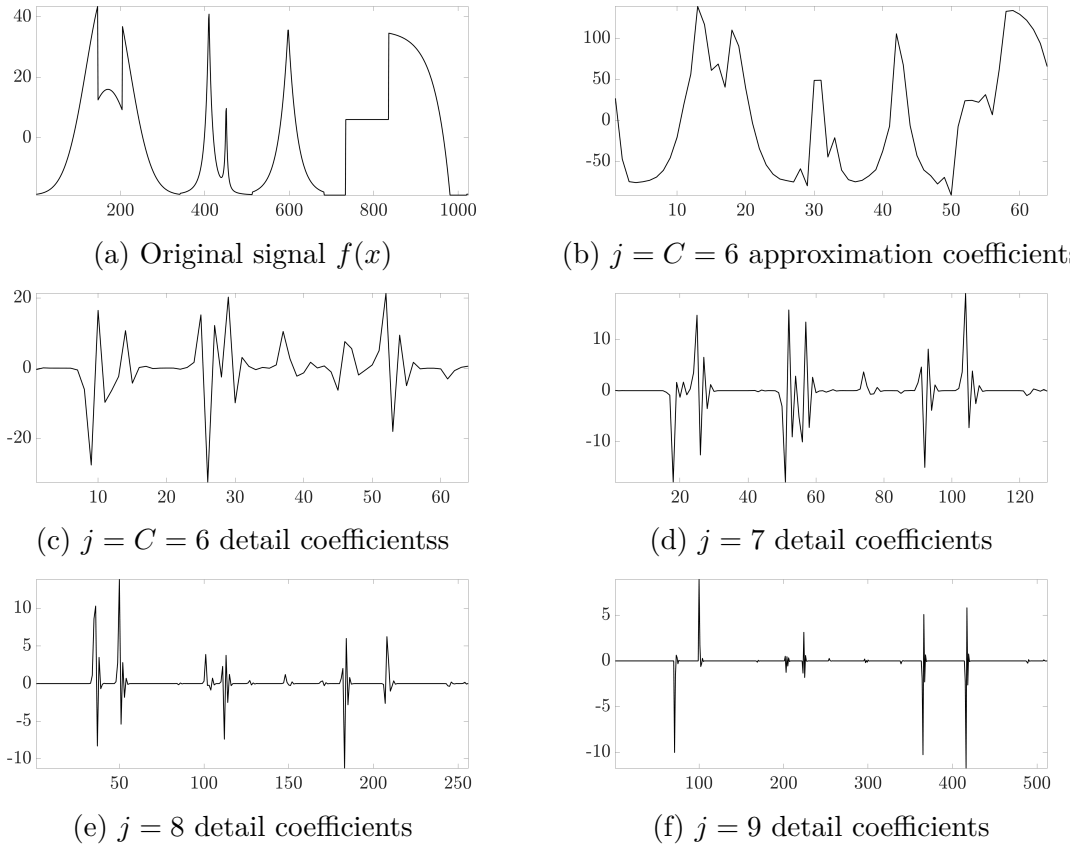

(a) Original signal $f(x)$

(b) $j = C = 6$ approximation coefficients

(c) $j = C = 6$ detail coefficientss

(d) $j = 7$ detail coefficients

(e) $j = 8$ detail coefficients

(f) $j = 9$ detail coefficients

Figure 3.4: Example decomposition of a 1D signal.

3.1.3.1 Boundary conditions

Formally, wavelets are defined in an infinite domain. In the practical computation of the DWT, certain boundary conditions must be considered in the convolution due to the finite extent of discrete signals. A common method of imposing boundary conditions is by extrapolating the signal assuming *periodic* repetition as shown in Figure 3.5 below. Periodic boundary conditions were first used in the original wavelet-based optical flow implementation of (Dérian et al., 2013) due to their simplicity and the ability to use circular convolution via the fast Fourier transform (FFT) to accelerate computation.

If the signal is not truly periodic, as is the case for most real datasets, the discontinuity present at the edges of the signal will result in large magnitude wavelet coefficients. These artefacts are not a property of the signal itself nor the wavelet basis but a side effect of how the DWT is computed in practise. Border effects have a greater effect on shorter signals, where the local regions around boundaries contribute to a greater proportion of full signal length. In the case of Fourier analysis, this motivates the use of zero-padding of the signal or premultiplication with windowing functions to mitigate edge effects caused by the non-periodicity (J M Foucaut et al., 2004).

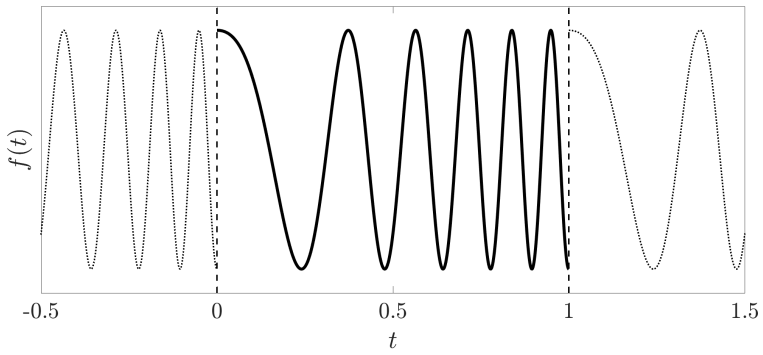

Figure 3.5: Example of period boundary conditions.

An alternative to periodic repetition is to reflect the signal at its borders, shown in Figure 3.6 below. This method creates local continuity between the signal and its extrapolated component, thus greatly minimising the distortions occuring in the periodic case. Symmetric boundary conditions that are *non-expansive*, i.e., do not produce more coefficients than input samples, require that the wavelet family itself be symmetric. As a property of their construction, and with the exception of the Haar wavelet, orthogonal wavelets cannot be (truly) symmetric by definition. Therefore, proper implementation of symmetric boundary conditions requires the use of *biorthogonal* wavelets which can be symmetric. The relevant considerations with respect to the biorthogonal wavelet setting will be discussed in an upcoming section.

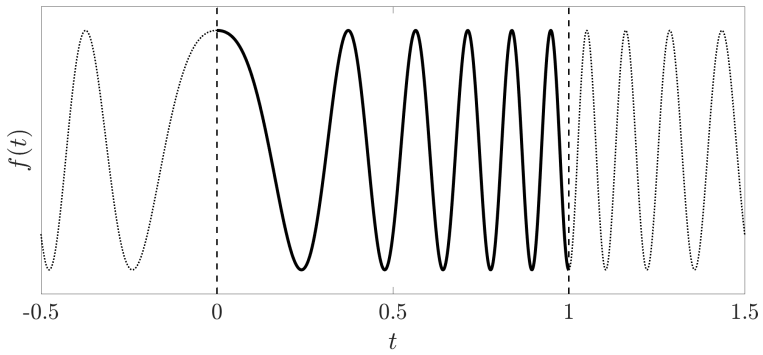

Figure 3.6: Example of symmetric boundary conditions.

More elaborate boundary conditions in wavelet transform do exist such as the boundary wavelet algorithm of (Cohen et al., 1993) and wavelet extrapolation method of (Amaratunga & Williams, 1997). The former is significantly more involved and often requires an extra preconditioning step in the wavelet transform to ensure it is stable. The latter boundary condition is *expansive* and thus produces additional coefficients ($> 2^j$ coefficients per subspace) in the DWT output, distorting the dyadic structure of the decomposition. This is computationally undesirable for algorithm performance in optical flow and complicates efficient implementation. Symmetric boundary conditions are an effective, well-known method of dealing with border effects also used in the wavelet transforms intrinsic in the famous JPEG-2000 image compression standard (Taubman & Marcellin, 2002).

3.1.3.2 Extension to two dimensions

The discussion thus far has considered wavelet transforms in a one dimensional setting. The final step before introducing the wavelet-based optical flow algorithm is to extend the one dimensional results to two dimensions in order to operate on matrices of size $2^F \times 2^F$. This is achieved by tensor product of the 1D wavelet bases to form the approximation space $\boldsymbol{V}_j = V_j \otimes V_j = \text{span}\{\phi_{j,k_1} \otimes \phi_{j,k_2}\}$ and the complementary detail space formed from $\boldsymbol{W}_j = W_j \otimes W_j = \text{span}\{\psi_{j_1,k_1} \otimes \psi_{j_2,k_2}\}$. The basis function tensor products are defined as:

$$\phi_{j,k_1} \otimes \phi_{j,k_2}(\boldsymbol{x}) := \phi_{j,k_1}(x_1)\phi_{j,k_2}(x_2) \tag{3.15}$$

$$\psi_{j_1,k_1} \otimes \psi_{j_2,k_2}(\boldsymbol{x}) := \psi_{j_1,k_1}(x_1)\psi_{j_2,k_2}(x_2) \tag{3.16}$$

The 2D wavelet basis now has parameters $\boldsymbol{j} = (j_1, j_2)$ and $\boldsymbol{k} = (k_1, k_2)$ to represent the scaling and translation parameters associated to each dimension, while the 2D scaling function basis still has a single scale parameter j. Analogously to the 1D case, the decomposition of a 2D function $f(\boldsymbol{x}) \in L^2(\mathbb{R}^2)$ is expressed as:

$$f(\boldsymbol{x}) = \sum_{\boldsymbol{k}=0}^{2^C-1} a_{C,\boldsymbol{k}}\phi_{C,k_1}(x_1)\phi_{C,k_2}(x_2) + \sum_{\boldsymbol{j}=C}^{F-1}\sum_{\boldsymbol{k}=0}^{2^j-1} d_{\boldsymbol{j},\boldsymbol{k}}\psi_{j_1,k_1}(x_1)\psi_{j_2,k_2}(x_2) \tag{3.17}$$

The 2D approximation and detail coefficients are similarly calculated as in the 1D case, using the inner product of $f(x)$ of with the respective 2D basis. The decomposition structure of the subspaces in the two dimensional setting can be derived by inserting equation 3.13 into $V_{j_1} \otimes V_{j_2}$[1]:

$$\begin{aligned} V_{j_1} \otimes V_{j_2} &= (V_0 \oplus V_0 \oplus W_1 \oplus W_2 \oplus \ ...W_{F-1}) \otimes (V_0 \oplus V_0 \oplus W_1 \oplus W_2 \oplus \ ...W_{F-1}) \\ &= (V_0 \otimes V_0) \oplus \bigoplus_{j_1=0}^{F-1}(V_0 \otimes W_{j_2}) \oplus \bigoplus_{j_2=0}^{F-1}(W_{j_1} \otimes V_0) \oplus \bigoplus_{j_1,j_2=0}^{F-1}(W_{j_1} \otimes W_{j_2}) \end{aligned} \tag{3.18}$$

The decomposition structure in equation 3.18 is computed by applying the 1D DWT to each row of the given discretised function or matrix until the desired coarse scale C is reached, then repeating the 1D decomposition for each column.

Similarly to (Dérian, 2012), in order to simplify notation for upcoming derivations in the following sections, the 2D DWT of a velocity field U_i will be expressed by:

$$\Theta_i = \Phi^{-1}(\boldsymbol{x})U_i(\boldsymbol{x}) \tag{3.19}$$

where Θ_i is the vector containing the full set of both approximation $a_{C,\boldsymbol{k}}$ and detail coefficients $d_{\boldsymbol{j},\boldsymbol{k}}$ and $\Phi^{-1}(\boldsymbol{x})$ is the vector formed from the scaling and wavelet basis functions. The inverse transform is written:

$$U_i(\boldsymbol{x}) = \Phi(\boldsymbol{x})\Theta_i \tag{3.20}$$

where $\Phi(\boldsymbol{x})$ is the operator enacting reconstruction of the wavelet coefficients.

[1]There are two different ways to introduce the detail spaces into a 2D MRA, leading to either the *isotropic* or *anisotropic* form of the 2D DWT. Only the anisotropic DWT is used in wOF. Taxonomy in wavelet literature varies and the anisotropic wavelet transform is equivalently referred to as the tensor product, tensorial, fully separable, hyperbolic or rectangular DWT.

3.1.3.3 Biorthogonal wavelets

Before introducing the wOF algorithm, it is important to discuss some distinctions when using biorthogonal wavelets. The conceptual framework of multiresolution analysis and decomposition structure described holds true for the biorthogonal setting. However, the formalism becomes more complex (Cohen et al., 1992). Orthogonality is a relatively stringent condition in wavelet analysis, and relaxing this constraint allows for more flexible design of wavelet families that allows for features such as symmetry which is advantageous for symmetric boundary conditions. In the orthogonal case, the wavelet basis functions ψ are orthogonal to translated or scaled forms of eachother:

$$\langle \psi_{m,n} \; ; \; \psi_{k,l} \rangle = \delta_{mn}\delta_{kl} \tag{3.21}$$

where δ is the dirac delta. The biorthogonal setting however requires the following relations:

$$\langle \phi_{j,p} \; ; \; \tilde{\phi}_{j,q} \rangle = \delta_{pq} \tag{3.22}$$

$$\langle \psi_{i,p} \; ; \; \tilde{\psi}_{j,q} \rangle = \delta_{ij}\delta_{pq} \tag{3.23}$$

$$\langle \phi_{j,p} \; ; \; \tilde{\psi}_{j,q} \rangle = 0 \tag{3.24}$$

$$\langle \tilde{\phi}_{j,p} \; ; \; \psi_{j,q} \rangle = 0 \qquad \forall i, j, p, q \in \mathbb{Z} \tag{3.25}$$

where $\tilde{\phi}$, $\tilde{\psi}$ are known as the *dual* scaling and wavelet functions respectively. Functions ϕ, ψ excluding the tilde ($\tilde{}$) are known as the *primal* scaling and wavelet functions. The biorthogonal case therefore has two wavelet functions and two scaling functions. The refinement relations for these is given similarly to the orthogonal case (equations 3.6 and 3.7), with the dual scaling and wavelet function associated to the dual filter $\tilde{h}(k)$ and $\tilde{g}(k)$. A biorthogonal wavelet family is defined by combination of both the dual filters $\tilde{h}(k)$, $\tilde{g}(k)$ and the primal filters $h(k)$, $g(k)$. However, they are related by:

$$g(k) = (-1)^{1-k}\tilde{h}(1-k) \tag{3.26}$$

$$\tilde{g}(k) = (-1)^{1-k}\tilde{h}(1-k) \tag{3.27}$$

Either the primal or dual basis can be used to compute a valid forward DWT. If the dual basis is used, the primal basis must be used for reconstruction, and vice versa. The primal and dual basis functions can have different properties which can be useful for applications where separate features are advantageous to the decomposition or reconstruction filters. In image compression for example, it is useful to have a high number of vanishing moments on the reconstruction filters so as to reduce artefacts and improve perceived visual quality in the compressed image (Mallat, 2009; Villasenor et al., 1995). Typically, the dual basis is used for decomposition. Use of the primal filters is sometimes referred to as the reverse biorthogonal decomposition (B. E. Schmidt & Sutton, 2020). In the orthogonal case, the primal and dual functions are identical $\tilde{\psi} = \psi$, $\tilde{\phi} = \phi$ and a distinction between the two is irrelevant. In the orthogonal case, the norm of the wavelet coefficients equals

the norm of the input signal $\sum|\Theta|^2 = \sum|U|^2$, satisfying Parseval's theorem. In the biorthogonal setting this no longer holds ($\sum|\Theta|^2 \neq \sum|U|^2$). For purposes in wOF, this lack conservation of energy between a signal and its wavelet representation is not detrimental since the inverse (biorthogonal) DWT still results in perfect reconstruction.

3.2 Implementation

The principle of wavelet-based optical flow is to perform the minimisation of the objective function in Equation 2.19 not over the physical velocity field $\boldsymbol{U} = (U_1, U_2)^T$, but over the coefficients $\boldsymbol{\Theta} = (\Theta_1, \Theta_2)^T$ resulting from the wavelet transform of the velocity field as per equation 3.19. This results in the following modified objective function:

$$\hat{\boldsymbol{\Theta}} = \arg\min_{\boldsymbol{\Theta}} J_D(I_0, I_1, \boldsymbol{\Theta}) + \lambda J_R(\boldsymbol{\Theta}) \tag{3.28}$$

The stages through the algorithm are shown in Figure 3.7. The algorithm begins at the coarsest scale C from an initial condition x_0 which is initially set to $\boldsymbol{U} = \boldsymbol{\Theta} = 0$. For a given scale j, x_0 has $2 \times 2^j \times 2^j$ elements. The minimisation process for the coarse scale converges to produce the optimised wavelet coefficients $\hat{\boldsymbol{\Theta}}_C$. These optimised coefficients are then included in the new initial condition x_0 to begin the minimisation for the subsequent finer scale $C + 1$. This process is repeated, using the optimised wavelet coefficients $\hat{\boldsymbol{\Theta}}$ from a previously completed scale j as the initial condition to begin the minimisation for the next subsequent scale $j + 1$. In this manner, the wavelet coefficients $\boldsymbol{\Theta}$ are optimised sequentially starting from the chosen coarsest scale ($j = C$), repeatedly for increasingly detailed scales $C \leq j \leq F$ until the finest scale ($j = F$) representing the image resolution is reached. At a given scale j, wavelet coefficients from *all* coarser scales are being included and optimised together. With this strategy, previous velocity estimates are continually updated as finer scale motion is determined while the algorithm proceeds to estimate velocity up to the pixel scale F. At the end of the optimisation process, the physical velocity field $\hat{\boldsymbol{U}}$ is recovered via application of the inverse 2D DWT from equation 3.20.

Computationally, performing the multiscale estimation through the wavelet multiscale framework overcomes the drawback of 'freezing' in classical optical flow methods by allowing the velocity field to self-correct itself during optimisation as finer scales of motion are determined. Traditional non-wavelet pyramidal multiresolution schemes do not relate the motion between different scales and velocity estimates at each scale are unchanged as motion in higher resolution scales is determined. The effect of 'freezing' previous velocity estimates at lower resolutions make them uncorrectable at later points of optimisation process, allowing this error to propagate through the multiresolution scheme. The wavelet expansion of the optical flow field provides a natural multiresolution scheme well-suited to represent the multi-scale nature of turbulence (Deriaz & Perrier, 2009; Farge et al., 1996) with the multiscale wavelet coefficients representing different velocity scales within the imaged motion. Velocity field estimates from coarser scales represent the larger scale fluid motion, while finer scale coefficients are associated with smaller scale motion. The nested coarse-to-fine optimisation of the velocity field is also advantageous in the minimisation of the DFD in the data term, which as stated previously is a highly non-linear

function of the velocity, making poor solutions from local minima a greater risk when using traditional multiscale schemes.

3.2.1 Minimisation

The minimisation of equation 3.28 is an unconstrained optimisation using the limited-memory Broyden-Fletcher-Goldfarb-Shanno (l-BFGS) algorithm (D. C. Liu & Nocedal, 1989). This quasi-Newton gradient-descent algorithm is well-suited for optimisation problems featuring a high degree of non-linearity and involving a large number of variables. Given the density of the velocity vector field, considerations for computational performance are important, particularly for large image sizes ($> 1024 \times 1024$). As inputs, l-BFGS only requires the data and regularization terms J_D, J_R and their gradients ∇J_D, ∇J_R with respect to the wavelet basis which are derived in the forthcoming sections. Classical optical flow algorithms use optimisation schemes (Brox et al., 2004; Horn & Schunck, 1981; Zimmer et al., 2011) that require derivation of the full Euler-Lagrange PDE equations of the objective function which the solution must satisfy. Depending on data and regularization terms used, this can result in a complex set of coupled equations requiring for advanced discretisation schemes for stable minimisation (Corpetti et al., 2002)

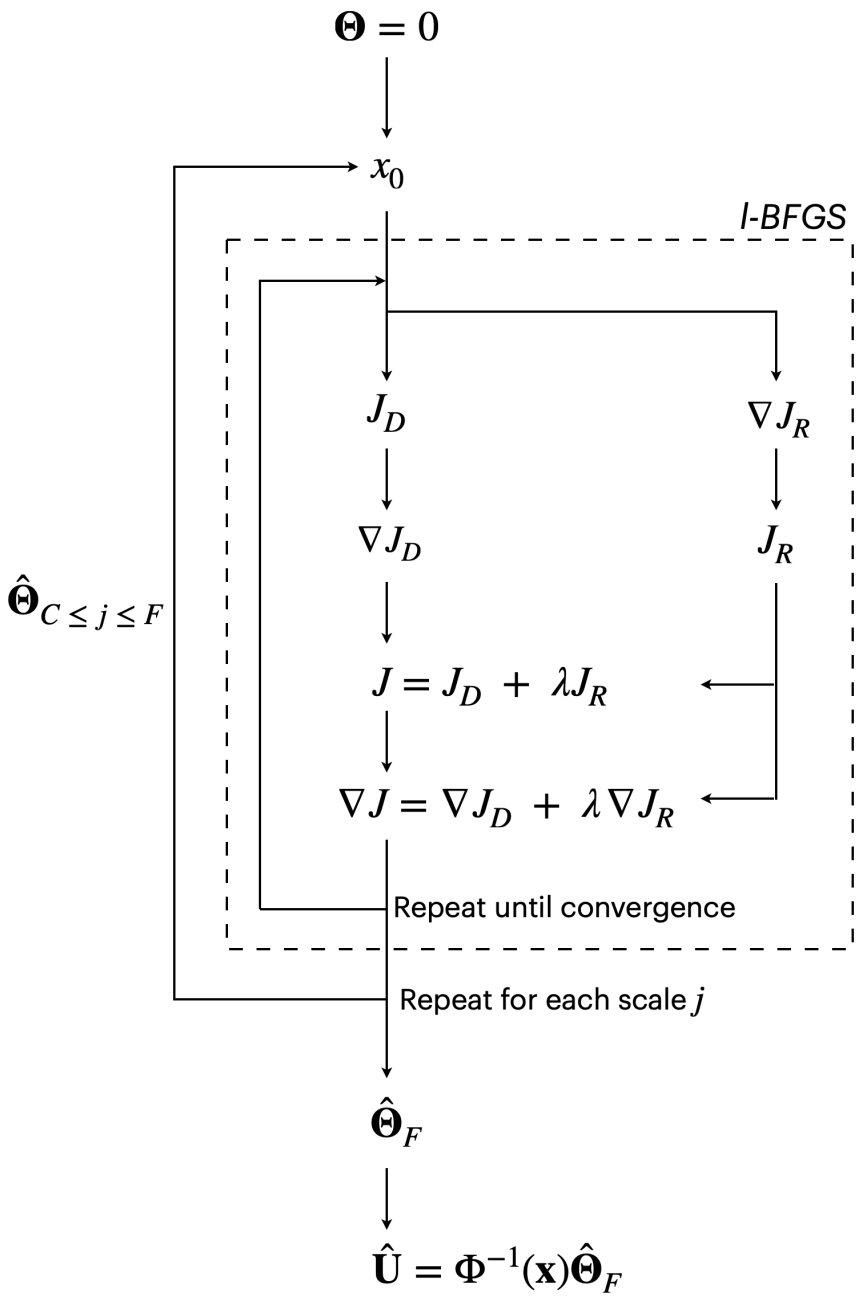

Figure 3.7: Flow chart of the wavelet-based optical flow algorithm

3.2.1.1 Algorithm parameters

The user selectable parameters in wavelet-based optical flow are the regularization weighting parameter λ and those related to the wavelet decomposition, namely the choice of wavelet basis and the coarsest scale C decomposed to. The current implementation uses the odd length biorthogonal nearly Coiflet wavelet basis (BNC 17/11) introduced by (Winger & Venetsanopoulos, 2001). This basis has a nearly maximum number of vanishing moments possible for a given biorthogonal wavelet filter size. Maximising the number of vanishing moments increases velocity estimation accuracy up to a degree (Dérian et al., 2013). This wavelet family is notable for the improved retention of fine details in its wavelet transform partial reconstructions which are implicit in the multiscale estimation process. The coarsest scale decom-

posed to (C) is typically set to zero, resulting in the full depth decomposition. The influence of this parameter has been investigated previously in (Dérian et al., 2013) where it was confirmed that maximising the number of scales decomposed to improves the dynamic range. It is also possible to set $C > 0$ as long as the solution $\hat{\boldsymbol{U}}$ is unchanged compared to $C = 0$. This improves the computation time and can be useful when performing repeated processing of a dataset with different values of λ.

3.2.2 Data term

The current implementation uses the DFD in a quadratic penalty as in equation 2.16. Inserting the wavelet representation of the velocity field (equation 3.20) into the data term defined in 2.16:

$$J_D = \frac{1}{2} \int_\Omega \left[I_0(\boldsymbol{x}) - I_1(\boldsymbol{x} + \boldsymbol{\Phi}(\boldsymbol{x})\boldsymbol{\Theta}) \right]^2 d\boldsymbol{x} \tag{3.29}$$

The gradient of J_D with respect to the wavelet coefficients can be derived using the chain rule:

$$\begin{aligned} \frac{\partial J_D}{\partial \boldsymbol{\Theta}} &= \int_\Omega - \left[I_0(\boldsymbol{x}) - I_1(\boldsymbol{x} + \boldsymbol{\Phi}(\boldsymbol{x})\boldsymbol{\Theta}) \right] \frac{\partial I_1(\boldsymbol{x} + \boldsymbol{\Phi}(\boldsymbol{x})\boldsymbol{\Theta})}{\partial \boldsymbol{x}} \frac{\partial (\boldsymbol{x} + \boldsymbol{\Phi}(\boldsymbol{x})\boldsymbol{\Theta})}{\partial \boldsymbol{\Theta}} d\boldsymbol{x} \\ &= \int_\Omega - \left[I_0(\boldsymbol{x}) - I_1(\boldsymbol{x} + \boldsymbol{\Phi}(\boldsymbol{x})\boldsymbol{\Theta}) \right] \frac{\partial I_1(\boldsymbol{x} + \boldsymbol{\Phi}(\boldsymbol{x})^T\boldsymbol{\Theta})}{\partial \boldsymbol{x}} \boldsymbol{\Phi}(\boldsymbol{x}) \, d\boldsymbol{x} \\ &= \left\langle - \left[I_0(\boldsymbol{x}) - I_1(\boldsymbol{x} + \boldsymbol{\Phi}(\boldsymbol{x})\boldsymbol{\Theta}) \right] \frac{\partial I_1(\boldsymbol{x} + \boldsymbol{\Phi}(\boldsymbol{x})\boldsymbol{\Theta})}{\partial \boldsymbol{x}} ; \boldsymbol{\Phi}(\boldsymbol{x}) \right\rangle \end{aligned} \tag{3.30}$$

It can be observed that the calculation of ∇J_D is therefore the wavelet transform of the product of the DFD with spatial gradient of the motion-compensated image $\nabla I_1(\boldsymbol{x} + \boldsymbol{U})$. The motion-compensated image $I_1(\boldsymbol{x} + \boldsymbol{U})$ is calculated using highly accurate 5^{th} order splines (Thevenaz et al., 2000). The spatial gradients of $\nabla I_1(\boldsymbol{x} + \boldsymbol{U})$ are computed using the 6^{th} order differencing scheme from (Bruhn et al., 2005).

3.2.3 Regularization term

The accuracy of different regularization terms was compared in prior studies (Corpetti et al., 2002; Dérian, 2012; B. E. Schmidt & Sutton, 2021) where the advantages of high-order regularization were repeatedly demonstrated. The Laplacian regularization can be informally proven to impart onto the velocity field in an analogous manner to fluid viscosity in a two-dimensional divergence free flow (B. E. Schmidt & Sutton, 2021). This physically-sound regularization was shown to be among the most accurate in (B. E. Schmidt & Sutton, 2021) where a slightly more general viscosity-based regularization term was proposed to account for apparent divergence or compressibility resulting from out-of-plane motion in the images. Both the authors' own tests on synthetic data and results from (B. E. Schmidt & Sutton, 2021) however conclude that the improvement brought by this viscosity-based regularization term is extremely marginal over the Laplacian regularization ($\approx 3\%$), but significantly increase the computation time due to having more terms to compute. The current work therefore uses the Laplacian regularization:

$$
\begin{aligned}
J_R &= \frac{1}{2}\int_\Omega |\nabla^2 U_1|^2 + |\nabla^2 U_2|^2 d\boldsymbol{x} \\
&= \frac{1}{2}\int_\Omega \left(\frac{\partial^2 U_1}{\partial x_1^2}\right)^2 + \left(\frac{\partial^2 U_1}{\partial x_2^2}\right)^2 + 2\left(\frac{\partial^2 U_1}{\partial x_1^2}\right)\left(\frac{\partial^2 U_1}{\partial x_2^2}\right) \\
&\quad + \left(\frac{\partial^2 U_2}{\partial x_1^2}\right)^2 + \left(\frac{\partial^2 U_2}{\partial x_2^2}\right)^2 + 2\left(\frac{\partial^2 U_2}{\partial x_1^2}\right)\left(\frac{\partial^2 U_2}{\partial x_2^2}\right) d\boldsymbol{x}
\end{aligned} \tag{3.31}
$$

The wavelet framework allows for stable implementation of high-order regularization schemes by transferring the velocity derivatives computation to the wavelet basis functions using results originally derived by (Beylkin, 1992). Computation of the regularization using wavelet calculus is referred to as the operator continuous approximation method in (Kadri-Harouna et al., 2013) and is also known as the wavelet Galerkin method (Amaratunga & Williams, 1997). The process involves the construction of matrices $N^{(\cdot)}$ which act as derivative operators on wavelet coefficients Θ_i via triple matrix products of the form $N^{(\cdot)}\Theta_i N^{(\cdot)T}$. The superscript $^{(\cdot)}$ indicates the derivation order with the respect to the wavelet basis and is not an exponent. The detailed derivation of these operators is included in Appendix A. In the wavelet domain, equation 3.31 is expressed as:

$$
J_R = \frac{1}{2}\Theta_i : \left(N^{(4)}\Theta_i N^{(0)T} + N^{(0)}\Theta_i N^{(4)T} + 2N^{(2)}\Theta_i N^{(2)T}\right) \tag{3.32}
$$

where : denotes the Frobenius product (element-wise product and sum) between Θ_i and the triple matrix products. The gradient of equation 3.32 with respect to the wavelet coefficients is given by:

$$
\frac{\partial J_R}{\partial \Theta_i} = N^{(4)}\Theta_i N^{(0)T} + N^{(0)}\Theta_i N^{(4)T} + 2N^{(2)}\Theta_i N^{(2)T} \tag{3.33}
$$

Chapter 4

Validation on Non-reacting Flow

The present chapter assesses the performance of the wavelet-based optical flow (wOF) method in obtaining highly resolved and accurate measurements of velocity and derived quantities such as the wall shear stress in turbulent wall-bounded flows. The influence of regularization on velocity results and normalised boundary layer quantities is investigated using synthetic particle images generated from DNS of a turbulent channel flow to understand the effect of this parameter. Results are compared to industry standard cross-correlation-based PIV. The final part of this chapter applies wOF to an experimental PIV dataset featuring a developing turbulent boundary layer. Results are compared to correlation-based PIV processing to demonstrate the advantages of wOF as an alternative technique in the study of turbulent wall-bounded flows.

4.1 Description of synthetic test case

In order to quantitatively assess wOF performance and λ parameter sensitivity in wall-bounded flows, it is first necessary to compare estimated velocity fields from wOF to a known ground truth velocity available from synthetic data. Synthetic data provide a useful test platform where parameters can be easily and independently controlled in an idealised image environment. In this work, the synthetic data are derived from direct numerical simulation (DNS) of a turbulent channel flow (Graham et al., 2016) hosted online at John Hopkins Turbulence Database (JHTDB) (Li et al., 2008). Details of the synthetic data are described below.

4.1.1 DNS dataset

Table 4.1 describes the simulation parameters of the JHTDB, which are stored in a nondimensional form based on the half-channel height h. One hundred temporally correlated velocity fields are extracted with a time separation of 2.5 δt (stored) DNS database timesteps from a subset of the DNS domain that includes the no-slip velocity grid point of the lower wall. The fields are of nondimensional size $0.17h \times 0.17h \times (5 \times 10^{-4})h$ and sampled from the database at a grid resolution of $1024 \times 1024 \times 3$ using fourth-order Lagrange polynomial interpolation (Berrut & Trefethen, 2004).

Bulk velocity U_b	0.99994
Centreline velocity U_c	1.1312
Friction velocity u_τ	0.0499
Kinematic viscosity ν	5×10^{-3}
Bulk velocity Reynolds number $Re_b = 2U_b h/\nu$	3.9998×10^4
Centreline velocity Reynolds number $Re_c = U_c h/\nu$	2.2625×10^4
Friction velocity Reynolds number $Re_\tau = u_\tau h/\nu$	999.35
DNS database timestep δt	0.0065
Full domain size	$8\pi h \times 2h \times 3\pi h$
Full grid resolution	$2048 \times 512 \times 1536$

Table 4.1: Simulation parameters (nondimensionalised) of the JHTDB channel flow DNS.

4.1.2 Particle image generation

Once the velocity fields from the DNS are extracted, it is necessary to determine tracer particle displacements between frames of each image pair as they are advected by the DNS velocity. For the initial frame of each image pair, synthetic particle tracer locations are initialised from a random distribution for each of the extracted DNS velocity fields. The velocity field is assumed to be constant between consecutive images and the tracers assumed to be spherical and massless. The displacement of each particle in each second frame is computed numerically using an explicit Runge–Kutta scheme (Dormand & Prince, 1980) and a modified Akima spline interpolation for the velocities at particle locations (Akima, 1974). The velocity fields and particle displacements are then scaled from the nondimensional DNS units to pixel displacements per unity inter-frame time interval ($dt = 1$) such that the maximum image plane velocity magnitude corresponds to $\approx 3.5\ px/dt$, and the maximum out-of-plane displacement is $\approx 0.8\ px/dt$.

The particle image pixel intensities are determined using classical methods of synthetic particle image generation (Raffel et al., 2018). The maximum particle intensity is governed by its diameter d_p and out-of-plane position $x_{3,p}$ within a Gaussian profile synthetic laser sheet:

$$I_p = d_p^2 \exp\left(\frac{-8(x_{3,LS} - x_{3,p})^2}{2\sigma_{LS}^2}\right) \tag{4.1}$$

The laser sheet position $x_{3,LS}$ is centred in the middle of the extracted DNS domain. The standard deviation of the laser sheet profile is set to $\sigma_{LS} = 2$ such that the $1/e^2$ profile thickness is equal to the out-of-plane x_3 thickness of the DNS volume subsection. In this way, the out-of-plane particle displacement is less than 1/4 of the laser sheet thickness as recommended by (Adrian & Westerweel, 2011). Each particle is randomly assigned a diameter that is drawn from a log-normal distribution of values:

$$PDF = \frac{1}{x\sigma\sqrt{2\pi}} \exp\left(\frac{-(\log x - \mu)^2}{2\sigma^2}\right) \tag{4.2}$$

with parameters $\mu = 0.90\ px$ and $\sigma = 0.76\ px$ for the mean and standard deviation, respectively. The particle seeding density is 0.03 particles per pixel^2

(PPP), representative of that estimated from the experimental data presented in Section 4.3. The in-plane pixel intensity is computed from the integral form of the Gaussian function solved analytically using error functions as in (Raffel et al., 2018). Assuming a Gaussian intensity distribution with standard deviation σ_p for each particle, the total intensity for a given pixel at location $(x_{1,px}, x_{2,px})$ is expressed by:

$$I(x_{1,px}, x_{2,px}) \propto I_p \int_{x_{1,px}-0.5}^{x_{1,px}+0.5} \exp\left(\frac{-(x_{1,px}-x_{1,p})^2}{2\sigma_p^2}\right) dx_1 \int_{x_{2,px}-0.5}^{x_{2,px}+0.5} \exp\left(\frac{-(x_{2,px}-x_{2,p})^2}{2\sigma_p^2}\right) dx_2$$

$$I(x_{1,px}, x_{2,px}) = QI_p \left[\operatorname{erf}\left(\frac{\sqrt{8}(x_{1,px}+0.5-x_{1,p})}{d_p}\right) - \operatorname{erf}\left(\frac{\sqrt{8}(x_{1,px}-0.5-x_{1,p})}{d_p}\right)\right] \left[\operatorname{erf}\left(\frac{\sqrt{8}(x_{2,px}+0.5-x_{2,p})}{d_p}\right) - \operatorname{erf}\left(\frac{\sqrt{8}(x_{2,px}-0.5-x_{2,p})}{d_p}\right)\right] \tag{4.3}$$

where Q is a proportionality constant, set to 0.05 in the current work. Equation 4.3 represents the transfer function of an ideal camera sensor with a fill factor of 1. This is a more representative method of how a camera integrates the light intensity over individual pixels compared to simply using the analytical Gaussian expression. Finally, after the pixel intensities have been determined, the values are scaled to the dynamic range of an 8-bit camera sensor and rounded to integers to mimic discretisation.

Once the particle images are rendered, the images are vertically shifted upwards by 160 pixels to create a masked wall region of zero intensity. This vertical shift avoids having the flow region near the bottom of the image where boundary conditions in the wavelet transforms of wOF can affect the near-wall velocity estimates. Moreover, this shift of the flow region from the image boundary is consistent with experimental images presented in section 4.3. As this masked region in the images has 0 intensity, it does not contribute to the DFD and is effectively ignored in the minimisation (B. E. Schmidt & Woike, 2021). An example of a rendered particle field image is shown in Figure 4.1.

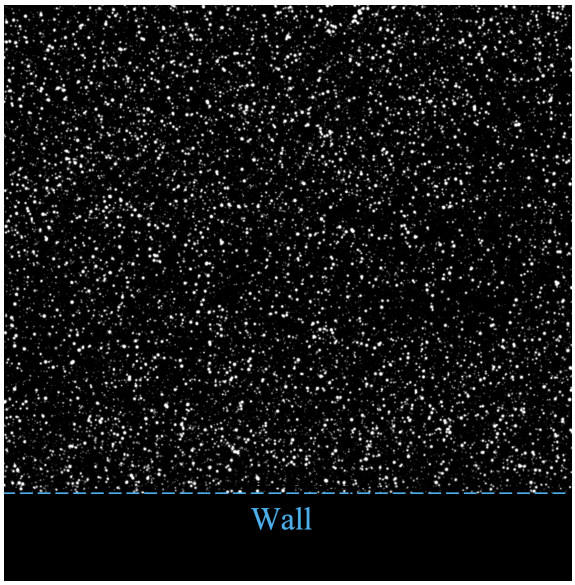

Figure 4.1: Example rendered particle field image from the channel flow DNS.

4.2 wOF assessment using synthetic data

In this section, wOF performance is assessed using the ground truth DNS data for comparison. In particular, the sensitivity of the wOF results to the regularization weighting λ is evaluated to understand how λ selection affects estimation of the turbulent boundary layer motion. wOF findings are reported for 6 values of $\lambda = [2, 40, 100, 180, 520, 1000]$. wOF for was initialised starting from a coarse initial scale of $C = 4$, rather than a full depth decomposition ($C = 0$) to accelerate computation. This range of λ covers velocity estimates ranging from under-regularized (visibly noise-dominated) to over-regularized (over-smoothed). The wOF error throughout the λ range is determined to identify suitable λ values where the wOF error outperforms PIV. In Section 4.2.1, characteristic velocity estimates for each λ are presented together with the error over the entire image domain. Section 4.2.2 evaluates the effect of λ on the calculation of wall units and the effect this has on the interpretation of the mean velocity within each region of the boundary layer.

PIV is also applied to the synthetic data, providing a benchmark to compare wOF with the current state of the art. A commercial cross-correlation-based PIV software (DaVis 10.0.05, LaVision) was used for PIV processing. The cross-correlation algorithm used 2 and 3 passes for the initial and final Gaussian-weighted IWs of size 64×64 down to 16×16 with 75% overlap. The anisotropic denoising filter in DaVis was applied to the PIV vector fields. The filter strength was selected for the most accurate results for the given IW size. Thus, it should be strongly emphasised that the PIV results presented are *optimised*. A geometric mask was placed 1 pixel below the no-slip grid point to capture the entire particle image region. This results in the first PIV velocity vector being 11 pixels above the no-slip pixel ($x_2 = 0$). For both PIV and wOF, the particle images were preprocessed using a min–max filter (Adrian & Westerweel, 2011) to account for changes in particle intensity resulting from out-of-plane motion within the synthetic laser sheet.

A notable feature of wOF is its ability to provide dense velocity estimates with per-pixel vector spacing. Although this impressive vector spacing is achievable, the

true spatial resolution of wOF is a subject not often discussed and requires thorough analysis which is beyond the scope of this work. The average spacing between particles can be considered to be a conservative estimate of wOF spatial resolution, since this is the average maximum distance between image features containing a genuine intensity signal. In the synthetic data, the average spacing between particles is 5.8 pixels. This value is considered as an upper bound for wOF's spatial resolution, as this estimate only considers the average distance between particle centers and does not take into account each particles' local intensity distribution for which additional valid vectors are associated. Additionally, because an explicit regularization scheme is used, the vectors in regions without particles will contain physically sound flow field information from regions containing genuine signals (B. E. Schmidt & Sutton, 2021). Such features would improve the true spatial resolution, but this requires further analysis. Thus, we report 5.8 pixels as the spatial resolution for wOF, while vectors are resolved per pixel. The PIV spatial resolution is reported as the final IW size (i.e., 16 pixels), while the vector spacing is 4 pixels.

4.2.1 λ sensitivity based on entire image domain

4.2.1.1 Single image analysis

The influence of λ is first described by evaluating features of the wOF velocity field within the entire image domain. Vector accuracy over the entire image domain is assessed by the normalised root-mean-square error:

$$\varepsilon_u = \sqrt{\frac{1}{n_v} \sum \frac{(U_1 - U_{1,DNS})^2 + (U_2 - U_{2,DNS})^2}{U_{1,DNS}^2 + U_{2,DNS}^2}} \tag{4.4}$$

In equation 4.4, n_v is the total number of vectors and U_i is the individual velocity value in the streamwise and normal direction denoted by subscripts $i = 1, 2$ respectively. Normalisation by the DNS velocity magnitude ensures that errors in regions of very low velocities near the wall are properly accounted for and not dominated by errors from large velocity magnitudes (McCane et al., 2001). Vectors from wOF outside the PIV masked boundary are ignored in the error calculation of wOF for equivalent comparison. For comparison with PIV, the DNS ground truth velocity is subsampled to a lower resolution grid using spline interpolation.

Figure 4.2 shows the instantaneous velocity field magnitude from a subset of four selected λ values. For comparison, the true velocity field from DNS and the corresponding velocity field from PIV are also shown. The associated ε_u value for each result is reported above each sub-figure. For wOF with $\lambda = 2$, the velocity estimate is under-regularized, leading to fine-scale noise visible as a speckle-like pattern within the velocity field and yields the highest ε_u of the results shown. As λ increases to 40, the regularity of the estimated flow field is increased and the noise becomes noticeably suppressed. At $\lambda = 180$, the noise is effectively removed from the velocity field and achieves the lowest ε_u, thus providing the closest agreement with the DNS. This λ value producing the minimum ε_u will be referred to as λ^*. Far beyond λ^* at $\lambda = 1000$, the flow field is considered over-regularized; the noise has been eliminated entirely at the expense of over-smoothing the flow and therefore deviating from the DNS with ε_u nearly doubling. PIV produces a high-quality velocity estimate with ε_u as low as the $\lambda = 40$ wOF result. With λ^*, a modest

improvement of $\approx 23\%$ in ε_u is achieved over PIV, demonstrating wOF's improved accuracy over the state of the art.

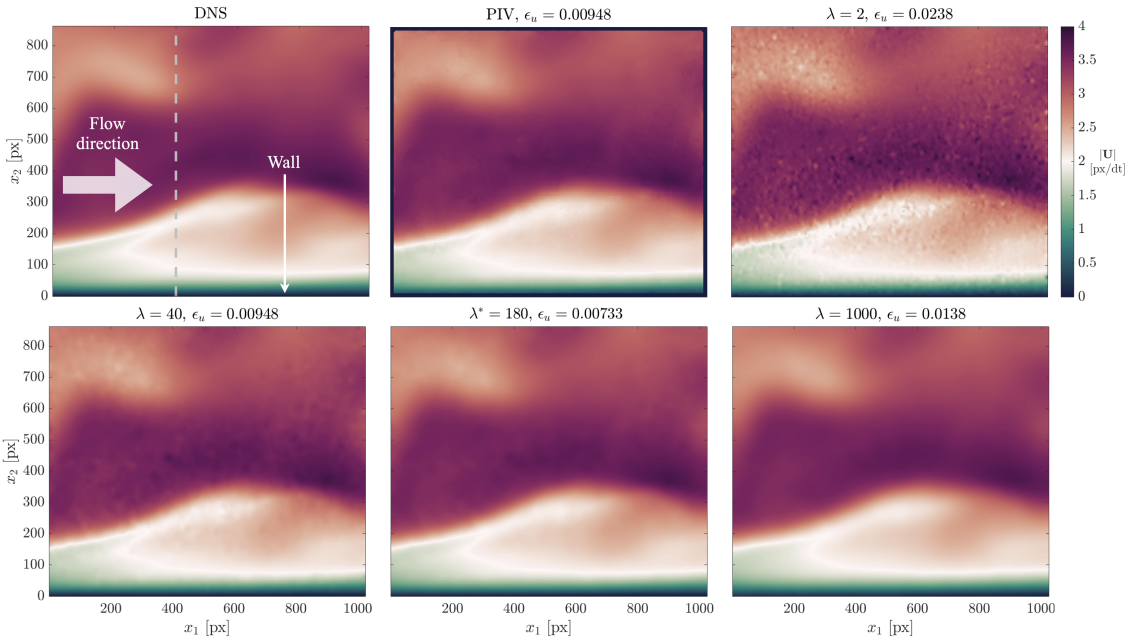

Figure 4.2: Instantaneous velocity magnitude for the DNS, PIV and wOF (λ = [2,40,180,1000]) results. The grey dashed line marks the location of the velocity profiles shown in Figure 4.3

.

Further assessment of how λ influences the estimated wOF velocity field is shown by evaluating local velocity profiles. Figure 4.3 shows the instantaneous streamwise velocity U_1 profiles extracted normal to the wall at pixel location $x_1 = 400$ marked by the grey dashed line in Figure 4.2. This x_1 location was chosen arbitrarily but reveals trends consistent across all x_1 locations. The characteristic noise present for the under-regularized $\lambda = 2$ is clearly seen as spurious small-scale velocity oscillations. These fluctuations are reduced significantly as λ is increased to λ^*, leading to overall better agreement with the DNS. In regions that contain high velocity gradients as shown near the inflection point at $x_2 = 240$ in Figure 4.3b), it is shown that $\lambda = 40$ follows the DNS better than $\lambda^* = 180$. Thus, even though λ^* is on average optimal for the entire imaged motion, localised regions of sharp velocity gradients may prefer a slightly lower λ to avoid washing out small-scale flow features. This is discussed later when considering the regional λ sensitivity. As λ exceeds λ^*, the over-smoothing effect is seen as a deviation from the DNS with velocity gradients becoming increasingly underestimated as clearly visible in Figure 4.3b). As a benchmark, PIV processing achieves good agreement with the DNS, but with the reduced vector spacing (1 vector per 4 pixels) as visible in Figure 4.3b).

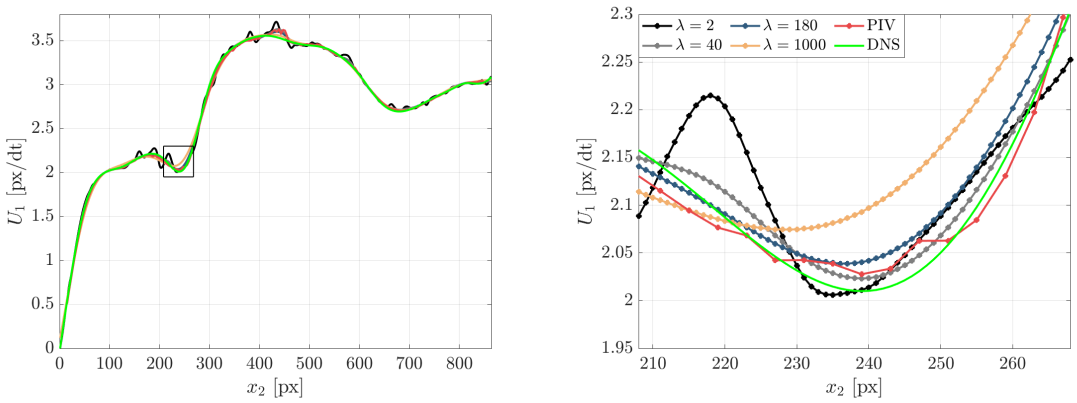

(a) (b)

Figure 4.3: a) Velocity profile along grey line location in Figure 4.3. b) Zoomed view of high velocity gradient region within velocity profile (extracted region marked by the square in a)).

The wOF ε_u sensitivity to λ is further evaluated for a broader range of λ computed across 118 values shown in Figure 4.4. Increments of $\delta\lambda = 1$ are used for the first 20 values to resolve the initial rapid ε_u variation, starting from $\lambda = 0.001$ to $\lambda = 20$, before changing to a coarser spacing of $\delta\lambda = 10$ for the remaining values. While this λ sensitivity is shown for a single image pair, trends are consistent for all image pairs within the 100 image sequence. The selected $\lambda = [2, 40, 100, 180, 520, 1000]$ values discussed throughout this work are shown in Figure 4.4. For clarity, these chosen λ values correspond to under-regularized ($\lambda = 2$), slightly under-regularized with ε_u equivalent to PIV ($\lambda = 40$), near minimum ε_u ($\lambda = 100$), minimum ε_u ($\lambda^* = 180$), slightly over-regularized with ε_u equivalent to PIV ($\lambda = 520$), and over-regularized ($\lambda = 1000$). The corresponding PIV error for the same image pair is marked by the red line for comparison.

As shown in Figure 4.4, wOF results for $\lambda < 40$ give unacceptable ϵ_u values significantly greater than PIV. The large ϵ_u is a result of the noise introduced into the under-regularized flow field. As λ increases above 40, ϵ_u values decrease less rapidly to the minimum ϵ_u at $\lambda^* = 180$. A gradual, linear increase in ϵ_u past λ^* ensues as the estimated velocity field becomes increasingly over-regularized. For the flow field in Figure 4.2, λ values in the range $\lambda = 40$ - 520 provide modestly more accurate velocity fields than PIV, at best reaching $\approx 23\%$ improvement in ϵ_u at λ^*. The exact range of λ yielding improvements over PIV varies slightly from image to image. However, it is positive to see a broad range of λ yield acceptable error values beyond the current state of the art and shows the strength of the current wOF approach.

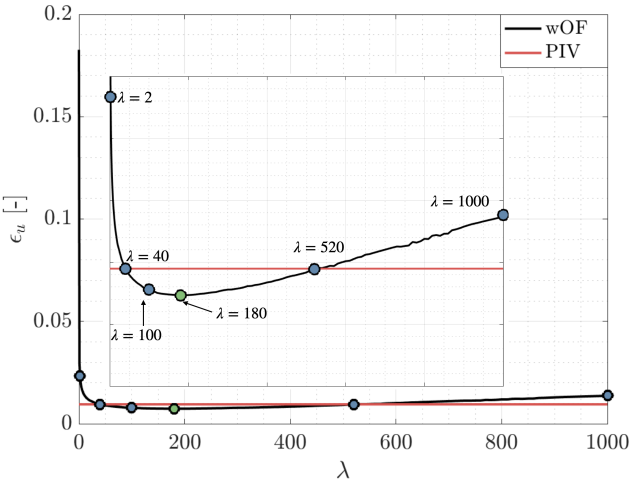

Figure 4.4: Sensitivity of wOF ϵ_u as a function of λ for the velocity field in Figure 4.2.

4.2.1.2 Image sequence analysis

The findings in the previous section consider a single image pair from the synthetic dataset. The influence of λ for the complete 100 image sequence, which involves a temporally varying wall-bounded flow, will be now considered. Figure 4.5a) shows the ε_u values for wOF at selected λ values, as well as for PIV across the image sequence. The 100 image average $\langle \varepsilon_u \rangle$ values are shown by the bar chart in Figure 4.5b).

For all results presented, the ε_u for a given image pair can be seen to vary slightly across the image sequence. This variation is dependent on the complexity of the instantaneous flow dynamics for a given image pair as coherent structures and streaks propagate across the image. Despite varying ε_u values across the image sequence, the trends remain consistent with those presented for the single image pair. In particular, ε_u values are exceptionally large for the under-regularized $\lambda = 2$ value, but ε decreases substantially as λ increases. ε_u values are lowest for $\lambda^* = 180$, but wOF findings with $\lambda = 100$ yield similarly low ε_u values, which is consistent with the broad local minimum curve feature shown in Figure 4.4. wOF findings with $\lambda = 40$, 520 yield comparable ε_u values as PIV. As λ increases beyond 180 values, ε_u gradually increases but remains lower than $\lambda = 2$.

Overall, the error analysis reveals that wOF can surpass PIV accuracy for a relatively broad range of λ values consistent with Figure 4.4. wOF can provide improvements in accuracy up to 24% compared to PIV. In addition, the gradual increase in ε_u for over-regularized λ values compared to the sharp rise in ε_u for under-regularized λ values suggests that in the absence of a ground truth reference, it may be preferable to select over-regularized as opposed to under-regularized velocity estimates. However, it should be emphasized that ε_u represents a spatially averaged value across the entire image domain. It is unlikely that a single λ value is optimal for all locations of the velocity field. This is already seen in Figure 4.3b), where it was shown that λ values closer toward the under-regularized side of λ^* were able to resolve sharp velocity gradients compared to λ^*. This finding is discussed further in the following section.

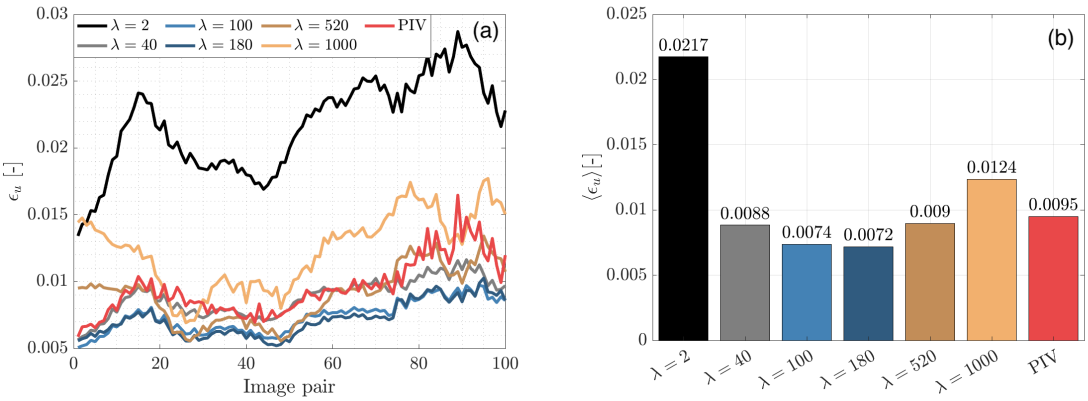

(a) (b)

Figure 4.5: a) wOF and PIV ε_u across the 100 image sequence. b) 100 image average value.

4.2.1.3 Regional λ sensitivity

A single λ value weighting applied to an entire image can lead to a non-optimal velocity estimation in various regions of an image. It is thus important to understand the local distribution of error across the individual boundary layer regions. In this section, the error from the ground truth is evaluated within each boundary layer region contained within the synthetic images. This analysis reveals the trend of λ to optimise wOF accuracy in each boundary layer region. For clarity, Figure 4.6a) shows the physical domain of the viscous sublayer ($y^+ < 5$), buffer layer ($5 < y^+ < 30$) and logarithmic region which covers the remainder of the image field of view ($30 < y^+ < 138$) in this dataset. In addition, the full viscous sublayer resolvable by wOF is considered in this analysis, as opposed to only considering the equivalent PIV region as performed for ε_u.

The unnormalised root-mean-square error (RMSE) is calculated to quantify the absolute error within each boundary layer region:

$$\mathrm{RMSE} = \sqrt{\frac{1}{n_v}\sum \left(U_1 - U_{1,DNS}\right)^2 + \left(U_2 - U_{2,DNS}\right)^2} \tag{4.5}$$

In contrast to ϵ_u, the absence of normalisation by the DNS magnitude in the RMSE avoids an exaggeration of errors closest to the wall where the velocity magnitude approaches zero. The 100 image average RMSE in each region is shown in Figure 4.6b-d) for the various λ values and for PIV.

In Figure 4.6, it can be seen that the RMSE trend as a function of λ is regionally dependent. In the logarithmic region, wOF performs exceptionally well for the previously acclaimed over-regularized $\lambda = 520$, 1000, but suffers from high RMSE as the velocity field becomes more under-regularized. In the buffer layer, wOF is sensitive to both under- and over-regularization; while the under-regularized $\lambda = 2$ still yields the highest RMSE, the RMSE for the over-regularized $\lambda = 520$, 1000 more than doubles compared to the logarithmic region and the optimal λ decreases from $\lambda = 520$ to $\lambda = 100$. In the viscous sub- layer, wOF now becomes more sensitive to over-regularization, as $\lambda = 1000$ now has the highest RMSE, while the RMSE for $\lambda = 2$ decreases substantially and the optimal λ decreases to 40. PIV performs

consistently well in each boundary layer region, however, wOF at its optimised λ values achieves RMSE improvements of 21%, 11% and 29% in accuracy over PIV in the viscous sublayer, buffer layer and logarithmic region, respectively.

This trend of wOF preferring lower λ values and becoming more sensitive to higher λ values as the wall is approached can be explained by considering the particular flow dynamics in these regions. In the logarithmic region, velocity gradients are weaker compared to closer to the wall. Therefore, effects of over-smoothing in the logarithmic region will have less of a detrimental effect on accuracy as the motion is predominantly uniform. As the wall is approached in the buffer layer, stronger velocity gradients exist requiring a slightly lower λ to resolve them without over-smoothing. In the viscous sublayer, where the lowest velocities are present, even lower λ values are preferred to resolve the sub-pixel particle displacements and consistently large velocity gradients, which are both significantly more sensitive to over-smoothing than noise compared to the regions away from the wall.

These findings demonstrate that a single λ value can slightly compromise the wOF accuracy within the various regions of the boundary layer. While spatially adaptive regularization schemes have been proposed in the literature (Lu et al., 2021; Ouyang et al., 2021; Stark, 2013; Zhang et al., 2020) implementation of these schemes is non-trivial and is beyond the scope of this work. Although wOF cannot be fully optimised using a single λ value, these findings positively demonstrate that values between λ = 100-180, including the optimal on average λ^*, provide well-balanced solutions in each region with wOF offering up to 23% improved accuracy over PIV.

4.2.2 λ sensitivity in the near-wall region

This section evaluates wOF's ability to estimate the mean velocity behaviour within the boundary layer by analysing the normalised velocity profiles depicted by u^+, y^+. The effect of lambda on wOF to accurately calculate $\langle U_1 \rangle$ and the near-wall velocity gradient γ is first assessed, since these variables are necessary to calculate u^+ and y^+. Subsequently, the fidelity of wOF to resolve the various turbulent boundary layer regions is evaluated. The ensemble mean velocity field presented in this section is composed from 100 velocity images and is evaluated separately for each λ, as well as for PIV.

4.2.2.1 Viscous sublayer mean velocity

The ensemble average streamwise velocity $\langle U_1 \rangle$ within the viscous sublayer ($y^+ < 5$) is shown in Figure 4.7a and a zoomed view closest to the wall is shown in Figure 4.7b. The $\langle U_1 \rangle$ profiles shown are extracted from the $x_1 = 400$ location marked by the dashed line in Figure 4.2. Immediately obvious in Figure 4.7 is the finer vector resolution for wOF compared to PIV; wOF provides vectors per pixel all to way to the wall, while PIV has one-fourth the vector spacing and resolves approximately half of the viscous sublayer region.

The effect of increasing λ on wOF is evident in Figure 4.7b). As λ increases, the streamwise velocity approaching the wall is elevated and increasingly deviates from the no-slip condition at the wall as the vector field becomes over-smoothed. For $\lambda \leq 180$, the deviation from the DNS is significantly less with low velocities of $\langle U_1 \rangle = 0.003$ to 0.01 at the wall. wOF with $\lambda = 2$, 40 provides the best agreement with

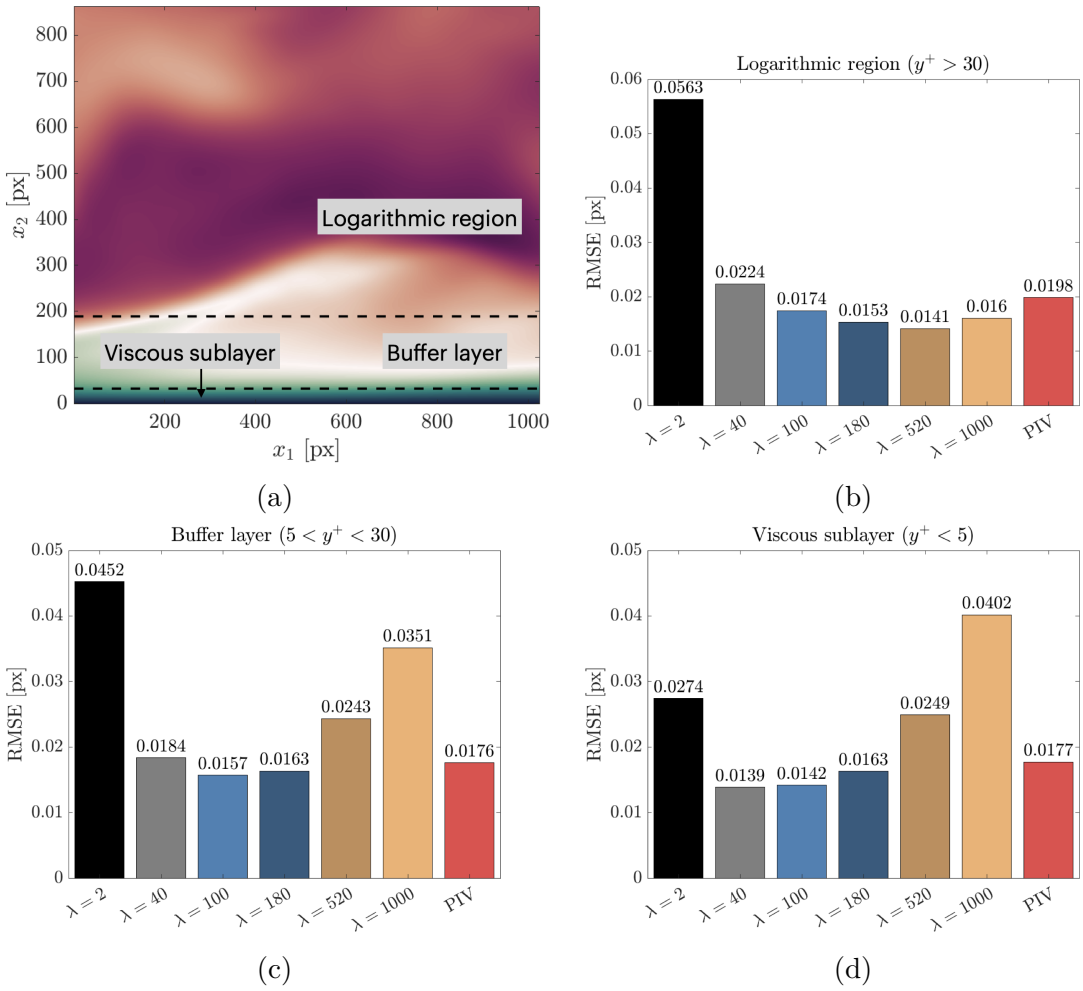

Figure 4.6: a) DNS velocity field with marked regions. Variation of average RMSE across image sequence as a function of λ for the b) Logarithmic region, c) Buffer layer and d) Viscous sublayer.

DNS, which is consistent with the analysis of the regional error distribution, showing slightly under-regularized wOF results produce the most accurate vector estimates in the viscous sublayer. However, the differences between $\lambda = 2$, 40 and $\lambda^* = 180$ are small ($< 3\%$). This smoothing effect of the regularization term J_R becomes particularly more apparent for $\lambda > 180$. This tendency for the regularization term to dominate and oversmooth at motion and image intensity discontinuities is well known in optical flow literature and is also influenced by using a quadratic penalty in J_R (Zach et al., 2007). Compared to the DNS and wOF results, PIV estimates a slightly lower velocity within the resolved PIV region down to $x_2 = 14$. Although relatively minor, this systematic error occurring in the vicinity of the wall is absent in all of the wOF results.

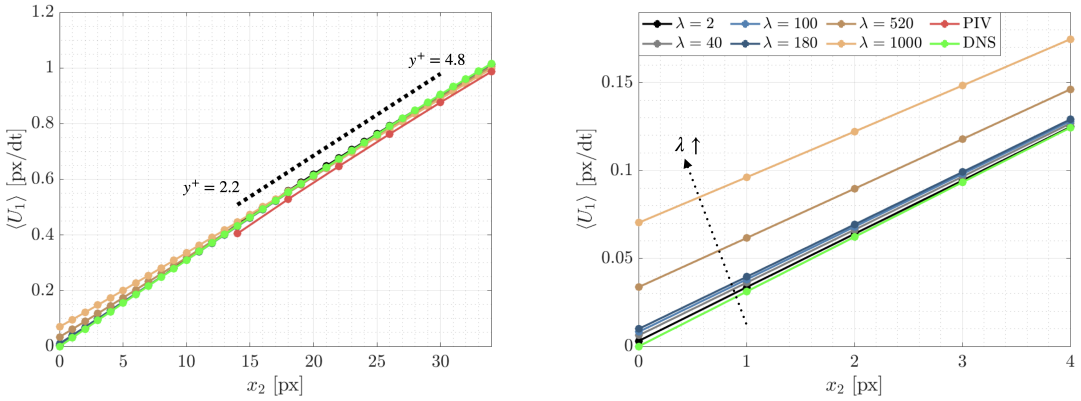

(a) (b)

Figure 4.7: a) DNS velocity field with marked regions. Variation of average RMSE across image sequence as a function of λ for the b) Logarithmic region, c) Buffer layer and d) Viscous sublayer.

4.2.2.2 Near-wall gradient

Having established how λ affects estimates of $\langle U_1 \rangle$ in the vicinity of the wall, it is necessary to understand how these effects propagate into deriving the near-wall gradient γ and therefore the friction velocity u_τ needed for the normalisation of boundary layer quantities. Accurate and direct estimation of γ can be challenging for several reasons. In particular, there is the need to resolve reliable velocity vectors as close to the wall as possible and maximise the spatial resolution. The sharp velocity gradient also needs to be resolved reliably in the presence of the image discontinuity (i.e., the masked wall region). The calculation of γ is performed by using a linear regression routine. For PIV, linear regression is performed from $y^+ = 4.8$ to the final vector at $y^+ = 2.2$ as illustrated by the dashed line in Figure 4.7. For wOF, linear regression is applied at $y^+ = 4.8$ and extends to $y^+ = 0.32$ to avoid the no-slip pixel at x2 = 0. The regression calculation includes five vectors for PIV and twenty eight vectors for wOF. A normalised percentage error in γ is calculated by:

$$\varepsilon_\gamma = \frac{|\gamma - \gamma_{DNS}|}{\gamma_{DNS}} \times 100 \tag{4.6}$$

The true γ_{DNS} is calculated using a linear regression across the same respective regions for each technique. The near-wall gradient error ε_γ is calculated at each valid pixel position for wOF away from the image edges and a subsampled γ_{DNS} is used for comparison with the lower resolution PIV grid. The mean average of the normalised near-wall gradient error ε_γ across the available x_1 distance is shown in Figure 4.8.

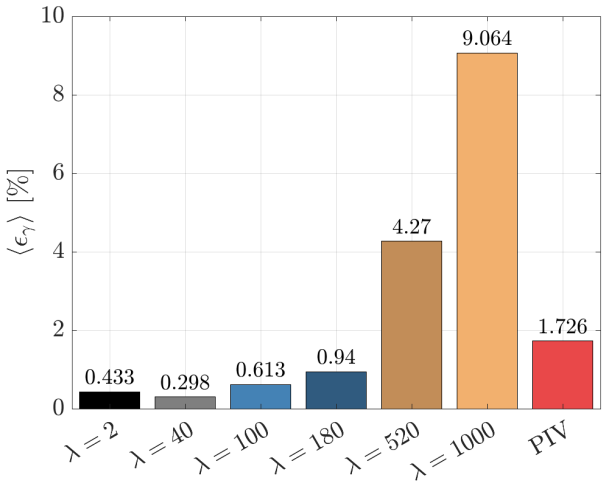

Figure 4.8: Average ϵ_γ error across the x_1 distance.

Figure 4.8 shows that the under-regularized λ values are more conducive to reduced error in ε_γ, with $\lambda = 40$ achieving the minimum $\langle \varepsilon_\gamma \rangle$ This trend is similar to the RMSE within the viscous sublayer (Figure 4.6d); however, now the under-regularized $\lambda = 2$ outperforms $\lambda = 100$, 180. wOF with $\lambda = 2$ performs better for ε_γ than for the RMSE because the noise present in each image at low λ is mostly washed out when calculating the ensemble mean velocity $\langle U_1 \rangle$. Despite the preference toward under-regularization, it must be emphasised that wOF results for $\lambda = 2$ to $\lambda^* = 180$ all provide higher accuracy than PIV. The ε_γ values for this λ range remain less than 1% and are a 45%–83% improvement over PIV. In contrast, the over-regularized $\lambda = 520$ and 1000 cases have serious and unacceptable levels of error, which are 147%–425% greater than PIV. These unacceptable errors are a result of over-smoothing the velocity field at the wall as shown in Figure 4.7. Clearly over-regularization should be avoided when evaluating velocity quantities closest to the wall.

4.2.2.3 Normalised mean velocity profile

The normalised u^+ velocity profiles are analysed to understand the effect of λ on wOF's ability to interpret the mean streamwise velocity in each region of the boundary layer. The inner-scaled profiles are presented in Figure 4.9, taken at the location marked by the dashed line in 4.2.

The relations for the linear $u^+ = y^+$ viscous sublayer and logarithmic region = $u^+ = 1/\kappa + \ln(y^+) + \beta$ with the constants $\kappa = 0.41$ and $\beta = 5.2$ (Pope, 2000) are indicated by the dashed lines. For the results in Figure 4.9, each profile is normalised using its respective u_τ calculated from γ.

When considering the results in Figure 4.9, it is first important to discuss the effect of γ on the velocity profiles. Recal that over-regularized $\lambda = 520$, 1000 yields an underestimation of γ due to over-smoothing the velocity field. According to Equations 2.6 and 2.7 an underestimated u_τ will decrease y^+ and increase u^+, creating a slight vertical and leftward shift in the normalised velocity profiles for $\lambda = 520$, 1000. In the viscous sublayer ($y^+ < 5$), this shift, as well as general over-smoothing of $\langle U_1 \rangle$, creates a deviation from DNS and the established linear $u^+ = y^+$ relationship. This shift also causes a mild deviation from the DNS throughout the buffer layer ($y^+ \approx$

5 - 30) followed by a more noticeable deviation in the logarithmic region ($y^+ \approx 30$ - 200). wOF findings from $\lambda = 2$ to $\lambda^* = 180$, which are not over-regularized, show excellent agreement with DNS throughout each region of the boundary layer. As shown in Figure 4.9, the noise associated with the under-regularized $\lambda = 2$ result is mostly washed out when considering the ensemble average velocity $\langle U_1 \rangle$. Although minor fluctuations due to under-regularization can be seen in the logarithmic region for $\lambda = 2$ (see Figure 4.9c), these fluctuations are smaller than the deviations present for over-regularized wOF results.

Figure 4.9 shows that PIV is broadly in good agreement with the DNS. A slight discrepancy in the logarithmic region exists for PIV, but not to the extent of $\lambda =$ 520, 1000. PIV resolves down to a minimum $y^+ = 2.21$ in the viscous sub- layer. Excluding the over-regularized $\lambda = 520$, 1000, wOF resolves 2 decades in wall units further than PIV, down to $y^+ = 0.15$ while maintaining agreement with the DNS with an error less than 0.05 δu+ for the final vector at the wall. Assuming a suitable λ is selected, these results show highly encouraging performance characteristics of wOF in terms of improved accuracy and increased vector density, which enables better interpretation of the viscous sublayer.

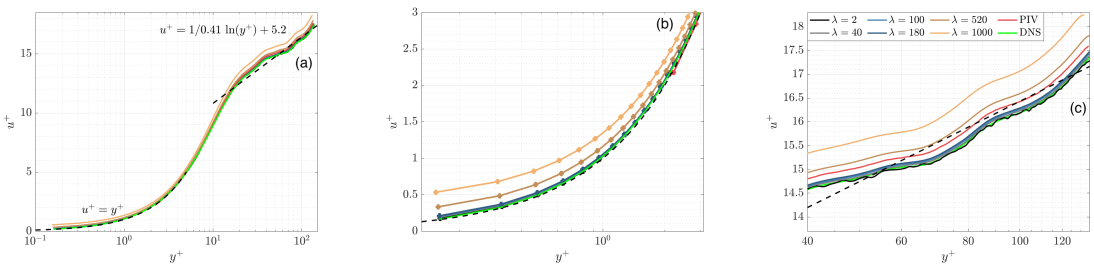

(a) (b) (c)

Figure 4.9: a) Inner-scaled mean velocity profiles. Zomed regions of the b) Viscous sublayer and c) Logarithmic region. Theoretical relations for the viscous sublayer and logarithmic region are shown in the dashed lines.

4.3 Application to experimental data

While synthetic data are key for quantifying and understanding error characteristics of wOF, it is essential to further evaluate the performance of the method on a real experimental dataset which departs from the simplicity of synthetic data. In Section 4.2, while it was shown that wOF provides improvements in accuracy over PIV, PIV performed exceptionally well for the synthetic data, which is absent of noise and other imaging artifacts. It should again also be emphasised that the degree of smoothing in the PIV results was optimised for maximum accuracy. This was only possible since the DNS ground truth velocity was available for comparison. True experimental data, on the other hand, do not have such a reference and often suffer from inherent camera noise, laser pulse variation and non-uniform illumination from reflections near the wall, which can present additional difficulties to obtain accurate velocity measurements. While image pre-processing methods can alleviate some of these effects, in practice, it is not possible to avoid them entirely. Applying the knowledge gained from the synthetic data, in this section, wOF is applied to experimental particle images of a developing turbulent boundary layer. wOF results

from a selection of λ values are compared to PIV, as well as a PIV + PTV approach, which provides higher spatial resolution than PIV. This comparison demonstrates the advantages of wOF over PIV and PTV to resolve the turbulent boundary layer flow features with improved vector resolution and accuracy.

4.3.1 Experimental setup

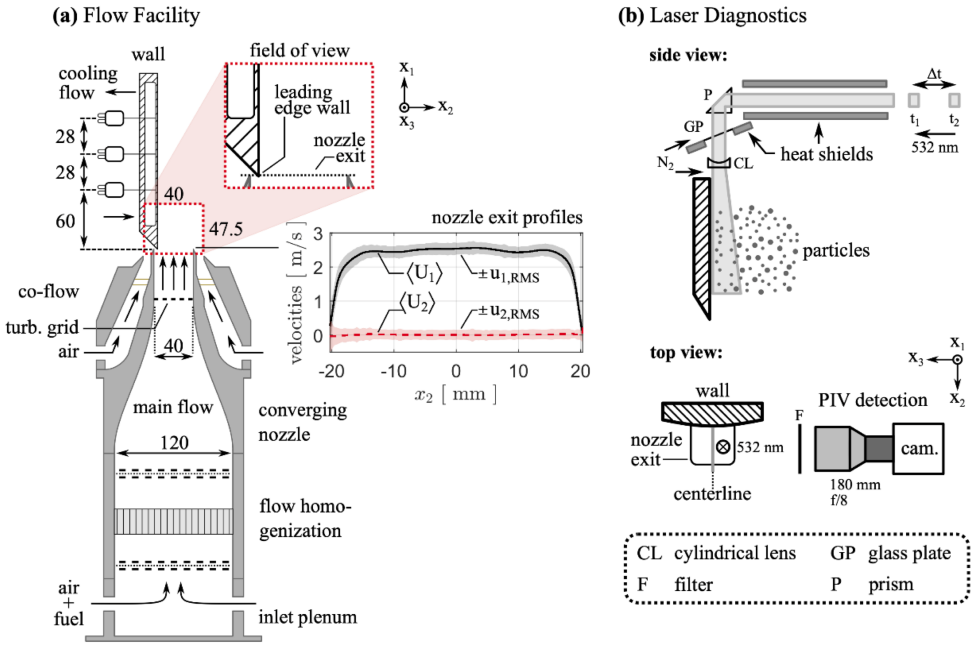

Figure 4.10: Schematic of a) Flow facility (SWQ-burner) b) Applied laser diagnostics in a side and top view. Numbers without units indicate spatial dimensions in millimeters.

Experiments are conducted in a flow facility in which a jet flow impinges onto a parallel wall, creating a developing turbulent boundary layer. The flow facility was originally designed to study flame-wall interactions in a side-wall quenching (SWQ) configuration (Jainski et al., 2018; Kosaka et al., 2018b, 2020; Zentgraf et al., 2021). For the purposes of this study, the flow facility operates under non-reacting, cold-flow conditions (i.e., no combustion). This experimental setup was recently presented in (Zentgraf et al., 2022) for characterising the nozzle exit velocity profiles of the SWQ-burner. A schematic of the facility is shown in Figure 4.10a). The central main flow (fully premixed CH4/air at $\phi = 1.00$; not ignited) was homogenised by meshes as well as a honeycomb structure and subsequently guided through a converging nozzle. At the square nozzle exit ($\approx 40{\times}40$ mm^2) the Reynolds number was maintained at 5900 and the inflow conditioning yielded a streamwise (x_1) velocity profile with a nearly top-hat shape (Zentgraf et al., 2022). For turbulent conditions at the nozzle exit, a turbulence grid was used, providing a turbulence intensity of 6-7 % (Jainski et al., 2018). The outlet flow impinged the sharp leading edge of a stainless-steel wall. The wall's surface has a mild curvature for improved optical access (radius: 300 mm, see top view in Figure 4.10 10b). The central main flow was shielded from the lab environment by a concentric square air co-flow. All flows operated at ambient temperature, which was in agreement with the wall temperature.

A low-speed (10 Hz) PIV setup was used as shown in Figure 4.10b. This setup was used previously to characterise the velocity profiles at the nozzle exit as boundary conditions (Zentgraf et al., 2022) and its optical arrangement closely matched the high-resolution, high-speed realisation in (Zentgraf et al., 2021). The main flow was seeded with Al2O3 particles (Zentgraf et al., 2021) which were illuminated using a dual-cavity Nd:YAG PIV laser (New Wave Research, Gemini PIV, G200, 10 Hz, 532 nm). Laser pulses were separated by $\triangle t = 40\mu s$. The laser sheets were guided vertically downward to the wall to minimise reflections at the wall. Measurements were taken in the x_1 x_2-symmetry plane of the facility, at the wall's centreline (x_3 = 0 mm). The origin of the coordinate system is defined at the leading edge of the wall along its centreline. Optics exposed to seeding were continuously purged by nitrogen during operation.

The resulting Mie-scattering was detected by a sCMOS camera (LaVision GmbH, Imager sCMOS) with an exposure time of 15 μs each frame. The camera was equipped with a 180-mm objective lens (Sigma, APO Macro DG HSM D, f/8) and a bandpass filter (Edmund Optics Inc., #65-216, central wavelength 532 nm, FWHM 10 nm) to suppress ambient light. The field of view (FOV) comprises ($\triangle x_1$, $\triangle x_2$) $\approx$ (40 mm,47.5 mm). For velocimetry, the images are cropped to ($\triangle x_1$, $\triangle x_2$) $\approx$ (38 mm,38 mm), comprised of 2048 $\times$ 2048 pixels with the FOV beginning at the wall's leading edge. At the downstream edge of the FOV, the Reynolds numbers based on the momentum thickness and friction velocity are $Re_\theta = 100$, $Re_\tau = 70$.

4.3.2 Vector field calculation

For the experimental dataset, wOF is benchmarked against PIV, as well as PIV + PTV, the latter of which is often used in experiments to improve vector resolution over PIV. It is emphasised that experiments were originally optimised for PIV/PTV. The seeding density was optimised to provide 6–8 particles per final interrogation window and particle displacement was within 1/4 of the final interrogation window size in the near-wall region of investigation. Velocity vector fields achieved average cross-correlation values of 0.77. It is therefore emphasized that the PIV quality is not intentionally compromised to exaggerate the advantages of wOF.

The wOF and PIV velocity fields were processed similarly to that of the synthetic data in Section 4.2. Mie scattering images were first pre-processed with subtraction of the ensemble minimum image followed by a min–max intensity normalisation (Adrian & Westerweel, 2011). PIV vector processing was performed using a multi-pass correlation with an initial IW size of 64 $\times$ 64 down to 16 $\times$ 16 with 75% overlap. The same anisotropic denoising filter used to optimise the PIV results on the synthetic data was applied to the experimental PIV vector fields. PIV + PTV processing was initialised from PIV. PTV was calculated for a particle size range from 1 to 8 pixels and with a correlation window size of 8 pixels. PTV vectors were converted to a structured 4 $\times$ 4 pixels^2 grid, as performed in previous boundary layer studies (Ding et al., 2019; M. Schmidt et al., 2021). This step was performed in DaVis using a "simple averaging / strong filter" scheme in DaVis, which provided the most reliable PTV results. A 3 $\times$ 3 Gaussian smoothing filter was applied to remove noise in the PTV vector fields. wOF was performed as described in Section 4.2.

Each velocimetry method provides a different vector spacing and spatial resolu-

tion. For PIV, the spatial resolution is 298 μm, as defined by the final IW size of 16 $\times$ 16, while 75% overlap provides a vector spacing of 74.3 μm (every 4 pixels). The converted 4 $\times$ 4 pixels^2 grid used for PIV + PTV provides a vector spacing of 4 pixels or 74.3 μm, which is equivalent to PIV. Since PTV assigns a vector to the centroid of each detected particle, an approximate PIV + PTV spatial resolution is reported as the average particle distance of 5.8 pixels or 107.8 μm. wOF provides a per-pixel vector spacing of 18.6 μm. A conservative estimate of wOF's spatial resolution is reported as the average particle spacing of 107.8 μm. As mentioned in Section 4.2, wOF's true spatial resolution is likely to be smaller than the average particle spacing since each particle pixel contains a valid vector, which likely makes the particle centroid spacing an upper limit.

The first vectors from the wall are located 279 μmm, 204 μmm and 149 μmm for PIV, PIV + PTV and wOF, respectively. These distances are based on geometric masks used to calculate vector fields that are offset from the wall location to avoid light reflections and reduce the frequency of spurious vectors at the wall for both methods. The wall location is approximated using the maximum intensity of the reflection present at the wall. This is then refined using the no-slip pixel position estimate from PIV and wOF $\lambda = 0.1$ $\langle U_1 \rangle$ profiles averaged over the downstream distance.

It should be emphasised that the experimental dataset is appreciably different from the synthetic dataset in Section 4.1, and this influences the optimisation of wOF. For example, the near-wall velocity gradient γ is larger and the viscous sublayer is much thinner for the experimental data than the synthetic data. In addition, the image size is 2048 $\times$ 2048 px compared to 1024 $\times$ 1024 px in the synthetic data. Therefore, not only is the absolute pixel-wise length halved, but the viscous sublayer comprises a smaller and less significant proportion of the full image FOV. Lastly, while the synthetic data have an average freestream particle displacement of 3 pixels, the experimental freestream flow field has a more substantial displacement of 6 pixels. All of these aspects, in addition to different image characteristics, will influence the regularization weighting for wOF, such that a suitable range of λ values will be significantly different between the experimental and synthetic datasets. This aspect is common within optical flow literature (Kadri-Harouna et al., 2013). In fact, the experimental data are significantly stricter and less forgiving compared to the synthetic data regarding selection of an acceptable λ. The absence of ground truth data means determining the true optimal λ is not possible. For the experimental data, wOF results from three values of $\lambda = 0.1$, 1, 20 are presented and the most appropriate λ is justified a posteriori based on physical principles as well as general comparison to PIV.

4.3.3 Instantaneous velocity fields

Assessment of wOF first considers the instantaneous velocity field in comparison with PIV and PIV + PTV. Figure 11 shows an instantaneous velocity magnitude field for PIV, PIV+PTV, and the three wOF results. An insert is shown for each image, which highlights details of a low- speed streak emerging from the wall.

PIV does well in resolving the overall velocity field. However, PIV can often struggle to resolve the velocity near the wall as shown by the pockets of unresolved velocity regions near the wall. PIV + PTV resolves closer to the wall than PIV but

resembles a noisier velocity field with similarity to the noise seen in $\lambda = 0.1$. It is noted that converting PTV to a larger grid size of 8×8 pixels^2 did not reduce the noise level in the PIV + PTV.

All three wOF results resolve similar general features as PIV, but the quality of the velocity field is determined by the choice of λ wOF with $\lambda = 0.1$ exhibits the high-frequency, speckle-like noise commonly associated with highly under-regularized findings. While $\lambda = 0.1$ resolves much of the same larger scale features as PIV and PIV + PTV, several artefacts of locally higher and lower velocities exist throughout the image. For wOF with $\lambda = 1$, the high-frequency noise is removed and the velocity field has strong agreement with PIV and PIV + PTV. The primary differences between $\lambda = 1$ and PIV are that wOF does not have spurious or missing vectors near the wall and wOF resolves velocities closer to the wall. In addition, $\lambda = 1$ does not contain the speckle-like noise presented in PIV + PTV. For $\lambda = 20$, the larger flow features are well captured, but the finer-scale features present in PIV, PIV + PTV, and $\lambda = 1$ are mostly removed, likely due to over-smoothing.

The fact that noticeable changes in the velocity field occur over a significantly smaller λ range confirms the challenge in selecting the appropriate λ for the experimental dataset. While it is not possible to determine a λ value that provides the highest accuracy, it would appear that $\lambda = 0.1$ is too under-regularized and $\lambda = 20$ is likely over-regularized. Further analysis of the findings within the turbulent boundary layer is performed to evaluate these aspects and to determine the suitability of $\lambda = 1$.

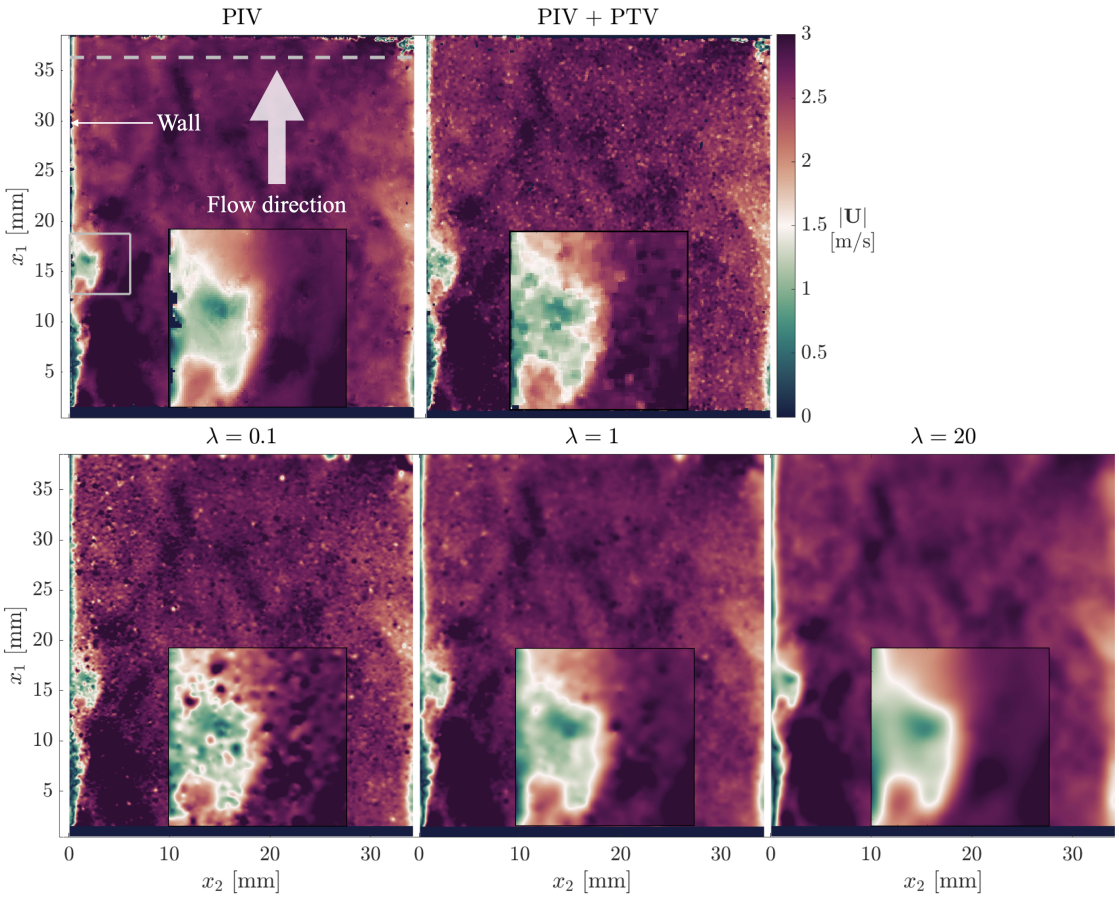

Figure 4.11: Instantaneous velocity magnitude fields. The insert shows a low-speed velocity streak emanating from the wall. The grey dashed line denotes the location where velocity profiles are extracted analysed in Figure 4.12.

4.3.4 Mean velocity profiles

The near-wall velocity profiles are shown in Figure 4.12a), with the normalised profiles shown in Figure 4.12b). The $\langle U_1 \rangle$ values are produced from a 100 image mean and the profiles are spatially averaged over a 2 mm streamwise x_1 distance centred at the location marked by the grey dashed line in Figure 4.11. The near-wall gradient γ is calculated from the ensemble average streamwise velocity fields using a linear regression in a similar manner to that described for the synthetic data. In the viscous sublayer ($y^+ < 5$), there are 15 velocity vectors for wOF compared to 3 velocity vectors for PIV and 4 for PIV + PTV. The linear regression for wOF and PIV + PTV uses each of the available vectors, while for PIV, only 2 out of the 3 available vectors are used since the final PIV vector nearest to the wall is frequently spurious. As described in Chapter 1, the estimation of γ has a direct effect on normalised wall units through u^+. The γ values calculated are γ_{PIV} = 1919, γ_{PTV} = 2402, $\gamma_{\lambda=0.1}$=0.1 = 2469, $\gamma_{\lambda=1}$ = 2288, $\gamma_{\lambda=20}$ = 1701 1/s, which provide the corresponding u_τ values $u_{\tau,PIV}$, PIV = 0.1697, $u_{\tau,PTV}$ = 0.1898 $u_{\tau,\lambda=0.1}$ = 0.1924, $u_{\tau,\lambda=1}$ = 0.1853, $u_{\tau,\lambda=20}$ = 0.1597. Incorrect estimates of γ can result in a strong offset from the exact $u^+ = y^+$ formulation shown by the green dotted line in Figure 4.12b). Comparison with this linear relation will be used as an approximate measure to judge the quality of the near-wall vectors in the absence of a ground

truth velocity.

In Figure 4.12a), the profiles above 1 mm from the wall are in excellent agreement. For $x_2 < 1$ mm, the $\lambda = 20$ profile shows increasing deviation from all other profiles as the wall is approached. In particular, velocity gradients are weaker leading to a flatter curve and significantly higher velocities at the wall. These features clearly indicate that $\lambda = 20$ is over-regularized; the excessive smoothing washes out the velocity gradient at the wall, creating an underestimate of u_τ. The resulting normalisation creates a strong deviation from $u^+ = y^+$ as shown in Figure 4.12b) and demonstrates that $\lambda = 20$ is not appropriate since the γ estimation is compromised.

In Figure 4.12a, good agreement is shown between $\lambda = 0.1$, 1, PIV, and PIV + PTV until $x_2 < 0.4$ mm, where PIV shows a milder gradient for $0.3 \leq x_2 \leq 0.4$ mm followed by a sharper velocity gradient at the last PIV data point. As will be shown, the last PIV data point is often erroneous, which biases the interpreted flow behaviour. In Figure 4.12b), PIV is offset from the $u^+ = y^+$, with an abnormal deviation in the curve for the last data point. PTV stays in closer agreement with $\lambda = 0.1$, 1 and is able to resolve closer to the wall than PIV although not to the same extent as wOF. The resulting normalisation to inner variables results in significantly closer alignment with $u^+ = y^+$ for PIV+PTV, although a slight offset remains. The $\lambda = 1$ result, on the other hand, shows perfect alignment with the $u^+ = y^+$ relation and remains in good agreement with a discrepancy of 0.04 δu^+ at the final vector. This suggests that $\lambda = 1$ provides accurate velocity estimates near the wall, as well as an accurate γ estimate. This also indicates that PIV, and to a lesser extent PTV, struggles to correctly estimate γ causing a slight shift in the normalised velocity profile, but not to the same extreme as $\lambda = 20$. The $\lambda = 0.1$ result exhibits the highest γ at the wall, creating a down- and rightward shift in the normalised velocity profile. This shift was not seen for the under-regularized values in the synthetic dataset, which further emphasises the higher sensitivity of λ for the more challenging experimental dataset compared to the synthetic data.

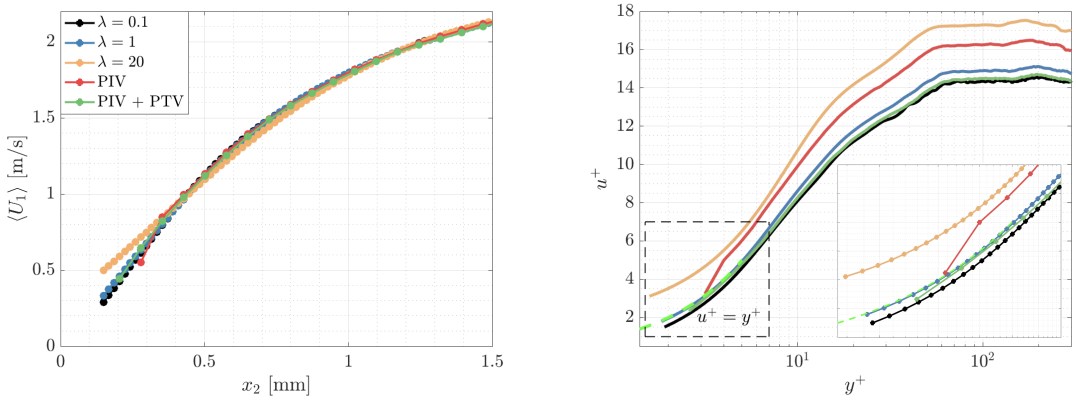

(a) (b)

Figure 4.12: a) Mean streamwise velocity profiles, b) Inner-scaled mean profiles. Profiles are spatially averaged over across a 2mm streamwise x_1 distance at the location marked by the gray dashed line Figure 4.11.

4.3.5 Normalised velocity fluctuation

The streamwise turbulent velocity fluctuations $u_1 = U_1 - \langle U_1 \rangle$ are analysed to further evaluate the capabilities of the velocimetry techniques. Velocity fluctuations provide an assessment of the data quality beyond the ensemble mean and are equally important to evaluate turbulent quantities in the boundary layer. Figure 4.13 shows the profile of the normalised streamwise velocity fluctuations $\langle u_1 u_1 \rangle^+$. The fluctuations and wall-normal coordinate in Figure 4.13 are normalised by the u_τ estimated from $\lambda = 1$ since this u_τ value provided the strongest agreement with $u^+ = y^+$. Normalising each case by u_τ, λ=1 removes the biased curve shifts as shown in Figure 4.12. Similar to $\langle U_1 \rangle$, the fluctuation profiles are spatially averaged across the 2 mm streamwise distance with the extent of a single standard deviation of these fluctuations illustrated by the shaded area in Figure 4.13. The standard deviation of the fluctuations within this 2 mm distance can be considered indicative of the reliability of the velocity estimate and its susceptibility to error.

In Figure 4.13, each curve follows a relatively similar trend from $y^+ = 200$ to $y^+ = 10$; $\langle u_1 u_1 \rangle^+$ values increase from the freestream region and exhibit a local maximum in the buffer layer at $y^+ \approx 10$ as seen in other boundary layer studies (e.g., (Spalart, 1988)). From $y^+ = 10$ toward the wall, each curve exhibits different trends. For PIV, $<u_1 u_1>^+$ values continue to increase quite substantially into the viscous sublayer. This trend is non-physical as the turbulent fluctuations are expected to decrease in the viscous sublayer as the wall is approached. PIV also exhibits a very large standard deviation below $y^+ = 10$, which is primarily caused by spurious vectors within the last 2–3 PIV vectors. This feature illustrates the challenges of PIV to accurately resolve small-scale fluctuations in the presence of strong velocity gradients. Reliable PIV measurements are often challenging directly near surfaces. While ensemble average PIV quantities can be represented with sufficient accuracy, higher-order velocity statistics and instantaneous velocity fields more clearly reveal challenges with PIV. PIV + PTV shows improvement from PIV; PTV resolves a greater extent of the buffer layer peak and initially shows the expected decrease in $\langle u_1 u_1 \rangle^+$ toward the wall. However, PIV + PTV still shows the non- physical increase in $\langle u_1 u_1 \rangle^+$ within the final 2–3 vectors at the wall and contains a large standard deviation. Although these artefacts are less severe compared to PIV, they demonstrate that PIV + PTV can still struggle to accurately resolve the flow nearest the wall

wOF findings, on the other hand, do not exhibit such large deviations in $\langle u_1 u_2 \rangle^+$, indicating that wOF is less susceptible to the same errors as PIV and PIV + PTV near the wall. Indeed, $\langle u_1 u_2 \rangle^+$ values are large for $\lambda = 0.1$ due to the results being under-regularized; however, $\langle u_1 u_2 \rangle^+$ values and their deviation are significantly lower than those for PIV or PIV + PTV near the wall. Below $y^+ = 10$, all wOF findings show the expected decrease in $\langle u_1 u_2 \rangle^+$. The $\lambda = 20$ profile shows a milder peak near $y^+ = 10$ and a milder decrease near the wall compared to other wOF results. The $\lambda = 20$ velocity is over-regularized for which excessive smoothing reduces the variation between peak and trough in the curve from $y^+ = 10$ to $y^+ = 1$. $\langle u_1 u_2 \rangle^+$ values for $\lambda = 1$ show the greatest decrease as the wall is approached, which follows the expected trend of turbulent fluctuations being suppressed within the viscous sublayer in close proximity to the wall. In addition, the extent of the shaded region for wOF remains constant near the wall suggesting that velocity errors are not being influenced by the proximity of the wall. Overall, wOF with $\lambda = 1$ shows the most

promising findings in terms of ensemble average values, as well as behaviour of the velocity fluctuations.

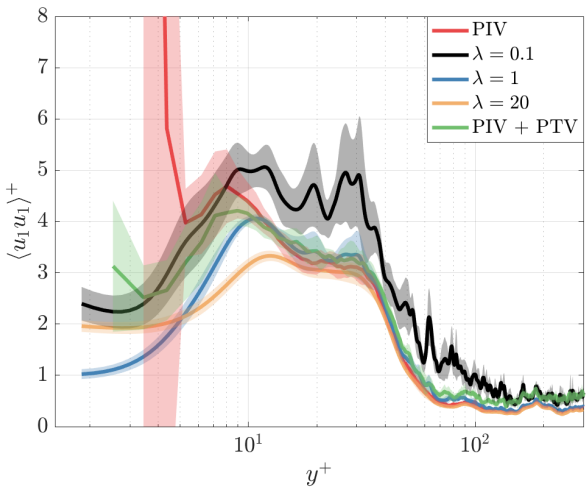

Figure 4.13: Streamwise turbulent fluctuations normalised by $u_{\tau,\lambda=1}$. The shaded regions indicate one standard deviation of the $\langle u_1 u_1 \rangle^+$ values within the 2mm region centred by the grey dashed line shown in Figure 4.11

4.3.6 Vorticity and turbulent flow structure

An example is presented which highlights the advantages of wOF in resolving turbulent flow phenomena within a boundary layer. This example is demonstrated for an instantaneous velocity field comparing the optimised wOF with $\lambda = 1$, PIV and PIV+PTV.

One of the added benefits of wOF over PIV or PIV + PTV is the improved vector spacing together with physically sound smoothing, and with that, the ability to better resolve velocity gradient quantities. Figure 4.14 shows the instantaneous vorticity field Ω for PIV, PIV + PTV, and wOF. The vorticity is calculated using the 8-point circulation approach described in (Raffel et al., 2018). Individual turbulent structures with relatively high vorticity magnitude are generated near the wall's leading edge and are advected downstream within the developing boundary layer. The inlays shown in Figure 4.14 highlight a region that captures a prograde vortex that was generated from the wall's leading edge. This is a particularly challenging region because of the vortex' proximity to the wall, where small pixel displacements coupled with the spatially varying sharp velocity gradients present difficulties for velocimetry techniques. Indeed, PIV has been used to resolve small-scale vortex structures near walls, but this is often accomplished by using high image magnifications yielding FOVs smaller than 5×5 mm^2 (Jainski et al., 2013), rather than a large FOV that is present in the current work.

The overall vorticity fields calculated from the velocimetry techniques are in good agreement; all methods show similar overall features such as the high vorticity regions extending from the wall's leading edge. PIV + PTV shows higher fluctuations in the vorticity field than PIV and wOF. This attribute is no doubt due to the higher degree of speckle-like noise present for PTV as shown in Figure 4.11. The inserts in Figure 4.14 highlight the capabilities of resolving the finer vorticity

structures near the wall for each method. Overall, the same spatial distribution of positive/negative vorticity structures is captured by each method, however, the effect of greater vector resolution is immediately seen; in particular, PIV and PIV + PTV images are substantially more pixelated compared to wOF. PIV can exhibit larger discontinuities in the vorticity field (i.e., larger changes from pixel-to-pixel), which are absent in the PIV + PTV and wOF results, with wOF achieving a highly resolved and more continuous vorticity field. The PIV + PTV vorticity field deviates more substantially from PIV and wOF with several strands of high vorticity extending from the larger vorticity structures. These elevated vorticity strands are likely due to elevated noise levels present in PIV + PTV as discussed in Figures 4.11 and 4.13. wOF is able to resolve the vorticity much closer to the wall and without troublesome unresolved regions from erroneous vector calculation as in the PIV and PIV + PTV fields. wOF faithfully preserves the features shown in both the PIV and PIV + PTV results, but achieves a much finer-detailed vorticity field.

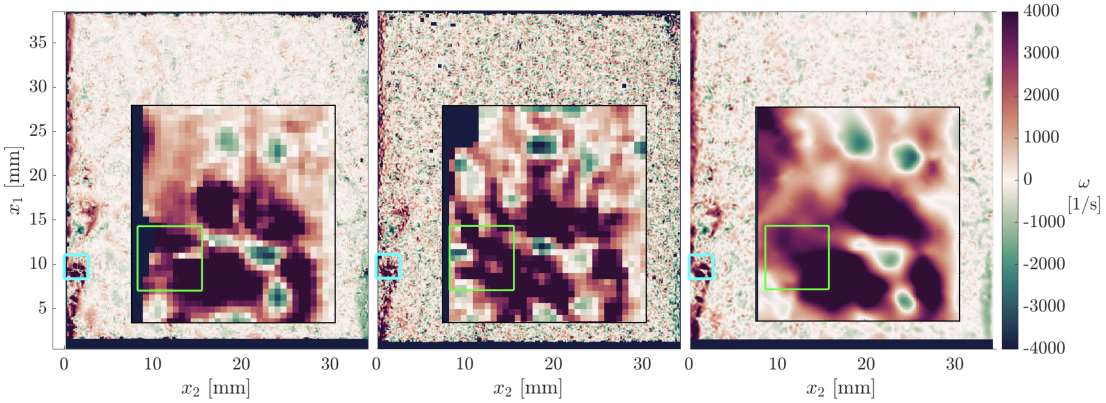

Figure 4.14: Instantaneous vorticity calculated for PIV (left), PIV + PTV (middle) and wOF (right). Inlays show a 0.8×0.8 mm^2 zoomed view of a vortex. The green rectangle indicates the location of the velocity vector field shown in Figure 4.15.

Figure 4.15 shows the corresponding vector field within the green rectangle shown in Figure 4.14. The vector field shows all available vectors for PIV, PIV + PTV and wOF shown in red, blue and black, respectively. wOF is capable of resolving the prograde vortex in much more detail than the other methods. While the vortex is visible in PIV and PIV + PTV, the vortex structure is more difficult to interpret due to sparser vector spacing and the presence of quasi-erroneous vectors that deviate from a vortical flow pattern. In Figure 4.15, all vector fields show good agreement above $x_2 = 0.6$ mm; most vectors are in alignment and are of the same magnitude. However, closer to the wall, there are larger disagreements between wOF and PIV. In many locations, PIV vectors are aligned orthogonally to wOF vectors. Some PIV vectors are clearly erroneous as they differ significantly from their neighbouring PIV vectors. Additionally, PIV vectors are absent in the upper left corner where spurious vectors are detected and removed during post-processing. Closest to the wall, PIV vectors point inwards toward the wall with a relatively large velocity magnitude, which strongly disagree with the wOF vectors directed parallel or outward from wall with a velocity magnitude more consistent with the neighbouring vectors. PIV + PTV improves on PIV in this regard with suitable quality vectors at the wall and calculates vectors in all regions. However, PIV +

PTV exhibits select vectors that disagree with PIV and wOF. In addition, PIV + PTV vectors near its vortex core centre are misaligned with its circulation and struggle to resemble a coherent vortex core. It is likely that PIV + PTV struggles to successfully resolve the strong gradients present in this region. The velocity field features shown in Figure 4.15 reveal some challenges cross-correlation-based PIV and combined PIV + PTV experience in resolving small-scale intricate flow dynamics with high velocity gradients in the vicinity of physical boundaries. Assuming a suitable λ is selected, these findings positively indicate that wOF is better suited to resolve these turbulent flow structures in the boundary layer region.

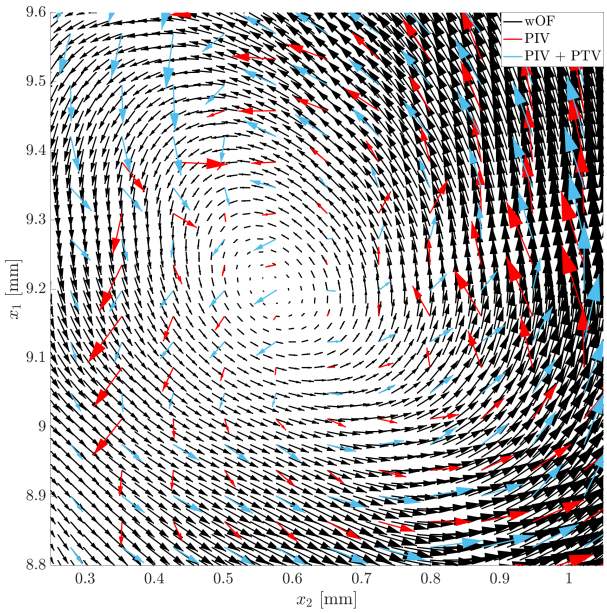

Figure 4.15: Vector field for PIV (red), PIV + PTV (blue) and wOF (black) within the green rectangle shown in Figure 4.14. Vector fields are shown at their original sampling resolutions.

4.3.7 Turbulent energy spectra

Lastly, to assess the potential of resolving fine-scale turbulent velocity fluctuations using wOF, the normalised streamwise turbulent kinetic energy spectrum ($E^*_{11}(\kappa_1)$) is analysed. This is calculated using the Fourier transform of the streamwise velocity fluctuations (u_1) across the entire field of view. Samples are filtered using a Hanning window to account for lack of periodicity in u_1 before computing the transform. The 1D turbulent kinetic energy spectrum, normalised by its peak value, is presented in Figure 4.16 for PIV, PIV + PTV and the optimised wOF with $\lambda = 1$. Due to the moderately low turbulence level, there is insufficient separation of scales to produce a significant inertial subrange ($-5/3$ region). The spectra reveal a high-frequency noise present for PIV at increasing wavenumbers. The PIV spectra do not show the classical energy decay at increasing wavenumbers, indicating the velocity measurement noise floor and spectral resolution limit have already been reached. The PIV + PTV spectra do not show the high-frequency noise present in the PIV profile. However, PIV + PTV spectra show elevated energy at all wavenumbers

compared to PIV together with a non-physical modulation after $\kappa_1 > 2{\times}10^4$. wOF is in close agreement with PIV and PIV + PTV at the low wavenumbers, but shows an energy decay at higher wavenumbers and resolves a significantly greater proportion of the energy spectrum without obvious indications that the measurement is being corrupted by noise or accuracy issues at high wavenumbers.

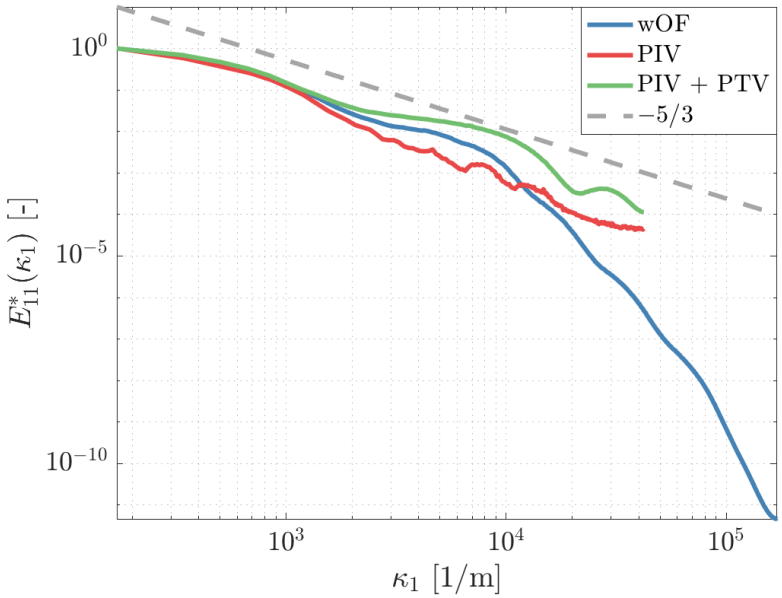

Figure 4.16: Normalised streamwise turbulent kinetic energy spectrum for PIV, PIV + PTV and wOF.

4.4 Conclusions

The performance of a wavelet-based optical flow (wOF) method was assessed in detail on synthetic and experimental particle images of turbulent wall-bounded flows. The ability to extract high-resolution estimates of instantaneous, mean and derived flow properties was evaluated in the vicinity of the wall. This was analysed in regards to selection of the regularization parameter λ, an aspect largely not discussed in other optical flow velocimetry works, and compared to results from correlation-based PIV.

Using synthetic PIV data generated from DNS of a turbulent boundary layer channel flow, a λ sensitivity analysis was performed over the entire field of view to establish a range of under-regularized, over-regularized and optimal wOF results. A regional λ sensitivity was investigated to understand the localised error behaviour and considerations necessary to optimise wOF within each region of the boundary layer. Away from the wall in the logarithmic layer, wOF is more sensitive to under-regularization, which introduces non-physical noise into the otherwise uniform velocity field. This noise causes significant deviation from the ground truth, leading to unacceptable errors nearly three times greater than PIV. The logarithmic region is less sensitive to over-regularization, since over-smoothing imposed by over-regularization removes noise and produces little deviation to the uniform velocity field. In the buffer layer, wOF is sensitive to both under- and over-regularization.

Over- regularization becomes problematic because over-smoothing washes out velocity gradients present in the buffer layer. In the viscous sublayer, wOF performs optimally when slightly under-regularized, which better resolves the velocity gradients at the wall in addition to sub-pixel particle displacements. In contrast, over-regularization yields the highest errors as it underestimates the near-wall velocity gradient (γ). This latter aspect is important when evaluating wall units (u^+, y^+) since an underestimated λ directly yields an over-estimated u^+ and underestimated y^+. Although wOF vectors at all locations cannot be optimal using a single λ value, results confirm a suitable range of λ values exist that outperform PIV in each boundary layer region with wOF also achieving significant improvement in resolving the viscous sublayer more effectively.

The accuracy and resolution improvement is more pronounced when wOF is applied to experimental images. Physically motivated selection of λ based on the expected linear relationship in the viscous sublayer allowed for wOF to better resolve the mean velocity closer to the wall and stay in excellent agreement with $u^+ = y^+$ down to the final vector. wOF further provided impressive vector resolution offering 15 vectors in the viscous sublayer, as opposed to PIV and PIV + PTV which, respectively, offered 3 and 4 vectors in the viscous sublayer with the last vector often being erroneous for PIV. Although PIV performed acceptably when resolving the mean velocity near the wall, evaluation of higher-order velocity statistics and instantaneous flow fields revealed the lower reliability of PIV near walls. In particular, estimates of the turbulent velocity fluctuations from PIV featured a non-physical increase near the wall with unreasonably high standard deviation for the last three vectors closest to the wall. PIV + PTV improved upon such errors, but still exhibited the non-physical increase in turbulent velocity fluctuations and large standard deviation near the wall. wOF did not exhibit these artefacts. Instantaneous velocity fields further demonstrate the spurious velocity estimations at the wall with PIV. While PIV + PTV exhibited less spurious velocity estimations, noise levels were comparable to the under-regularized wOF findings, which made it more difficult for PIV + PTV to provide reliable vorticity fields. wOF does not yield such erroneous velocity estimates, which, together with the improved spatial resolution, allowed for more accurate estimates of derivative quantities detailing complex flow structure in the vicinity of the wall. These findings positively indicate that wOF is well suited to estimate the flow dynamics in the presence of physical boundaries.

Chapter 5

Application to Reacting Flow

5.1 Introduction

With the relevant validation study on non-reacting wall-bounded flows complete, next wOF is applied to the same SWQ burner experimental setup now run under reacting conditions. This is a significantly more challenging dataset in multiple aspects; the flow dynamics are significantly altered by the combustion process which increases the image plane particle displacements and decreases the image signal-to-noise ratio (SNR) particularly in regions near the wall compared to the non-reacting case. Additionally, effects of thermal expansion across the flame front result in transient local regions of decreased particle seeding density when the flame is in close proximity to the wall. Higher seeding densities are in general preferable for PIV (Raffel et al., 2018) and more so for wOF (B. E. Schmidt & Sutton, 2019). The risk of spurious vectors near the wall for both velocimetry methods is therefore increased. Previously, wOF has previously been applied to a highly turbulent (Reynolds number = 58000) reacting jet flow (B. E. Schmidt & Sutton, 2020; B. E. Schmidt et al., 2021), demonstrating the ability to resolve the dissipation range of the turbulent energy cascade. To the best of the authors' knowledge, application of an optical flow technique to a wall-bounded turbulent reacting flow, with the aim of studying the novel flow phenomena, as opposed to being part of a comparison study with PIV, has never been done before.

Previous studies of (Steinhausen et al., 2023; Zentgraf et al., 2021) have suggested that the turbulent flow field plays a key role in FWI behaviour, including flame topology and flame quenching behaviour. Thus, investigating the intrinsically coupled dynamics of the flame and turbulent flow is necessary to understand these phenomena. Of particular interest is a flame vortex interaction, shown previously in Chapter 1 which is hypothesised by (Zentgraf et al., 2021) to be a transport mechanism responsible for presence of cold burnt gas products in the unburnt gases in the vicinity of the flame quenching point. This unique thermochemical state of low temperature (<450K) and high concentration CO_2 near the wall does not occur in the laminar case and therefore resolving the turbulent flow field is key in understanding this process. The DNS study of (Steinhausen et al., 2023) provided supporting evidence of the entrainment of the burnt gases into the unburnt reactants in the vicinity of the flame tip at the quenching location. Although the vortex responsible for this transport process has been inferred from elevated regions of Q-criterion in these studies, the actual flow field associated with the vortex and facilitating the

transport process, has never actually been explicitly revealed. This chapter adopts a Lagrangian reference frame to reveal the vortical flow field combined with vortex tracking and conditional analysis to study the influence of this unique flame vortex interaction on local flame quenching behaviour. Quadrant analysis of the velocity fluctuations is used to investigate dominant coherent flow motions facilitating mass transport processes in the boundary layer. Previous studies have reported that the quadrant distribution of the turbulent flow is significantly altered in the presence of a flame front, as compared to the canonical non-reacting case (T. Alshaalan & Rutland, 2002; Jainski et al., 2018).

The advantage of improved resolution from wOF is used to resolve a greater range of lengthscales present in the turbulent flow field as well as achieve a generally higher fidelity representation of the flow phenomena under investigation together with increased statistics. The wOF results are supplemented with the robust but also lower resolution measurements from PIV. Findings from the two methods are in agreement with each other. This chapter only presents wOF findings. Example comparisons of figures with the supporting PIV results are available in Appendix B.

5.1.1 Experimental setup

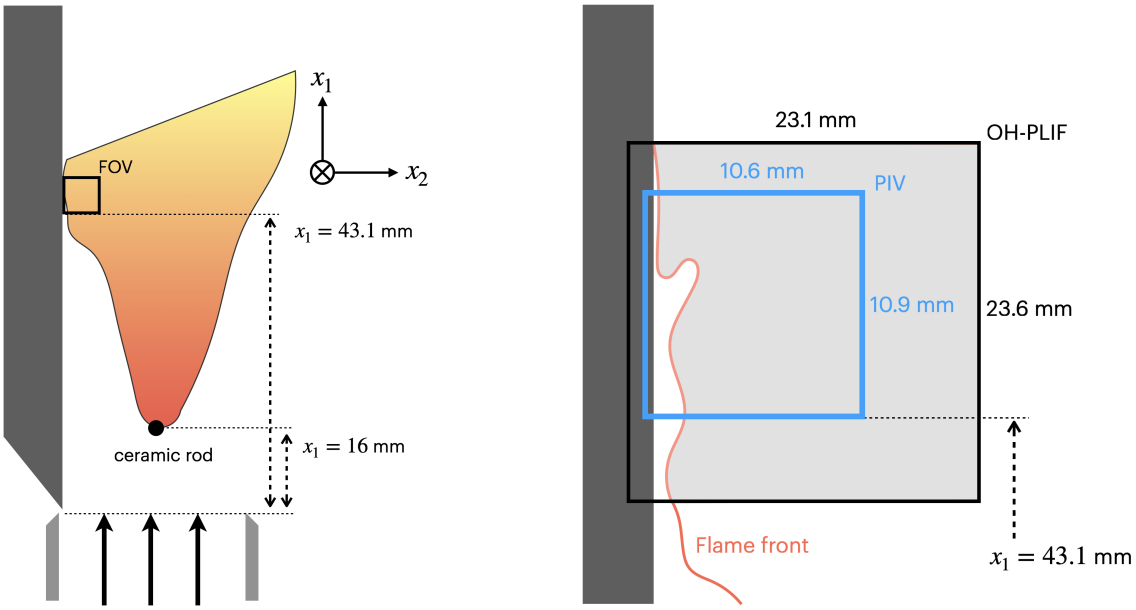

Figure 5.1: a) Schematic of experimental setup. b) Measurement region.

A schematic of the SWQ experimental setup for the reacting case is shown in Figure 5.1 a). This setup has been extensively studied for FWI investigations (Jainski et al., 2018; Zentgraf et al., 2021, 2022) and is an established experimental facility. The pertinent details specific to the reacting operating conditions are summarised below. Other experimental parameters are as described in Chapter 4. The flow through the burner is a premixed mixture of dimethyl ether (DME)-air with an equivalence ratio of $\Phi_{EQ} = 0.83$. The main flow is ignited and the V-shaped flame stabilised on a $1mm$ diameter ceramic rod acting as the flame holder. One

branch of the flame impinges on a stainless steel wall which is actively water cooled to maintain a surface temperature of 330K.

Additional characteristics of the experimental setup are summarised in Table 5.1. The Reynolds number of $Re = 5900$ is calculated based on the hydraulic nozzle diameter ($D = 41.7$mm) and the average bulk flow velocity ($U_B = 2.2$m/s) from the volume flow rate. The velocity profile at the nozzle exit is as shown in Figure 4.10 in Chapter 4 previously.

Non-dimensional parameters relevant to this experiment include the Damkohler number Da, characterising the ratio of the turbulent flow time scale to the chemical reaction time scale. Assuming the laminar flame thickness and Kolmogorov length scales in the calculation of Da leads to the Karlovitz number Ka. Based on these numbers, the Borghi-Peters regime diagram classifies the turbulent flame structure. The flame in the present experiment is reported as being in the wrinkled flamelet regime (Zentgraf et al., 2021), therefore the flame front is mildly stretched and wrinkled by turbulent fluctuations that are below the laminar flame speed. The Peclet number Pe is the ratio of the quenching distance (height from the wall where the reaction extinguishes) to the laminar flame thickness. This is frequently used to characterise near-wall quenching phenomena, with typical values reported as being $Pe \approx 7$ and $Pe \approx 3$ for side-wall quenching (SWQ) and head-on quenching (HOQ) respectively (T. Poinsot & Veynante, 2005).

Flame characteristics	
Laminar flame thickness l_f (Zentgraf, n.d.)	400μm
Laminar flame speed U_f (Qin & Ju, 2005)	0.35 - 0.39m/s
Adiabatic flame temperature (Kosaka et al., 2018b)	2190K
Nozzle exit velocity characteristics	
Re (Zentgraf et al., 2021)	5900
$u_{i,RMS}$	0.18 m/s
Turbulence intensity	7.2%

Table 5.1: Experimental parameters.

The laser diagnostics used in this investigation are simultaneous high-speed PIV and planar laser-induced fluorescence (LIF) imaging of the OH radical. The experiments were performed by Florian Zentgraf at the Technical University of Darmstadt and are described in full detail in (Zentgraf et al., 2022). A frequency-doubled Nd-YAG laser operating at 532nm and a repetition rate of 4kHz was used for PIV. The laser provided two laser pulses separated by $\triangle t = 10\mu s$, which describes the time-pulse separation between the Mie scattering images. Alumina particles (Al_2O_3) with a nominal diameter of 300nm were used as the tracer. These particles were introduced into the air stream prior to the air mixing with fuel by a customised vibrational seeder. Mie scattering images were recorded by a high-speed CMOS camera (Phantom v2640 by Vision Research Inc.) operating in double frame mode. The camera was equipped with a 180mm objective lense and extension tubes equally 180mm in length to provide a high image magnification of 2.25.

For OH-LIF, a frequency-doubled high-speed dye laser pumped by a frequency-doubled Nd-YAG laser was used to provide a laser pulse at 283.1nm to excite the $Q_1(6)$ transition of OH. The OH-LIF laser operated at 4kHz repetition rate and the OH-LIF laser pulse was synchronised in between the two PIV pulses. The OH-LIF

images were acquired by a scientific high-speed CMOS camera (Fastcam SA-X2 by Photron) coupled to a high-speed image intensifier (HS-IRO by LaVision). The HS-IRO was equipped with a 150mm UV lense and bandpass filters to detect the OH signal from 300-320nm. The LIF field of view is $(\Delta x_1, \Delta x_2) = 23.6 \times 23.1\text{mm}^2$ and is centred around the PIV field of view of $(\Delta x_1, \Delta x_2) = 10.6 \times 10.9\text{mm}^2$ as shown in Figure 5.1b). Both field of views are coincident in the out-of-plane (x_3) direction at the wall centreline.

5.1.2 LIF image processing

In order to analyse and quantitatively correlate the flame front position with the velocity field dynamics, it is necessary to extract the flame front contour from the LIF images. The sequence of processing steps is shown in Figure 5.2. All LIF images are initially cropped to the PIV field of view, reducing the final LIF image size from 1052×1039 pixels^2 to 494×475 pixels^2. Firstly to remove noise, the raw image is filtered with a non-local means filter (Buades et al., 2005). Unlike classical Gaussian filtering schemes, this filtering operation is both edge preserving and adept at reducing visible noise. Two subsequent operations are then performed separately on the filtered image: (1) the filtered image is binarised using an adaptive thresholding technique (Bradley & Roth, 2007) and (2) edge detection is performed using a derivative of Gaussian filter followed by calculation of the quadratic gradient magnitude $|\nabla I|^2 = (\partial I/\partial x_1)^2 + (\partial I/\partial x_2)^2$. The contour of the binarised region, shown in red in Figure 5.2c-d),f) is extracted and used to extract the gradient magnitude values travelling along the contour. The values of the trace are then normalised between 0 and 1. The quenching point is next detected in a similar manner to (Jainski et al., 2018; Zentgraf et al., 2021) as the point where the gradient magnitude values first exceed a threshold T_{QP} when travelling along the flame front in the upstream direction. Below this value, the LIF signal is too diffuse and does not feature the signature sharp OH gradient representative of a reacting flame front. The contour and binarised image downstream of this point are then set to 0. Not all LIF images involve flame quenching and can have a continuous unquenched flame within the cropped PIV field of view. Therefore, to avoid artificially detecting a false quenching point, a minimum (unnormalised) gradient ($|\nabla I|^2$) must exist. All parameters involved in the above operations are summarised in Table 5.2.

Non-local Means Filter	
Degree of Smoothing	100
Search Window Size	41
Comparison Window Size	21
Adaptive Threshold	
Threshold sensitivity	0.55
Neighbourhood size	71
Statistics	Gaussian
Derivative of Gaussian filter	
Sigma	3
Quenching Point Detection	
Minimum $\|\nabla I\|^2$	1×10^{-4}
T_{QP}	0.08

Table 5.2: Parameters in the image processing routine.

The described LIF image processing methodology produces similar results to the methods used in (Jainski et al., 2018; Zentgraf et al., 2021). However, the current method is also adapted to accurate detection of flame front regions of high curvature, as well as producing more continuous flame fronts without use of edge-linking or region-growing algorithms following edge detection. These benefits are advantageous when sampling flow quantities normal to the flame surface as will be done in a forthcoming section for the strain-rate.

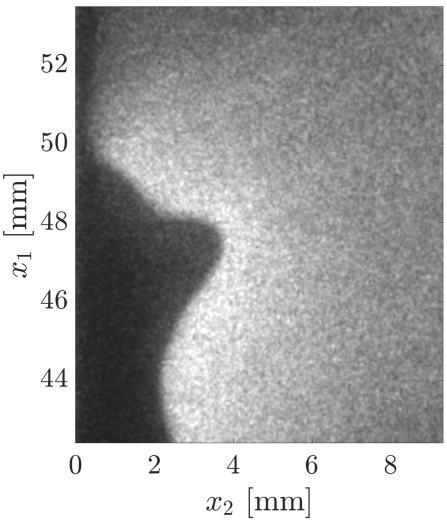

(a) Raw LIF image.

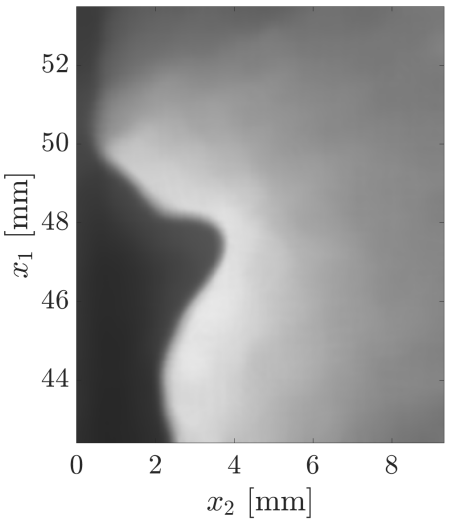

(b) Non-local means filtered.

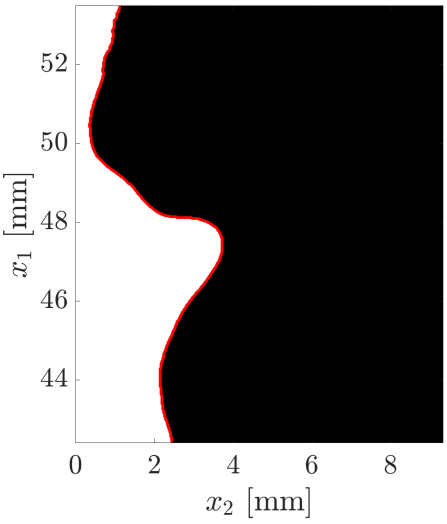

(c) Binarised image.

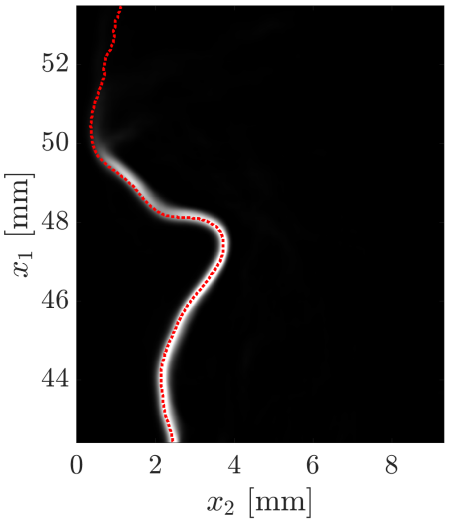

(d) Quadratic gradient magnitude $|\nabla I|^2$.

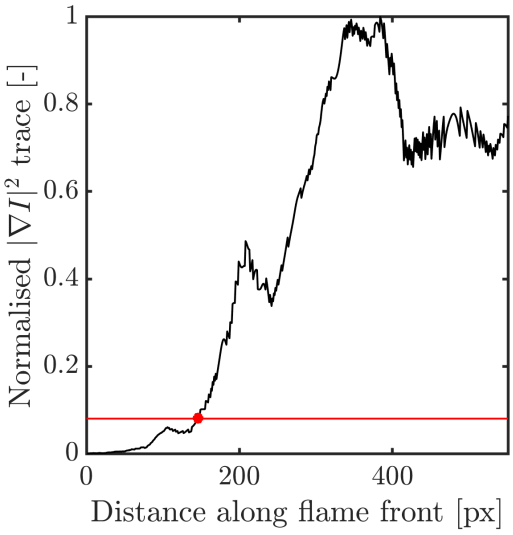

(e) Trace of $|\nabla I|^2$ along binarised contour.

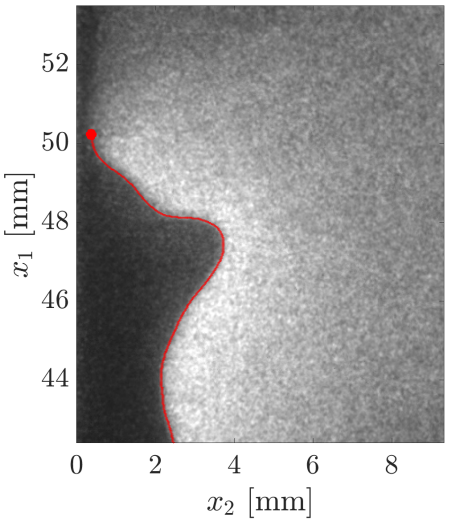

(f) Final flame contour and quenching point

Figure 5.2: Image preprocessing and flame front detection routine.

A flame probability map or averaged progress variable can be calculated from the ensemble mean average of the binarised LIF images Figure 5.2c) and is shown in Figure 5.3. A mean flame front is defined as the 0.5 isocontour of the flame probability map in this work, marked as the dotted line in Figure 5.3.

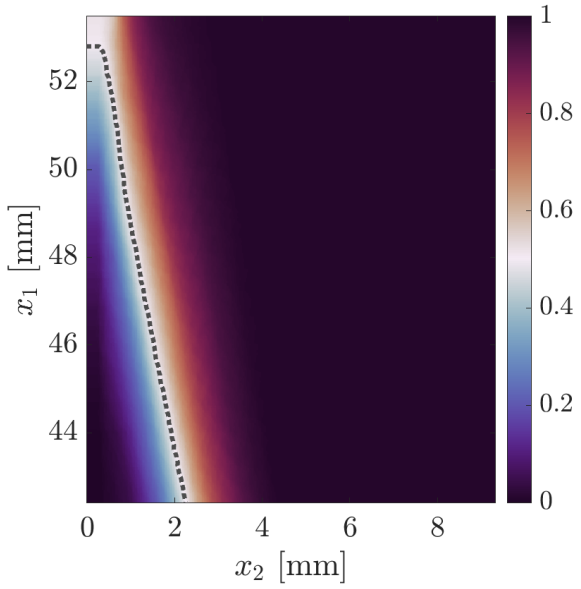

Figure 5.3: Flame probability map. The dotted line indicates the 0.5 isocontour.

5.1.3 Vector field processing

Tracer particle images are preprocessed similarly to the experimental data in Chapter 4. This involves the subtraction of the ensemble minimum image from each individual particle image, followed by min-max normalisation filter of length 9 pixels. Lastly, a 3×3 Gaussian smoothing filter was applied [1].

PIV processing used multipass cross-correlation beginning with 2 passes starting with IWs of size 64 × 64 pixels^2 and 50% overlap down to a final size of 32 × 32 pixels^2 using 3 passes and 75% overlap. An intermediate setting of 4/7 was used for the anisotropic denoising filter. Vectors with correlation values < 0.9 and groups with less than 5 vectors are removed. A single pass median filter with universal outlier detection (filter region 11 x 11) is used to detect erroneous vectors. The reported PIV spatial resolution is 188μm here based on the final IW size. From the IW overlap, the final PIV vector spacing is 1 vector every 8 pixels (1 vector every 47 μm).

As described previously, an appropriate λ value must be set for wOF. A similar approach to Chapter 4 is used to motivate appropriate selection where the smoothing effect in regularization is understood through its impact on the near-wall velocity gradient γ. Resolving the wall shear stress τ_w is not the aim of the present investigation, and the $u^+ = y^+$ relation used to validate selection in Chapter 4 is not

[1]The image preprocessing parameters for the PIV images were jointly optimised by the author together with Dr Florian Zentgraf whose valuable assistance is kindly acknowledged here. The particle image preprocessing sequence was intended to optimise correlation values in the PIV results. While the final processed particle images were suitable for wOF, it should be noted that they are not *necessarily* optimal for wOF but do allow for direct comparison with the robust PIV results here, as well as those in related publications such as (Zentgraf et al., 2021).

a priori known to be valid in a reacting turbulent boundary layer. The near-wall velocity can still be used to guide approximate λ selection by revealing when the smoothing effect inherent in regularization becomes excessive and non-physical.

The streamwise mean velocity $\langle U_1 \rangle$ for wOF, $\lambda = 10$ is shown in Figure 5.4a) below. In Figure 5.4b), the velocity profiles from additional results from $\lambda = 1, 5, 20$ averaged over the dashed x_2 region in Figure 5.4a). The inlay shows the characteristic effect of increasing λ creating a progressive deviation from the no-slip condition as presented previously. This example already demonstrates some of the challenges of near-wall measurements in the reacting case since the PIV vector nearest to the wall is seen to be erroneous. It is reassuring that wOF results at any λ do not show the same non-physical high magnitude velocity.

Of the 4 λ values processed, $\lambda = 10$ is the final selection for this study as it closely resemble the PIV profile down to $x_2 \approx 0.2$ before the wOF profiles start deviating more substantially. While this does show a slightly elevated velocity from the λ =5 result, a higher λ is preferable here for increased robustness against noise given the decreased particle image SNR. The elevated λ is also analogous to using the larger IW size of 32×32 (compared to 16×16 in the non-reacting case) for the PIV processing. It should be noted that the conclusions of the investigation are not influenced by the λ setting. The wOF per pixel vector spacing results in 1 vector every 5.88 μs which is 8$\times$ the density of the PIV vectors.

A geometric mask is applied for PIV images, resulting in the first PIV vector being x_2 =0.1734mm from the wall. Images for wOF are masked slightly closer to the wall with the first vectors beginning at x_2 =0.1087mm. The wall position is estimated from the no-slip condition using the $\langle U_1 \rangle$ profiles averaged across the streamwise extent in a complementary non-reacting PIV dataset. Since the LIF and PIV images are spatially referenced, the same wall position for particle images applies to the LIF images.

Note that 2 imaging artefacts are present in the upstream and downstream regions of the FOV at $x_2 \approx 3$. This artefact is also described in the thesis of (Zentgraf, n.d.). These intensity range of these artefacts varies throughout the image sequence and intermittently contributes to non-physical high magnitude velocities for both PIV and wOF. These regions are masked out during postprocessing for both velocimetry methods. The total number of PIV image pairs processed is 1000. The processing time for PIV is approximately $\approx$ 3-4 hours, while for wOF it is considerably longer at $\approx$48 hours with the image sequence distributed among 3 workstations running in parallel. This is largely due to the fact that the wOF vector field is 64$\times$ more dense than the PIV. It should also be noted that the wOF code is written in MatLab and further optimisation is possible, as done using GPU acceleration in (Dérian et al., 2015) for example.

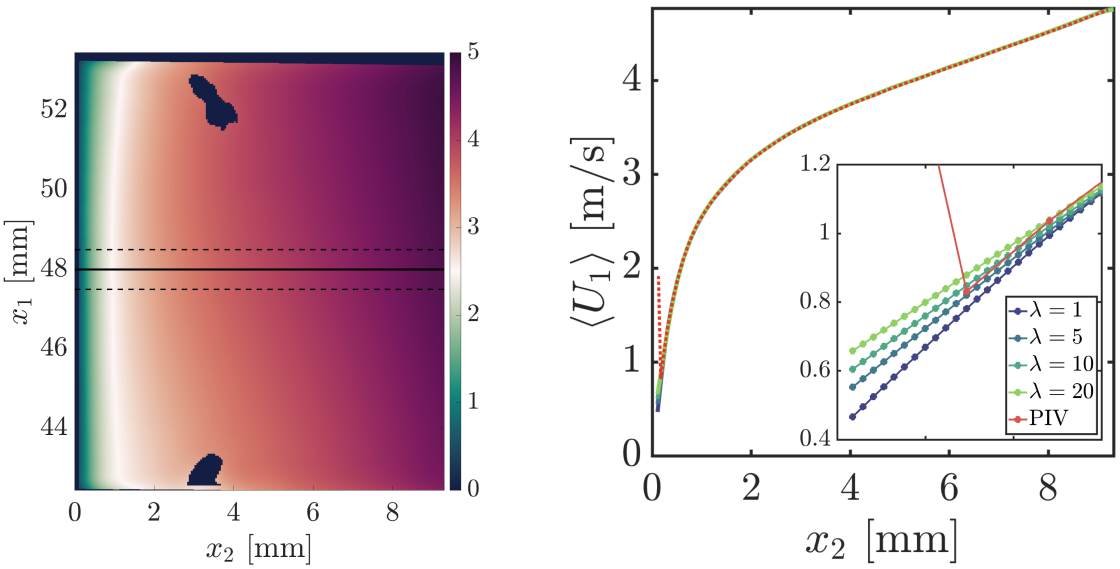

Figure 5.4: a) Mean streamwise velocity $\langle U_1 \rangle$ from $\lambda = 10$. b) Mean $\langle U_1 \rangle$ profile from the dashed region.

5.2 Transient FWI dynamics

In FWI environments, the turbulent flow field strongly influences the transient flame dynamics. Characteristic features of the flame front topology evolution resulting from the turbulence is described in this section. An example LIF image sequence is shown in Figure 5.5 with the detected flame front overlaid. Images are shown every 1ms corresponding to every 4^{th} image.

The flame is seen to approach the wall in a flapping motion, alternating between side wall quenching-like (SWQ) and head on quenching-like (HOQ) topologies. At $t = 0$ms, the flame features a curved shape with a large spatially-extended region oriented parallel to the wall. At $t = 1$ms, this wall parallel region has propagated closer in the normal direction nearer to the wall at $x_2 = 0$mm. This characteristic flame topology was referred as head on quenching-like ('HOQ') in the work of (Zentgraf et al., 2021). A pocket of fresh gases extends from the wall, creating a large concave flame shape present in the upstream field of view at $t = 1$ms. This local flame feature has also been referred to as a 'tongue' (T. Poinsot & Veynante, 2005). The flame quenches between $t = 2 - 3$ms and the flame topology transitions from 'HOQ' to 'SWQ' where the flame front contacts the wall at a shallow angle. The flame quenching point is identified from the end of the flame contour. The quenching point travels in the downstream direction with the flame front between $t = 2 - 3$ms as the flame front assumes a configuration parallel to the wall that resembles an HOQ topology. From $t = 3 - 4$ms, the parallel-oriented flame front propagates towards the wall, eventually quenching and producing the SWQ state again at $t = 5$ms.

This characteristic event sequences repeats itself in a quasi-periodic manner, with the flame continuously alternating between the dominant HOQ and SWQ topologies. Intermittent periods of only burnt gas from downstream of the quenching point, or a continuous unquenched flame front are also occasionally observed between periods

occupied by the flame in the dominant HOQ/SWQ states. As will be described in a later section, vortices embedded within the streamwise flow evolve relative to these unique flame geometries.

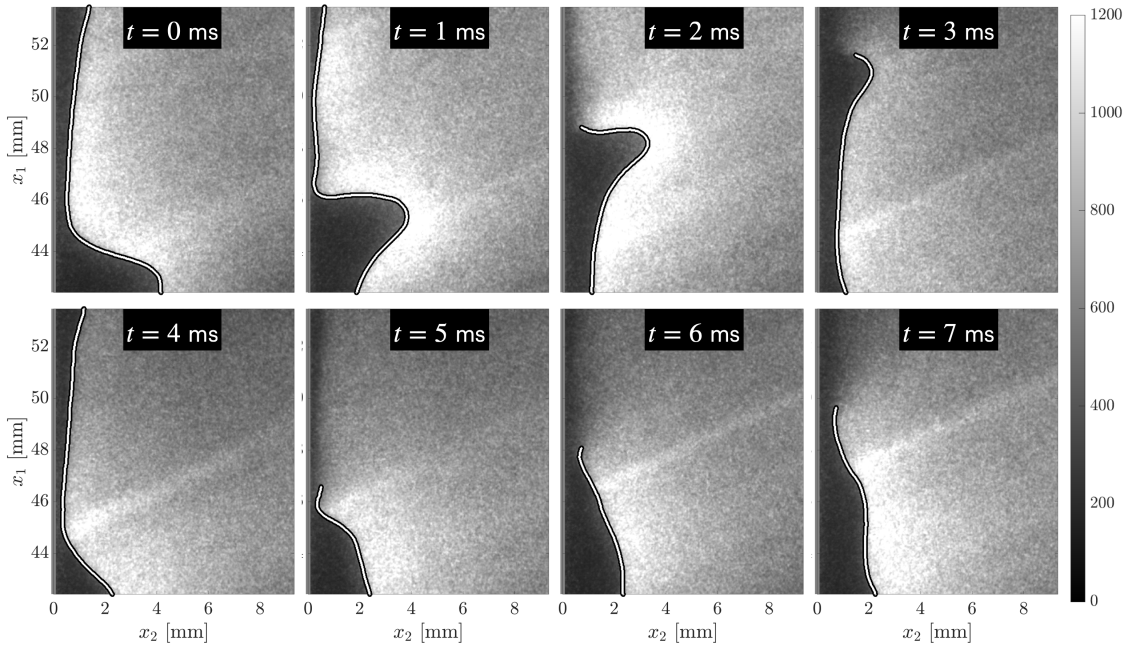

Figure 5.5: Example of a transient flame quenching sequence. Images are shown every 1 ms (every every 4 images). The contour indicates the detected flame front.

5.2.1 Instantaneous quantities

To investigate the action of the turbulent flow field on FWI, previous studies of (Steinhausen et al., 2023; Zentgraf et al., 2021) used the Q criterion (Hunt et al., 1988) to identify regions of vortical motion embedded within the turbulent flow. Regions of elevated Q, believed to be associated to vortices, would influence the shape of the shape flame front, seemingly pushing the flame closer to the wall and inducing the transition from HOQ to SWQ as the flame quenches. Larger scale flame wrinkles and unburnt gas 'tongue' described above were also altered by the presence of vortical motion/vortices suggested by the Q criterion. Previous DNS studies of (T. Alshaalan & Rutland, 2002; Gruber et al., 2010) also highlighted the importance of vortical structures in pushing the flame front reaction zone closer to the wall. Thus, resolving the instantaneous flow field and the vortices being convected by it is key in understanding FWI behaviour.

As described in Chapter 1, the derivative-based galilean invariant vortex detection criteria, such as the Q criterion and others (e.g. Δ, λ_2, λ_{ci} criteria), can be shown to be equivalent in 3D when the appropriate threshold is considered (P. Chakraborty et al., 2005). The projected 2D form of the criteria results in some minor differences due to slightly different weightings of terms associated with divergence ($\partial U_i/\partial x_i$). In practise, very similar results are obtainable from any of these well-known methods and this can also be inferred from the similarity of their respective 2D equations as discussed in (Q. Chen et al., 2015). The current work proposes the use of the swirling strength (λ_{ci}) criterion (Zhou et al., 1999). The analytical 2D form of λ_{ci} can be derived as:

$$\lambda_{ci} = \mathrm{Re}\left(\sqrt{-\frac{\partial U_2}{\partial x_1}\frac{\partial U_1}{\partial x_2} + \frac{1}{2}\frac{\partial U_2}{\partial x_2}\frac{\partial U_1}{\partial x_1} - \frac{1}{4}\left(\left(\frac{\partial U_2}{\partial x_2}\right)^2 + \left(\frac{\partial U_1}{\partial x_1}\right)^2\right)} \right) \tag{5.1}$$

where Re represents the real component of the argument. In the calculation of equation 5.1, values not associated with swirling motion, and therefore associated with shearing motion are set to 0 as in both (Jainski et al., 2014) and the commercial PIV software DaVis.

The swirling strength (λ_{ci}) is a scalar field with units of s^{-1} and describes the orbital period of a revolution around the vortex rotational axis through $2\pi/\lambda_{ci}$. This gives λ_{ci} an immediate kinematic interpretation. Similarly to the other derivative-based vortex detection methods, λ_{ci} does not discriminate between clockwise (CW) and counter clockwise (CCW) rotational motion. Therefore, it is common to associate a sign to the swirling strength based on the vorticity of the fluctuating velocity field $\omega = \partial u_1/\partial x_2 - \partial u_2/\partial x_1$ (Natrajan et al., 2007; Tomkins & Adrian, 2003; Y. Wu & Christensen, 2006) through:

$$\Lambda_{ci} = \lambda_{ci}\,\frac{\omega}{||\omega||} \tag{5.2}$$

where positive and negative values indicate CCW and CW rotating motion respectively. Swirling strength hereinafter will always refer to the signed form (Λ_{ci}) in Equation 5.2. As discussed in Chapter 1, a minimum lower bound threshold $T_{\Lambda_{ci}}$ is typically set on Λ_{ci} to isolate the stronger swirling regions $|\Lambda_{ci}| > T_{\Lambda_{ci}}$. The threshold in the current work is calculated similarly to the work of (Zentgraf et al., 2021) for the Q criterion as the median of all absolute swirl values $T_{\Lambda_{ci}} = (|\Lambda_{ci}|)$ =153.4s^{-1}. Isolated Λ_{ci} regions satisfying this threshold represent the stronger half of possible vortical regions.

The instantaneous velocity magnitude $\mathbf{U}$ and swirling strength Λ_{ci} are shown in columns of Figure 5.6. The figure shows the full temporally-resolved sequence (every image, 250μs in between) beginning at t = 4ms from Figure 5.5. Streamlines from the instantaneous velocity field are superimposed on $\mathbf{U}$. The thresholded swirling strength is overlaid on the LIF images in the third column of Figure 5.6. This region is also highlighted by the white contour in the second column representing the full Λ_{ci} field in Figure 5.6. For visualisation purposes an additional constraint is also added that $|\Lambda_{ci}| > T_{\Lambda_{ci}}$ regions must have an area >0.5mm^2. Figure 5.6 shows the evolution of the flow field as the flame transitions from its HOQ state until it reaches the SWQ topology at t = 5ms.

The flame is initially in a HOQ topology at t = 4ms. Close to the wall, the unburnt gases bounded by the flame front have significantly lower velocities to the flow in the burnt gas region as visible in the first column of Figure 5.6. The streamlines, which are approximately parallel in the unburnt gases, show the flow field expanding through the flame front and being diverted away from the wall. The low velocity region in $\mathbf{U}$ grows from t =4 - 4.75ms and is attributable to cold unburnt gases initially escaping the flame quenching passage and separating the wall from the hot burnt gases according to (Jainski et al., 2018). As the flame fully transitions to a SWQ topology at t =5 ms, this region becomes associated with the growth of a new boundary layer downstream of the quenching point.

Considering the swirling strength in Figure 5.6, an expansive cloud-like region of high Λ_{ci} is present directly above the flame front at t =4ms. From t =4 - 4.75ms, the flame moves closer to the wall, possibly under the influence of the vortical region identified through Λ_{ci} as postulated by (Zentgraf et al., 2021). This large vortical region persists during this period and an accumulation of small, albeit strong, regions of Λ_{ci} form near the flame location closest to the wall where quenching imminently occurs. At t =5ms, the cloud-like region previously present directly above the flame has become more fragmented and features reduced Λ_{ci} generally. Regions of high Λ_{ci} remain in the vicinity of the flame tip following quenching. Although not shown in Figure 5.6, these regions of Λ_{ci} remain closely associated with the flame tip beyond t =5ms and move together with the flame tip in the downstream direction. It is these elevated Λ_{ci} (or Q criterion) regions that are hypothesised by (Steinhausen et al., 2023; Zentgraf et al., 2021) to be responsible for the flame vortex interaction that transports burnt gases into the fresh gas mixture in the vicinity of the flame tip as depicted previously in Figure 1.2.

Evidently, vortex structures identifiable from Λ_{ci} are closely associated with the flame dynamics and quenching phenomena. While local regions of high Λ_{ci} are a scalar indicator of rotational motion present within the flow, it is the vortical flow field itself which facilitates the transport process and this flow field remains completely unknown in the literature. Analysis of the instantaneous flow fields in Figure 5.6 does not reveal closed or spiralling streamlines indicating vortical motion or flow circulation. To study these flame vortex interactions and their associated transport phenomena in detail, it is therefore necessary adopt a Lagrangian reference frame moving with the flow to study the dynamical phenomena.

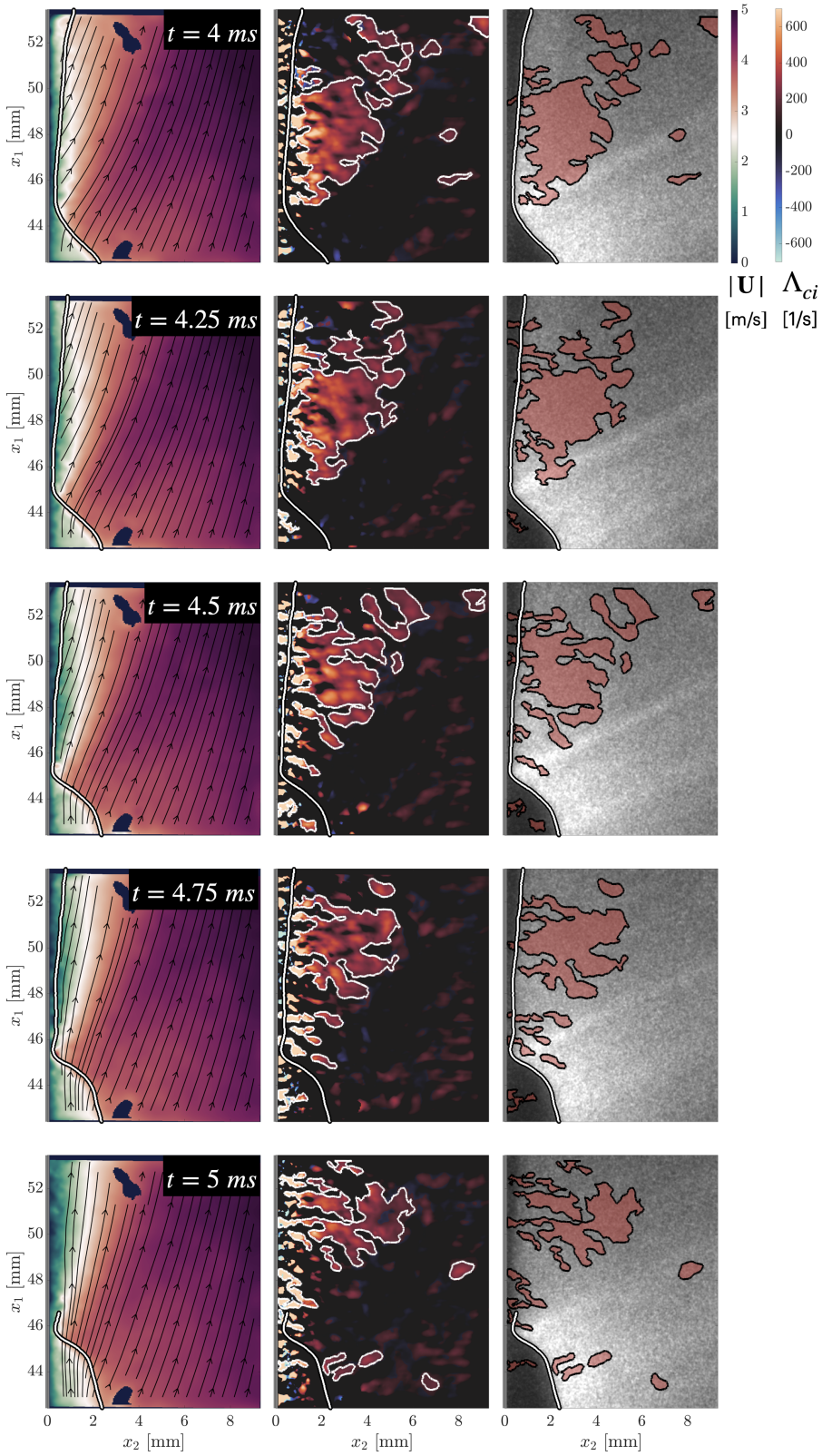

Figure 5.6: 1st column: Velocity magnitude $|\mathbf{U}|$. 2nd column: Swirling strength Λ_{ci}. 3rd column: Thresholded Λ_{ci} overlaid on the raw LIF image. Timing between images is 250μs.

5.2.2 Reynolds decomposition

As discussed in Chapter 1, the organisation of wall-turbulence features vortices that are embedded in and convected by the bulk streamwise flow. A vortex is defined as per (Kline & Robinson, 1990) as a closed set of streamlines viewed in a reference frame travelling with the vortex core. Therefore, in order to reveal vortices embedded in the boundary layer flow, it is necessary to subtract, from the instantaneous velocity, some background velocity component representing the underlying flow that is advecting the vortices.

By subtracting this background component, the reference frame is changed from the instantaneous flow field as seen by a stationary observer, to one of moving with the flow, resulting in a Lagrangian point of reference. A classical example of this is Galilean decomposition, involving the subtraction of a single constant streamwise velocity from the full instantaneous velocity field and is common in boundary layer research (Adrian, Meinhart, & Tomkins, 2000; Jodai & Elsinga, 2016; Natrajan et al., 2007; Y. Wu & Christensen, 2006). Other techniques include, the classical Reynolds decomposition, frequency filtering schemes, proper orthogonal decomposition (POD) and Large Eddy Simulation (LES) filtering schemes, among possible others (Adrian, Christensen, & Liu, 2000).

In the present work, it is proposed to use the Reynolds decomposition $u_i = U_i - \langle U_i \rangle$. There are several advantages to this; firstly, Reynolds decomposition is known to reveal a broad range of vortices, at least in non-reacting boundary layers (Adrian, Christensen, & Liu, 2000), since most vortices have a convection velocity broadly similar to the mean (Elsinga et al., 2012). Conversely, Galilean decomposition cannot simultaneously reveal multiple vortices which have different convection velocities, as exampled in Figure 2.4 of Chapter 2. Secondly, Reynolds decomposition produces directly interpretable turbulence quantities in terms of turbulent velocity fluctuations which are analysed in this chapter. Thirdly, it is simple and computationally efficient which is advantageous when dealing with large memory datasets such as the wOF results which contain over 3 billion vectors for the 1000 image sequence. This can make using methods such as POD computationally prohibitive or at least extremely costly on standard computing hardware. Lastly, Reynolds decomposition does not require any parameter setting as would be the case if using POD (number of modes to reconstruct) or a frequency filtering scheme (cut-off frequency). Although not presented in this chapter, tests on the PIV vector fields with a Fourier frequency filtering scheme or POD produce similar results and conclusions for the present analysis, albeit with substantially more effort.

An example Reynolds decomposition is shown in Figure 5.7 below. The instantaneous flow field in Figure 5.7a) exhibits a uniform flow field in the streamwise direction. Similarly to the flow fields presented in Figure 5.6, no vortical flow structures are observed within the instantaneous flow field. Subtraction of the ensemble mean shown in Figure 5.7 b) for this particular velocity field instants reveals the existence of three distinct vortex types that are prominent in this dataset. These types are referred to as Type 1-3 and are labelled in Figure 5.7c) accordingly. These three vortex types are frequently observed in the burnt gas region and have a persistent correlation with distinct flame behaviour in turbulent FWI.

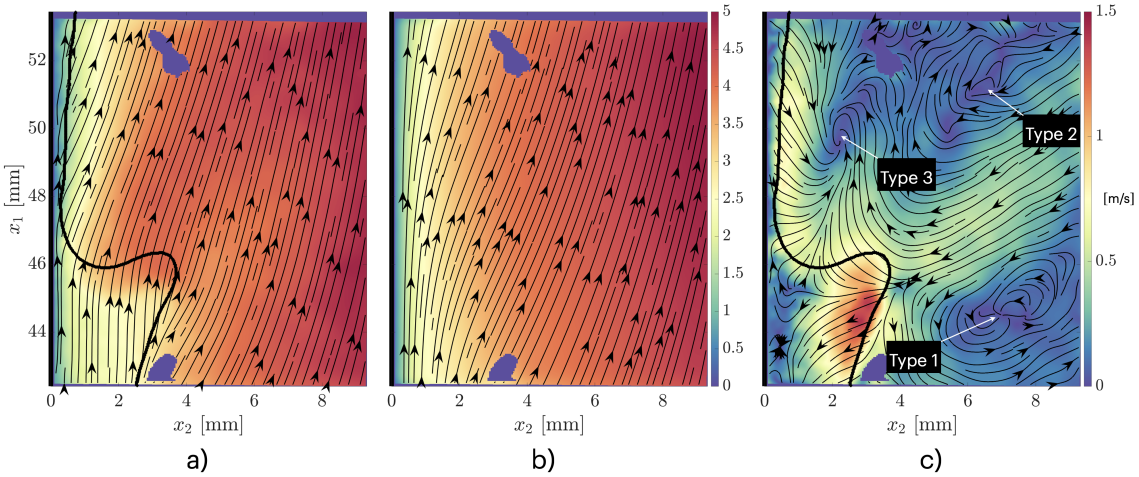

Figure 5.7: a) Instantaneous velocity field. $|U|$ b) Mean velocity magnitude. $|\langle U \rangle|$ c) Fluctuating velocity field $|u|$.

To visualise the vortices from Figure 5.7 in more detail, Figure 5.8 shows a 2 $\times$ 2mm^2 highlight of the vector field for each respective vortex. Every 32$^{\text{nd}}$ vector is shown. The full circulation of the vector is clearly apparent for the Type 1 and 3 vortices in 5.7a) and c). The Type 2 shows a less coherent swirling flow for this specific time instant where all three vortex types are present. However, this vortex showed a more prominent circulation in an earlier time instant and this is discussed further in the forthcoming section.

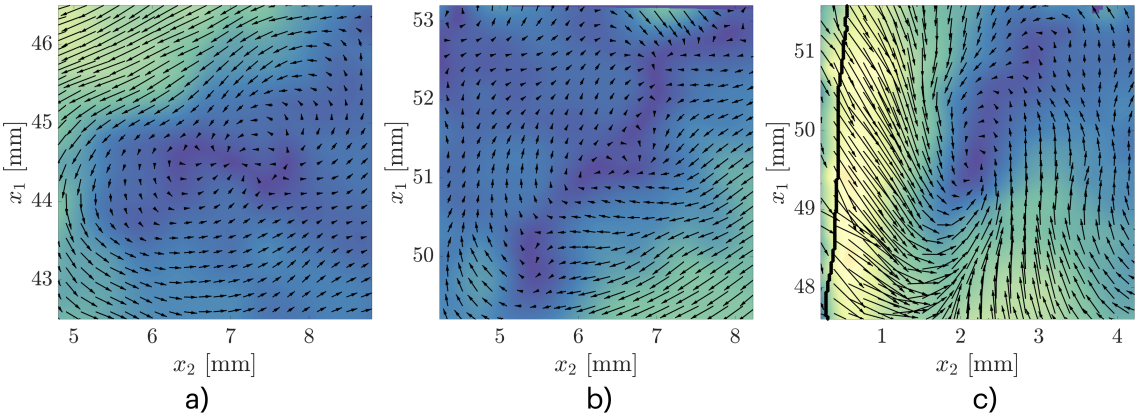

Figure 5.8: Highlights of the a) Type 1 b) Type 2 c) Type 3 vortex from Figure 5.7. Every 32$^{\text{nd}}$ vector is shown. Colour scale is identical to Figure 5.7c).

The canonical sequence of interactions for these vortex types with the flame front is depicted in Figure 5.9. At t_0, a flame hook-shaped geometry is present, with the flame front in an HOQ state featuring the spatially extended flame front near the wall. The flame hook features two vortices in close proximity: a CCW rotating vortex Type 1 vortex upstream, and CW rotating Type 2 vortex downstream of the flame hook. A Type 3 vortex, also CCW rotating, is present further downstream of the Type 2 vortex, above the flame front nearest to the wall. At t_1, the flame hook has been pushed forward in the downstream direction by the Type 1 and Type 2 counter-rotating vortex pair. The Type 2 vortex also moves further away from the wall. During this time, the Type 3 vortex descends towards the flame, pushing the

flame front closer to the wall. At t_3, the flame has transitioned from HOQ to SWQ as it quenches. The Type 1 vortex remains and continues to move in the downstream direction with a slight movement away from the wall. The Type 3 vortex, following impact with the flame front, travels together with the quenched flame front in the downstream direction, always remaining in close proximity of the flame tip.

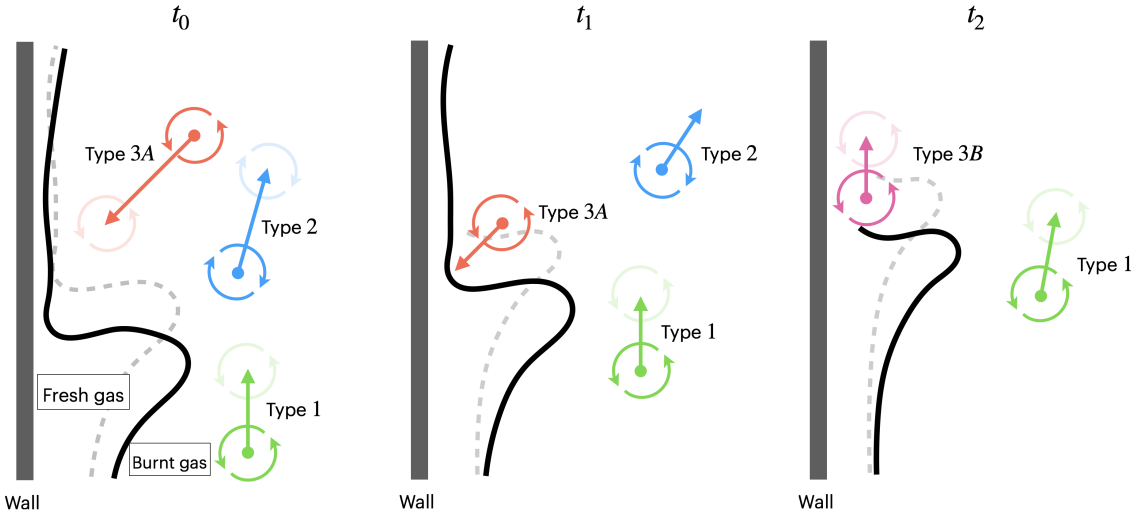

Figure 5.9: Illustration of a canonical quenching event.

It should be explicitly pointed out that these vortex types and their interactions are *not* present in the non-reacting case, which features the classical horseshoe vortices well-known in non-reacting wall-turbulence (Robinson, 1991). It is unknown exactly what is the origin or exact cause of these unique vortex types in the reacting case. Since they are always observed in proximity to and interacting with the flame, it is possible that the vortex formation results from the presence of the flame front itself. A potential source contributing to their formation may result from *flame-generated vorticity*, which has been observed in experimental (Mueller et al., 1996; Steinberg et al., 2008) and numerical studies (Louch & Bray, 2001; Pan et al., 2002) of turbulent reacting flows. The cause of flame generated vorticity can be understood by considering the transport of vorticity equation:

$$\frac{D\Omega}{Dt} = (\Omega \cdot \nabla) U + \nu \nabla^2 \Omega + \frac{1}{\rho^2} (\nabla \rho \times \nabla P) - \Omega (\nabla \cdot U) + \xi \tag{5.3}$$

In equation 5.3 the first term represents tilting or stretching of vorticity due to velocity gradients. The second term is the viscous diffusion of vorticity. The fourth term is the stretching of vorticity due to dilatation effects and the final term ξ represents effects of viscosity gradients. The mechanism of flame-generated vorticity has been attributed to the third term (Mueller et al., 1996), which is the the baroclinic torque. This is caused by a misalignment between between the density and pressure gradients. The density gradient is normal to the flame front, therefore a pressure gradient tangential to the flame front is required to produce baroclinic torque. Knowledge of the pressure field would be needed to further investigate this as a causal mechanism of the three characteristic vortices in the present experiment, however. The unique attributes of the vortices and effect on the flame are exampled in further detail in the forthcoming sections.

5.2.2.1 Type 1 vortex

A Type 1 vortex is a CCW rotating vortex that always remains upstream of a protruding flame hook geometry. Examples of Type 1 vortices, together with inlays of the actual vector field, are shown in Figures 5.10. The vector field is downsampled to display every 16th vector. All examples depict entirely separate quenching events that feature the characteristic flame hook geometry. The nature of this vortex is similar to streamwise vortices reported previously by (T. Alshaalan & Rutland, 2002; Gruber et al., 2010; Zentgraf et al., 2021) which appear to push the flame.

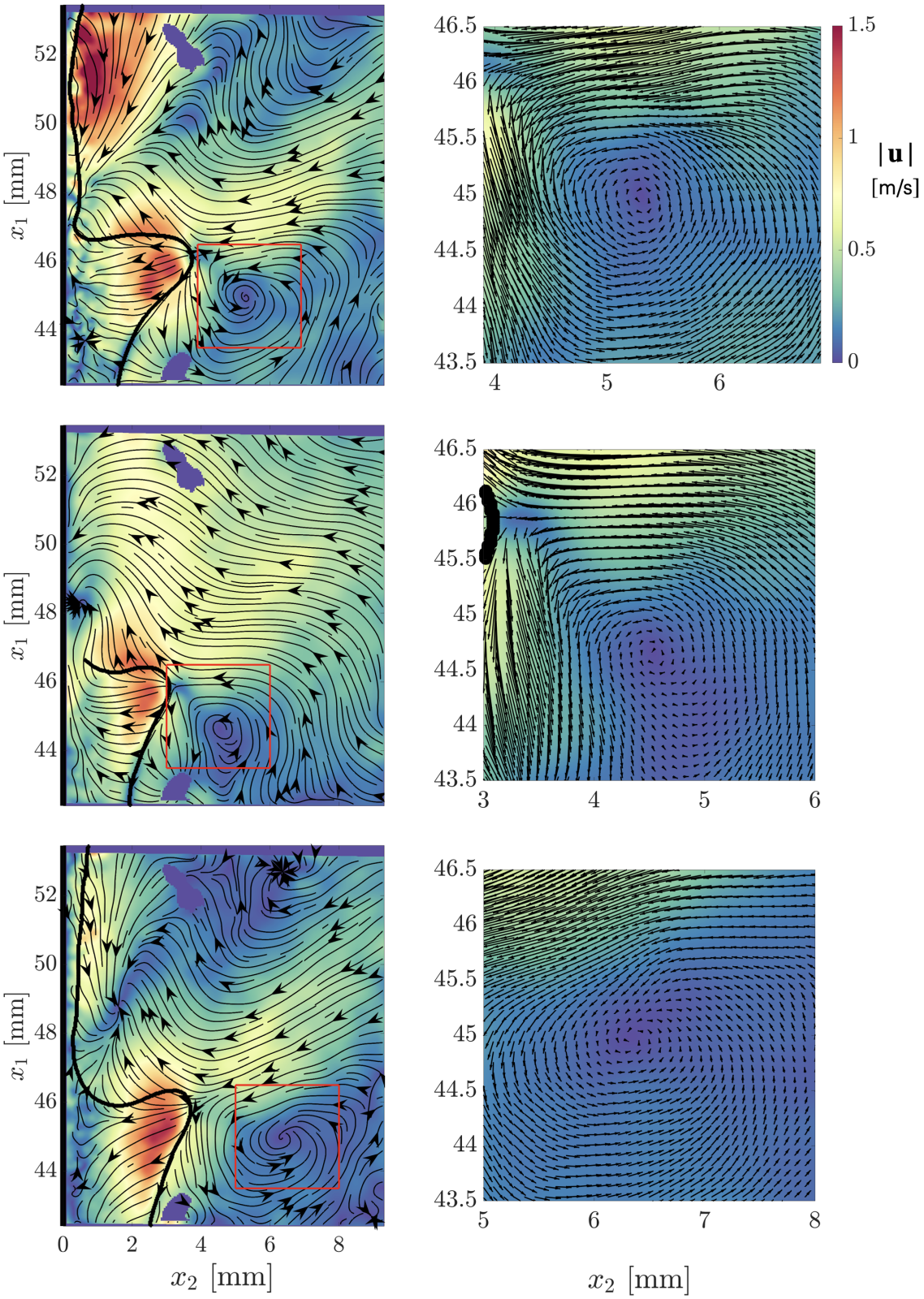

Figure 5.10: Examples of Type 1 vortices (left column) and highlightx of the respective vortex region (right column). Vectors are downsampled ×8.

5.2.2.2 Type 2 vortex

The Type 2 vortex is a CW rotating vortex. Three examples of Type 2 vortices are shown in Figures 5.11. The presence of the Type 2 vortex is always observed to be downstream of a flame hook. While some images reveal the presence of a flame hook without the presence of Type 2 vortex (not shown), a Type 2 vortex is never observed without the presence of a flame hook or high positive curvature. As the flame transitions from HOQ to SWQ topologies, the Type 2 vortex is seen to travel in the North-eastern direction out of the FOV. In general, compared to a Type 1 vortex, a Type 2 vortex is also seen to dissipate within the FOV, eventually resulting in a less coherent circulation as shown previously in Figure 5.8.

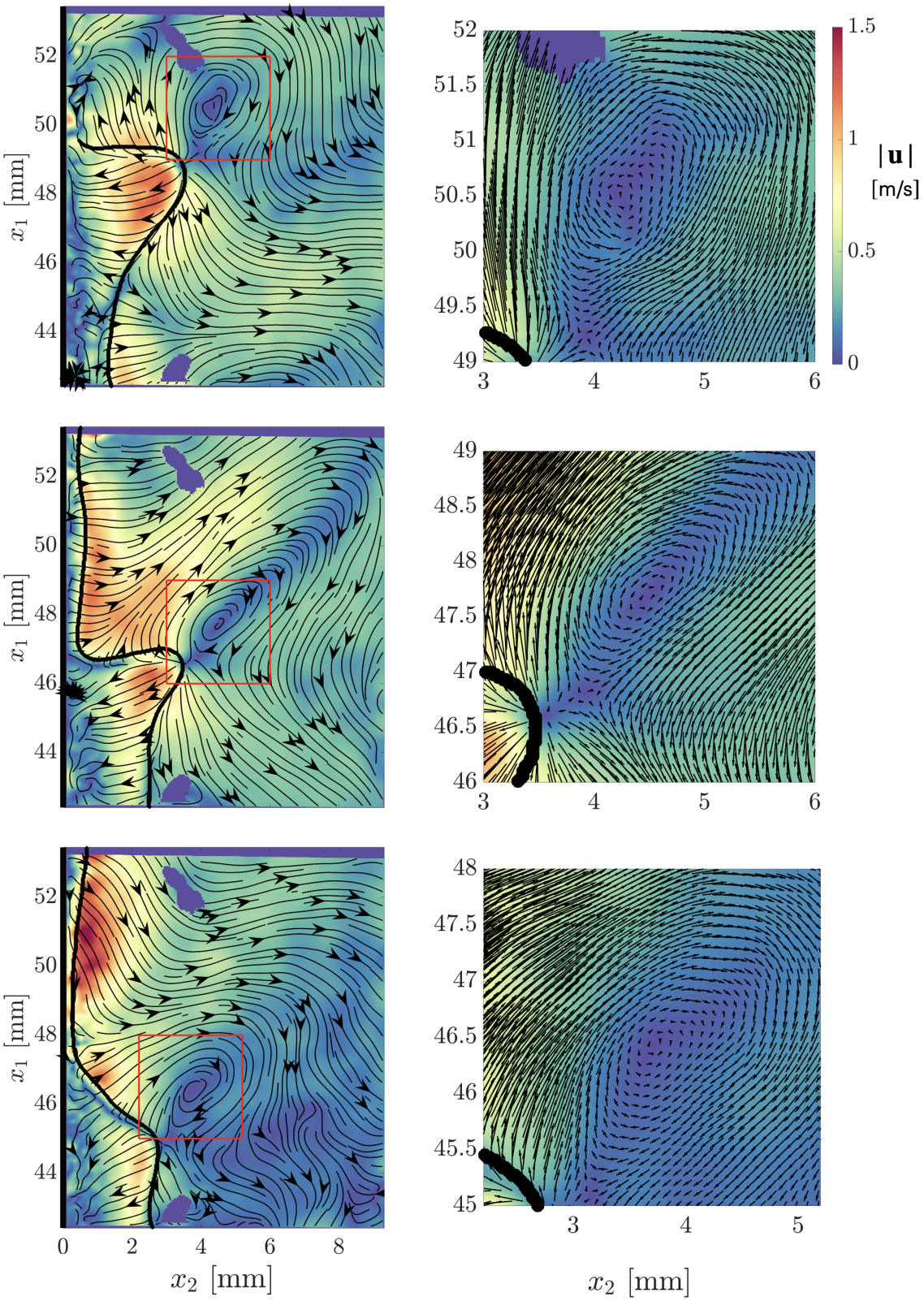

Figure 5.11: Examples of Type 2 vortices (left column) and a highlight of the respective vortex region (right column). Vectors are downsampled ×8.

5.2.2.3 Type 3 vortex

The Type 3 vortex is a CCW rotating vortex frequently observed in the burnt gas region above the flame in an HOQ orientation. An example quenching event depicting the full temporal evolution (every image, 250μs between images) of a Type 3 vortex is shown in Figure 5.12. The corresponding highlights of the vortex vector fields are shown in the bottom rows with every 16^{th} vector shown.

The sequence depicts the descent of a Type 3 vortex, coinciding with the flame quenching as the vortex impacts the wall. The Type 3 vortex is observed to impact the wall location where the flame is closest to the wall and has strong negative curvature. This is typically the wall location where the flame front transitions from its wall-parallel orientation as part of the HOQ topology to the flame tip in the SWQ state. The Type 3 vortex is unique in that once formed it travels quickly downwards towards the wall, appearing to impact the wall and coincide with flame quenching. In most cases this process typically occurs in the order of 0.5 - 1ms (2 - 4 images). The continuation of Figure 5.12 is shown in Figure 5.13. Following impact with the wall and flame quenching, the Type 3 vortex is observed to travel in the downstream (x_1) direction along the wall, remaining in close proximity with the quenching point.

The lifespan of the Type 3 vortex therefore appears to have two stages. The first stage termed the 'vortex descent' includes the progress to impacting the wall and is coincident with the flame transition from HOQ to SWQ. The second stage following quenching is the 'vortex travel' where the vortex now travels in the downstream direction along the wall while remaining directly ahead of the flame tip. The presence of a vortex at this location is synonymous with the transport mechanism postulated by (Steinhausen et al., 2023; Zentgraf et al., 2021) which has never previously been explicitly revealed. The subset of Type 3 (T3) vortices associated with the descent stage will be referred to as Type 3A (T3A) vortices while the remaining 'travel' subset will be termed Type 3B (T3B) vortices in the subsequent analysis.

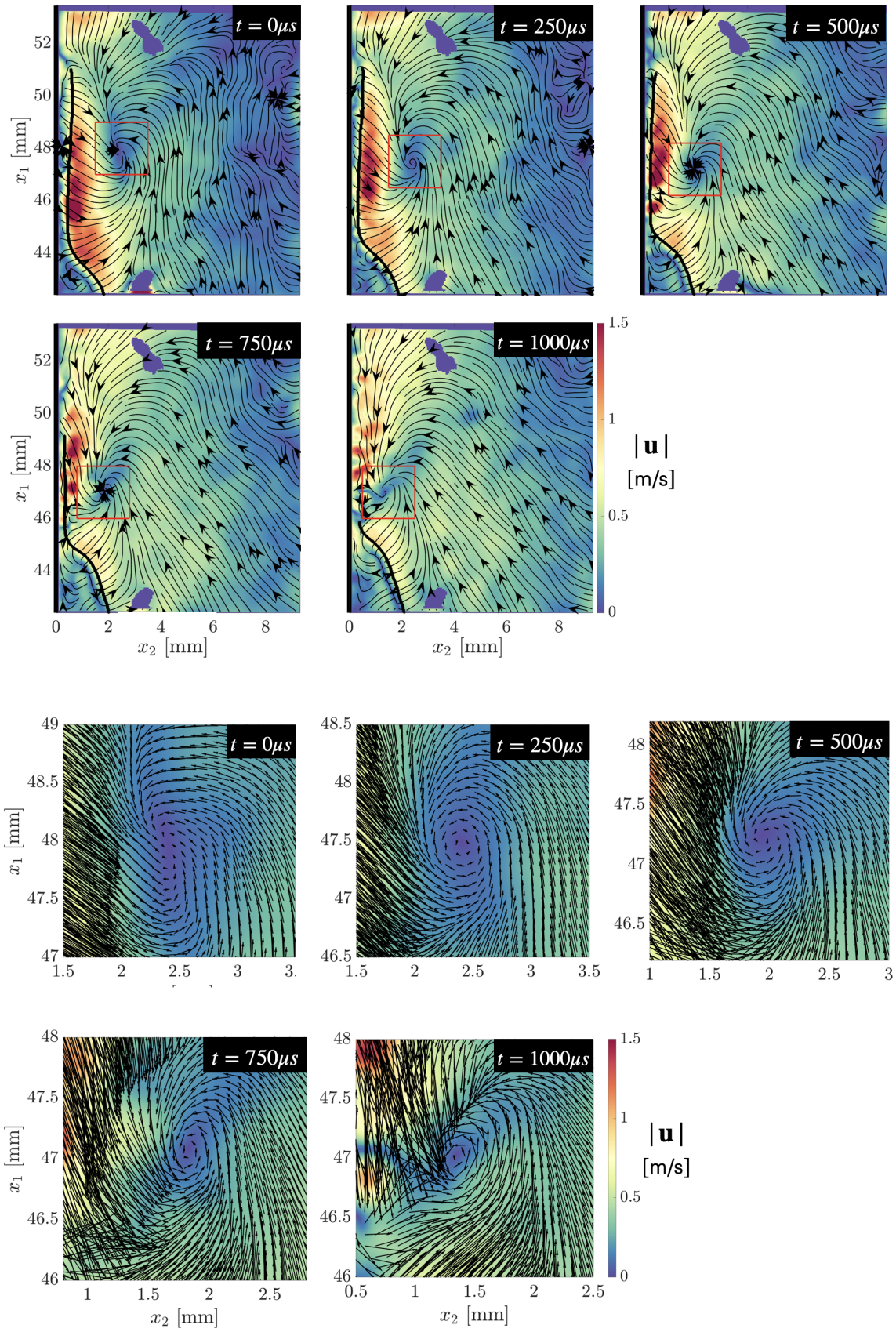

Figure 5.12: Sequence depicting a Type 3A vortex descent. The colour scale displays the fluctuating velocity magnitude $|\mathbf{u}|$. The lower sequence shows the corresponding vortex vector fields from the red marked squares. Every 16^{th} vector is shown.

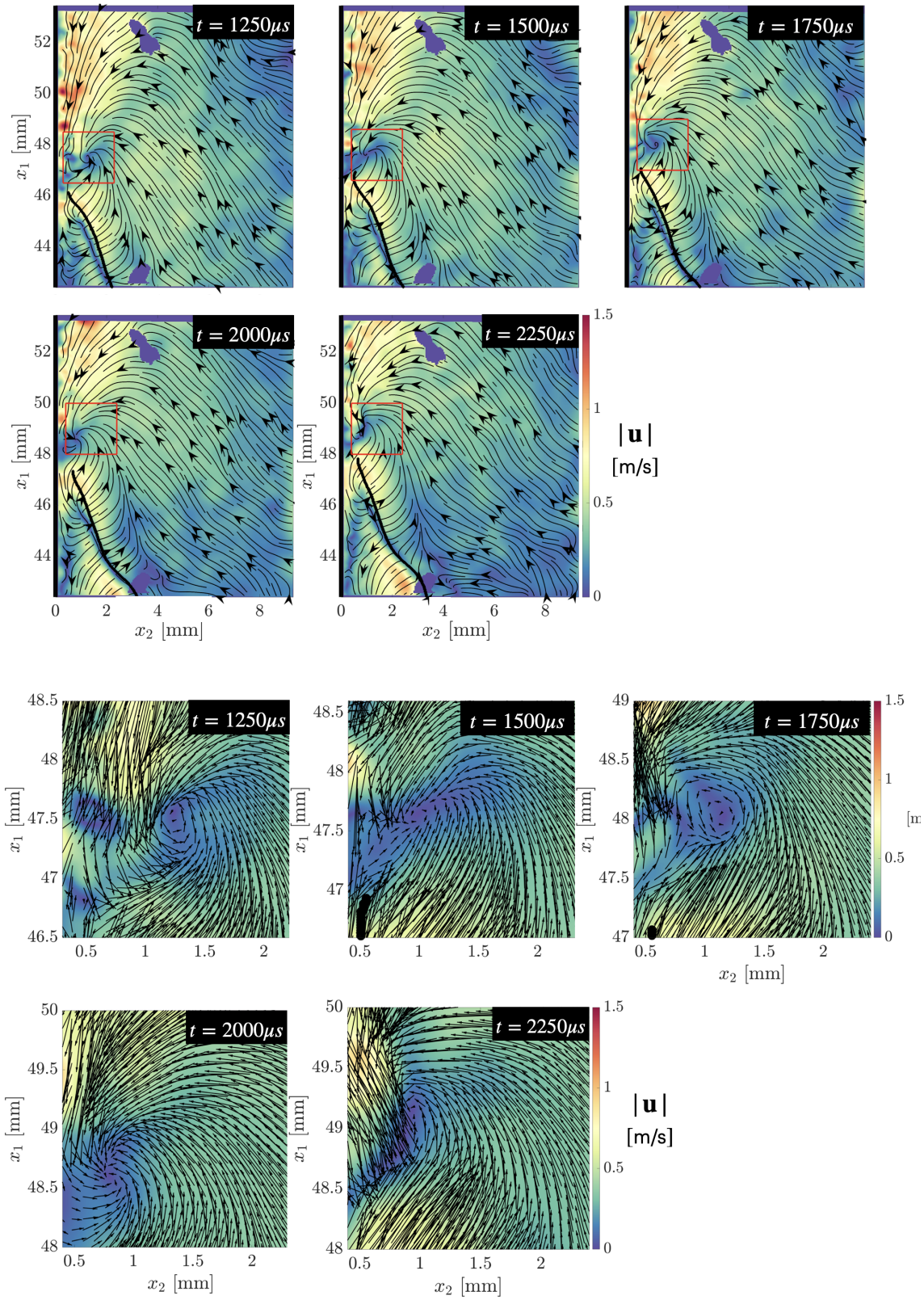

Figure 5.13: Sequence depicting a Type 3B vortex travel. The colour scale displays the fluctuating velocity magnitude $|\mathbf{u}|$. The lower sequence shows the corresponding vortex vector fields from the red marked squares. Every 16$^{\text{th}}$ vector is shown.

5.2.2.4 Relationship between T3 vortex and Λ_{ci}.

The presence of high local Λ_{ci} regions in the flow field has now been demonstrated, together with the presence of unique vortex types visible in the vector fields of the velocity fluctuations $\mathbf{u}$. This section discusses the relationship between the two to evaluate how and whether the regions of elevated Λ_{ci} are in fact related to the vortices revealed in the Reynolds decomposition. This evaluation will assist understanding whether the vortical motion in the fluctuating flow field $\mathbf{u}$ is physical, or is potentially an artefact. Additionally, this comparison provides a connection from the vortex vector fields to the transport mechanism proposed by (Zentgraf et al., 2021). Figure 5.14 shows the swirling strength (Λ_{ci}) calculated for the image sequence shown previously in Figure 5.12 depicting the T3A vortex descent. As before, the white contour indicates the thresholded Λ_{ci} region marked in the LIF image. The streamlines of the fluctuating velocity field ($\mathbf{u}$) are shown, with the identified Type 3 vortex centre marked by a green plus sign (+).

Similarly to the Λ_{ci} sequence shown earlier in Figure 5.6, the sequence in Figure 5.14 reveals a large region of high Λ_{ci} located above the flame front which is in an HOQ configuration. At $t = 0\mu s$, the Type 3 vortex is located near the centre of this expansive Λ_{ci} region. From $t = 250 - 500\mu s$, the Type 3 vortex is observed to move vertically downwards within the region of elevated Λ_{ci}. As this area of increased Λ_{ci} fragments into smaller regions, the location of the Type 3 vortex is always associated with a region of high magnitude Λ_{ci} throughout the descent of the vortex. At each point in the sequence, the location of the T3 vortex identified from the Reynolds decomposition is always seen to coincide with a region of high magnitude Λ_{ci} throughout the descent of the vortex, even though this region is not always be the largest size in the thresholded Λ_{ci} images. Both the vortex and regions of high Λ_{ci} progress towards the wall, impacting at $t = 1000\mu s$ where the flame is seen to locally quench and transition from an HOQ to an SWQ topology. The sequence following this transition is shown in Figure 5.15. The vortex centre remains closely associated with the elevated Λ_{ci} regions as it travels in the downstream direction with the quenching point.

In comparison to the streamline representation, the field of Λ_{ci} is in general noisier. This is also seen in the Q criterion results from (Zentgraf et al., 2021) where a relatively large PIV IW size (48×48 pixels^2) was also used. The noise or 'patchy' appearance is most likely due to Λ_{ci} being calculated from only planar velocity data. The contribution of the terms in the velocity gradient tensor $\nabla\mathbf{U}$ associated to the out-of-plane (x_3) direction is missing. All Galilean invariant vortex detection criteria (Q, λ_{ci}, Δ, λ_2) require full 3D data for their full calculation, which explains why the 3D DNS study of (Steinhausen et al., 2023) resolves a visually more continuous field of Q criterion associated to the flame vortex interaction.

Figures 5.14 and 5.15 clearly demonstrate how the Type 3 vortex visualised in the Reynolds decomposition is closely associated to the vortical structure indicated by Λ_{ci} (or Q criterion in previous works (Steinhausen et al., 2023; Zentgraf et al., 2021)). In other words, the Type 3 vortex identified from the Reynolds decomposition is the vortical structure from Λ_{ci} as observed *relative to the mean flow*. This aspect can be simply confirmed by performing a Galilean decomposition where the point instantaneous velocity at the vortex centre identified in the Reynolds decomposition (green cross) is subtracted from the instantaneous field to create a Galilean decomposition. If a vortex exists in the Galilean, as well as in the Reynolds decomposition, it is

confirmed that the fluctuating vector field **u** is an adequate representation as per the definition of (Kline & Robinson, 1990).

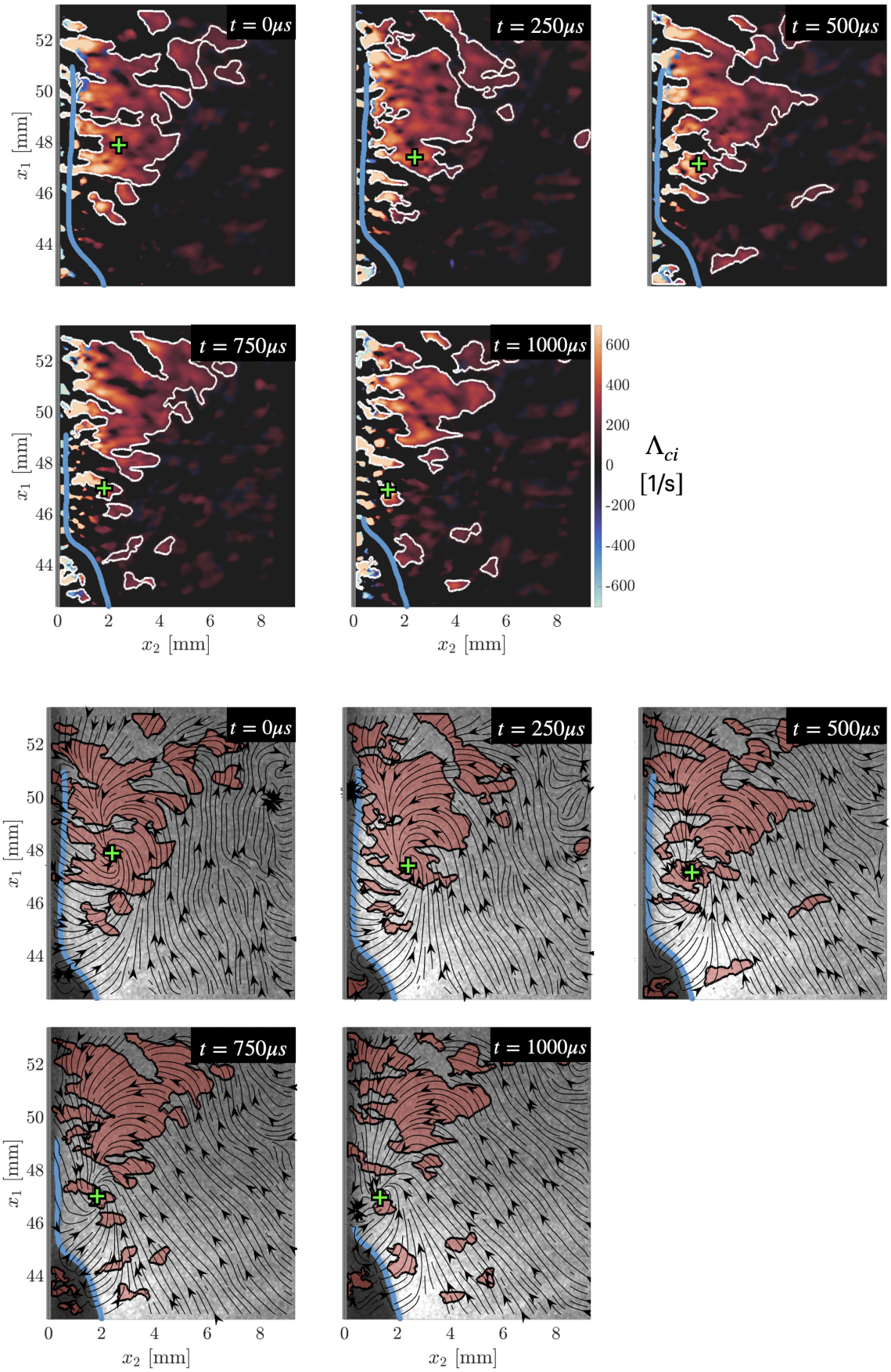

Figure 5.14: The top sequence shows the swirling strength Λ_{ci} for the Type 3 vortex sequence from Figure 5.12. The Type 3 vortex centre is marked by the green +. Bottom sequence shows the thresholded Λ_{ci} contour overlaid on the raw LIF images. Streamlines depict the fluctuating flow field $\mathbf{u}$.

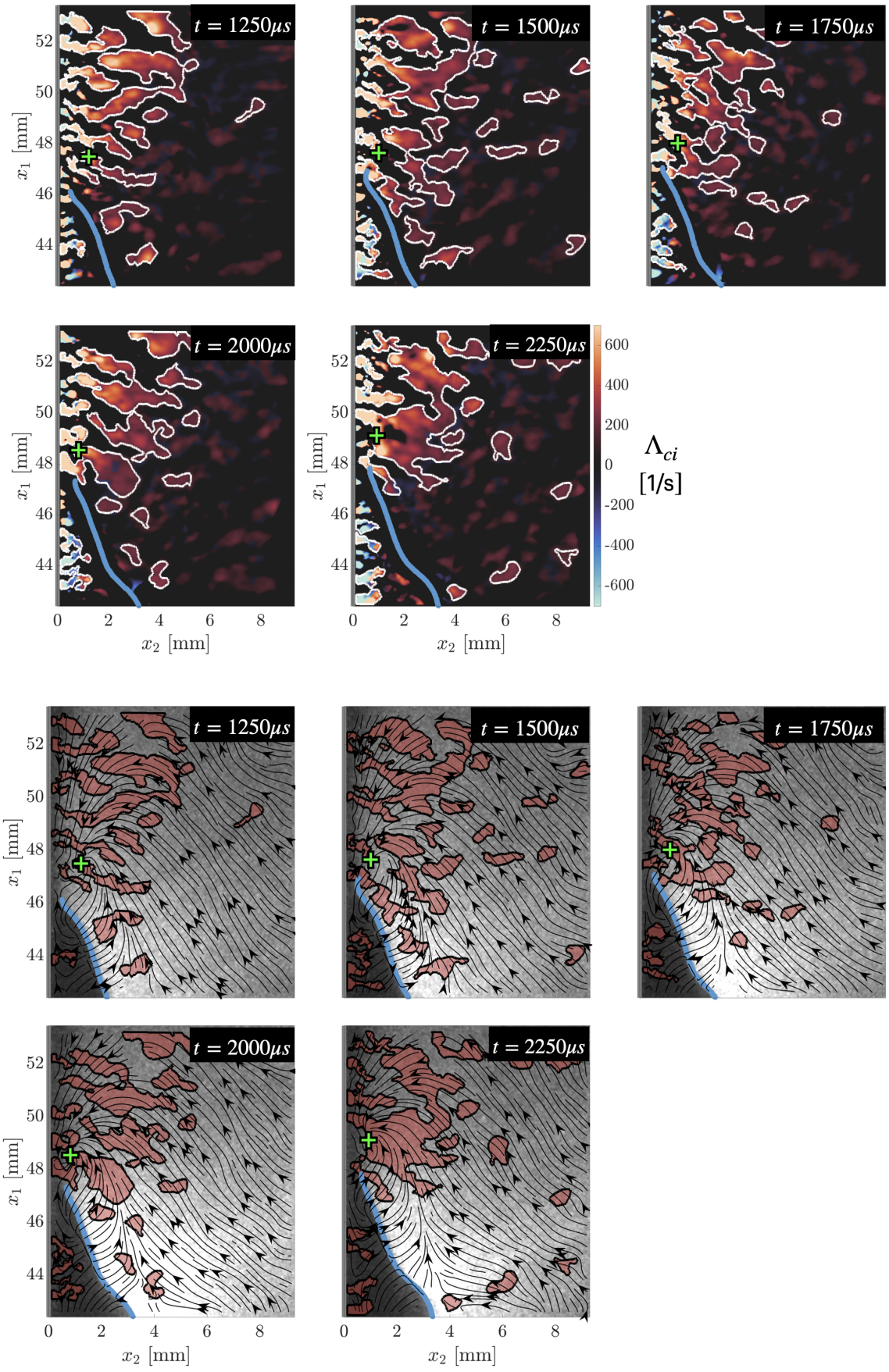

Figure 5.15: The top sequence shows the swirling strength Λ_{ci} for the Type 3 vortex sequence from Figure 5.13. The T3 vortex centre is marked by the green +. Bottom sequence shows the thresholded Λ_{ci} contour overlaid on the raw LIF images. Streamlines depict the fluctuating flow field $\mathbf{u}$.

The following section describes a conditional analysis used to study the Type 3 vortex further. There are several reasons for motivating particular interest in the Type 3 vortices specifically. Firstly, the Type 3 vortices persist longer in the FOV than either Type 1 or Type 2 vortices. The Type 1 and 2 vortices either leave the FOV as described or appear to dissipate. This may also be caused by out-of-plane motion of the vortices eventually leaving the laser sheet. It is also possible that the convection velocity of the Type 1 and Type 2 vortex departs sufficiently from the mean flow through its trajectory such that the Reynolds decomposition no longer provides a suitable frame of reference for identifying it. Other decomposition methods may be preferable for studying these vortex types individually and this is a potential avenue for future investigations. A final motivation for focusing the subsequent analysis on specifically Type 3 vortices is because they seem to be directly correlated with the quenching process and gas transport mechanism hypothesised by (Zentgraf et al., 2021). This is not to say that other vortices, both Type 1-2 and undiscovered vortices, do not play any role in FWI, but the current results suggest this could be more of a supportive role rather than the dominant one.

Out of the 1000 images processed, there are 35 local quenching events, with evidence of an associated Type 3 vortex featured in all of them. In several quenching sequences, the Type 3 vortex is not as clearly seen through the entirety of its descent (3A) and travel (3B) phase, despite the fluctuating flow field having similar features to the examples shown. Although this occurs significantly less than for the other vortex types, this is again possibly due to out-of-plane motion or temporary inadequacy of the mean flow representing the underlying vortex convection. In cases where the vortex is in proximity to both the wall and flame, transient decreases in seeding density together with decreased image SNR can also promote risk of erroneous vectors for both wOF and PIV which will contribute to this.

5.3 Conditional analysis

A conditional analysis is used to achieve an averaged representation of the dynamical sequence of events describing a descending T3A vortex being involved in flame quenching before evolving to the T3B travel vortex involved in the gas transport mechanism postulated by (Zentgraf et al., 2021). The methodology to be described conditions vortices relative by their centres, similarly to the fundamental wall-bounded turbulence study of (Carlier & Stanislas, 2005). This approach has the advantage of revealing the dominant flow features and approximate lengthscales involved.

5.3.1 Vortex centre identification

For this conditioning procedure, it is first necessary to accurately identify vortex centres. An effective methodology of vortex centre identification known as the Γ_1 criterion was proposed in (Graftieaux et al., 2001). The discretised form of this criterion is expressed by:

$$\Gamma_1 = \frac{1}{N} \sum_S \frac{\left(\overrightarrow{PM} \times \overrightarrow{U_M}\right)}{||\overrightarrow{PM}|| \cdot ||\overrightarrow{U_M}||} \tag{5.4}$$

The Γ_1 criterion is calculated from the local flow field topology, considering the normalised cross product of a vector $\overrightarrow{PM}$ from a reference location P to a scanned location M, and the direction of the velocity vector $\overrightarrow{U_M}$ at point M. The average of these values over a given scan domain area S is averaged to give the value of $|\Gamma_1|$ at a point in the flow field. This is shown schematically in Figure 5.16. Values of the angle θ_M between vectors $\overrightarrow{PM}$ and $\overrightarrow{U_M}$ closer to 90° indicate a more circular vortex and maximises the value of $|\Gamma_1|$. Γ_1 values range from -1 (CW rotation) to +1 (CCW rotation). Values around 0 indicate little to no rotational motion within the scan domain S. Local maxima value in the $|\Gamma_1|$ indicate the location of vortex centre. Only 1 parameter L, known as the filter length, is required as user input. The selection of L sets the size of domain $S = L \times L$ and has the role of a spatial filter. A filter length of 0.48mm in physical space is used for both wOF and PIV results, corresponding to 81 vectors for wOF and 9 vectors for PIV. The location of a given vortex centre is not sensitive to this parameter as explored in (Graftieaux et al., 2001).

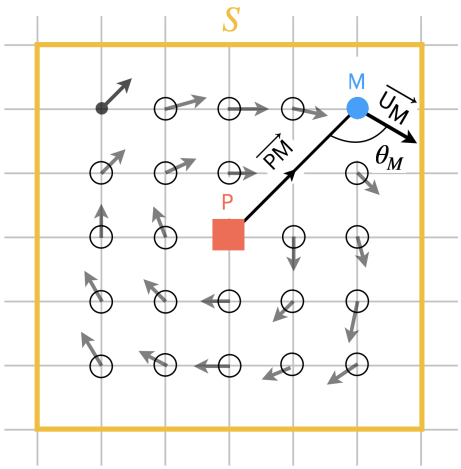

Figure 5.16: Schematic of the calculation of the Γ_1 criterion.

The Γ_1 criterion is calculated for each fluctuating velocity field $\mathbf{u} = (u_1, u_2)^T$ in the image sequence. Computation of $|\Gamma_1|$ can be performed efficiently using the convolution-based implementation presented in (Zigunov et al., 2020). Type 3 vortex centres can then be identified from local maxima in the vortex region. In order to establish an objective quality measure of the detected vortices, a threshold of $\Gamma_1 > 0.5$ is selected. Identification of Type 3 vortices satisfying this quality constraint is performed for the full the 1000 image pair sequence through a manual sorting procedure. Automatic point tracking algorithms, such as those based on a simple nearest neighbour search (Jainski et al., 2014) or more advanced methods based solutions to the linear assignment problem are also possible (Stevens & Sciacchitano, 2021) but a manual method was found to be simper and more robust for this dataset. After a vortex completes its downward decent and impacts the wall, the vortex is classified as a T3B vortex from the subsequent frame onwards. The total number of images featuring a detected T3 vortex is 381, 149 of which are T3A (39.1%) and 232 are T3B (60.9%).

Example of accepted vortices satisfying the $\Gamma_1 > 0.5$ threshold and rejected vortices failing it are shown in Figures 5.17 and 5.18. The zoomed-in FOV is centred

around each vortex centre and respective Γ_1 values associated to each respective vortex are quoted. The bottom right vortex in both Figures 5.17 and 5.18 is a Type 3B (travelling) vortex, while all others shown are Type 3A. The use of a Γ_1 threshold enables rejection of low quality results dominated by noise or erroneous vectors as visible in the bottom left 5.18. While some visually adequate seeming vortices (e.g. 5.18 top left) are rejected, it was preferred in the current study to maximise selections of *quality* T3 vortices, rather than attempt to arbitrarily maximise statistics by including all potential T3 vortex-like regions. The use of the selected Γ_1 threshold as a quality constraint therefore results in a more conservative selection of the full possible set of visually observable T3 vortices.

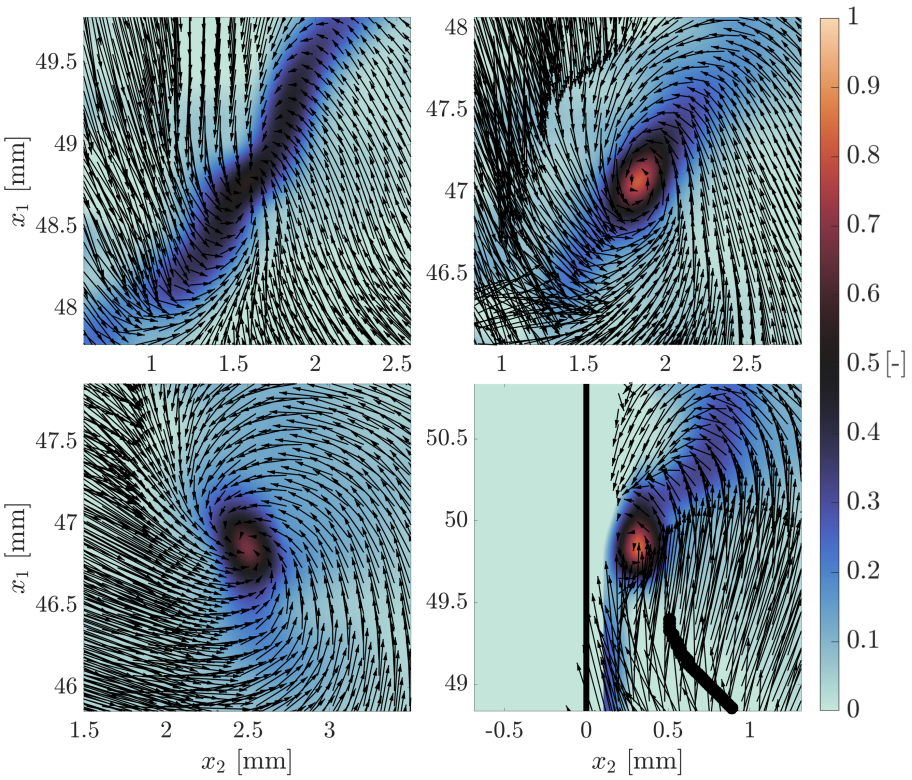

Figure 5.17: Examples of accepted vortices. Γ_1 values corresponding to each respective vortex centre are: 0.54 (top left), 0.81 (top right), 0.67 (bottom left), 0.85 (bottom right).

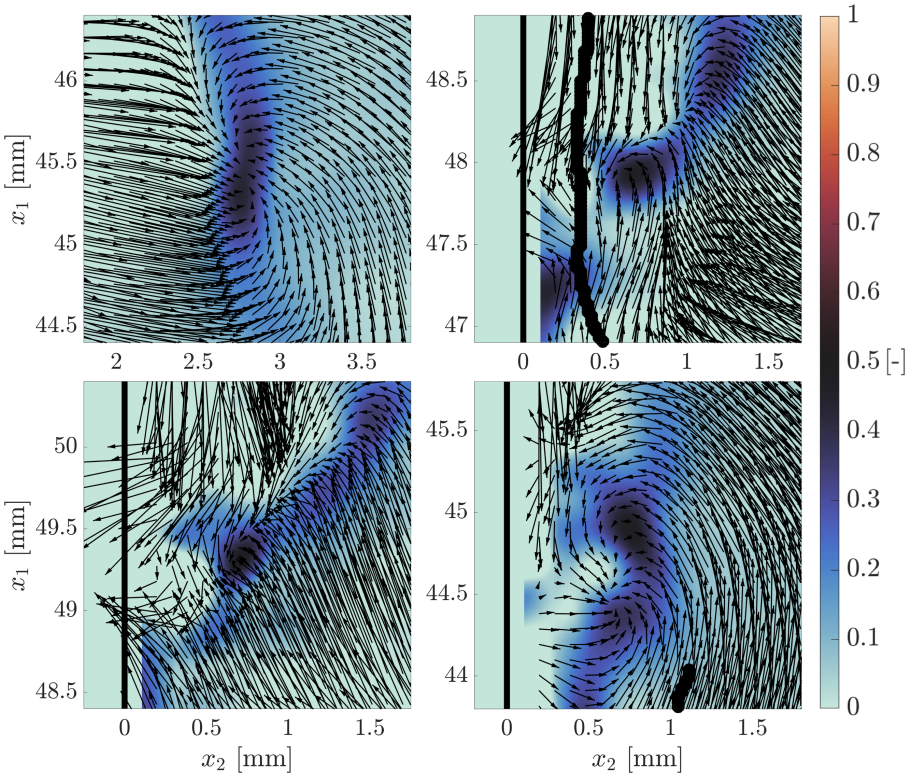

Figure 5.18: Examples of rejected vortices. Γ_1 values corresponding to each respective vortex centre are: 0.48 (top left), 0.44 (top right), 0.48 (bottom left), 0.48 (bottom right).

Of the 35 quenching events, the $\Gamma_1 = 0.5$ criterion successfully identified 20 sequences which include the full transient sequence of the vortex impacting the wall together with flame quenching (T3A), followed by a vortex travel event (T3B). The trajectories of these 20 events is shown in Figure 5.19. Note that this figure shows only the subset of transient T3 vortex sequences featuring a mostly continuous transition from a descent state (T3A) to a travel (T3B) state. This does not include the total number of detected vortices where resolving the full transition from T3A to T3B was unavailable. This is sometimes due to the flame quenching upstream of the image field of view, therefore only the travelling T3B vortex is seen as it enters the image. Alternatively, while visual semblance of a Type 3 vortex is always observed during quenching it may not meet the $\Gamma_1 = 0.5$ quality threshold to be included in the statistics.

The vortex trajectories can be seen to be spatially distributed across the FOV in Figure 5.19 a). Dashed lines (–) indicate where a vortex was not detected between frames, leading to a brief gap in the recorded trajectory. The red squares mark locations where a descending T3A vortex, shown by black lines, becomes classed as a travelling T3B, after which its trajectory is indicated by red lines. The distributed spatial arrangement of the trajectories demonstrates how the T3 vortices can potentially exist at any x_1 location in the FOV. This is unlikely to be the case if, for example, the T3 vortices are a non-physical artefact of the Reynolds decomposition which would restrict them occurring at only one specific location due to the alignment between the instantaneous (U_i) and mean ($\langle U_i \rangle$) velocity fields. The association of high Λ_{ci} with vortex centres described previously further supports

that the T3 vortices are a legitimate phenomenon.

Figure 5.19b) shows the trajectories aligned to a common centre that indicates the start of the T3B vortex state. This aligned coordinate system is labelled by the x_1', x_2' axes. A commonality between T3A descent patterns and subsequent T3B travel is immediately apparent from this representation, with the vortices descending to hte wall in an arc-like trajectory. The vortex identification strategy using the Γ_1 criterion is therefore able to successfully delineate the T3 vortex from its T3A states and T3B states. This detection allows for a conditional sampling of the vortex location to investigate the influence of the T3A vortex in flame quenching, together with potential gas transport mechanisms related to the T3B state. These aspects are explored through the remainder of this chapter.

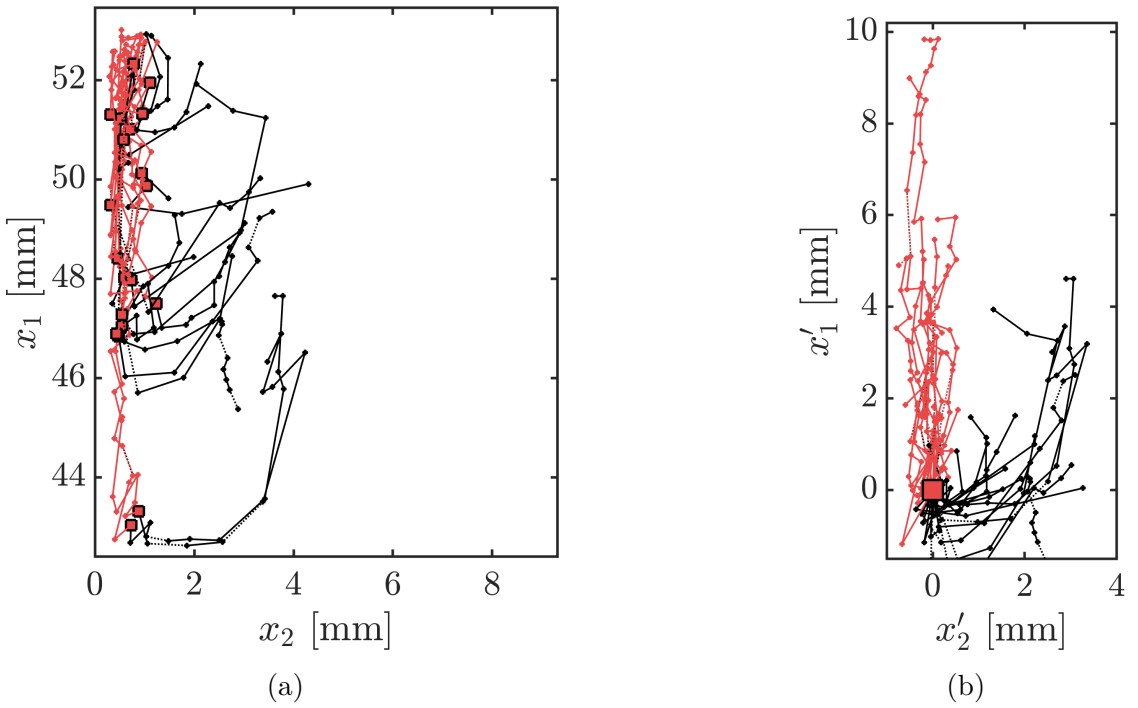

Figure 5.19: a) Trajectories across full FOV. b) Trajectories aligned relative to a common T3B transition point.

5.3.2 Type 3 conditioning procedure

The motivation behind the conditioning procedure is to produce an averaged spatiotemporal representation of the T3 vortex during its descent and subsequent travel phase. In this respect, it is possible to characterise and investigate the average flow features and phenomena with respect to the flame quenching and gas transport dynamics.

The proposed conditioning strategy therefore initially consists of separating all T3 vortices into whether they are a T3A or T3B vortex. This is followed by a conditioning of only the T3A vortex subset depending on the wall-normal (x_2) distance from the wall. The conditioning procedure is shown schematically in Figure 5.20. The minimum and maximum wall-normal x_2 extent spanned by all detected T3A vortices is divided into different bins. Flow quantities (e.g. velocity, vorticity fields) are then shifted based on the distance of the vortex locations $\mathbf{x}_v = (x_{1,v}, x_{2,v})$ from

the bin centre. This methodology results in conditioned quantities in a common coordinate system designated (x_1^*, x_2^*) where the original vortex locations $\mathbf{x}_v = (x_{1,v}, x_{2,v})$ are now aligned along a common axis passing through $(x_1^*, x_2^*) = (0, 0)$. This sets the reference frame as being relative to the vortex as it is advected by the mean flow. Flow quantities (e.g. $\mathbf{u}$) in this conditioned coordinate system will be denoted by an asterisk ($\mathbf{u}^*$).

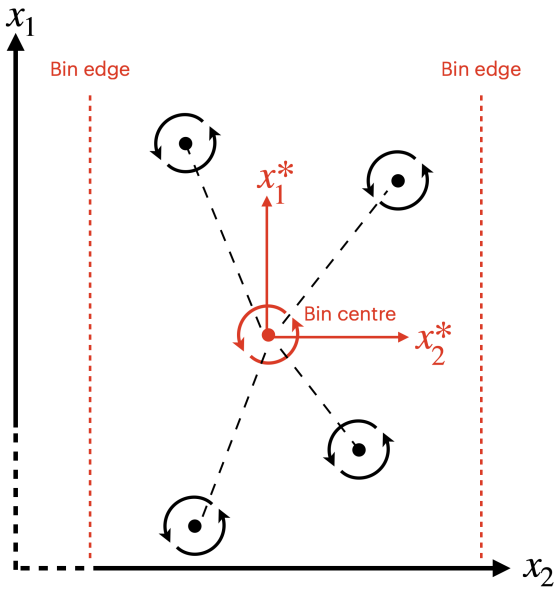

Figure 5.20: Schematic of the T3A vortex conditioning process.

There is a trade-off between the resolution of the T3A vortex descent and number of samples, i.e., a higher number of T3A bins results in potentially more stages of the descent being resolved but with less vortices in each (thinner) bin. From the full image sequence, it is observed that most T3A vortex descents are rapid and exist for between 2 - 4 images (500μs to 1000μs). Therefore, using 3 bins of equal width (1.32mm) in the current study was selected for a balanced representation.

Bin 3 includes T3 vortices within 2.98-4.30mm from the wall, which is typically when the T3A vortex is first identified and represents the earliest state of a descend event. Bin 2 includes vortex locations from 1.67-2.98mm which represents the intermediate stage of the descent sequence. Bin 1 considers T3A vortices closest to the wall (0.35 - 1.67mm) when the vortex is about to impact the wall, prior to or during flame quenching. Following impact with the wall, the T3A vortex is then classified as a T3B vortex representing the travel state. The T3B vortices are conditionally sampled accordingly and are not subject to the bin separation by x_2 distance as for the T3A subset. The spatial distribution of the T3 vortices associated to each bin and histograms of the x_2 distribution are shown in Figure 5.21 below. Conditioned T3A vortices will subsequently be denoted T3A - Bin 1, 2, 3 respectively. The total number of vortex samples (i.e., images with a vortex) is 24, 48, 77 for Bins 3, 2, 1 respectively and 232 for T3B.

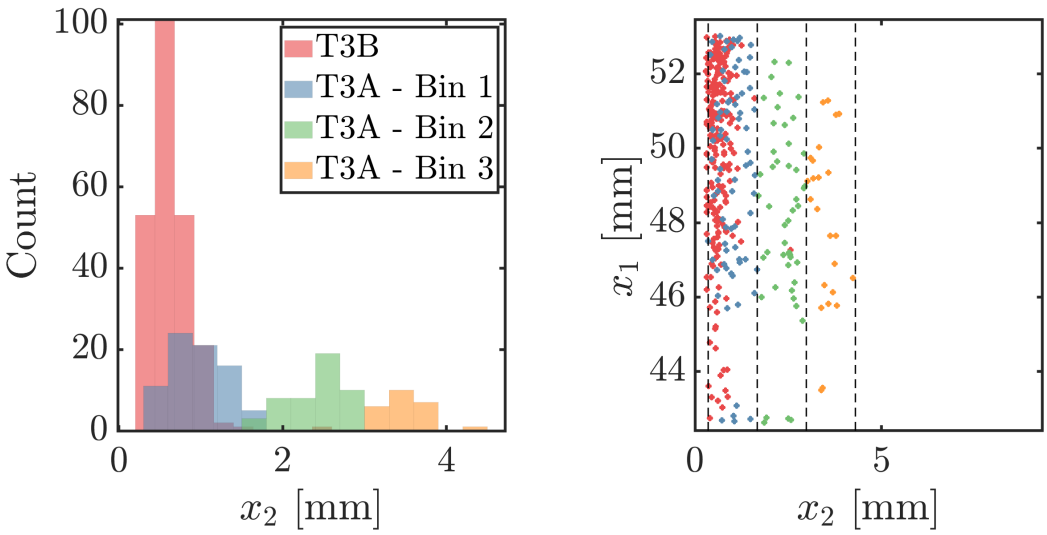

Figure 5.21: a) Locations of all detected T3 vortices. Colours correspond to either a T3B vortex or the respective bin for T3A vortices. b) Histogram of sample number conditioned bin.

5.3.3 Conditioned flame and vortex contours

Previously, the dynamics of the T3 vortex have been demonstrated for single quenching events. This section presents the statistical similarity between all quenching events involving a T3 vortex to demonstrate that the T3 vortices are not isolated phenomena and feature a strong correlation with the flame dynamics.

After accepted ($\Gamma_1 > 0.5$) T3 vortices are obtained, each individual vortex has a contour associated with it defined by the $\Gamma_1 = 0.4$ isoline. This region bounded by the vortex contour is not used directly for sampling statistics but is presented here as an approximate representation of the vortex shape. The conditioned vortex and flame front contours is shown in Figure 5.22. Note that the colour scale range for the T3A and T3B vortex contours differs. $1 \times 1\text{mm}^2$ highlights of the conditioned vortex centres are shown in Figure 5.22. Since the results are conditioned relative to the vortex centre, the wall position is shifted for each image. Therefore, the grey line for each conditioned bin in Figures 5.22 represents the most probable wall position. This is calculated from the probability density function (PDF) of the wall positions from the vortex centres for each set of conditioned results.

Figure 5.22 admirably portrays the evolution of the T3 vortex with respect to the flame and the wall. In T3A Bin 3, the vortex is furthest from the wall, while the flame fronts neighbouring are in a wall parallel HOQ configuration below the vortex. T3A Bin 2 portrays the intermediate stage of the descent. Several flame hook-like geometries, protruding out from the wall are seen to enter the FOV. In T3A Bin 1, the vortex is in the process of impacting the wall and quenching the flame. The vortex location is coincident with the flame region closest to the wall, where the flame transitions from an HOQ to an SWQ topology. Higher flame curvatures upstream of the vortex are apparent. The T3B conditioned results depict the conditioned T3B vortex in its travel state which is slightly downstream of the flame fronts which are quenched at this stage. Note that approximately 4 flame fronts have not been

detected as quenched by the image processing routine and are seen to extend beyond the conditioned T3B vortex. Given that the set of T3B vortices includes >200 individual samples, these misclassified flame fronts represent a minute proportion.

The conditionally averaged progression of the vortex with respect to the flame and wall shown in Figure 5.22 reveals the statistical prominence of a unique flame vortex interaction phenomenon under the turbulent operating conditions explored in this thesis. Namely, the T3 vortex originating in the burnt gas region impacts the wall, coinciding with flame quenching and a transition from HOQ to SWQ flame topology. Following flame quenching, the vortex persists downstream of the flame tip until the flame exists the field of view. Evidently, the Type 3 vortex apparently has a significant influence on flame quenching and its persistence after quenching is likely to influence mass transport in the vicinity of the flame quenching point. These aspects are evaluated in greater detail in the remainder of the chapter.

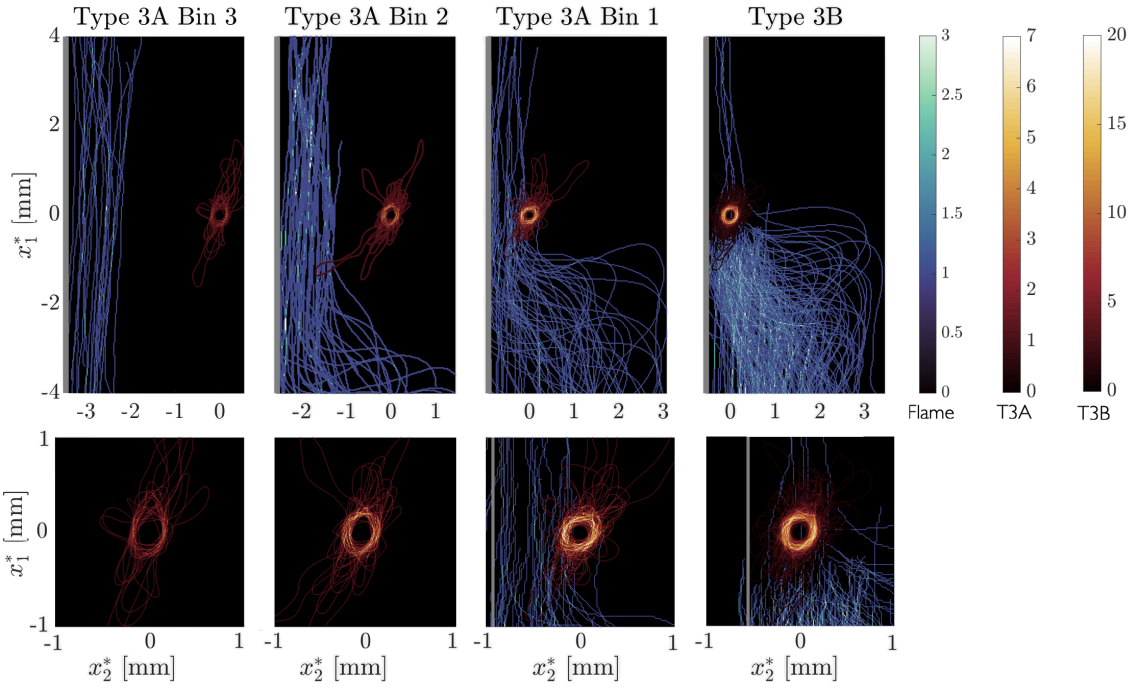

Figure 5.22: Conditioned vortex and flame contours.

5.3.4 Conditioned sample number

Prior to analysing conditioned flow quantities, it is important to report the number of individual samples present at each spatial location in the conditioned results. Recalling that the flow field quantities are conditioned relative to the T3 vortex centres, the local number of statistical samples that constitute the conditioned average will vary at different spatial locations.

The number of samples is shown in Figure 5.23 with the conditioned fluctuating velocity field overlaid. Each colour scale ranges from 0 to the maximum of number of samples for each conditioned state (each T3A bin and T3B). The black plus (+) marks the location of the conditioned vortex centre and the dashed line (–) marks the most probable wall location as previously. A mean flame front, shown in black, is represented by the 0.5 isocontour of the conditioned binarised LIF images and is used to represent an average flame location for the respective conditioned state.

The number of samples is highest in the vicinity of the vortex and decreases away from the vortex centre. In T3A Bin 3, immediately upstream and downstream of the vortex there is a slight reduction in sample number due to the vortices being in close proximity to the imaging artefact described earlier in Section 5.1.3. In proximity of the wall the sample number decreases for T3A, particularly T3A Bins 3 and 2, and therefore results in this region must be interpreted with caution.

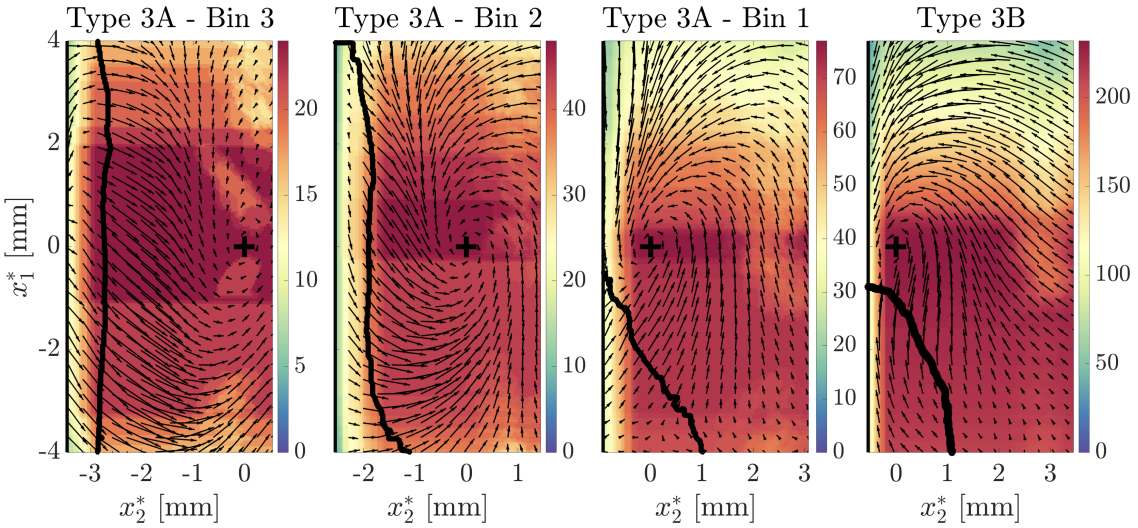

Figure 5.23: Conditioned number of samples. Note that each conditioned result has its own colour scale.

5.4 Quenching phenomena

Having conditioned the T3 vortices to achieve an averaged spatiotemporal representation of the T3 vortex evolution during the quenching process, this section will investigate hydrodynamic effects of the T3 vortex that can contribute to flame quenching. Local flame quenching can be caused by factors that sufficiently decrease the reaction rate of the combustion process to a negligible value (Meneveau & Poinsot, 1991). A PDF of the full flame front x_2 positions is shown in Figure 5.24a) with a PDF of only the quenching distances in Figure 5.24b). The modal value of the quenching distances in Figure 5.24b) is $x_2 = 0.72$mm with a minimum value of $x_2 = 0.24$mm. Compared to values of ≈0.25mm in the laminar case from the work of (Kosaka et al., 2018a), quenching distances are increased in the present turbulent case. Hydrodynamic effects due to turbulence are therefore highly influential in the flame dynamics and quenching process, with intense turbulence capable of causing flame extinction (Böhm et al., 2009). Two relevant kinematic properties of the T3 vortex, which have differing effects on flame behaviour, are investigated; the strain-rate and the vorticity.

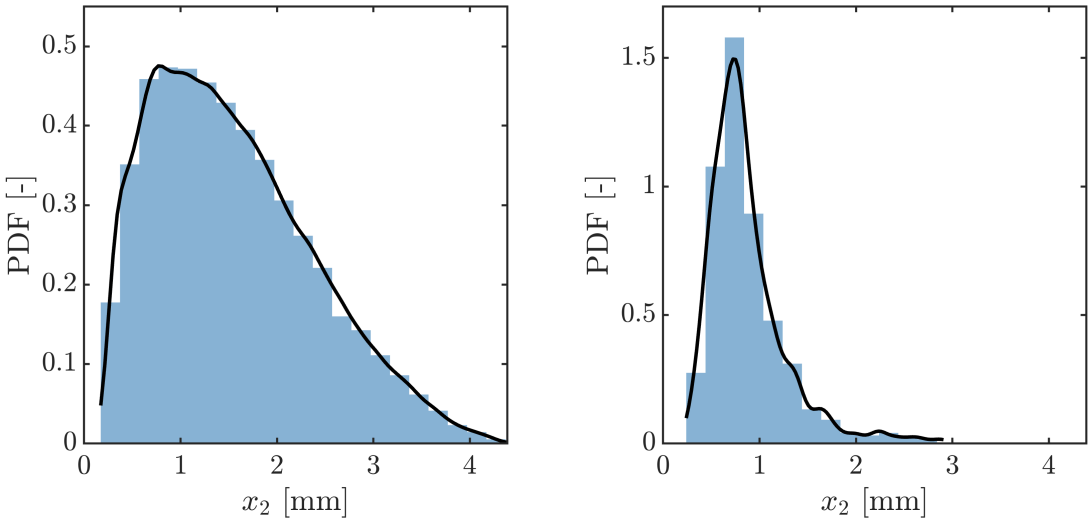

Figure 5.24: PDFs of wall-normal x_2 positions for a) all flame front and b) quenching point position.

Hydrodynamic strain of the flow field is involved in generating flame surface area through stretching of the flame front (Candel & Poinsot, 1990). Excessive strain on a flame is known to quench flames (T. Poinsot et al., 1991) by sufficiently stretching the flame surface to an extent that the combustion process is suppressed. The local strain field induced by the T3 vortex during its descent to impact the wall could be a determining factor in imparting sufficient strain to the quench flame. The shear imparted by the strong velocity gradient $\partial U_1/\partial x_2$ due to the wall will also contribute to straining the flame depending on the flame x_2 location. Decoupling and isolating the separate strain influences of the wall and the turbulent flow field involving the T3 vortex is important in assessing the influence of this kinematic property in quenching the flame through effects of flame stretch.

While strain is involved in generating flame surface area through stretching of the flame front, vorticity is associated with wrinkling and redistribution of the existing flame surface (Steinberg & Driscoll, 2009). Thus, the T3 vortex can be involved in a unique interaction of affecting flame geometry and pushing the flame against the wall during its descent, promoting sufficient heat loss to the wall to quench the flame. The spatial correlation of the descent of the T3 vortex with the flame front moving closer to the wall is assessed to investigate this possible quenching mechanism. The action of vortices within FWI pushing the flame front to the wall was reported qualitatively in the FWI numerical studies of (Bruneaux et al., 1996; Gruber et al., 2010). Isolated test cases from the DNS of (T. Alshaalan & Rutland, 2002) discovered that strong vortices were able push the flame to the wall to promote heat flux, while weak vortices had little effect. Thus, characterising the strength of the T3 vortex during its evolution to impact the flame is important in assessing the likely potential of the vortex to affect the flame geometry.

Heat loss is a significant factor affecting flame quenching (Meneveau & Poinsot, 1991) but unfortunately cannot be investigated in this work as measurements of heat flux are not available for this dataset. Given the complexity of the multiphysics phenomena present in turbulent combustion and flame quenching, naturally there are limitations to the conclusions that can be drawn from strictly 2D velocity data with-

out simultaneous coupled measurements of other variables. The following therefore presents the first attempt at a detailed characterisation of the flow dynamics and dominant kinematic effects of the T3 vortex during the quenching process. It is anticipated that results from this section can be used to guide further experimental and numerical investigations to study heat transfer and three-dimensional flow field attributes in greater detail.

5.4.1 Influence of strain

Assuming the flamelet regime, flame stretch κ describes the change in flame surface area (Candel & Poinsot, 1990):

$$\begin{aligned}\kappa &= (-\overrightarrow{n} \cdot (\overrightarrow{n} \cdot \nabla)\,\mathbf{U} + \nabla \cdot \mathbf{U}) + s_l \nabla \cdot \overrightarrow{n} \\ &= (\delta_{ij} - n_i n_j)\,\frac{\partial u_i}{\partial x_j} + s_l \frac{\partial n_i}{\partial x_i} \\ &= a_t + \kappa_c\end{aligned} \tag{5.5}$$

where s_l is the laminar flame speed and $\overrightarrow{n}$ is the unit normal vector oriented towards the reactants from the flame surface. The term a_t is the component of the hydrodynamic strain rate acting normal to the flame surface by the flow. This includes two terms; the component of the strain-rate tensor acting normal to the flame ($-\overrightarrow{n} \cdot (\overrightarrow{n} \cdot \nabla)\,\mathbf{U}$), and the effect of dilatation ($\nabla \cdot \mathbf{U}$) due to volumetric expansion of the fluid. The second term κ_c represents stretching of the flame front due to propagation of a curved surface in the normal direction.

The hydrodynamic strain-rate therefore acts through a_t to stretch the flame and generate surface area. This section investigates the influence of the resolvable in-plane strain $S = \partial U_1/\partial x_2 + \partial U_2/\partial x_1$ in quenching the flame. Compared to the out-of-plane strain components ($\partial U_1/\partial x_3 + \partial U_3/\partial x_1$ and $\partial U_2/\partial x_3 + \partial U_3/\partial x_2$), the in-plane component typically dominates the strain contribution in non-reacting wall-bounded flows as a result of the no-slip condition inducing strong gradients in the wall-normal x_2 direction, but not in the streamwise x_1 or in the out-of-plane x_3 directions. The in-plane strain S is therefore assumed to be the major component of the strain-rate tensor in the present experiment.

There exist two unique sources of strain capable of producing flame quenching through effects of stretch. Firstly, the strong shear imparted by the wall will be experienced by the flame front depending on its wall-normal position x_2 and thus location in the shear layer. This contribution from the wall is present even if the flow was laminar. The second source of strain is due to the turbulent flow field. This includes the strain field induced by the T3 vortex during its descent and interaction with the flame.

5.4.1.1 Strain sampling methodology

The methodology used to characterise the strain experienced by the flame front is first described. The hydrodynamic strain S is sampled at each discrete point on the flame front in the normal direction oriented towards the reactants as shown in a highlighted strain field in Figure 5.25. The flame unit normal vector for each point on the flame contour is initially calculated from the LIF image grid where the flame

front is detected, before being upsampled to the higher density grid spacing of the wOF grid, or downsampled for the PIV grid.

The presence of the flame front can induce thermophoretic effects in the tracer particles which will manifest as errors in velocity measurements and subsequently derived quantities. An initial distance of 0.15mm from the flame front is therefore initially excluded to mitigate some error that may result from thermophoresis of the PIV tracer particles. Following the 0.15mm exclusion distance, strain values are sampled 0.25mm normal to the flame in the unburnt gas region. These sampled values are averaged to produce a strain value for a given discrete point along the flame front. A sensitivity study using sampling distances of $0.15, 0.5$ had a mild affect on absolute values of strain, due to including differing amounts of the elevated strain regions in the sample averages, as visible by the sampling extent in Figure 5.25. This does not affect the main conclusions of the present analysis however.

The strain sampled on the flame using the described methodology will be termed the *flame strain* in the following analysis. However, it is should be pointed out that technically this is not exactly the strain imparted on the flame in $-\overrightarrow{n} \cdot (\overrightarrow{n} \cdot \nabla)\,\mathbf{U}$ as part of the flame stretch in equation 5.5. Only the component of the hydrodynamic strain acting normal to the flame is actually responsible for the flame stretch, and this can be calculated from the eigenvalues of the strain-rate tensor (N. Chakraborty & Swaminathan, 2007) or from an unstructured grid arrangement for derivative calculation (Steinberg et al., 2009). Knowledge of the orientation of both the flamelet normal and the principal strain-rate axes in 3D space is required for the full calculation of $-\overrightarrow{n} \cdot (\overrightarrow{n} \cdot \nabla)\,\mathbf{U}$ in equation 5.5. The hydrodynamic strain still acts as a suitable quantity for assessing spatiotemporal variations in the flame stretching process (Steinberg & Driscoll, 2009), however.

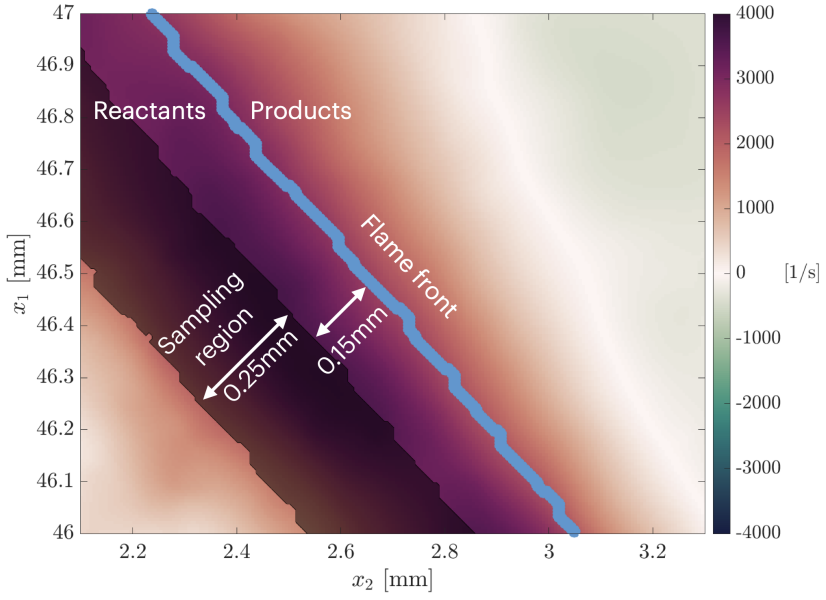

Figure 5.25: Highlight of an instantaneous strain field S with the strain sampling region.

5.4.1.2 Instantaneous strain example

The prominent strain distributions and their presence relative to the flame is first exampled. An instantaneous strain field is shown in Figure 5.26a), together with strain trace in the unburnt gas region in Figure 5.26b). The flame front contour is coloured by its length l in Figure 5.26a) and the same colour reference is shown in the trace to aid visual interpretation. The figure shows an unquenched flame, with regions close to and extending further away from the wall. In the downstream region of the FOV ($x_1 > 50$mm), the flame resembles the HOQ configuration. At this current time instant, the flame is not detected as quenching, but is observed to quench 1ms (4 image instants) later at the edge of the FOV.

Within the individual images, three important features can be seen. First, the fluid region near the wall experiences high positive (extensive) strain as expected in boundary layers due to the contribution of the strong streamwise velocity gradient $\partial U_1/\partial x_2$ to the strain-rate S. This positive strain distribution extends approximately 1mm from the wall and continues across the entire downstream (x_1) distance in the FOV, regardless of the flame proximity to the wall. Secondly, the flame portion far from the wall ($4 < l < 8$mm) is shown to experience high strains over 3000s^{-1}. Although the flame experiences these elevated strain regions, the flame at this location away from the wall does not quench or show signs of a weakening flame.

The third notable features is that the flame region beyond $x_1 = 50\text{mm}/l = 8$mm close to the wall continues to experience high strain due to its proximity to the wall shear layer. The strain magnitude near the wall in this region of $x_1 > 50$mm is consistent with the strain magnitude downstream of this position when the flame is away from the wall. The cross (x) marked on the flame in Figure 5.26 marks the start of a defined influence region due to the wall that is analysed subsequently.

It is not until 1ms (4 image frames) after this image, when the HOQ region of the flame is observed to move closer to the wall and quench. Thus, it is clear that the flame can experience strain rates due to the wall in excess of 3000s^{-1} for an appreciable amount of time before the flame is quenched. It is not clear yet whether this strain magnitude is attributable to flame quenching, or whether the proximity of the flame to the wall or the presence of the T3 vortex is a contributing factor yet. However, the image sequence shows the flame does not appear to immediately quench when the flame experiences high strain values up to 4000s^{-1}.

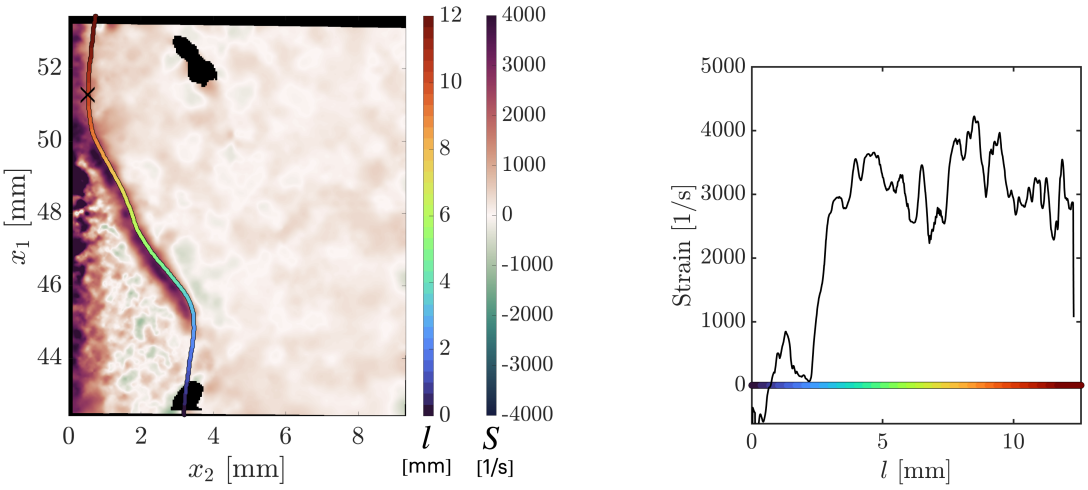

Figure 5.26: a) Instantaneous strain field S. b) Strain trace along flame front. Colour corresponds to the distance l travelling along the flame.

5.4.1.3 Strain due to wall shear

The instantaneous strain during quenching is next assessed using the conditioned strain field S^* shown in Figure 5.27 with the conditioned instantaneous flow field $\mathbf{U}^*$ overlaid. As discussed previously in Figure 5.23, it is important to recall that the conditioning procedure results in the highest number of samples in the vicinity of the T3 vortex, and that the sample number decreases considerably near the wall for T3A Bin 3 and Bin 2 such that the results in this region should be interpreted with some caution for these two bins. The strain acting on the flamefrom the wall will be analysed in more detail subsequently. The conditioned strain S^* however provides a representation of the overall evolution of the instantaneous strain during the quenching process as the T3 vortex proceeds to impact the wall.

In T3A Bin 3, higher strains are apparent between the wall and the mean flame front shown by the black line. The strain near below the flame near the wall is ≈2000 - 2500s^{-1}. Several regions of increased strain up to ≈3000s^{-1} appear in T3A Bin 2 and slightly elevated strains extend slightly further out from the wall. T3A Bin 1 represents the samples prior to and during quenching. The strain values near the wall are comparable in magnitude to those of T3A Bins 3, 2 and become weaker beyond the T3 vortex centre at $(x_1^*, x_2^*) = (0, 0)$ in the downstream direction. The conditioned strain field in T3B, representing the already quenched flames and the travelling vortex, features significantly higher strains upstream region of the vortex centre ($x_2^* < 0$) primarily in the unburnt gases, compared with the burnt gases downstream where the S^* becomes weaker primarily due to a decrease in U_1 and therefore $\partial U_1/\partial x_2$. The conditioned field S^* in Figure 5.27 reveals that elevated strains are always present at the wall and the flame position varies in its proximity to this region.

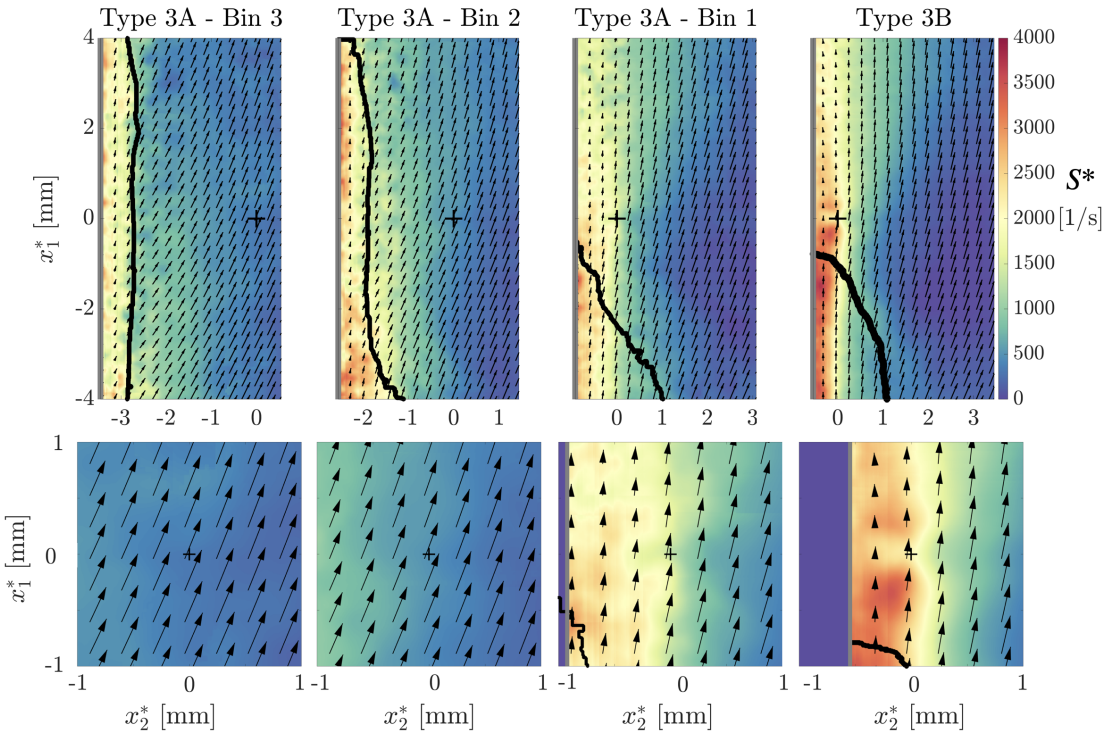

Figure 5.27: Conditioned instantaneous strain S^*.

The strain acting on the flame during quenching is analysed in more detail by considering a subset of region of the flame influenced by the wall. For each flame front in the T3A bins, the location of the flame closest to the wall is detected. This minimum flame x_2 location is marked by the cross (x) in Figure 5.26. Beyond this minimum x_2 point, flame fronts are spatially extended in the downstream direction, characteristic of the HOQ topology. The minimum flame x_2 location nearest to the wall is where quenching is seen to occur in the image sequence. The flame front region past the minimum x_2 point in the downstream direction is defined as the region of influence due to shear from the wall. By considering the statistics of the flame strain specific to this region, the progression of strain from the wall acting on this local flame region during quenching can be evaluated. The results are shown in Figure 5.28 and are separated according to the flame fronts associated to each T3A bin to reveal an average temporal progression represented by unquenched flame fronts in T3A Bin 3 - 2 to Bin 1 which is the state during quenching.

The PDFs reveal that the flame strains due to the wall are predominantly positive with similar modal values of 2000s^{-1} for T3A Bins 3, 2 which is in agreement with the conditioned strain S^*. The distribution of T3A Bin 1 shifts to a modal value of a slightly higher strains and a broader distribution as the flame is quenching in T3A Bin 1. The PDF of T3A Bin 1, features a heavier tail with some values extending upwards of 6000s^{-1}. These more extreme values, associated with a very minor probability, are due to occasional erroneous vectors close to the wall and is not a physical effect. Figure 5.28 does indicate that an increase in strain is experienced by the flame during its progression to quenching.

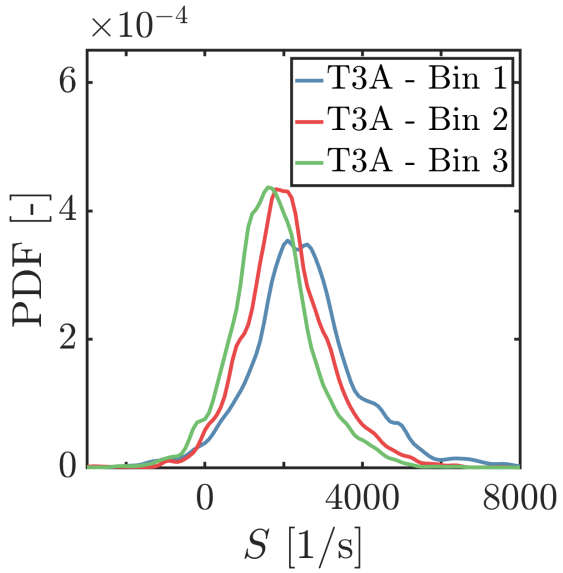

Figure 5.28: PDFs of flame strain S due to the wall.

However, spatial information about the flame front position within the wall shear layer is not captured by the statistics shown in Figure 5.28 alone. This aspect is next analysed from the PDFs of the flame wall-normal x_2 positions for wall-influenced flame front regions, shown in Figure 5.29. The PDFs of the flame position reveal that the flame positions do change as the flame proceeds to quench. The modal values of the PDF decrease between T3A Bin 3 to T3A Bins 2, 1, indicating that the flame front moves closer to the wall during quenching. The tails of the PDFs become restricted to smaller x_2 values, therefore the flame is increasingly likely to be close to the wall during its progression to quenching at Bin 1, compared to its HOQ topology in Bins 2, 3.

Therefore, the flame strain does increase through the conditioned quenching sequence and this increase is associated with the flame extending closer to the wall and deeper into the shear layer, thus experiencing higher magnitude strains. This change in flame front position is more attributable to a wrinkling effect due to vorticity rather than strain-rate (Steinberg & Driscoll, 2009) and is analysed separately in a forthcoming section.

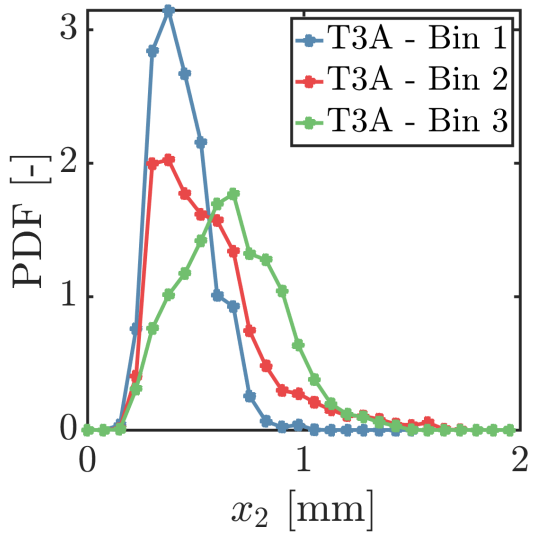

Figure 5.29: PDF of x_2 flame positions.

The shear layer of the wall therefore does contribute to the strain experienced by the flame during quenching. This effect is also seen in the instantaneous strain example of Figure 5.26, where high strains acting on the flame front away from the wall are continue as the flame moves in proximity of the wall.

As a final assessment of the influence of strain due to the wall, the flame strain statistics for all flame fronts are analysed. This includes all regions across the flame front and is not restricted to the influence region considered previously for Figures 5.28 and 5.29. The results are shown in Figure 5.30. The solid lines (-) denote the flame strain and the dashed lines (- -) indicate the overall unburnt strain statistics which includes those of the flame strain. The PDFs are calculated across 1mm x_2 intervals up to 4mm to separate the PDF distributions as a function of the wall-normal x_2 distance to investigate the influence of the proximity of the wall.

The flame strain PDFs together with the overall strain PDFs shift towards higher positive values as the wall is approached, reflecting the general influence of the shear layer on the overall strain distribution present in the flow field. Strain flame PDFs for $x_2 > 2$ show similar peak values to the unburnt strain however features heavier tails compared to the unburnt strain, indicating that the strongest strains up to $\approx 3800 s^{-1}$ in the unburnt flow field are experienced by the flame within this wall-normal region.

For x_2 = 1-2mm, the modal value of the flame strain (red solid line) is increased compared to the total unburnt strain (red dashed line). The flame strain in this region also features a heavier tail, with a similar maximum positive extent of $\approx 3800 s^{-1}$ as for x_2 >2mm indicating the flame strain occupies the upper proportion of the total unburnt strain.

The highest extensive strains are experienced for 0 - 1mm in closest proximity of the wall. The distribution of strain on the flame (blue solid line) at 0 - 1mm closely aligns with the modal value and extent of the general strain inthe reactants (- -) within this x_2 distance. It is therefore evident that the flame strain experienced in this region is significantly imparted by the wall. In addition to the wall shear, the strain field induced by the vortex may further contribute to the strain necessary to quench the flame as the vortex descends to impact the wall. This aspect is investigated in the following.

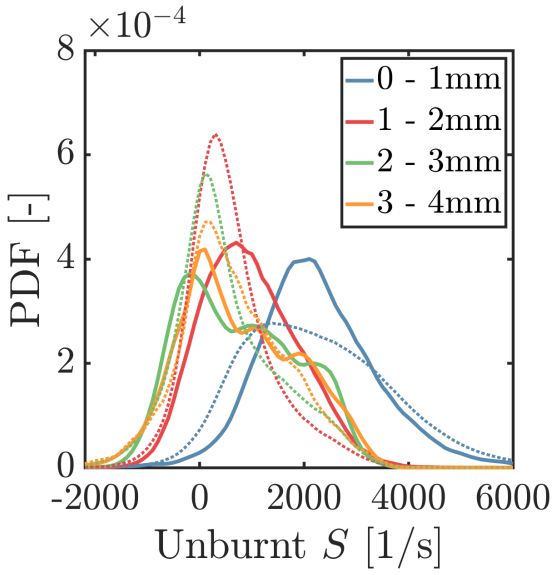

Figure 5.30: PDF distribution for (-) flame strain and (- -) total strain in unburnt region.

5.4.1.4 Strain due to T3 vortex

Vortices inducing sufficient strain in their local vicinity have been shown to quench flames (T. Poinsot et al., 1991). The T3 vortex is revealed in the fluctuating velocity **u** via the Reynolds decomposition which is equivalent to a reference frame moving with the mean flow. The strain imparted by the vortical flow field is thus calculated from **u**, i.e., the strain of the velocity fluctuations, which is commonly termed the fluctuating strain (Honkan & Andreopoulos, 1997) and is denoted s. An additional motivating factor for investigating the fluctuating strain is that the Reynolds decomposition effectively removes a significant contribution of the shear induced by the wall (Elsas & Moriconi, 2017), since a significant proportion is contained in the streamwise mean flow gradient $\partial\langle U_1\rangle/\partial x_2$.

The fluctuating strain field s is exampled in Figure 5.31 for the same image shown previously for S in Figure 5.26. The region $x_2 < 1$mm that was previously dominated by strong extensive strain from the wall in the Figure 5.26 now features features significantly reduced strain magnitude with both positive and negative regions present in s. Previous variations in strain at the wall in Figure 5.26 were challenging to identify because they were masked by the shear from the wall.

An important feature apparent in Figure 5.31 is that the increased strain region present along the flame front away from the wall in ($4 < l < 8$) has been largely preserved and features slightly reduced but comparable magnitudes to the instantaneous trace. Thus, the masking effect of the mean shear at the wall is removed when considering the fluctuating strain, while significant strain variations present on the flame are retained.

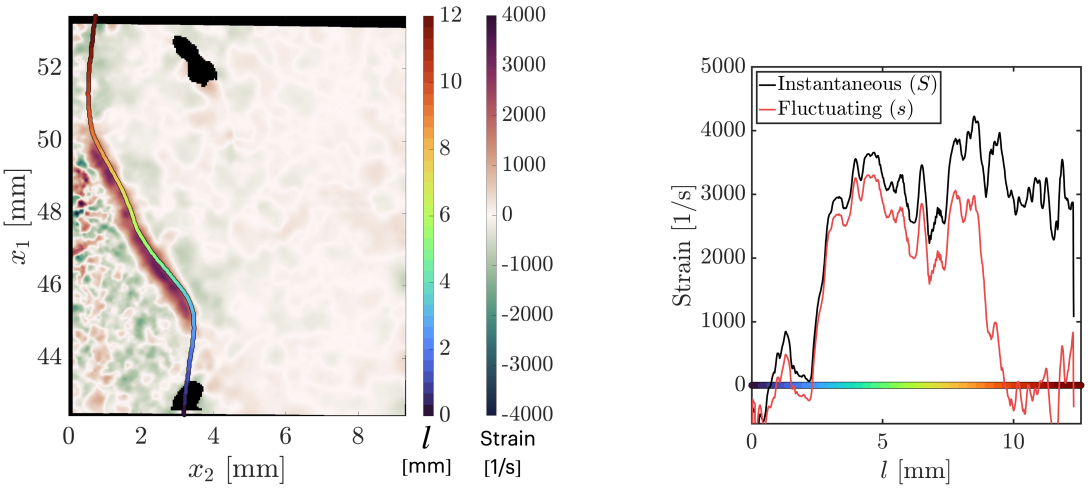

Figure 5.31: a) Fluctuating strain field s. b) Strain trace along flame front. Colour corresponds to the length along the flame.

The influence of the fluctuating strain from the T3A vortex is first assessed from the conditioned fluctuating strain s^* shown in Figure 5.32. Unlike in the conditioned instantaneous strain S^* where only positive (extensive) strain is observed, regions of both positive (extensive) and negative (compressive) fluctuating strain are present as also visible in the above example.

In T3A Bin 3, a region of negative strain is present at the wall, while weak positive strains exist away from the wall and in the vicinity of the T3A Bin 3 vortex as visible in the highlight. The positive strain distribution remains similar in T3A Bin 2 and the negative strain region from the wall decreases and is replaced with positive strains in the upstream region of the conditioned FOV at x_2^*= -4mm. For T3A Bin 1, the positive strain region surrounding the vortex has been moved closer to the wall and a slight strain increase in the vicinity of the vortex becomes apparent. The increase is mild however and contained within a small radius of the T3A vortex centre. A more substantial increase follows in T3B when the flame is already quenched and the vortex is in its travel state. From the sequence in T3A Bins 3 - 1, it is apparent that there are some weak extensive strains induced by the vortex, with the strongest magnitudes forming in the local vicinity of the vortex core in T3A Bin 1.

The vortex does alter the fluctuating strain distribution through its descent, bringing mildly increased extensive fluctuating strains in proximity of the flame in T3A Bin 1. Although the magnitude of a fluctuating quantity, such as s, is expected to be lower than its corresponding instantaneous quantity (S), the progression in fluctuating strain in T3A Bins is observed to be mild in the conditioned sequence and only becomes apparent in T3A Bin 1 and following flame quenching in T3B as visible in the highlighted $1\times1\text{mm}^2$ regions.

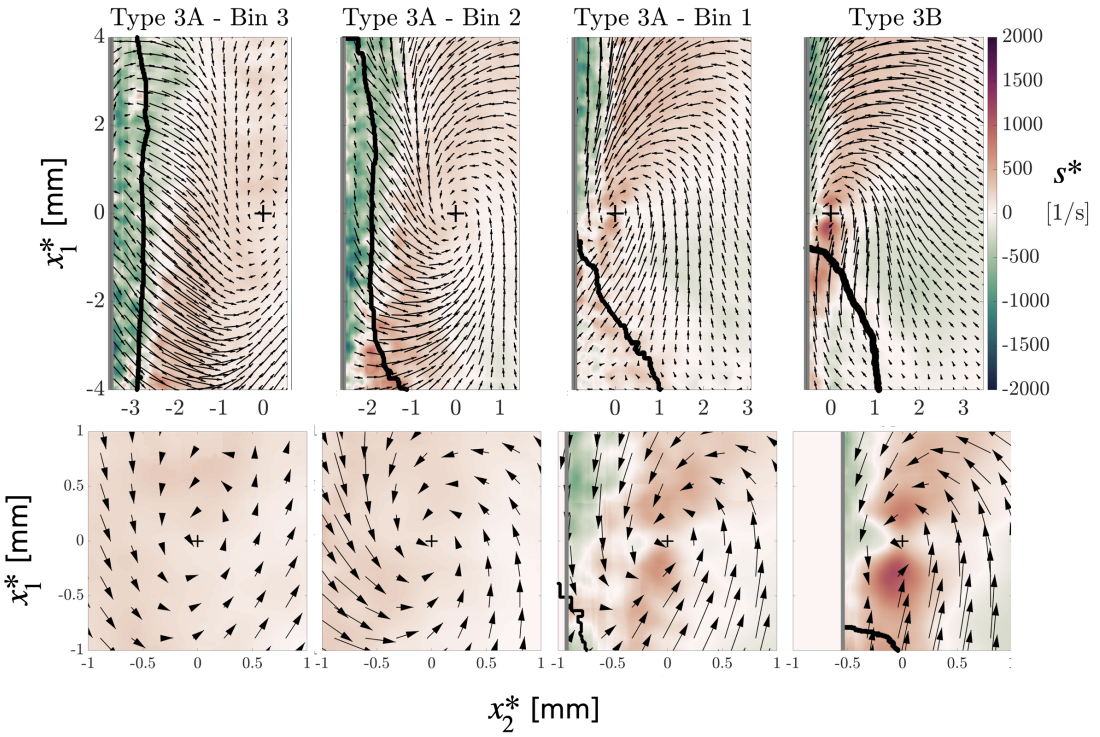

Figure 5.32: Conditioned fluctuating strain s^*.

The strength of the strain fields induced by all the detected T3 vortices is next assessed statistically to evaluate a potential contribution to the quenching process compared the mean shear. Both the instantaneous strain S and the fluctuating strain s in the local vicinity of the T3 vortices are evaluated for a comprehensive characterisation of their strain influence. Analysis of the instantaneous strain S of the T3 vortices is important in order to compare the strain of the T3 vortices relative to the strain present across the boundary layer due to the wall. Investigation of the fluctuating strain s is also needed as this represents the strain due to the vortical flow field that is visible in the fluctuating velocity $\mathbf{u}$ from the Reynolds decomposition. The two are related, as a sufficiently strong fluctuating strain s would also manifest itself as locally increased instantaneous strain S.

The strength of the strain field of each individual T3 vortex is characterised by averaging strain values over a circular area of 0.25mm radius centred around each individual T3 vortex centre that was included in the conditioning methodology. Using larger sized sampling regions does not alter the trends presented in the following statistics, but decreases absolute values since the strain field is strongest in the local vicinity of the vortex core, as visible in s^* shown previously. Therefore, including strain values beyond the elevated strain around the vortex centre has the effect of diluting the final strain value of each vortex because weaker strain values become included in the average.

The results are shown in Figure 5.33a) for the instantaneous strain S and Figure 5.33b) for the fluctuating strain s. The datapoints are coloured by the respective conditioned bin of each T3A vortex. The mean value of the datapoints in each bin is shown by the respectively coloured bold markers. A trendline using the sum of two exponentials $ae^{bx_2} + ce^{dx_2}$ is fitted using each of the individual vortex points shown to statistically characterise the general distribution. The mean wall-normal strain distribution $\langle S \rangle$, averaged temporally and in the streamwise x_1 direction, is

plotted in Figure 5.33 to compare the instantaneous strain of the T3 vortices with the mean shear contribution due to the wall.

Figure 5.33a) shows that the instantaneous strain contained within the T3 vortices increases as the wall is approached. The increase is initially gradual between T3A Bin 3 and Bin 2, before rising for T3A Bin 1 where the vortex is in closest proximity of the flame. This increase is in agreement with the conditioned results shown in Figure 5.27 where S^* showed little variation between T3A Bin 2 and Bin 3, before rising for Bin 1. While T3B is associated to the travel state of the vortex and not quenching, it is still included in the statistics of Figure 5.33 for completeness. The general trend as indicated by the fitted curve very closely resembles the ensemble average strain of the flow $\langle S \rangle$ and is only mildly increased in comparison. This shows that the instantaneous strain of the T3 vortices is comparable to the mean strain generally present in the boundary layer, i.e., the strain field of the vortices is not very significant as the shear due to the wall dominates the strain in the boundary layer.

Figure 5.33b) shows that the fluctuating strain induced by the vortices between T3A Bin 3 and T3A Bin 2 is effectively the same and a marginal increase follows for T3A Bin 1. The average of the strain values within each bins remains considerably low across all bins for T3A Bins 3, 2, 1 respectively which is in agreement with the trends visible in the conditioned representation s^*. At lower x_2 values, the scatter of the datapoints increases, with some vortices also capable of inducing a compressive (negative) strain field as opposed to an extensive strain. The fact that the strain contribution from the T3 vortex does not feature a consistently signed and significantly elevated strain, even in T3A Bin 1, supports the result that the strain field due to the vortex is unlikely to be the causal factor in flame quenching. The location of the flame within the shear layer due to the wall is therefore determined to be the more significant contributor to straining the flame compared to the induced strain of the vortex. The change in flame x_2 position leading up to quenching may suggest that the flame is being pushed to the wall by the vortex, rather than being strained by it. This is investigated in the following section.

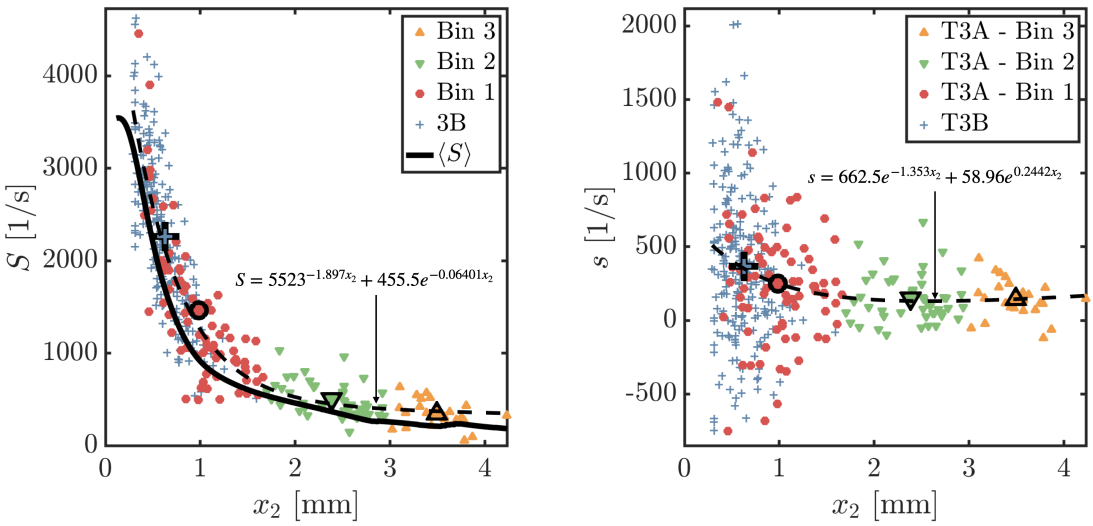

Figure 5.33: a) Instantaneous (S) and b) fluctuating (s) strain of the T3 vortices.

5.4.2 Influence of vorticity

The following section analyses the influence of the rotational, rather than shearing properties of the flow field and T3 vortex on flame quenching. As described previously, vorticity is involved in wrinkling the flame front and thus modifying the topological distribution of existing flame surface (Steinberg & Driscoll, 2009). While analysis the previous section concluded that the strain due to the T3 vortex is unlikely to be a leading factor in flame quenching, the vortex is may be capable of pushing the flame closer to the wall and deeper into the shear layer, thus leading to quenching through a combined effect of experiencing higher shear from the wall and increased heat loss.

The angular velocity or strength of the vortex rotational motion is first assessed to determine if the vortex is likely to influence the flame. Unlike in (T. Alshaalan & Rutland, 2002), where the vortex strength (set by the vortex' circulation) was *a priori* defined in simulation test cases, assessment of the vortex strength in the present experimental data is complicated by the presence of strong vorticity at the wall, since the streamwise velocity gradient $\partial U_1/\partial x_2$ is a component of both the instantaneous vorticity Ω and of the strain S. Ω can therefore be a misleading quantity since both rotational motion about an axis and regions of shear are both described by elevated vorticity values. This effect is particularly prominent in a wall-bounded flows as also described in Chapter 2, and has also been observed in turbulent reacting free shear flows (Gamba et al., 2012). Therefore, it is necessary to isolate the vortical motion intrinsic to the vortex. Analysis of both the fluctuating vorticity ω, and the swirling strength Λ_{ci} will be used for a robust assessment of the vortex strength and thus the potential of the vortex to influence the flame. Following analysis of this kinematic attribute of the vortex, the correlation between the descending T3A vortex to movement of the flame towards the wall is investigated.

5.4.2.1 T3 vortex fluctuating vorticity (ω)

Similarly to the fluctuating strain s, the fluctuating vorticity ω is directly associated to the vortex flow field as observed in the fluctuating velocity field $\mathbf{u}$ from the Reynolds decomposition. The vortex strength is first analysed through the conditioned fluctuating vorticity ω^* sequence shown in Figure 5.34. Both positive (CCW) and negative vorticity (CW) are shown and the conditioned fluctuating velocity field $\mathbf{u}^*$ is overlaid.

In T3A Bin 3, the vortex is far from the flame and is in a region of weak, spatially distributed positive ω that extends across the conditioned streamwise distance x_1^* and is above the mean flame front indicated by the black line. A region of negative vorticity is present nearer to the wall. In T3A Bin 2, the positive ω^* region around the vortex follows a minor increase visible in the highlights. A local ω peak is difficult to discern from the ω^* fields of T3A Bin 3 - 2 from among the general spatial positive ω distribution. At T3A Bin 1, the ω^* field becomes concentrated around the T3 vortex centre, with a well localised and clearly discernible peak directly coincident with the T3 vortex centre. In T3B, when the vortex is in its travel state following quenching, ω^* is further increased compared to Bin 1. A weaker distribution of ω^* follows downstream of the vortex centre for these two bins.

The T3 vortex is always associated to the region of positive ω^* throughout the conditioned sequence. Between T3A Bin 3 to Bin 1, the magnitude of ω^* in the local

vicinity of the vortex increases considerably and coalesces around the T3A vortex centre. This suggests that the vortex, as observed in the fluctuating velocity field, actually grows in strength as it descends closer to the wall and interacts with the flame in T3A Bin 1.

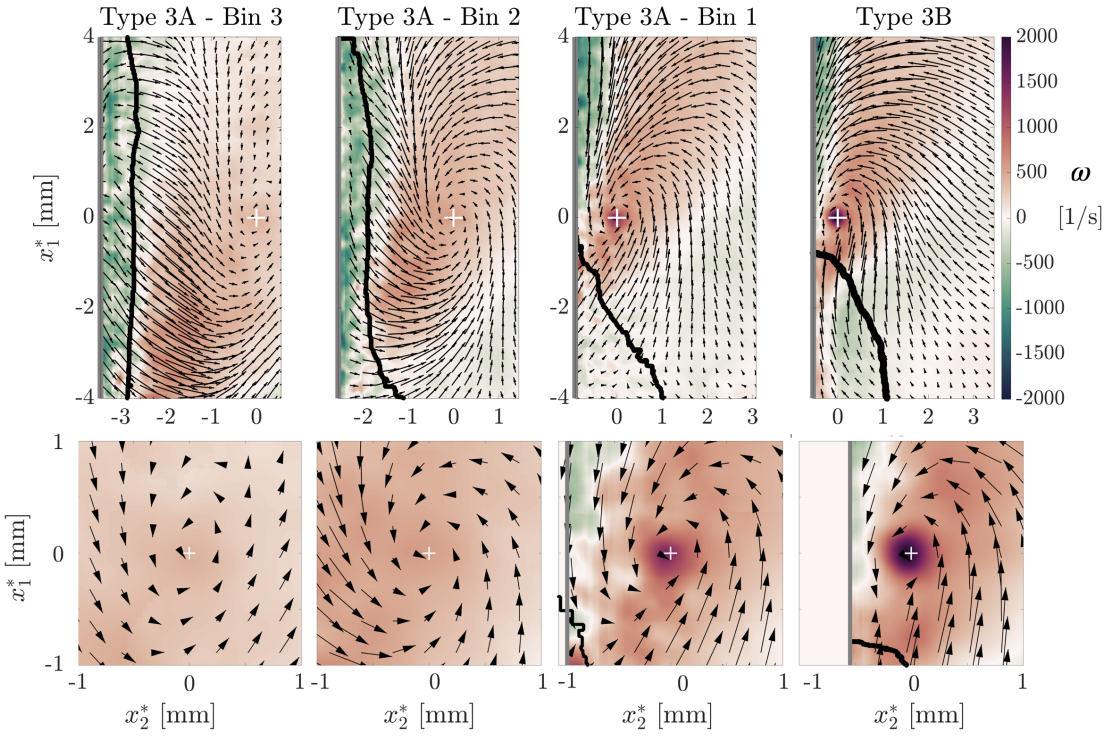

Figure 5.34: Conditioned instantaneous vorticity ω^*

The indication of the vortex growing stronger during its descent is suggestive of the potential of the vortex to influence the flame. This is analysed further by sampling the local fluctuating vorticity ω of each individual T3 vortex in a similar manner as performed with the strain in Figure 5.25 using the same 0.25mm sampling radius. The fluctuating vorticity ω of the T3 vortex cores is presented in Figure 5.35.

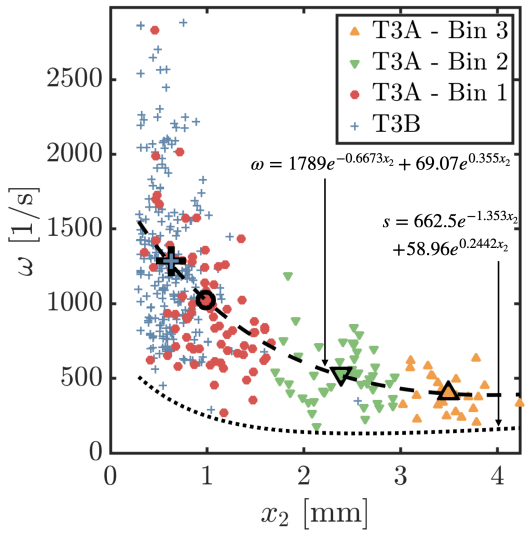

Figure 5.35: ω distribution of each T3 vortex.

A general trend of ω increasing as the T3 vortex approaches the wall is apparent in Figure 5.35. The increase is initially gradual between T3A Bin 3 and T3A Bin 2 as visible by the change in average values. The mean ω of the T3 vortex cores then increases substantially from T3A Bin 2 to T3A Bin 1 where the vortex interacts with the flame. A slight further increase in ω is present as the vortex is in its T3B travel state although the T3B state is following quenching. The trend evidenced by the vortex core statistics is in agreement with the conditioned sequence in Figure 5.34, where there is a minor change in ω^* between those T3A Bin 3, 2, followed by a considerable increase to T3A Bin 1.

The trendline from the fluctuating strain s shown previously in Figure 5.25 is overlaid in Figure 5.35. Comparison of the variation in ω with that of the fluctuating strain s is important to discern the relative importance of these two kinematic properties of the vortex during the quenching process. Across the entire wall-normal x_2 distance, the trend and distribution of ω values is significantly higher than the trend of fluctuating strain s. While the trend in s increases slightly after T3A Bin 2, the evolution in ω is still higher at these bins where the vortex is further from the wall. Even when s increases slightly between T3A Bin 2 to T3A Bin 1, the trend in ω features a sharper increase resulting in the difference between ω and s of the vortex cores being particularly significant in Bin 1 which is associated to quenching.

It can therefore be concluded that effects of the fluctuating vorticity of the T3 vortex are predominant over local strain effects induced due to the vortical flow field. This is indicative that the T3 vortex is therefore more likely influence the flame through wrinkling and pushing, rather than effects of stretch due to the vortex. It is important to consider that ω is calculated from the fluctuating velocity field $\mathbf{u}$ and therefore represents vorticity of the T3 vortex in a reference frame moving relative to the mean flow. This is not the only possible reference frame to view the vortex, therefore there may be potential for trends in ω to vary if a different decomposition method (e.g. frequency filtering) is used to extract the T3 vortex flow field. Thus, confirmation of the strength of the vortex is needed through assessment of the galilean invariant swirling strength of the vortices.

5.4.2.2 T3 vortex swirling strength (Λ_{ci})

As described in Chapter 2, Λ_{ci} is independent of the reference frame and unlike the instantaneous vorticity Ω, is advantageous in decoupling shearing and rotating motions, resulting in this criterion having been extensively used in turbulent boundary layer studies (Adrian, Meinhart, & Tomkins, 2000; Christensen & Adrian, 2001; Natrajan et al., 2007; Y. Wu & Christensen, 2006; Zhou et al., 1999). Analysis of Λ_{ci} will provide a robust characterisation of the vortex strength, without the influence of shearing effects which can contribute to vorticity calculations due to the wall. Indeed, it was the Q criterion, which is of the same family of vortex detection methods as Λ_{ci} (P. Chakraborty et al., 2005) as described in Chapter 2, that was used to identify vortical structures pushing the flame in the DNS study of (Gruber et al., 2010). The evolution of Λ_{ci} during quenching is first investigated using the averaged spatiotemporal representation in the conditioned Λ^*_{ci} sequence shown in Figure 5.36, before considering the statistics of Λ_{ci} contained within the T3 vortex cores. The swirling strength Λ_{ci} is calculated from the instantaneous velocity fields $\mathbf{U}$. In Figure 5.36 however, the conditioned fluctuating velocity field is overlaid for reference to relate Λ_{ci} to the vortical flow field in $\mathbf{u}^*$. Although Λ^*_{ci} can assume both

positive (CCW) and negative (CW) values, there is almost no negative swirl in Λ_{ci}^* so only the positive colour scale range is shown.

In Figure 5.36, T3A Bin 3 show a cloud-like, expansive region of elevated Λ_{ci}^* away from the flame which is in agreement with the Λ_{ci} features discussed previously in the transient sequence shown earlier in Figure 5.14. This broad region of Λ_{ci} has increased magnitude compared with the surrounding regions and the peak Λ_{ci} is directly centred on the T3A Bin 3 vortex centre as visible in the inlay. The Λ_{ci}^* region below the flame front in close proximity to the wall is relatively noisey. As described previously, a lower sample number near the wall in Bin 3 contributes to this effect. In the present analysis using Λ_{ci} this does become accentuated by the fact that, unlike for ω (or Ω), the calculation of Λ_{ci} involves the square of derivatives in equation 5.1 which has a slight noise enhancing effect.

In T3A Bin 2 as the vortex moves closer to both the flame and the wall, the cloud-like Λ_{ci} region is observed to concentrate around the T3A Bin 2 vortex centre, while the peak values around the vortex centre stay reasonably constant. At T3A Bin 1, representing the T3 vortex prior to and during flame quenching, a clearer and more coherent region of strong Λ_{ci} forms. Following quenching in T3A Bin 1, the strength of the vortex increases further with the large magnitude of Λ_{ci} from T3A Bin 1 growing around the vortex centre in T3B. Some regions of elevated Λ_{ci}^* near the wall and upstream in the unburnt gas region ($x_2^* < 0$) are also present in T3B but are of a significantly lower Λ_{ci} magnitude compared to the T3B vortex centre.

The trends described in the conditioned representation of Λ_{ci}^* are therefore in agreement with the fluctuating vorticity ω^*. As the T3 vortex grows in strength during its descent, it becomes more distinct in the localised fluctuating vorticity ω^* peak shown previously in T3A Bin 1 of Figure 5.34, but is difficult to distinguish earlier in T3A Bin 3 and Bin 2. In the representation of Λ_{ci}^* however, the peak value Λ_{ci}^* is spatially coincident with the T3 vortex centre across all stages (T3A Bins 3, 2, 1 and T3B) of the conditioned sequence which demonstrates the ability of the Λ_{ci} to isolate the intrinsic vortical motion and provide a robust characterisation of the strength attributes of the T3 vortex. The fact that the peak values of the Galilean invariant Λ_{ci}, which is calculated independently from instantaneous velocity $\mathbf{U}$, aligns with the vortex centres obtained using the Γ_1 criterion applied to the fluctuating velocity $\mathbf{u}$ also confirms the suitability of the Reynolds decomposition to reveal the T3 vortical flow field. Should that not have been the case, the peaks of Λ_{ci} fields would not be so closely aligned with the conditionally averaged vortex centres marked by the plus symbol in Figure 5.36.

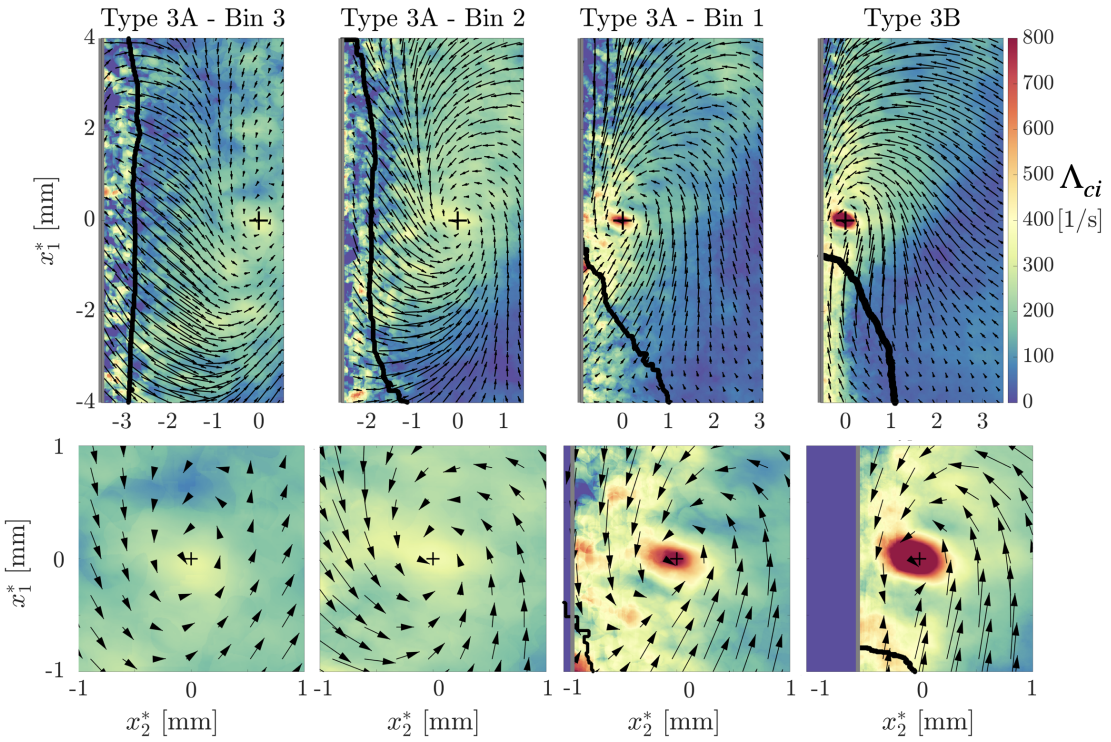

Figure 5.36: Conditioned swirling strength (Λ_{ci}).

The evolution of strength of all T3 vortex cores as a function of wall-normal distance x_2 is shown in Figure 5.37, similarly as for Figure 5.35. The average Λ_{ci} within each vortex core is calculated by averaging all non-zero Λ_{ci} values, therefore associated with swirl, within a 0.25mm radius from each T3 vortex centre. This is compared to the ensemble average swirling strength $\langle\Lambda_{ci}\rangle$ present in the flow field to characterise the relative strength of the T3 vortices compared to swirling motion in the overall flow statistics. $\langle\Lambda_{ci}\rangle$ is calculated by averaging in time and in the x_1 direction, to represent the average swirling strength as a function of wall-normal distance x_2. The $\langle\Lambda_{ci}\rangle$ distribution shown by the black line in 5.37 shows a generally flat distribution until $\leq$ 1mm from the wall where $\langle\Lambda_{ci}\rangle$ rises and peaks close to the wall, followed by a slight decrease.

A similar trend of increasing vortex strength shown previously in Figure 5.35 is apparent from Figure 5.37. The Λ_{ci} contained within the T3 vortex cores stays approximately constant between Bin 3 and Bin 2 which rises significantly from Bin 2 to Bin 1. A further slight increase is observed from T3A Bin 1 to T3B. In all cases, the Λ_{ci} within the T3 vortex cores is significantly higher than the average $\langle\Lambda_{ci}\rangle$ at all x_2 locations.

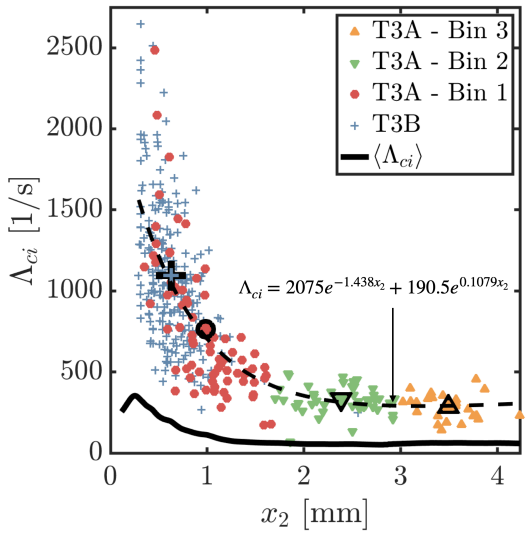

Figure 5.37: Mean Λ_{ci} for each T3 vortex.

Therefore, assessment of the T3 vortex strength from the vorticity of its flow field in $\mathbf{u}$, together with the galilean invariant swirling strength Λ_{ci} calculated from $\mathbf{U}$ corroborate the trend of the vortex increasing in strength during its evolution to impact the wall. This increase is highest between T3A Bin 2, representing the T3 vortex in the intermediate stage of its descent, and T3A Bin 1 representing the vortex during flame quenching instances. At all stages during the descent, the rotational motion of the vortex is a significantly stronger kinematic effect than the strain field induced by the vortex. This concludes that effects of the vortex due to wrinkling or pushing of the flame front are highly likely to be significant, compared to the contribution of strain from the T3 vortex which is comparatively minor compared to the existing shear from the wall. A correlation of the descending vortex position with the flame moving closer to the wall is next investigated.

5.4.3 Vortex pushing flame

Having established the kinematic potential of the vortex to influence the flame primarily by virtue of its rotational, rather than shearing effects, this section investigates the possible mechanism of the T3A vortex pushing the flame to the wall, leading to quenching due to both excessive heat loss and also forcing the flame deeper into the shear layer leading increased strains experienced from the wall. A correlation between the position of the T3A vortex with respect to the change in flame front position during quenching events is assessed in this section.

The methodology employed is depicted in Figure 5.38. A flame front in an HOQ topology is visible with a T3A vortex in mid-descent. In the T3 vortex trajectories shown previously in Figure 5.19b), the T3A vortices were shown to have a commonality in descent patterns with the T3A vortices approaching the wall in a diagonal or arc-like trajectory impacting the flame at the location nearest the wall. This flame location nearest to the wall is marked by the red circle in Figure 5.38. The region of the flame pushed by the descending vortex is defined as the flame coordinates beyond this minimum flame x_2 location, similarly to the definition of the flame region influenced by wall shear in the previous section and is marked in red in the Figure

5.38.

The x_2 coordinates of the flame front in the influence region are averaged to indicate the average flame front position D_F for every image involving a T3A vortex. Next, the distance D_V of the T3A vortex centre to the minimum flame x_2 location is calculated. As the vortex descends towards its eventual impact point, the action of pushing the influenced region of the flame front closer to the wall would be observable as a positive correlation of the two variables D_F and D_V.

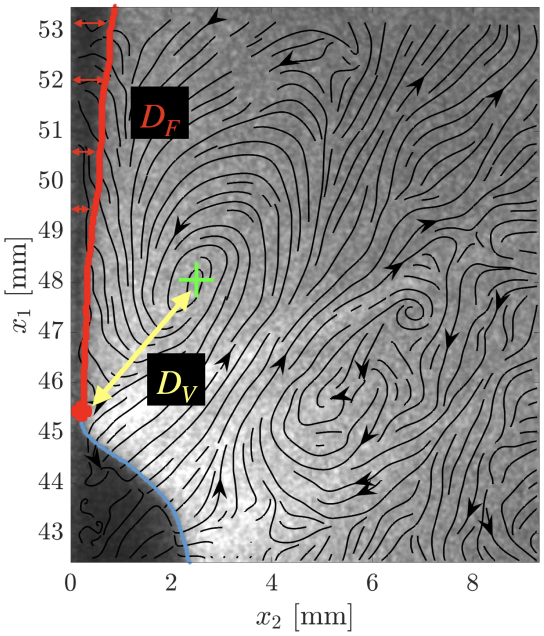

Figure 5.38: Schematic of the distance metrics used to assess the vortex pushing the flame.

The results are shown in Figure 5.39. The points associated with the T3A vortices are coloured according to their respective T3A bin. T3B vortices are excluded from this analysis since the flame is already quenched in those instances. A trendline using an exponential function $D_F = 0.3038e^{0.1449D_V}$ is fitted through all the points shown. In the methodology, described, any images where a vortex is present and there is no flame, i.e., the entire FOV features burnt gas, are excluded from the statistics. The final number of images included is 103 out of the 136 available T3A vortex images.

Figure 5.39 does reveal a correlation with the closer the vortex is to impacting the wall, the closer the influenced flame front region is to the wall. The trendline shown by the dashed line features a shallower gradient for vortices nearer to the impact location which suggests that the vortex proximity may be having slightly less influence on affecting the flame, potentially due to less distance being available for the flame to move closer to the wall.

An additional factor that can affect the flame response to the vortex is a potential time dependency. Indeed, time delays between hydrodynamic effects such as vortices and flame response have been reported in turbulent premixed flames (Mueller et al., 1996) which complicates accurate prediction of the flame front distance from the wall based on the vortex position. As mentioned previously, the T3A vortex features a

rapid descent before quenching the flame, usually lasting between 2 - 4 images (500μs - 1000μs). Thus, investigating the temporal dependency of the flame front with the existence of the vortex would benefit from increased temporal resolution of the velocity data to accurately investigate this effect. However, The R^2 of the fitted curve is a moderate value of R^2= 0.69 which is supportive of a relationship that the vortex is indeed pushing the flame.

The conclusion of the investigation in quenching phenomena can be summarised as follows. A shear layer due to the wall is present within the flow field. Following formation of the T3 vortex, it rapidly descends towards the wall and its angular velocity increases in the process. During its descent, the flame front is pushed closer to the wall under the influence of the vortex. As the flame moves closer to the wall, it experiences increasing shear from the wall which contributes to straining the flame. At the same time, the increasing proximity of the flame to the wall during this process results in increased heat flux. The relative importance of the flame strain compared to heat loss cannot be discerned in the current experiment. However, the combination of these two mechanisms is believed to be the causal mechanism of quenching based on the available data. The T3 vortex is highly influential in the quenching process by virtue of its rotational motion which pushes the flame, as opposed to the shear induced in vicinity of the vortex core which is largely insignificant compared to the strains experienced by the flame due to the strong shear layer present at the wall.

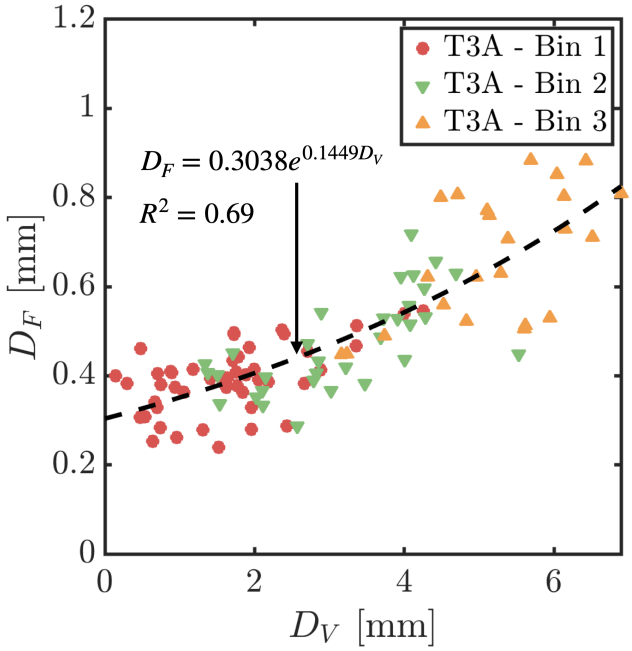

Figure 5.39: Comparison of vortex x_2 distance to D_F.

5.5 Transport phenomena

Following quenching, the T3 vortex travels downstream with the flame in vicinity of the flame quenching point. This section investigates the role of the T3 vortex in facilitating the gas transport mechanism hypothesised in (Zentgraf et al., 2021)

where burnt gases downstream of the quenching transport are transported back into the reactants, leading to unique thermochemical states of cold product gases mixed with the reactants that is not present under laminar conditions.

The transport properties of the T3 vortex are analysed using the quadrant analysis scheme of (Wallace et al., 1972) which partitions the fluctuating velocity field **u** into four possible quadrants depending on the sign of the respective u_1, u_2 velocity fluctuations. By assessing the quadrant distribution within the turbulent flow field, the characteristics of the dominant coherent motions facilitating mass transport can be assessed. Indeed, the original motivation and first application of quadrant analysis (according to (Wallace, 2016)) was by (Wallace et al., 1972) to quantify the observations in the landmark visualisation studies of (Brodkey et al., 1974)[2].

The quadrant splitting scheme is summarised in Table 5.3. The characteristic quadrant events in the non-reacting case of the SWQ experiment are first briefly described. An example quenching sequence in the reacting case is next presented, before considering the ensemble probabilities of the quadrant distribution during the conditioned quenching sequence. Finally, the local flow topology and angular distribution of the quadrant flows around each conditioned vortex centre is analysed.

Quadrant	**Name**	u_1	u_2
1	Outward interaction	+	+
2	Ejection	−	+
3	Inward interaction	−	−
4	Sweep	+	−

Table 5.3: Summary of the quadrant splitting scheme.

5.5.1 Quadrant distribution in non-reacting case

In a non-reacting wall-bounded turbulent flow, Q2 (ejection) and Q4 (sweep) motions manifest as strong organised events that dominate turbulence activity in the viscous sublayer and buffer layer. Canonical examples of these types of events are shown in Figures 5.40 and 5.41 where the Reynolds stress u_1u_2 is shown together with the fluctuating velocity field **u**. These examples are from wOF measurements of the SWQ experiment run under non-reacting conditions, similarly to Chapter 4 but with the FOV equivalent to the reacting case.

The turbulence activity of the region x_2 >8mm in the examples is due to vortex shedding from the flame holder in the experiment. It is important to note that the coherent motions in this region at the edge of imaged FOV are *not* boundary layer quadrant events in the canonical sense. The influence of this wake region is not present in the reacting case (Zentgraf et al., 2021, 2022).

These coherent flow motions are key in facilitating mass transport across the boundary layer. Q2 motions (ejection: $u_1 = -, u_2 = +$) transport slow moving flow away from the wall and against the mean flow. The influence of vortices is closely associated with modifying the spatial distribution of the quadrants as can be seen by the vortex inducing the strong Q2 event in Figure 5.40b). Q4 events (sweep:

[2]Some footage from the original visualisation study of (Corino & Brodkey, 1969) can be found: https://www.youtube.com/watch?v=_LSrtOaE8KM.

$u_1 = +, u_2 = -$) transport fluid from regions further out in the boundary layer down to the wall.

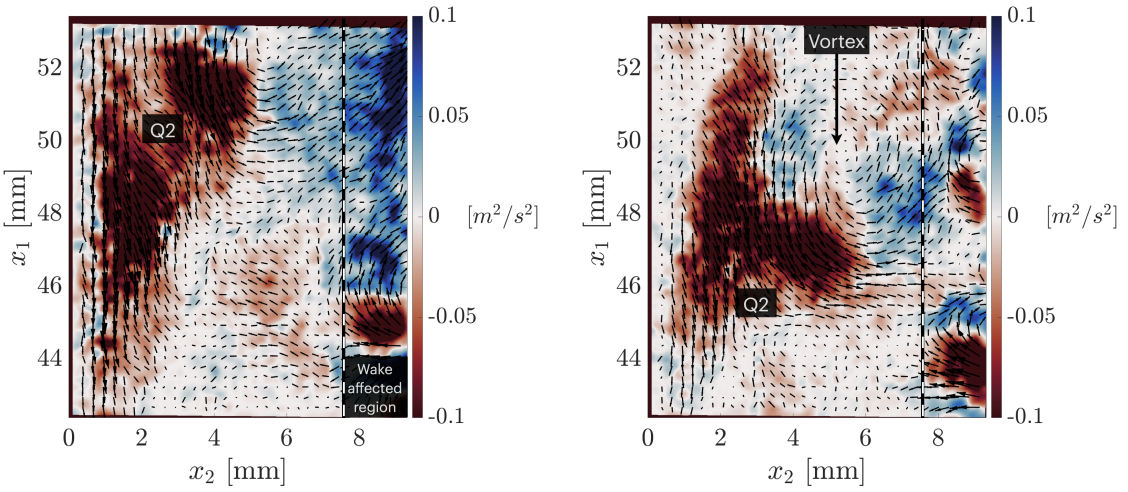

Figure 5.40: Examples of canonical Q2 (ejection) events in a non-reacting turbulent boundary layer.

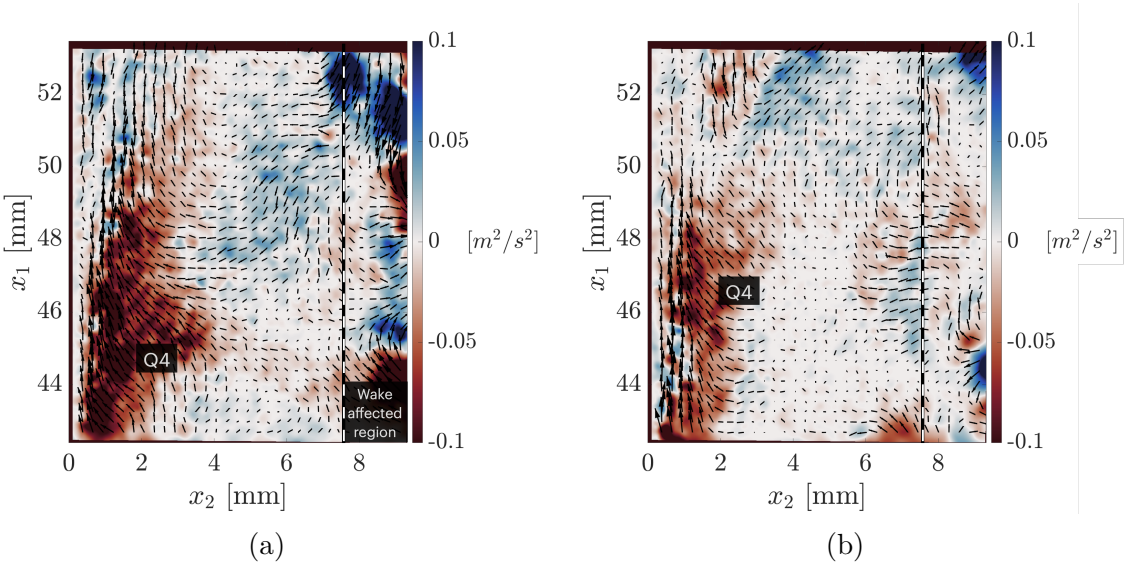

Figure 5.41: Examples of canonical Q4 (sweep) events in a non-reacting turbulent boundary layer.

The repeating presence of these characteristics events manifests in the statistical distribution of quadrants as shown in Figure 5.42. The x_2 axis is limited to exclude the wake region. The sum of the Reynolds stresses partitioned into the four quadrants produces the ensemble Reynolds stress $u_1 u_2$ shown by the black line.

The dominance of Q2 and Q4 events in the near wall region is evident in the wall-normal distribution shown in Figure 5.42, with strong peaks in the buffer layer. Q1 and Q3 events have a minimal influence in comparison. Characteristic, quasi-repeating structures of Q1 and Q3 also do not occur in a non-reacting boundary

layer, unlike Q2 and Q4, exampled in Figures 5.40 and 5.41 which feature prominent and identifiable flow patterns. The result shown in Figure 5.42 represents the classical distribution that is well-known for non-reacting turbulent boundary layers (Wallace, 2016).

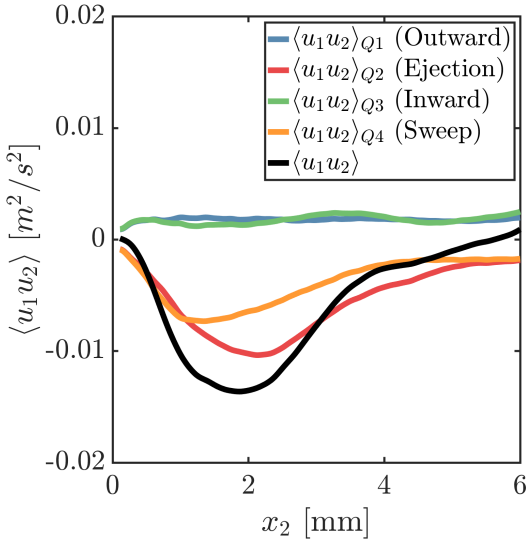

Figure 5.42: Quadrant distribution in a non-reacting turbulent boundary layer.

5.5.2 Quadrant analysis of reacting case

As discussed in the literature review in Chapter 1, the FWI studies of (T. Alshaalan & Rutland, 2002) and (Jainski et al., 2018) demonstrated that the reacting turbulent boundary layer case features both an increased probability of Q1/Q3 events in the vicinity of the flame front and these events are stronger are stronger than Q2/Q4. An example of the quadrant distribution in the reacting case is shown in Figure 5.43b) with the downstream location of the sampled profile indicated by the white dashed line shown on the flame probability map in Figure 5.43a). Compared to the canonical non-reacting case in Figure 5.42, the strength of Q1/Q3 events is significantly increased in the presence of the flame front, which also suppresses Q2/Q4 events in its local vicinity in agreement with previous studies (T. Alshaalan & Rutland, 2002; Jainski et al., 2018). The magnitude of the Q1/Q3 events is substantially higher than any quadrant events present in the non-reacting case. These important differences are suggestive of a considerably different set of coherent flow events and transport processes present.

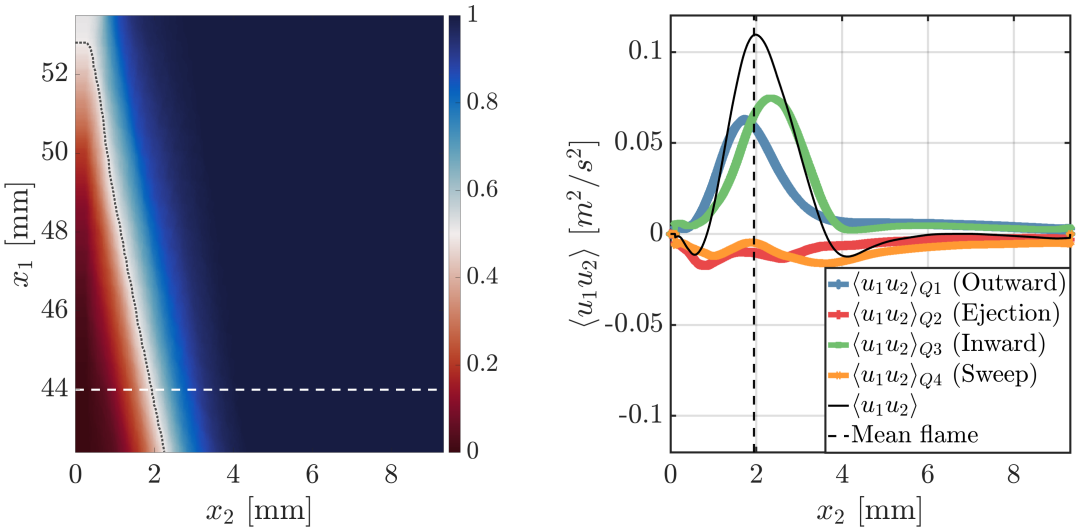

Figure 5.43: a) Flame probability map with location of quadrant profile (white line) and b) quadrant distribution in a reacting turbulent boundary layer.

The actual phenomenological processes in the turbulent flow field that produce the increased Q1/Q3 are unknown however. Vortices in the fluctuating velocity field **u** are intrinsically linked to quadrant events due to their ability to modify the surrounding quadrant distribution as part of the vortical flow field. Therefore, T3 vortices are expected to be key in facilitating the transport processes postulated in the mechanism of (Zentgraf et al., 2021) through their influence on quadrant events. The effect of the T3 vortex modifying the quadrant distribution is first exampled on a quenching event sequence, before considering the quadrant evolution in the conditioned sequences and the local transport properties of the T3 vortical flow fields.

5.5.2.1 Individual realisation

The quadrant distribution during a quenching event is shown in Figure 5.44. The fluctuating velocity field **u** is overlaid on the LIF image sequence and is respectively coloured depending on the quadrant associated to each vector. The T3A vortex centre is marked by the plus symbol.

The flame is in an HOQ configuration at $t = 0\mu$s with the dominant quadrant being a Q2 (ejection) flow emanating outwards from the flame front and a Q1 (outward) in the upstream region of the FOV. A minor presence of Q4 (sweep) is visible in the downstream region in the unburnt gases. Between $t = 250 - 500\mu$s, a Q3 (inward) grows in the region downstream of the vortex and begins to occupy the area of the Q2 (ejection). As the T3 vortex descends towards the wall and quenches the flame between $t = 750 - 1250\mu s$, the area occupied by the near-wall Q2 region is completely removed and instead replaced by a strong growth of Q3 flow. This Q3 inward flow occupies a large portion of the region above and downstream of the T3 vortex.

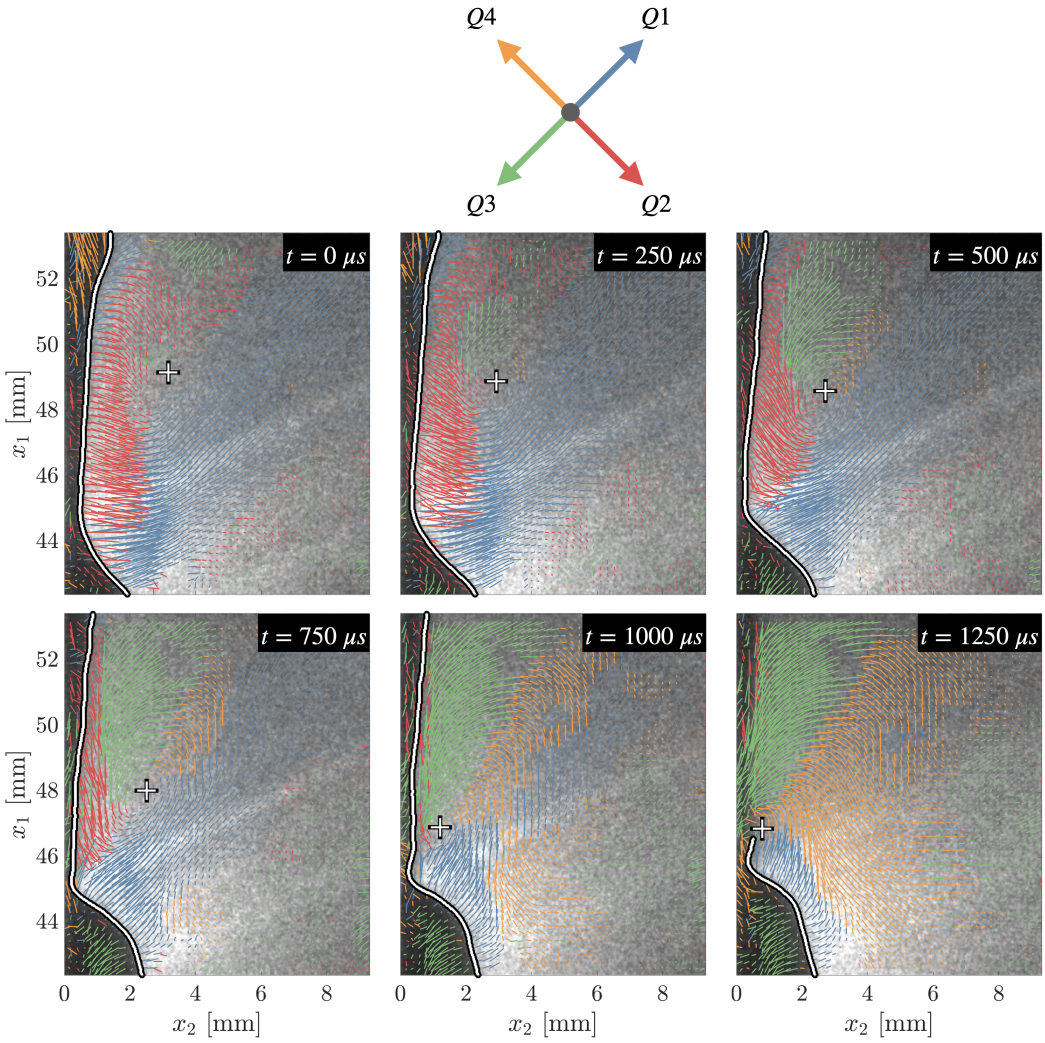

Figure 5.44: Distribution of quadrants during an example flame quenching sequence.

Following flame quenching, 3 subsequent time instances (every second image, 500μs between images) when the vortex is in a travel state are shown in 5.44 after $t = 1250$. The flow features a similar distribution to $t = 1250\mu$s and the inward flow continues to be prominent above the vortex and near the passage between the wall and flame tip. A large Q4 (sweep) is present above the vortex and evolves into the Q3 (inward) event as part of the vortex circulation. This inward event strongly emulates the mechanism hypothesised in (Zentgraf et al., 2021) where burnt gases are transported through the quenching passage between the flame and the wall into the reactants.

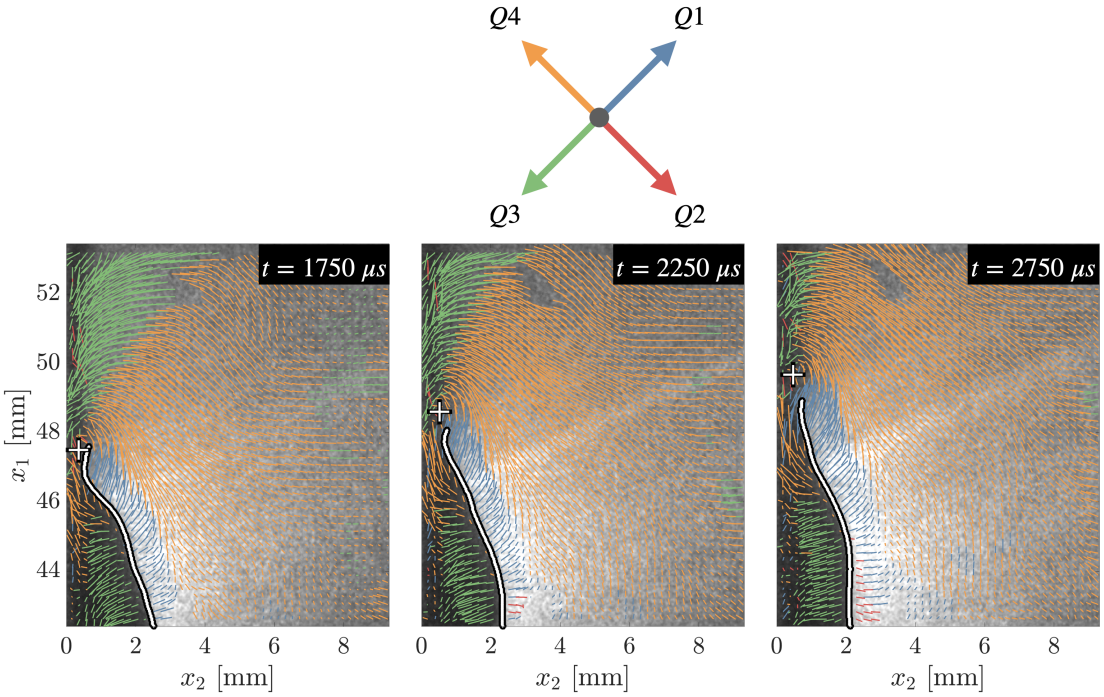

Figure 5.45: Distribution of quadrants following quenching, during T3B vortex travel.

5.5.2.2 Conditioned quadrant probability

The previous section exampled the significance of the T3 vortex in modifying the spatial distribution of quadrants for a single quenching event. The vortex was shown to modify the directional distribution of **u** during its descent, bringing the a strong inward interaction from the burnt gas region to the wall and flame tip, which is then sustained as the vortex is in its travel state. A similar progression of the quadrant spatial distribution due to the T3 vortex is observable in all quenching events within the dataset.

The commonality between the quadrant evolution from separate quenching events will be analysed statistically using the probability map of the quadrant distribution in the vortex-centred conditioned results sequence. This will assess the similarity in the quadrant flows between all individual quenching sequences, thus revealing the dominant flow motions facilitating transport processes within the quenching process. The probability distribution will also establish the consistency of the prominent flow patterns relative to the T3 vortex evolution. Of particular significance to transport phenomena are events corresponding to a negative u_1 component such as Q2 or Q3 (ejection or inward) events since these indicate fluid regions moving slower than the mean flow ($u_1 < 0$) and therefore are supportive of the entrainment of burnt gases downstream of the vortex into the unburnt gases downstream of flame quenching point.

The probability maps are calculated by segmenting each **u** velocity field matrix into separate binary regions associated with each of the four possible quadrants, where a value of 1 indicates the presence of a given quadrant flow and 0 otherwise. Applying the vortex-centred conditioning procedure described previously in this chapter to the binarised quadrant indicator fields then produces the probability

distribution of a given quadrant event during the conditioned sequence. The probability evolution during the conditioned vortex descent from T3A Bin 3 - 1 followed by vortex travel in T3B for each quadrant is shown in Figure 5.46. The conditioned fluctuating velocity field $\mathbf{u}^*$ is overlaid on each. The colour scale indicates the quadrant event probability, ranging from from 0, indicating that the fluctuating velocity field is never in this quadrant at the conditioned location, to a maximum value of 1 indicating that the quadrant event is always present.

The conditioned probability of Q1 (outward interaction) is shown in the first row of Figure 5.46. The Q1 probability is particularly strong in the initial phases of the slam (T3A bin 3) with a broad spatial extent that expands beyond the analysable FOV away from the wall. As the vortex descends from Bin 3 to Bin 1, the probability of the Q1 event and its spatial extent are seen to decrease, reaching the smallest extent and probability when the vortex is in its travel state in T3B and the elevated probability of Q1 is more distributed along the mean flame front, upstream of the vortex centre. The strong probability Q1 in the vicinity of mean flame front, particularly after T3A Bin 3, is in agreement with trends reported in (T. Alshaalan & Rutland, 2002) where increased Q1 is observed in the vicinity of the flame front.

The Q2 (ejection) probability is shown in the second row of Figure 5.46. When the vortex is far from the wall, a near certain likelihood (> 0.9) exists of a very large ejection ejection region between the vortex and the wall. This region decreases in size and probability as the vortex is generally closer to the wall in Bin 2, although remains significant. In Bin 1, which represents vortices prior to and during quenching, the ejection probability has decayed rapidly. This is due to the vortex proximity to the wall, which limits the available fluid region for a strong Q2 flow. Between Bin 1 and T3B, this region shrinks slightly as the vortex transitions to its final state which is closer to the wall. As the vortex travels in T3B, the presence of the wall, together with the Q1 region emanating from the flame front limits the size of the ejection however it is present with a non-negligible probability as part of the vortex circulation.

The Q3 (inward) flow probability is shown in the third row of Figure 5.46. The Q3 event is initially relatively mild in T3A Bin 3, with a moderate regional extent continuing downstream of the vortex ($x_2^* > 0$). The probability of this region downstream of the vortex increases considerably in Bin 2 as the vortex is in the intermediate stages of its descent and the spatial extent of the Q3 region broadens, as visible by the expansion of the red high probability region. In Bin 1, the probability remains moderately high during Bin 1. Therefore, at instances during the quenching process itself where the flame front is being quenched, a moderate Q3 probability is indeed present and therefore suggestive that an entrainment of the burnt gases may already start occurring even prior the vortex has completed its descent. The probability remains moderate as the vortex is travelling with the quenched flame. The spatial extent of the Q3 region remains reaches beyond the vortex centre at $x_2^* = 0$ into the burnt gas and the probability increases mildly. From Bin 1 to T3B, it seems that part of Q3 region is also inhibited by the wall, similarly to the Q2 for T3B. The increased presence of Q3 in the vicinity of the flame front in T3A Bin 1 and T3B is supportive of a high likelihood of an inward flow that can support entrainment of burnt gases that are initially downstream of the vortex ($x_1^* > 0$), towards and past the vortex core itself at $x_1^* = 0$ leading to an accumulation and mixing of burnt gas upstream of the vortex in the unburnt gases. The strong probabilites revealed in the

conditioned sequence is suggestive of this effect being significant for all T3 vortices.

The Q4 (sweep) event probability is shown in the final row of Figure 5.46. The Q4 region starts of particularly small, of comparable size to the Q2 probability in Bin 1. A considerable growth in probability is observable as the vortex is in Bin 2. In Bin 1, the probability remains similar and the spatial extent of the Q4 region is seen to extent in a triangle-like pattern on the right of he vortex. This large spatial extent indicates that a large region of the vortex is likely to be occupied by Q4 vectors. When the vortex is travelling in T3B, the large sweep region increases in probability, indicating a near certainty of sweep above the vortex when it is travelling. Considering the counter clockwise flow motion around the vortex core in T3B, the sweep region is the quadrant prior to the flow field changing angle significantly enough for u_1 to switch from $u_1 = +$ to $u_1 = -$ and therefore is part of the circulation flow pattern that supplies the Q3 event with burnt gases.

The combination of Q3 and Q2 strongly supports the potential transport mechanism leading to the unique thermochemical states postulated by (Zentgraf et al., 2022) and supported by DNS results of (Steinhausen et al., 2023). Without the inward (Q3) component, it would not be possible to entrain burnt gas upstream relative to the mean flow to mix with the reactants. A detailed analysis of the local vortical flow field around each vortex centre is performed in the following section to assess whether the local vortical flow field topology can facilitate transport.

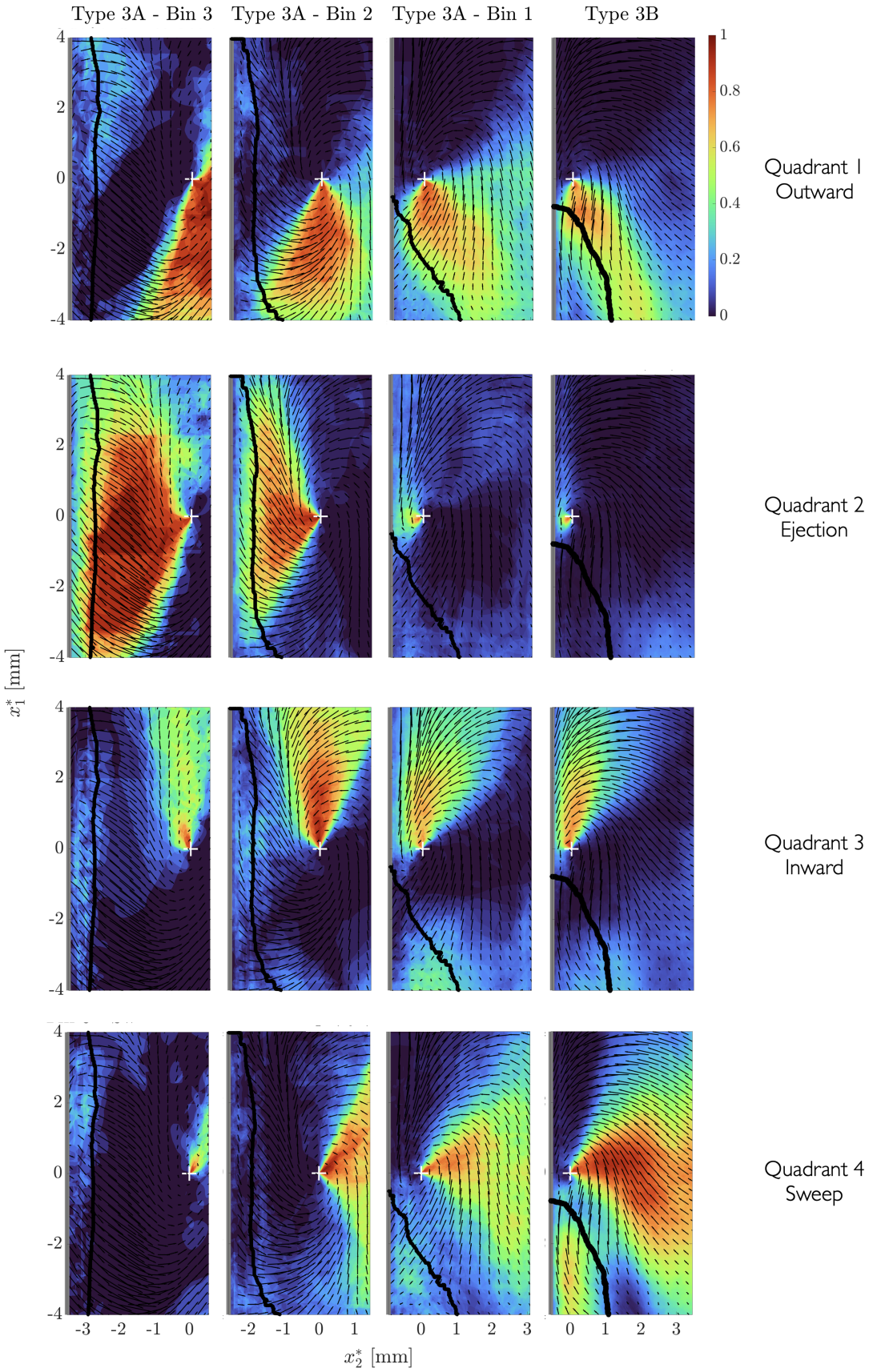

Figure 5.46: Quadrant probabilities during the conditioned vortex sequence.

5.5.3 Vortex transport mechanism

The evolution of the probability distribution provides valuable information into the dominant flow features and their spatial extents. To more accurately characterise whether the flow topology associated to the T3 vortex is indeed responsible of the transport of burnt gases into the unburnt region, a further characterisation of the local velocity surrounding each vortex is performed.

The conditioned fluctuating velocity field is studied as a function of angle around each vortex centre. A 1mm radius circular sampling region is used and vectors are spatially averaged within 30° segments to give an indication of the average strength of the velocity vectors as a function of the azimuthal position around the vortex centre at $(x_1^*, x_2^*) = (0, 0)$. A schematic of this sampling scheme is shown in Figure 5.47. The colour coding in Figure 5.47 represents the angular segment starting with 0° and proceeding counterclockwise from the x_2^* axis.

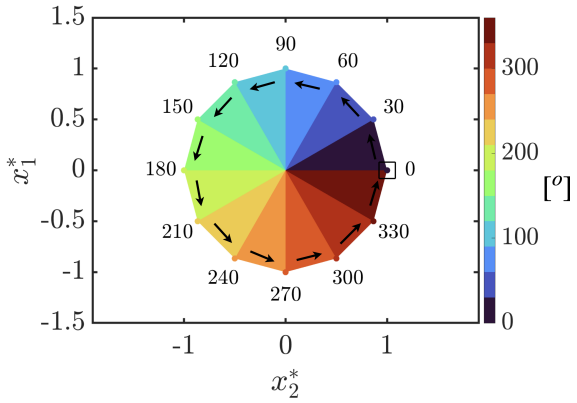

Figure 5.47: Schematic of the vector circular sampling scheme for a generic vortex. The discrete colour labels each angular segment that vectors are averaged in. The sampling region is centred around each conditioned vortex centre at $(x_1^*, x_2^*) = (0, 0)$

.

The results of the circular sampling scheme is shown in Figure 5.48. The left column shows the fluctuating velocity magnitude $|\mathbf{u}^*|$ from T3A Bin 3 to T3B. The extent of the sampling region is indicated and the discrete angle segments are coloured as per Figure 5.47. Any sampling regions that extend below the most probable wall position (T3A Bin 1 and T3B) in the conditioned vortex are excluded. The right column shows the associated results of the vector sampling scheme. The points are plotted in the u_1, u_2 quadrant plane to associate each angular segment with a respective quadrant and thus characterise the local vortex vector field topology in terms of its quadrant distribution (which establishes the transport properties). The starting angle segment (0 - 30°) in the CCW direction is marked with a square in the right column. The colour of each marker point corresponds to the coloured angle segment around the 1mm region.

A variety of information is available from the representation in Figure 5.48. For a given marker point, its colour represents its azimuthal position with respect to the conditioned vortex centre $(x_1^*, x_2^*) = (0, 0)$. The radial extent of the point from the origin at $(u_1, u_2) = (0, 0)$ denotes the magnitude of the velocity for the given angular segment. The respective quadrant a point is located in indicates the sign of the fluctuating component and thus the directionality of the flow in that local

region.

The first main trend apparent in Figure 5.48 is that the area bounded by the polygon progressively grows through the conditioned vortex sequence, particularly from T3A Bin 3 to Bin 1 prior to the vortex assuming its travel state in T3B. The perimeter of the polygon bounded by the marker points extends further outward from the axes origin at $(u_2, u_1) = (0, 0)$. This increased perimeter extent indicates the overall fluctuating velocity magnitude contained within the 1mm diameter sampling region is increasing. This effect is visible in fluctuating velocity magnitude in the left column of Figure 5.48, where vectors in the local vicinity of the vortex core grow/increase. This further supports that the vortex is indeed getting stronger, which is in agreement with the trends in metrics of vortex strength discussed previously.

Figure 5.48 reveals that the occupancy of each quadrant changes throughout the conditioned vortex sequence. Beginning at T3A Bin 3, the majority of points are associated to the Q1 (outward) and Q2 (ejection), with little to no Q3 (inward) or Q4 (sweep). These dominant Q1 and Q2 regions are visible in the slightly elevated magnitudes going CCW around the T3A Bin 3 vortex magnitude plot from 120 - 210^0 for Q2 and 270^0 - 30^0 for Q1. The bounded polygon of T3A is an approximately elliptical shape that is oriented vertically. The vertical orientation indicates the directional distribution of vortex flow, as indicated in the quadrant distribution, varies faster around 0^0 and 180^0, compared to the perpendicular directions at 90^0 and 270^0

At T3A Bin 2, the vortex in the intermediate stage of its descent. A more circular flow topology is visible in $\mathbf{u}^*$. This is reflected in the T3A Bin 2 scatter plot where the distribution of points has changed from T3A Bin 1 to a more even distribution where a similar number (3-4) of points occupy each quadrant. The quadrant featuring the strongest velocity is still the Q2 (ejection) that is at 180^o to the vortex. This strong ejection is the signature of the large ejection between the vortex and wall discussed in Figure 5.46 previously. A significant growth of Q4 (sweep) and Q3 (inward) compared to T3A Bin 3 is visible. The change in quadrant distribution indicates the vortex flow topology is evolving, which is also visible by the fact that more circular, rather than elliptical, vortical flow field is visible in the magnitude image

At T3A Bin 1, the quadrant distribution has evolved further. Firstly, the ejection has been largely suppressed due to the presence of the wall. The angular extent of the Q2 (ejection) flow, represented by the number of points in the Q2 region, has been distributed to the Q1 (outward) and Q3 (inward) flow. The Q4 (sweep) remains of comparable magnitude to the previous T3A Bin 2. The dominant flow patterns are now the Q1 and Q3 flow, as evidenced by the extents of the major axis of the bounded polygon being in the Q1 and Q3 quadrants, therefore indicating the magnitude of the vortical flow is strongest when it occupies these quadrants. Q1 dominates the flow on the side of the vortex away from the wall between angles 240-360^o. Q3 on the otherhand, dominates a similar angular extent from 60 and 180^o which is the key region oriented downstream and toward the wall. At the same time, the magnitude of the flow in these quadrants has increased in comparison to T3A - Bin 2. Therefore, more of the vortical flow in the T3 vortex is now associated to inward flow that can transport burnt gas into the vicinity of the quenching point.

The distribution of the flow topology in T3B is similar to that T3A Bin 1, with

the primary difference visible as a slight offset of the bounded polygon toward Q4. A minor decrease in the maximum Q3 velocity results, likely due to the wall similarly inhibiting the available region for Q3, similarly to Q2. The majority of the points are associated to Q3, which indicates that the majority of the flow within 1mm across 60 to 210^o degrees of the vortex is indeed associated entraining fluid that is downstream of the vortex into the vortex and vicinity of the flame quenching point. A strong Q1 and Q4 flow is present across 240- 360^o degrees which is part of the circulation of the burnt gases. Going CCW around the vortex, the Q4 flow rapidly transitions into the Q3 which is of comparable strength. The ejection is minimal in the T3B vortex, which may suggest a progressive accumulation of the burnt gas following transport by the Q3 flow.

The angular extent of the Q3 region strongly indicates the potential for the T3B vortex to entrain burnt gases. While the extent of the Q3 flow alone might not suffice, coupling it with the considerable Q3 velocity magnitude reinforces the likelihood of the T3B vortex' capacity to entrain burnt gases.

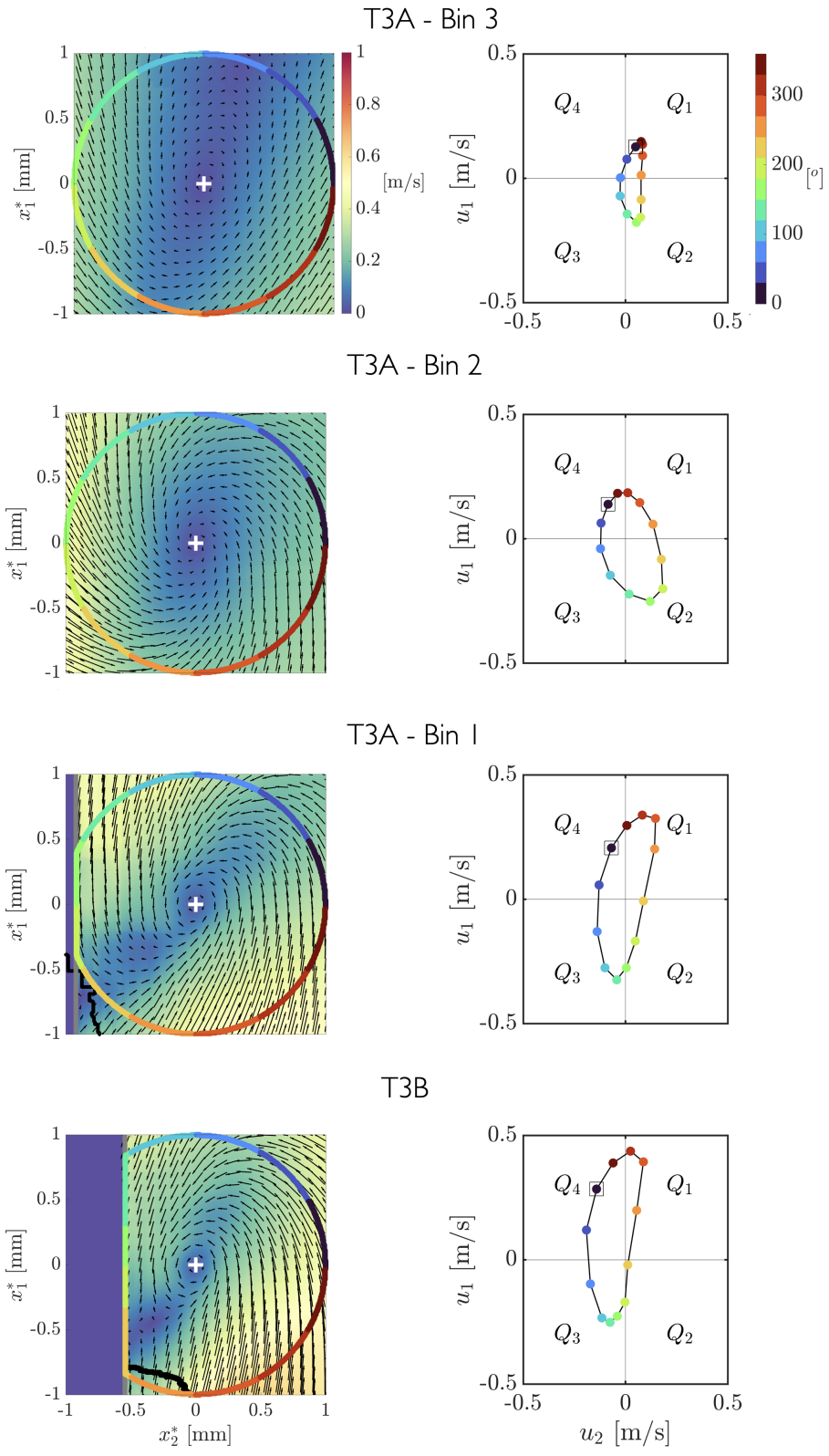

Figure 5.48: Angular distribution of quadrants around a 1mm circular region around each conditioned vortex.

5.6 Conclusions

wOF was applied to experimental PIV data of a reacting turbulent boundary layer in a SWQ burner setup to investigate hydrodynamic effects in flame quenching and vortex transport phenomena in flame wall interaction (FWI) previously hypothesised by (Zentgraf et al., 2021). The Reynolds decomposition was used to analyse the flow dynamics through a Lagrangian reference frame moving with the mean flow. The vortical flow fields revealed through this decomposition showed a strong correlation with flame behaviour. The main conclusions investigating can be summarised as follows:

- The Reynolds decomposition revealed 3 dominant vortex types with characteristic behaviours. The Type 1 vortex is CCW rotating vortex that pushes protrusions or hooks of the flame in the downstream direction. the Type 2 vortex is a CW rotating vortex, closely associated with the Type 1 vortex as a counter rotating vortex pair. A CCW rotating Type 3 (T3) vortex showed a direct involvement with flame quenching and transport phenomena. The T3 vortex, once formed, descends rapidly from the burnt gas to strike the flame front and the wall. Following flame quenching, the T3 vortex travels downstream in close proximity with the quenching point.

- Investigation into flame quenching phenomena revealed that the shear layer due to the no-slip condition of the wall plays a significant role in imparting the strain experienced by the flame. The strain contribution induced by the T3 vortex flow field is minor in comparison. The strain acting on the flame increases during the quenching process and is correlated with the flame front moving deeper into the shear layer where stronger strains are then experienced.

- While the strain field induced by the vortex was found to be mild when compared to the shear layer of the wall, the vorticity of the vortex was confirmed to increase during its descent. The strength of the vortex increasing is indicative of this effect to influence the flame topology.

- The T3 vortex was confirmed to have a pushing effect on the flame. In addition to the flame experiencing increased strains due to proximity to the wall, increased heat loss to the wall will contribute to quenching. The result of the T3 vortex pushing the flame to the wall is the first experimental validation of this phenomenon reported in the numerical studies of (T. Alshaalan & Rutland, 2002; Bruneaux et al., 1996; Gruber et al., 2010).

- The T3 vortex is intrinsic to the modification of the quadrant distribution of the fluctuating flow field. The T3 vortex brings a significant increase of inward (Q3) flow processes which entrain burnt gases products, against the mean flow past and through the quenching passage upstream into the reactants. This confirms the transport mechanism that was first hypothesised by (Zentgraf et al., 2021) and later supported by results in the DNS of (Steinhausen et al., 2023).

Chapter 6

Conclusion

This dissertation has implemented and assessed the performance of a wavelet-based optical flow (wOF) algorithm in extracting high fidelity velocity measurements from PIV images of wall-bounded turbulence with superior accuracy and resolution over state-of-the-art cross-correlation techniques. The research focused on two main themes: (1) validation and sensitivity analysis of the wOF algorithm on a non-reacting turbulent flow, (2) application to a reacting turbulent boundary layer to investigate quenching and transport phenomena in flame-wall interaction (FWI).

wOF was first evaluated using synthetic particle images generated from a channel flow DNS of a turbulent boundary layer. The sensitivity of wOF to the regularization parameter (λ) was quantified and results are compared to cross-correlation-based PIV. Results on synthetic particle images indicated different sensitivity to under-regularization or over-regularization depending on which region of the boundary layer is being analysed. Nonetheless, tests on synthetic data revealed that wOF can modestly outperform PIV in vector accuracy across a broad λ range. wOF showed clear advantages over PIV in resolving the viscous sublayer and obtaining highly accurate estimates of the wall shear stress and thus normalising boundary layer variables.

wOF was applied to experimental data of a developing turbulent boundary layer in side-wall quenching (SWQ) burner setup run under non-reacting conditions. Overall, wOF revealed good agreement with both PIV and a combined PIV + PTV method. wOF was able to successfully resolve the wall shear stress and correctly normalise the boundary layer streamwise velocity to wall units where PIV and PIV + PTV showed larger deviations. Analysis of the turbulent velocity fluctuations revealed spurious results for PIV in close proximity to the wall, leading to significantly exaggerated and non-physical turbulence intensity in the viscous sublayer region. PIV + PTV showed only a minor improvement in this aspect. wOF did not exhibit this same effect, revealing that it is more accurate in capturing small-scale turbulent motion in the vicinity of boundaries. The enhanced vector resolution of wOF enabled improved estimation of instantaneous derivative quantities and intricate flow structure both closer to the wall and more accurately than the other velocimetry methods. These aspects show that, within a reasonable λ range that can be verified using physical principles in non-reacting boundary layers, wOF can provide improvements in diagnostics capability in resolving turbulent motion occurring in the vicinity of physical boundaries.

Following validation of the wOF algorithm on non-reacting wall-bounded tur-

bulence, wOF was next applied to the SWQ experiment operated under reacting conditions to study flow phenomena in FWI. A Reynolds decomposition was used to analyse the flow dynamics from a Lagrangian perspective in a frame of reference moving with the mean flow. This decomposition revealed three prominent types of vortices which showed strong correlation with the flame dynamics. Counter-clockwise rotating (CCW) Type 1 vortices were found to push protruding hook-shaped flame regions forward. Clockwise rotating (CW) Type 2 vortices were found downstream of the flame hooks and were frequently associated with a Type 1 vortex as a counter-rotating vortex pair. A CCW rotating Type 3 (T3) vortex was discovered to form in the burnt gas region, before rapidly descending and impacting the wall and quenching the flame in the process. The Type 3 vortex showed a strong correlation with flame quenching behaviour and was associated to each of the 35 quenching events detected. Following flame quenching, the T3 vortex travelled downstream with the quenched flame while remaining in close proximity of the flame quenching point.

A vortex-centred conditional analysis was used to achieve a spatiotemporal representation of the T3 vortex evolution during its impact (T3A phase) and subsequent travel (T3B phase). Hydrodynamic effects influencing flame quenching phenomena were investigated with the aid of the conditioned representation of flow quantities. The strain acting on the flame due to shear from the wall was found to increase during the quenching process. This was closely associated with the positional change of the flame fronts moving deeper into the shear layer and thus experiencing increased strains. The strain field induced from the T3 vortex during its descent was found to be minor in comparison, such the wall shear likely dominates effects of flame stretch that contribute to quenching.

Analysis of the vorticity revealed that the vortex increases its strength during its descent, making it highly likely to influence the flame dynamics. The increase in strength was confirmed using the swirling strength as galilean invariant measure of the vortex angular velocity. A correlation between the descending vortex position and the flame being pushed against the wall was discovered, confirming observations from the DNS studies of (T. Alshaalan & Rutland, 2002; Bruneaux et al., 1996; Gruber et al., 2010) for the first time. This action of pushing the flame against the wall leads to increased heat losses, and also results in increased strains acting on the flame due to stronger shear being experienced closer to the wall. Although the relative importance of these two factors cannot be decoupled with velocity measurements alone, the combined action of these effects is expected to be the causal mechanism of flame quenching in the present experiment.

To investigate transport phenomena, the local flow distribution of the T3 vortex during its descent and subsequent travel with the flame tip was investigated based on the quadrant distribution of the fluctuating velocity field. The T3 vortex was found to be key in modifying the flow quadrant present during quenching, diminishing a strong Q2 (ejection) event present at the wall while bringing a strong Q3 (inward) to the wall during the vortex descent. This Q3 flow is sustained during the vortex travel and features both a strong velocity magnitude and a wide angular extent around the vortex core. These two features are strongly supportive of the vortex ability to transport burnt gases through the flame quenching passage and mix with unburnt gases, leading to the unique thermochemical states of cold burnt gases mixed with reactants reported in (Zentgraf et al., 2021). The vortical flow field facilitating this

flame vortex interaction has been explicitly revealed and confirmed for the first time.

wOF measurements were found to be good in agreement with robust but lower resolution results from cross-correlation-based PIV. Compared to PIV, wOF measurements afforded an improved number of statistics due to the increased vector density and achieved a higher fidelity representation of the FWI phenomena investigated. To the best of the authors' knowledge, this is the first application of any optical flow method for velocity measurements in a scenario as challenging as a wall-bounded turbulent reacting flow. The author would also like to point out that this experiment was *not* specifically designed for wOF. Indeed, a higher seeding density and a lower maximum freestream particle displacement would actually have been preferable for wOF, and optical flow methods in general (T. Liu & Shen, 2008; B. E. Schmidt & Sutton, 2019). This result is important from a diagnostics perspective, as optical flow techniques are typically assumed to be unsuitable for more challenging experimental measurements. It is anticipated that the results of this thesis can motivate future use of optical flow methods as part of diagnostics within the fluid mechanics community.

Bibliography

Abramovich, F., Benjamini, Y., Donoho, D. L., & Johnstone, I. M. (2006). Adapting to unknown sparsity by controlling the false discovery rate.

Adrian, R. J., Christensen, K. T., & Liu, Z.-C. (2000). Analysis and interpretation of instantaneous turbulent velocity fields. *Experiments in fluids*, *29*(3), 275–290.

Adrian, R. J. (2007). Hairpin vortex organization in wall turbulence. *Physics of fluids*, *19*(4).

Adrian, R. J., Meinhart, C. D., & Tomkins, C. D. (2000). Vortex organization in the outer region of the turbulent boundary layer. *Journal of fluid Mechanics*, *422*, 1–54.

Adrian, R. J., & Westerweel, J. (2011). *Particle image velocimetry*. Cambridge university press.

Akima, H. (1974). *A Method of Bivariate Interpolation and Smooth Surface Fitting Based on Local Procedures* (tech. rep.).

Alshaalan, T., & Rutland, C. J. (2002). Wall heat flux in turbulent premixed reacting flow. *Combustion science and technology*, *174*(1), 135–165.

Alshaalan, T. M., & Rutland, C. J. (1998). Turbulence, scalar transport, and reaction rates in flame-wall interaction. *Symposium (International) on Combustion*, *27*(1), 793–799.

Amaratunga, K., & Williams, J. R. (1997). Wavelet-Galerkin solution of boundary value problems. *Archives of Computational Methods in Engineering*, *4*(3), 243–285. https://doi.org/10.1007/BF02913819

Arnal, D., & Michel, R. (2012). *Laminar-Turbulent Transition: IUTAM Symposium Toulouse/France September 11–15, 1989*. Springer Science & Business Media.

Aubert, G., Deriche, R., & Kornprobst, P. (1999). Computing optical flow via variational techniques. *SIAM Journal on Applied Mathematics*, *60*(1). https://doi.org/10.1137/S0036139998340170

Bakewell Jr, H. P., & Lumley, J. L. (1967). Viscous sublayer and adjacent wall region in turbulent pipe flow. *The Physics of Fluids*, *10*(9), 1880–1889.

Bakushinskii, A. B. (1984). Remarks on choosing a regularization parameter using the quasi-optimality and ratio criterion. *USSR Computational Mathematics and Mathematical Physics*, *24*(4), 181–182.

Bandyopadhyay, P. (1980). Large structure with a characteristic upstream interface in turbulent boundary layers. *Physics of Fluids*, *23*(11), 2326–2327.

Barenblatt, G. I., & Monin, A. S. (1979). Similarity laws for turbulent stratified shear flows. *Archive for Rational Mechanics and Analysis*, *70*(4), 307–317.

Baritaud, T., Poinsot, T., & Baum, M. (1996). *Direct numerical simulation for turbulent reacting flows*. Editions Technip.

Barron, J. L., Fleet, D. J., & Beauchemin, S. S. (1994). Performance of optical flow techniques. *International Journal of Computer Vision*, *12*(1). https://doi.org/10.1007/BF01420984

Bauer, F., & Kindermann, S. (2008). The quasi-optimality criterion for classical inverse problems. *Inverse Problems*, *24*(3), 35002.

Beauchemin, S. S., & Barron, J. L. (1995). The Computation of Optical Flow. *ACM Computing Surveys (CSUR)*, *27*(3). https://doi.org/10.1145/212094.212141

Berrut, J. P., & Trefethen, L. N. (2004). Barycentric Lagrange interpolation. *SIAM Review*, *46*(3). https://doi.org/10.1137/S0036144502417715

Beylkin, G. (1992). On the representation of operators in bases of compactly supported wavelets. *SIAM Journal on Numerical Analysis*, *29*(6). https://doi.org/10.1137/0729097

Bisset, D. K., Antonia, R. A., & Browne, L. W. B. (1990). Spatial organization of large structures in the turbulent far wake of a cylinder. *Journal of Fluid Mechanics*, *218*, 439–461.

Black, M. J., & Anandan, P. (1996). The robust estimation of multiple motions: Parametric and piecewise-smooth flow fields. *Computer Vision and Image Understanding*, *63*(1). https://doi.org/10.1006/cviu.1996.0006

Blackwelder, R. F., & Haritonidis, J. H. (1983). Scaling of the bursting frequency in turbulent boundary layers. *Journal of Fluid Mechanics*, *132*, 87–103.

Blackwelder, R. F., & Swearingen, J. D. (1990). The role of inflectional velocity profiles in wall bounded flows. *Near-Wall Turbulence*, 268–288.

Blasius, H. (1907). *Grenzschichten in Flüssigkeiten mit kleiner Reibung*. Druck von BG Teubner.

Böhm, B., Heeger, C., Boxx, I., Meier, W., & Dreizler, A. (2009). Time-resolved conditional flow field statistics in extinguishing turbulent opposed jet flames using simultaneous highspeed PIV/OH-PLIF. *Proceedings of the Combustion Institute*, *32*(2), 1647–1654.

Bradley, D., & Roth, G. (2007). Adaptive thresholding using the integral image. *Journal of graphics tools*, *12*(2), 13–21.

Brodkey, R. S., Wallace, J. M., & Eckelmann, H. (1974). Some properties of truncated turbulence signals in bounded shear flows. *Journal of Fluid Mechanics*, *63*(2), 209–224.

Brox, T., Bruhn, A., Papenberg, N., & Weickert, J. (2004). High Accuracy Optical Flow Estimation Based on a Theory for Warping BT - Computer Vision - ECCV 2004. In T. Pajdla & J. Matas (Eds.). Springer Berlin Heidelberg.

Bruhn, A., Weickert, J., & Schnörr, C. (2005). Lucas/Kanade Meets Horn/Schunck: Combining Local and Global Optic Flow Methods. *International Journal of Computer Vision*, *61*(3), 211–231. https://doi.org/10.1023/B:VISI.0000045324.43199.43

Bruneaux, G., Akselvoll, K., Poinsot, T., & Ferziger, J. H. (1996). Flame-wall interaction simulation in a turbulent channel flow. *Combustion and flame*, *107*(1-2), 27–44.

Bruneaux, G., Poinsot, T., & Ferziger, J. H. (1997). Premixed flame–wall interaction in a turbulent channel flow: budget for the flame surface density evolution equation and modelling. *Journal of Fluid Mechanics*, *349*, 191–219.

Buades, A., Coll, B., & Morel, J.-M. (2005). A non-local algorithm for image denoising. *2005 IEEE computer society conference on computer vision and pattern recognition (CVPR'05)*, *2*, 60–65.

Cai, S., Mémin, E., Dérian, P., & Xu, C. (2018). Motion estimation under location uncertainty for turbulent fluid flows. *Experiments in Fluids*, *59*(1). https://doi.org/10.1007/s00348-017-2458-z

Cai, S., Zhou, S., Xu, C., & Gao, Q. (2019). Dense motion estimation of particle images via a convolutional neural network. *Experiments in Fluids*, *60*, 1–16.

Cai, T. T. (2002). On block thresholding in wavelet regression: Adaptivity, block size, and threshold level. *Statistica Sinica*, 1241–1273.

Candel, S. M., & Poinsot, T. J. (1990). Flame stretch and the balance equation for the flame area. *Combustion Science and Technology*, *70*(1-3), 1–15.

Cantwell, B. J. (1981). Organized motion in turbulent flow. *Annual review of fluid mechanics*, *13*(1), 457–515.

Carlier, J., & Stanislas, M. (2005). Experimental study of eddy structures in a turbulent boundary layer using particle image velocimetry. *Journal of Fluid Mechanics*, *535*, 143–188.

Chakraborty, N., & Swaminathan, N. (2007). Influence of the Damköhler number on turbulence-scalar interaction in premixed flames. I. Physical insight. *Physics of Fluids*, *19*(4).

Chakraborty, P., Balachandar, S., & Adrian, R. J. (2005). On the relationships between local vortex identification schemes. *Journal of fluid mechanics*, *535*, 189–214.

Chen, L. F., Liao, H. Y. M., & Lin, J. C. (2002). Wavelet-based optical flow estimation. *IEEE Transactions on Circuits and Systems for Video Technology*, *12*(1). https://doi.org/10.1109/76.981841

Chen, Q., Zhong, Q., Qi, M., & Wang, X. (2015). Comparison of vortex identification criteria for planar velocity fields in wall turbulence. *Physics of Fluids*, *27*(8).

Chen, X., Zillé, P., Shao, L., & Corpetti, T. (2015). Optical flow for incompressible turbulence motion estimation. *Experiments in Fluids*. https://doi.org/10.1007/s00348-014-1874-6

Cheng, R. K., Bill Jr, R. G., & Robben, F. (1981). Experimental study of combustion in a turbulent boundary layer. *Symposium (International) on Combustion*, *18*(1), 1021–1029.

Christensen, K. T., & Adrian, R. J. (2001). Statistical evidence of hairpin vortex packets in wall turbulence. *Journal of Fluid Mechanics*, *431*, 433–443.

Clark, L. G., & Kook, S. (2018). Correlation of spatial and temporal filtering methods for turbulence quantification in spark-ignition direct-injection (SIDI) engine flows. *Flow, Turbulence and Combustion*, *101*, 161–189.

Cohen, A., Daubechies, I., & Feauveau, J.-C. (1992). Biorthogonal bases of compactly supported wavelets. *Communications on pure and applied mathematics*, *45*(5), 485–560.

Cohen, A., Daubechies, I., & Vial, P. (1993). Wavelets on the Interval and Fast Wavelet Transforms. *Applied and Computational Harmonic Analysis*, *1*(1), 54–81. https://doi.org/https://doi.org/10.1006/acha.1993.1005

Coles, D. (1956). The law of the wake in the turbulent boundary layer. *Journal of Fluid Mechanics*, *1*(2), 191–226.

Corino, E. R., & Brodkey, R. S. (1969). A visual investigation of the wall region in turbulent flow. *Journal of Fluid Mechanics*, *37*(1), 1–30.

Corpetti, T., Heitz, D., Arroyo, G., Mémin, E., & Santa-Cruz, A. (2006). Fluid experimental flow estimation based on an optical-flow scheme. *Experiments in Fluids*, *40*(1). https://doi.org/10.1007/s00348-005-0048-y

Corpetti, T., Mémin, É., & Pérez, P. (2002). Dense estimation of fluid flows. *IEEE Transactions on Pattern Analysis and Machine Intelligence*, *24*(3). https://doi.org/10.1109/34.990137

Correia, T., Gibson, A., Schweiger, M., & Hebden, J. (2009). Selection of regularization parameter for optical topography. *Journal of biomedical optics*, *14*(3), 34044.

Cucitore, R., Quadrio, M., & Baron, A. (1999). On the effectiveness and limitations of local criteria for the identification of a vortex. *European Journal of Mechanics-B/Fluids*, *18*(2), 261–282.

Daubechies, I. (1992). *Ten lectures on wavelets*. SIAM.

Dennis, D. J., & Nickels, T. B. (2011). Experimental measurement of large-scale three-dimensional structures in a turbulent boundary layer. Part 1. Vortex packets. *Journal of Fluid Mechanics*, *673*. https://doi.org/10.1017/S0022112010006324

Dérian, P., Héas, P., Herzet, C., & Mémin, E. (2013). Wavelets and optical flow motion estimation. *Numerical Mathematics*, *6*(1). https://doi.org/10.4208/nmtma.2013.mssvm07

Dérian, P. (2012, November). *Wavelets and Fluid Motion Estimation* [Doctoral dissertation].

Dérian, P., Mauzey, C. F., & Mayor, S. D. (2015). Wavelet-based optical flow for two-component wind field estimation from single aerosol lidar data. *Journal of Atmospheric and Oceanic Technology*, *32*(10), 1759–1778.

Deriaz, E., & Perrier, V. (2009). Direct Numerical Simulation of Turbulence Using Divergence-Free Wavelets. *Multiscale Modeling & Simulation*, *7*(3), 1101–1129. https://doi.org/10.1137/070701017

Ding, C.-P., Peterson, B., Schmidt, M., Dreizler, A., & Böhm, B. (2019). Flame/flow dynamics at the piston surface of an IC engine measured by high-speed PLIF and PTV. *Proceedings of the Combustion Institute*, *37*(4), 4973–4981.

Donoho, D. L., & Johnstone, I. M. (1995). Adapting to Unknown Smoothness via Wavelet Shrinkage. *Journal of the American Statistical Association*, *90*(432), 1200–1224. https://doi.org/10.1080/01621459.1995.10476626

Dormand, J. R., & Prince, P. J. (1980). A family of embedded Runge-Kutta formulae. *Journal of Computational and Applied Mathematics*, *6*(1), 19–26. https://doi.org/10.1016/0771-050X(80)90013-3

Drake, M. C., & Haworth, D. C. (2007). Advanced gasoline engine development using optical diagnostics and numerical modeling. *Proceedings of the Combustion Institute*, *31*(1), 99–124.

Dreizler, A., & Böhm, B. (2015). Advanced laser diagnostics for an improved understanding of premixed flame-wall interactions. *Proceedings of the Combustion Institute*, *35*(1), 37–64.

Efimov, D. V., de Goey, P., & van Oijen, J. A. (2020). QFM: quenching flamelet-generated manifold for modelling of flame–wall interactions. *Combustion Theory and Modelling*, *24*(1), 72–104.

Elsas, J. H., & Moriconi, L. (2017). Vortex identification from local properties of the vorticity field. *Physics of Fluids*, *29*(1).

Elsinga, G. E., Poelma, C., Schröder, A., Geisler, R., Scarano, F., & Westerweel, J. (2012). Tracking of vortices in a turbulent boundary layer (2012/03/06). *Journal of Fluid Mechanics*, *697*, 273–295. https://doi.org/DOI:10.1017/jfm.2012.60

Enkelmann, W., & Nagel, H. H. (1986). An Investigation of Smoothness Constraints for the Estimation of Displacement Vector Fields from Image Sequences. *IEEE Transactions on Pattern Analysis and Machine Intelligence*, *PAMI-8*(5). https://doi.org/10.1109/TPAMI.1986.4767833

Falco, R. E. (1977). Coherent motions in the outer region of turbulent boundary layers. *The Physics of Fluids*, *20*(10), S124–S132.

Farge, M., Kevlahan, N., Perrier, V., & Goirand, E. (1996). Wavelets and turbulence. *Proceedings of the IEEE*, *84*(4), 639–669. https://doi.org/10.1109/5.488705

Fitzpatrick, J. M., & Pederson, C. A. (1988). A method for calculating fluid flow in time dependant density images. *Electronic Imaging*, *1*, 347–352.

Gamba, M., Clemens, N. T., & Ezekoye, O. A. (2012). Volumetric PIV and 2D OH PLIF imaging in the far-field of a low Reynolds number nonpremixed jet flame. *Measurement Science and Technology*, *24*(2), 24003.

Ganapathisubramani, B., Longmire, E. K., & Marusic, I. (2003). Characteristics of vortex packets in turbulent boundary layers. *Journal of Fluid Mechanics*, *478*, 35–46.

Gao, Q., Ortiz-Duenas, C., & Longmire, E. K. (2011). Analysis of vortex populations in turbulent wall-bounded flows. *Journal of Fluid Mechanics*, *678*, 87–123.

George, W. K. (2006). Recent advancements toward the understanding of turbulent boundary layers. *AIAA journal*, *44*(11), 2435–2449.

George, W. K. (2007). Is there a universal log law for turbulent wall-bounded flows? *Philosophical Transactions of the Royal Society A: Mathematical, Physical and Engineering Sciences*, *365*(1852), 789–806.

George, W. K., & Castillo, L. (1997). Zero-Pressure-Gradient Turbulent Boundary Layer. *Applied Mechanics Reviews*, *50*(12), 689–729. https://doi.org/10.1115/1.3101858

Gevelber, T. S., Schmidt, B. E., Mustafa, M. A., Shekhtman, D., & Parziale, N. J. (2022). Determining velocity from tagging velocimetry images using optical flow. *Experiments in Fluids*, *63*(6), 104.

Golub, G. H., Heath, M., & Wahba, G. (1979). Generalized cross-validation as a method for choosing a good ridge parameter. *Technometrics*, *21*(2), 215–223.

Goudar, M. V., Breugem, W.-P., & Elsinga, G. E. (2016). Auto-generation in wall turbulence by the interaction of weak eddies. *Physics of Fluids*, *28*(3).

Graftieaux, L., Michard, M., & Grosjean, N. (2001). Combining PIV, POD and vortex identification algorithms for the study of unsteady turbulent swirling flows. *Measurement Science and technology*, *12*(9), 1422.

Graham, J., Kanov, K., Yang, X. I., Lee, M., Malaya, N., Lalescu, C. C., Burns, R., Eyink, G., Szalay, A., Moser, R. D., & Meneveau, C. (2016). A web services accessible database of turbulent channel flow and its use for testing a new integral wall model for LES. *Journal of Turbulence*, *17*(2). https://doi.org/10.1080/14685248.2015.1088656

Gruber, A., Sankaran, R., Hawkes, E. R., & Chen, J. H. (2010). Turbulent flame–wall interaction: a direct numerical simulation study. *Journal of Fluid Mechanics*, *658*, 5–32.

Haimes, R., & Kenwright, D. (1999). On the velocity gradient tensor and fluid feature extraction. *14th Computational Fluid Dynamics Conference*, 3288.

Hansen, P. C. (1992). Analysis of discrete ill-posed problems by means of the L-curve. *SIAM review*, *34*(4), 561–580.

Hansen, P. C. (1999). The L-curve and its use in the numerical treatment of inverse problems.

Hansen, P. C., & Jørgensen, J. H. (2011). Total variation and tomographic imaging from projections. *36th Conf. Dutch-Flemish Numer. Anal. Communities Woudschouten*.

Hasse, C., Bollig, M., Peters, N., & Dwyer, H. (2000). Quenching of laminar iso-octane flames at cold walls. *Combustion and flame*, *122*(1-2), 117–129.

Head, M. R., & Bandyopadhyay, P. (1981). New aspects of turbulent boundary-layer structure. *Journal of fluid mechanics*, *107*, 297–338.

Heas, P., Herzet, C., Memin, E., Heitz, D., & Mininni, P. D. (2013). Bayesian estimation of turbulent motion. *IEEE Transactions on Pattern Analysis and Machine Intelligence*, *35*(6). https://doi.org/10.1109/TPAMI.2012.232

Héas, P., Mémin, E., Heitz, D., & Mininni, P. D. (2012). Power laws and inverse motion modelling: Application to turbulence measurements from satellite images. *Tellus, Series A: Dynamic Meteorology and Oceanography*, *64*(1). https://doi.org/10.3402/tellusa.v64i0.10962

Heitz, D., Mémin, E., & Schnörr, C. (2010). Variational fluid flow measurements from image sequences: Synopsis and perspectives. *Experiments in Fluids*, *48*(3). https://doi.org/10.1007/s00348-009-0778-3

Herpin, S., Stanislas, M., & Soria, J. (2010). The organization of near-wall turbulence: a comparison between boundary layer SPIV data and channel flow DNS data. *Journal of Turbulence*, (11), N47.

Honkan, A., & Andreopoulos, Y. (1997). Vorticity, strain-rate and dissipation characteristics in the near-wall region of turbulent boundary layers. *Journal of Fluid Mechanics*, *350*, 29–96.

Horn, B. K., & Schunck, B. G. (1981). Determining optical flow. *Artificial Intelligence*, *17*(1-3). https://doi.org/10.1016/0004-3702(81)90024-2

Huang, Y., & Yang, V. (2004). Bifurcation of flame structure in a lean-premixed swirl-stabilized combustor: transition from stable to unstable flame. *Combustion and Flame*, *136*(3), 383–389. https://doi.org/https://doi.org/10.1016/j.combustflame.2003.10.006

Hunt, J. C. R., Wray, A. A., & Moin, P. (1988). Eddies, streams, and convergence zones in turbulent flows. *Studying turbulence using numerical simulation databases, 2. Proceedings of the 1988 summer program.*

J M Foucaut, J Carlier, & M Stanislas. (2004). PIV optimization for the study of turbulent flow using spectral analysis. *Measurement Science and Technology*, *15*(6), 1046. https://doi.org/10.1088/0957-0233/15/6/003

Jainski, C., Lu, L., Sick, V., & Dreizler, A. (2014). Laser imaging investigation of transient heat transfer processes in turbulent nitrogen jets impinging on a heated wall. *International Journal of Heat and Mass Transfer*, *74*, 101–112.

Jainski, C., Lu, L., Dreizler, A., & Sick, V. (2013). High-speed micro particle image velocimetry studies of boundary-layer flows in a direct-injection engine. *International Journal of Engine Research*, *14*(3), 247–259. https://doi.org/10.1177/1468087412455746

Jainski, C., Rißmann, M., Jakirlic, S., Böhm, B., & Dreizler, A. (2018). Quenching of Premixed Flames at Cold Walls: Effects on the Local Flow Field. *Flow, Turbulence and Combustion*, *100*(1). https://doi.org/10.1007/s10494-017-9836-8

Jeong, J., & Hussain, F. (1995). On the identification of a vortex. *Journal of fluid mechanics*, *285*, 69–94.

Jodai, Y., & Elsinga, G. E. (2016). Experimental observation of hairpin auto-generation events in a turbulent boundary layer. *Journal of Fluid Mechanics*, *795*, 611–633.

Kachanov, Y. S. (1994). Physical mechanisms of laminar-boundary-layer transition. *Annual review of fluid mechanics*, *26*(1), 411–482.

Kadri-Harouna, S., Dérian, P., Héas, P., & Mémin, E. (2013). Divergence-free wavelets and high order regularization. *International Journal of Computer Vision*, *103*(1). https://doi.org/10.1007/s11263-012-0595-7

Kähler, C. J., Astarita, T., Vlachos, P. P., Sakakibara, J., Hain, R., Discetti, S., La Foy, R., & Cierpka, C. (2016). Main results of the 4th International PIV Challenge. *Experiments in Fluids*, *57*(6). https://doi.org/10.1007/s00348-016-2173-1

Kähler, C. J., Scharnowski, S., & Cierpka, C. (2012a). On the resolution limit of digital particle image velocimetry. *Experiments in Fluids*, *52*(6). https://doi.org/10.1007/s00348-012-1280-x

Kähler, C. J., Scharnowski, S., & Cierpka, C. (2012b). On the uncertainty of digital PIV and PTV near walls. *Experiments in Fluids*, *52*(6). https://doi.org/10.1007/s00348-012-1307-3

Kalmoun, E. M. (2018). An investigation of smooth TV-like regularization in the context of the optical flow problem. *Journal of Imaging*, *4*(2). https://doi.org/10.3390/jimaging4020031

Kane, D., Bex, P., & Dakin, S. (2011). Quantifying "the aperture problem" for judgments of motion direction in natural scenes. *Journal of Vision*, *11*(3), 25.

Kapulla, R., Hoang, P., Szijarto, R., & Fokken, J. (2011). Parameter sensitivity of optical flow applied to PIV Images. *Proceedings of the Fachtagung "Lasermethoden in der Strömungsmesstechnik", Ilmenau, Germany*, 6–8.

Keane, R. D., Adrian, R. J., & Zhang, Y. (1995). Super-resolution particle imaging velocimetry. *Meas. Sci. Technol*, *6*, 754–768.

Khalid, M., Pénard, L., & Mémin, E. (2017). Application of optical flow for river velocimetry. *2017 IEEE International Geoscience and Remote Sensing Symposium (IGARSS)*, 6243–6246.

Klebanoff, P. (1955). *Characteristics of turbulence in boundary layer with zero pressure gradient* (tech. rep.).

Kline, S. J., Reynolds, W. C., Schraub, F. A., & Runstadler, P. W. (1967). The structure of turbulent boundary layers (2006/03/28). *Journal of Fluid Mechanics*, *30*(4), 741–773. https://doi.org/DOI:10.1017/S0022112067001740

Kline, S. J., & Robinson, S. K. (1990). Quasi-coherent structures in the turbulent boundary layer. I-Status report on a community-wide summary of the data. *Near-wall turbulence*, 200–217.

Kosaka, H., Zentgraf, F., Scholtissek, A., Bischoff, L., Häber, T., Suntz, R., Albert, B., Hasse, C., & Dreizler, A. (2018a). Wall heat fluxes and co formation/oxidation during laminar and turbulent side-wall quenching of methane and dme flames. *International Journal of Heat and Fluid Flow*, *70*, 181–192.

Kosaka, H., Zentgraf, F., Scholtissek, A., Bischoff, L., Häber, T., Suntz, R., Albert, B., Hasse, C., & Dreizler, A. (2018b). Wall heat fluxes and CO formation/oxidation during laminar and turbulent side-wall quenching of methane and DME flames. *International Journal of Heat and Fluid Flow*, *70*. https://doi.org/10.1016/j.ijheatfluidflow.2018.01.009

Kosaka, H., Zentgraf, F., Scholtissek, A., Hasse, C., & Dreizler, A. (2020). Effect of Flame-Wall Interaction on Local Heat Release of Methane and DME Combustion in a Side-Wall Quenching Geometry. *Flow, Turbulence and Combustion*, *104*(4). https://doi.org/10.1007/s10494-019-00090-4

Krawczyk-Stańdo, D., & Rudnicki, M. (2007). Regularization parameter selection in discrete ill-posed problems—The use of the U-curve. *International Journal of Applied Mathematics and Computer Science*, *17*(2), 157–164.

Kwon, S.-G. (n.d.). Superconvergence of Biorthogonal Wavelet Differentiation Rules.

L JONES, R. (1997). Catalytic combustion effects in internal combustion engines. *Combustion science and technology*, *129*(1-6), 185–195.

Li, Y., Perlman, E., Wan, M., Yang, Y., Meneveau, C., Burns, R., Chen, S., Szalay, A., & Eyink, G. (2008). A public turbulence database cluster and applications to study Lagrangian evolution of velocity increments in turbulence. *Journal of Turbulence*, *9*. https://doi.org/10.1080/14685240802376389

Liu, D. C., & Nocedal, J. (1989). On the limited memory BFGS method for large scale optimization. *Mathematical Programming*, *45*(1), 503–528. https://doi.org/10.1007/BF01589116

Liu, T., Merat, A., Makhmalbaf, M. H., Fajardo, C., & Merati, P. (2015). Comparison between optical flow and cross-correlation methods for extraction of velocity fields from particle images. *Experiments in Fluids*, *56*(8). https://doi.org/10.1007/s00348-015-2036-1

Liu, T., & Shen, L. (2008). Fluid flow and optical flow. *Journal of Fluid Mechanics*, *614*. https://doi.org/10.1017/S0022112008003273

Long, R. R., & Chen, T.-C. (1981). Experimental evidence for the existence of the 'mesolayer'in turbulent systems. *Journal of Fluid Mechanics*, *105*, 19–59.

Louch, D., & Bray, K. (2001). Vorticity in unsteady premixed flames: Vortex pair–premixed flame interactions under imposed body forces and various degrees of heat release and laminar flame thickness. *Combustion and flame*, *125*(4), 1279–1309.

Lu, J., Yang, H., Zhang, Q., & Yin, Z. (2021). An accurate optical flow estimation of PIV using fluid velocity decomposition. *Experiments in Fluids*, *62*(4). https://doi.org/10.1007/s00348-021-03176-w

Lucas, B. D., & Kanade, T. (1981). An iterative image registration technique with an application to stereo vision. *IJCAI'81: 7th international joint conference on Artificial intelligence*, *2*, 674–679.

Lugt, H. J. (1979). The dilemma of defining a vortex. In *Recent developments in theoretical and experimental fluid mechanics: Compressible and incompressible flows* (pp. 309–321). Springer.

Luo, M., & Liu, D. (2018). Pollutants emissions of CO and soot from flame-wall interactions in fundamental and practical energy conversion systems: a review. *ES Energy & Environment*, *3*(2), 4–24.

Mallat, S. (2009). *A Wavelet Tour of Signal Processing*. https://doi.org/10.1016/B978-0-12-374370-1.X0001-8

Mallat, S., & Zhong, S. (1992). Characterization of signals from multiscale edges. *IEEE Transactions on pattern analysis and machine intelligence*, *14*(7), 710–732.

McCane, B., Novins, K., Crannitch, D., & Galvin, B. (2001). On benchmarking optical flow. *Computer Vision and Image Understanding*, *84*(1). https://doi.org/10.1006/cviu.2001.0930

Meneveau, C., & Poinsot, T. (1991). Stretching and quenching of flamelets in premixed turbulent combustion. *Combustion and Flame*, *86*(4), 311–332.

Metcalfe, R. W., Hussain, A., Menon, S., & Hayakawa, M. (1987). Coherent structures in a turbulent mixing layer: a comparison between direct numerical simulations and experiments. *Turbulent Shear Flows 5: Selected Papers from the Fifth International Symposium on Turbulent Shear Flows, Cornell University, Ithaca, New York, USA, August 7–9, 1985*, 110–123.

Millikan, C. B., & Laboratory, G. A. (1938). *A Critical Discussion of Turbulent Flows in Channels and Circular Tubes*. Guggenheim Aeronautical Laboratory. https://books.google.co.uk/books?id=GkUTyAEACAAJ

Mueller, C. J., Driscoll, J. F., Reuss, D. L., & Drake, M. C. (1996). Effects of unsteady stretch on the strength of a freely-propagating flame wrinkled by a vortex. *Symposium (international) on Combustion*, *26*(1), 347–355.

Natrajan, V. K., Wu, Y., & Christensen, K. T. (2007). Spatial signatures of retrograde spanwise vortices in wall turbulence. *Journal of Fluid Mechanics*, *574*, 155–167.

Ng, T. T., Cheng, R. K., Robben, F., & Talbot, L. (1982). Combustion-turbulence interaction in the turbulent boundary layer over a hot surface. *Symposium (International) on Combustion*, *19*(1), 359–366.

Nielsen, O. M. (1998). Wavelets in scientific computing.

Örlü, R., Fransson, J. H. M., & Alfredsson, P. H. (2010). On near wall measurements of wall bounded flows—the necessity of an accurate determination of the wall position. *Progress in Aerospace Sciences*, *46*(8), 353–387.

Ouyang, Z., Yang, H., Huang, Y., Zhang, Q., & Yin, Z. (2021). A circulant-matrix-based hybrid optical flow method for PIV measurement with large displacement. *Experiments in Fluids*, *62*, 1–18.

Pan, K.-L., Qian, J., Law, C. K., & Shyy, W. (2002). The role of hydrodynamic instability in flame-vortex interaction. *Proceedings of the Combustion Institute*, *29*(2), 1695–1704.

Perry, A. E., & Chong, M. S. (1982). On the mechanism of wall turbulence. *Journal of Fluid Mechanics*, *119*, 173–217.

Perry, A. E., Henbest, S., & Chong, M. (1986). A theoretical and experimental study of wall turbulence. *Journal of Fluid Mechanics*, *165*, 163–199.

Poinsot, T., Veynante, D., & Candel, S. (1991). Quenching processes and premixed turbulent combustion diagrams. *Journal of Fluid mechanics*, *228*, 561–606.

Poinsot, T. J., Haworth, D. C., & Bruneaux, G. (1993). Direct simulation and modeling of flame-wall interaction for premixed turbulent combustion. *Combustion and Flame*, *95*(1-2), 118–132.

Poinsot, T. (1996). Using direct numerical simulations to understand premixed turbulent combustion. *Symposium (international) on combustion*, *26*(1), 219–232.

Poinsot, T., & Veynante, D. (2005). *Theoretical and numerical combustion*. RT Edwards, Inc.

Pope, S. B. (2000). *Turbulent flows*. Cambridge university press.

Prandtl, L. (1905). Uber Flussigkeitsbewegung bei sehr kleiner Reibung. *Verhandl. 3rd Int. Math. Kongr. Heidelberg (1904), Leipzig*.

Prandtl, L. (1925). 7. Bericht über Untersuchungen zur ausgebildeten Turbulenz. *ZAMM-Journal of Applied Mathematics and Mechanics/Zeitschrift für Angewandte Mathematik und Mechanik*, *5*(2), 136–139.

Qin, X., & Ju, Y. (2005). Measurements of burning velocities of dimethyl ether and air premixed flames at elevated pressures. *Proceedings of the Combustion Institute*, *30*(1), 233–240.

Raffel, M., Willert, C. E., Scarano, F., Kähler, C. J., Wereley, S. T., & Kompenhans, J. (2018). *Particle Image Velocimetry: A Practical Guide*.

Reichel, L., & Rodriguez, G. (2013). Old and new parameter choice rules for discrete ill-posed problems. *Numerical Algorithms*, *63*(1), 65–87.

Renaud, A., Ding, C.-P., Jakirlic, S., Dreizler, A., & Böhm, B. (2018). Experimental characterization of the velocity boundary layer in a motored IC engine. *International Journal of Heat and Fluid Flow*, *71*, 366–377.

Richard, G., & Escudie, D. (1999). Turbulence effect on the flame-wall interaction. *First Symposium on Turbulence and Shear Flow Phenomena*.

Robinson, S. K., Kline, S. J., & Spalart, P. R. (1989). A review of quasi-coherent structures in a numerically simulated turbulent boundary layer. *Quasi-Coherent Structures in the Turbulent Boundary Layer, part 2. Verification and New Inform. from a Numerically Simulated Flat-Plate Layer at Memorial Intern. Seminar on Near-Wall Turbulence*, (NASA-TM-102191).

Robinson, S. K. (1991). Coherent motions in the turbulent boundary layer. *Annual review of fluid mechanics*, *23*(1), 601–639.

Rudin, L. I., Osher, S., & Fatemi, E. (1992). Nonlinear total variation based noise removal algorithms. *Physica D: Nonlinear Phenomena*, *60*(1-4). https://doi.org/10.1016/0167-2789(92)90242-F

Ruhnau, P., & Schnörr, C. (2006). Optical Stokes flow estimation: an imaging-based control approach. *Experiments in Fluids*, *42*(1). https://doi.org/10.1007/s00348-006-0220-z

Scarano, F., & Riethmuller, M. L. (2000). Advances in iterative multigrid PIV image processing. *Experiments in fluids*, *29*(Suppl 1), S051–S060.

Schlichting, H., & Gersten, K. (2016). *Boundary-Layer Theory*. https://doi.org/10.1007/978-3-662-52919-5

Schmidt, B. E., Skiba, A. W., Hammack, S. D., Carter, C. D., & Sutton, J. A. (2021). High-resolution velocity measurements in turbulent premixed flames using

wavelet-based optical flow velocimetry (wOFV). *Proceedings of the Combustion Institute*, *38*(1). https://doi.org/10.1016/j.proci.2020.07.028

Schmidt, B. E., & Sutton, J. A. (2019). High-resolution velocimetry from tracer particle fields using a wavelet-based optical flow method. *Experiments in Fluids*, *60*(3). https://doi.org/10.1007/s00348-019-2685-6

Schmidt, B. E., & Sutton, J. A. (2020). Improvements in the accuracy of wavelet-based optical flow velocimetry (wOFV) using an efficient and physically based implementation of velocity regularization. *Experiments in Fluids*, *61*(2). https://doi.org/10.1007/s00348-019-2869-0

Schmidt, B. E., & Sutton, J. A. (2021). A physical interpretation of regularization for optical flow methods in fluids. *Experiments in Fluids*, *62*(2). https://doi.org/10.1007/s00348-021-03147-1

Schmidt, B. E., & Woike, M. R. (2021). Wavelet-based optical flow analysis for background-oriented schlieren image processing. *AIAA Journal*, *59*(8). https://doi.org/10.2514/1.J060218

Schmidt, M., Ding, C.-P., Peterson, B., Dreizler, A., & Böhm, B. (2021). Near-wall flame and flow measurements in an optically accessible SI engine. *Flow, Turbulence and Combustion*, *106*(2), 597–611.

Seroussi, G., & Barsky, B. A. (1991). *A Symbolic Derivation of Beta-splines of Arbitrary Order*. University of California, Berkeley, Computer Science Division.

Smits, A. J., McKeon, B. J., & Marusic, I. (2011). High–Reynolds Number Wall Turbulence. *Annual Review of Fluid Mechanics*, *43*(1), 353–375. https://doi.org/10.1146/annurev-fluid-122109-160753

Spalart, P. R. (1988). Direct simulation of a turbulent boundary layer up to Rθ= 1410. *Journal of fluid mechanics*, *187*, 61–98.

Sroka, Z. J. (2012). Some aspects of thermal load and operating indexes after downsizing for internal combustion engine. *Journal of Thermal Analysis and Calorimetry*, *110*(1), 51–58. https://doi.org/10.1007/s10973-011-2064-x

Stanislas, M., Okamoto, K., Kähler, C. J., & Westerweel, J. (2005). Main results of the Second International PIV Challenge. *Experiments in Fluids*, *39*(2). https://doi.org/10.1007/s00348-005-0951-2

Stark, M. (2013). *Optical Flow PIV: Improving the Accuracy and Applicability of Particle Image Velocimetry*. ETH, Department of Mechanical; Process Engineering. https://books.google.co.uk/books?id=p92MnQEACAAJ

Stein, C. M. (1981). Estimation of the mean of a multivariate normal distribution. *The annals of Statistics*, 1135–1151.

Steinberg, A. M., Driscoll, J. F., & Ceccio, S. L. (2009). Temporal evolution of flame stretch due to turbulence and the hydrodynamic instability. *Proceedings of the Combustion Institute*, *32*(2), 1713–1721.

Steinberg, A. M., & Driscoll, J. F. (2009). Straining and wrinkling processes during turbulence–premixed flame interaction measured using temporally-resolved diagnostics. *Combustion and Flame*, *156*(12), 2285–2306.

Steinberg, A. M., Driscoll, J. F., & Ceccio, S. L. (2008). Measurements of turbulent premixed flame dynamics using cinema stereoscopic piv. *Experiments in Fluids*, *44*, 985–999.

Steinhausen, M., Luo, Y., Popp, S., Strassacker, C., Zirwes, T., Kosaka, H., Zentgraf, F., Maas, U., Sadiki, A., & Dreizler, A. (2021). Numerical investigation of local heat-release rates and thermo-chemical states in side-wall quench-

ing of laminar methane and dimethyl ether flames. *Flow, Turbulence and Combustion*, *106*, 681–700.

Steinhausen, M., Zirwes, T., Ferraro, F., Scholtissek, A., Bockhorn, H., & Hasse, C. (2023). Flame-vortex interaction during turbulent side-wall quenching and its implications for flamelet manifolds. *Proceedings of the Combustion Institute*, *39*(2), 2149–2158. https://doi.org/https://doi.org/10.1016/j.proci.2022.09.026

Stevens, P., & Sciacchitano, A. (2021). Application of clustering and the Hungarian algorithm to the problem of consistent vortex tracking in incompressible flowfields. *Experiments in Fluids*, *62*, 1–11.

Stitou, A., & Riethmuller, M. L. (2001). Extension of PIV to super resolution using PTV. *Measurement Science and Technology*, *12*(9), 1398.

Stopper, U., Meier, W., Sadanandan, R., Stöhr, M., Aigner, M., & Bulat, G. (2013). Experimental study of industrial gas turbine flames including quantification of pressure influence on flow field, fuel/air premixing and flame shape. *Combustion and Flame*, *160*(10), 2103–2118. https://doi.org/https://doi.org/10.1016/j.combustflame.2013.04.005

Suter, D. (1994). Motion estimation and vector splines. *Proceedings of the IEEE Computer Society Conference on Computer Vision and Pattern Recognition*. https://doi.org/10.1109/cvpr.1994.323929

Taubman, D. S., & Marcellin, M. W. (2002). JPEG2000: standard for interactive imaging. *Proceedings of the IEEE*, *90*(8), 1336–1357. https://doi.org/10.1109/JPROC.2002.800725

Tennekes, H., & Lumley, J. L. (1972). *A first course in turbulence*. MIT press.

Theodorsen, T. (1952). Mechanism of turbulence. *2nd Midwestern conference on Fluid Mechanics, Ohio State University, 1952*.

Thevenaz, P., Blu, T., & Unser, M. (2000). Interpolation revisited [medical images application]. *IEEE Transactions on Medical Imaging*, *19*(7), 739–758. https://doi.org/10.1109/42.875199

Tomkins, C. D., & Adrian, R. J. (2003). Spanwise structure and scale growth in turbulent boundary layers. *Journal of Fluid Mechanics*, *490*, 37–74.

Townsend, A. A. R. (1976). *The structure of turbulent shear flow*. Cambridge university press.

Tu, Z., Huerst, W., Xie, W., Xiong, S., & Qin, Q. (2012). Weighted root mean square approach to select the optimal smoothness parameter of the variational optical flow algorithms. *Optical Engineering*, *51*(3), 37202. https://doi.org/10.1117/1.OE.51.3.037202

Ullman, S. (1979). *The interpretation of visual motion.* Massachusetts Inst of Technology Pr.

Villasenor, J. D., Belzer, B., & Liao, J. (1995). Wavelet filter evaluation for image compression. *IEEE Transactions on image processing*, *4*(8), 1053–1060.

Wallace, J. M. (2016). Quadrant analysis in turbulence research: history and evolution. *Annual Review of Fluid Mechanics*, *48*, 131–158.

Wallace, J. M., Eckelmann, H., & Brodkey, R. S. (1972). The wall region in turbulent shear flow. *Journal of Fluid Mechanics*, *54*(1). https://doi.org/10.1017/S0022112072000515

Wang, H., Peng, G., Chen, M., & Fan, J. (2019). Analysis of the interconnections between classic vortex models of coherent structures based on DNS data. *Water*, *11*(10), 2005.

Weickert, J., & Schnörr, C. (2001). A theoretical framework for convex regularizers in PDE-based computation of image motion. *International Journal of Computer Vision*, *45*(3). https://doi.org/10.1023/A:1013614317973

Westerweel, J., Geelhoed, P. F., & Lindken, R. (2004). Single-pixel resolution ensemble correlation for micro-PIV applications. *Experiments in Fluids*, *37*(3). https://doi.org/10.1007/s00348-004-0826-y

Winger, L. L., & Venetsanopoulos, A. N. (2001). Biorthogonal nearly coiflet wavelets for image compression. *Signal Processing: Image Communication*, *16*(9), 859–869. https://doi.org/10.1016/S0923-5965(00)00047-3

Wu, Y., & Christensen, K. T. (2006). Population trends of spanwise vortices in wall turbulence. *Journal of Fluid Mechanics*, *568*, 55–76.

Wu, Y. T., Kanade, T., Li, C. C., & Cohn, J. (2000). Image registration using wavelet-based motion model. *International Journal of Computer Vision*, *38*(2). https://doi.org/10.1023/A:1008101718719

Xiao, S. (2017). Image inpainting method based on total variation regularization. *Recent Advances in Electrical & Electronic Engineering (Formerly Recent Patents on Electrical & Electronic Engineering)*, *10*(3), 242–247.

Yuan, J., Schnörr, C., & Mémin, E. (2007). Discrete orthogonal decomposition and variational fluid flow estimation. *Journal of Mathematical Imaging and Vision*, *28*(1). https://doi.org/10.1007/s10851-007-0014-9

Zach, C., Pock, T., & Bischof, H. (2007). A Duality Based Approach for Realtime TV-{\itshape L}¡Superscript¿1¡/Superscript¿ Optical Flow. *Pattern Recognition*, *4713*.

Zentgraf, F. (n.d.). *Investigation of Reaction and Transport Phenomena during Flame-Wall Interaction Using Laser Diagnostics* [Doctoral dissertation, Technical University of Darmstadt].

Zentgraf, F., Johe, P., Cutler, A. D., Barlow, R. S., Böhm, B., & Dreizler, A. (2021). Classification of flame prehistory and quenching topology in a side-wall quenching burner at low-intensity turbulence by correlating transport effects with CO2, CO and temperature. *Combustion and Flame*. https://doi.org/10.1016/j.combustflame.2021.111681

Zentgraf, F., Johe, P., Steinhausen, M., Hasse, C., Greifenstein, M., Cutler, A. D., Barlow, R. S., & Dreizler, A. (2022). Detailed assessment of the thermochemistry in a side-wall quenching burner by simultaneous quantitative measurement of CO2, CO and temperature using laser diagnostics. *Combustion and Flame*, *235*. https://doi.org/10.1016/j.combustflame.2021.111707

Zhang, X. Y., Wang, L. M., Liu, B., Luo, Y., & Han, X. C. (2020). Hybrid Adaptive Wavelet-Based Optical Flow Algorithm for Background Oriented Schlieren (BOS) Experiments. *Mathematical Problems in Engineering*, *2020*. https://doi.org/10.1155/2020/5138153

Zhou, J., Adrian, R. J., Balachandar, S., & Kendall, T. (1999). Mechanisms for generating coherent packets of hairpin vortices in channel flow. *Journal of fluid mechanics*, *387*, 353–396.

Zigunov, F., Sellappan, P., & Alvi, F. S. (2020). Dynamics of the slanted cylinder afterbody vortices. *AIAA Scitech 2020 Forum*, 1322.

Zimmer, H., Bruhn, A., & Weickert, J. (2011). Optic flow in harmony. *International Journal of Computer Vision*, *93*(3), 368–388. https://doi.org/10.1007/s11263-011-0422-6

Appendix A

Derivation of wavelet derivative operators

The following sections derive the results necessary for constructing the derivative operators used in the computation of the regularization term. The necessary preliminary results from wavelet calculus are first introduced, before presenting these in the context of derivatives of the velocity field. For notational simplicity, the following results are initially derived for the orthogonal case, with this appendix concluding with relevant considerations for constructing the derivatives in the biorthogonal case used in the algorithm. The derivation closely follows those presented in (Dérian, 2012; Nielsen, 1998; B. E. Schmidt & Sutton, 2020).

A.1 Connection Coefficients

First, it is necessary to derive the expression for the derivative of a scaling function ϕ. This will be used to introduce the following theoretical result for wavelet *connection coefficients* which later arise in the later derivation of the regularization term. Applying the derivative operator to the refinement relation 3.6 with $j = 0$:

$$\frac{\partial \phi(y)}{\partial y} = \sqrt{2}\frac{\partial \phi}{\partial y}(2y - k) \times 2 \tag{A.1}$$

Recursive application of differentiation to the above equation produces the result:

$$\frac{\partial^n \phi(y)}{\partial y^n} = 2^n\sqrt{2}\frac{\partial^n \phi}{\partial y^n}(2y - k) = 2^n\phi^{(n)} \tag{A.2}$$

where n, with $n \geq 0$ being the derivative order. The connection coefficients are defined by the inner product of the product of a scaling function ϕ and its n^{th} order derivative at a single scale:

$$I_\phi^{(n)} = 2^n \int_{\mathbb{R}} \phi(y)\phi^{(n)}(y - x)dy \tag{A.3}$$

The connection coefficients are dependent on the derivative order n and the chosen wavelet family which defines the (primal) filter h. Inserting the refinement relation in equation A.3:

$$
\begin{aligned}
I_{\phi}^{(n)} &= 2^n \int_{\mathbb{R}} \phi(y)\phi^{(n)}(y-x)\, dy \\
&= 2^n \int_{\mathbb{R}} \left(\sqrt{2}\sum_{m\in\mathbb{Z}} h(m)\phi(2y-m)\right)\left(\sqrt{2}\sum_{n\in\mathbb{Z}} h(n)\phi^{(n)}(2(y-x)-n)\right) \\
&= 2^n \sum_{m\in\mathbb{Z}}\sum_{n\in\mathbb{Z}} 2h(m)h(n)\int_{\mathbb{R}} \phi(2y-m)\phi^{(n)}(2(y-x)-n)\, dy
\end{aligned}
\tag{A.4}
$$

Inserting the change of variable $n = m - k$ into equation A.4:

$$
\begin{aligned}
I_{\phi}^{(n)} &= 2^n \sum_{m\in\mathbb{Z}}\sum_{n\in\mathbb{Z}} 2h(m)h(n)\int_{\mathbb{R}} \phi(2y-m)\phi^{(n)}(2(y-x)-n)\, dy \\
&= 2^n \sum_{m\in\mathbb{Z}}\sum_{k\in\mathbb{Z}} 2h(m)h(m-k)\int_{\mathbb{R}} \phi(2y-m)\phi^{(n)}(2(y-x)-m+k)\, dy \\
&= 2^n \sum_{m\in\mathbb{Z}}\sum_{k\in\mathbb{Z}} 2h(m)h(m-k)\int_{\mathbb{R}} \phi(2y-m)\phi^{(n)}(2y-m-(2x-k))\, dy
\end{aligned}
\tag{A.5}
$$

Applying the refinement relations from 3.6 to A.5:

$$
\begin{aligned}
I_{\phi}^{(n)} &= 2^n \sum_{m\in\mathbb{Z}}\sum_{k\in\mathbb{Z}} 2h(m)h(m-k)\int_{\mathbb{R}} \phi(2y-m)\phi^{(n)}(2y-m-(2x-k))\, dy \\
&= 2^n \sum_{m\in\mathbb{Z}}\sum_{k\in\mathbb{Z}} h(m)h(m-k)\int_{\mathbb{R}} \phi(y)\phi^{(n)}(y-(2x-k))\, dy \\
&= 2^n \sum_{m\in\mathbb{Z}}\sum_{k\in\mathbb{Z}} h(m)h(m-k)\int_{\mathbb{R}} \phi(y)\phi^{(n)}(y-(2x-k))\, dy \\
&= 2^n \sum_{k\in\mathbb{Z}} i(k) I_{\phi}^{(n)}(2x-k)
\end{aligned}
\tag{A.6}
$$

where $i(k) = \sum_{m\in\mathbb{Z}} h(m)h(m-k)$. Equation A.6 can be written as the linear system:

$$
H I_{\phi}^{(n)} = \frac{1}{2^n} I_{\phi}^{(n)} \tag{A.7}
$$

where H is a diagonal matrix assembled with the elements of $i(k)$. Values of connection coefficients $I_{\phi}^{(n)}$ are then computed via the solution of an eigenvalue problem, with the connection coefficients being the eigenvector of H associated to eigenvalue $1/2^n$ (Beylkin, 1992). The connection coefficients are then normalised according to (Kwon, n.d.):

$$
I_{\phi}^{(n)} = \frac{I_{\phi}^{(n)} n!(-1)^n}{\sum_k k^n \Gamma_{\phi(k)}^{(n)}} \tag{A.8}
$$

The connection coefficients are then assembled into the operator matrix $M^{(n)}$ which enacts differentiation on the approximation coefficients from the scaling function basis ϕ. The same boundary conditions assumed in the wavelet transforms (periodic or symmetric) must also be considered in the assembly of $M^{(n)}$ (B. E. Schmidt & Sutton, 2020).

A.2 Single scale derivative operator

With the theoretical results for computing connection coefficients now complete, the example derivation of the first term:

$$J_{eg} = \frac{1}{2}\int_{\mathbb{R}^2}\left(\frac{\partial U_1^2}{\partial x_1^2}\right)^2 d\boldsymbol{x} \tag{A.9}$$

in Equation 3.32 is now presented. The derivation of all other terms in equation 3.31 follow similarly. Inserting the wavelet representation of the velocity field at the finest scale $U_1 = \sum_{\boldsymbol{k}} a_{F,\boldsymbol{k}}\phi_{F,k_1}(x_1)\phi_{F,k_2}(x_2)$ into equation A.9:

$$\begin{aligned}
J_{eg} &= \frac{1}{2}\int_{\mathbb{R}^2}\left(\frac{\partial U_1^2}{\partial x_1^2}\right)^2 d\boldsymbol{x} \\
&= \frac{1}{2}\int_{\mathbb{R}^2}\left[\sum_{\boldsymbol{k}} a_{F,\boldsymbol{k}}\frac{\partial}{\partial x_1^2}\left(\phi_{F,k_1}(x_1)\phi_{F,k_2}(x_2)\right)\right]^2 d\boldsymbol{x} \\
&= \frac{1}{2}\sum_{\boldsymbol{k}} a_{F,\boldsymbol{k}}^2\int_{\mathbb{R}}\frac{\partial\phi_{F,k_1}(x_1)}{\partial x_1^2}\frac{\partial\phi_{F,k_1}(x_1)}{\partial x_1^2}\,dx_1\int_{\mathbb{R}}\phi_{F,k_2}(x_2)\phi_{F,k_2}(x_2)\,dx_2 \\
&= \frac{1}{2}\sum_{\boldsymbol{k}} a_{F,\boldsymbol{k}}^2\langle\phi_{F,k_1}(x_1)^{(2)};\phi_{F,k_1}(x_1)^{(2)}\rangle\langle\phi_{F,k_1}(x_1);\phi_{F,k_1}(x_1)\rangle
\end{aligned} \tag{A.10}$$

The term $\langle\phi_{F,k_1}(x_1)^{(2)};\phi_{F,k_1}(x_1)^{(2)}\rangle$ can be shown to be equivalent to $-\langle\phi_{F,k_1}(x_1);\phi_{F,k_1}(x_1)^{(4)}\rangle$ using integration by parts (Kadri-Harouna et al., 2013) which puts this term into the form of equation A.3. Equation A.10 is then represented using the matrix form:

$$J_{eg} = \frac{1}{2}a_F : \left(M^{(4)}a_F M^{(0)T}\right) \tag{A.11}$$

where : denotes the element-wise product and sum, also known as the Frobenius product. The gradient of equation A.11 is then given by:

$$\frac{\partial J_{eg}}{\partial a_F} = M^{(4)}a_F M^{(0)T} \tag{A.12}$$

A.3 Multiscale derivative operator

The above derivation demonstrates the computation of the single scale derivative operator. The full multiscale representation, including both approximation and detail coefficients, is used in the wOF algorithm. The multiscale form of $M^{(\cdot)}$ can be recovered by applying the 2D DWT to the matrix M:

$$N^{(\cdot)} = WM^{(\cdot)}W^T \tag{A.13}$$

where W is the wavelet transform operator represented in matrix form (B. E. Schmidt & Sutton, 2020). The reason for this simple change to the multiscale form results from the wavelet function also satisfying the refinement relation used in the derivation of the connection coefficients from the scaling function. In the biorthogonal case, the decomposition in A.13 is done via:

$$N^{(\cdot)} = W^*M^{(\cdot)}W^{\#T} \tag{A.14}$$

The wavelet transform matrix W^* is assembled from the *primal* filters h, g, which are typically the reconstruction filters. The matrix $W^{\#} = W^{-1}$ is the inverse of W being the wavelet transform operator assembled from the *dual* filters $\tilde{h}$, $\tilde{g}$ (B. E. Schmidt & Sutton, 2020). In the orthogonal case $W^* = W^{\#} = W$. The relevant operators $N^{(0)}$, $N^{(2)}$, $N^{(4)}$ for Laplacian regularization are precomputed and stored in memory before the beginning the minimisation process.

Appendix B

Comparison of PIV & OF results

This appendix examples several results of Chapter 5 comparing wOF ($\lambda = 10$) and PIV (32×32) px^2. The results are presented here for reference and are not discussed further. To compare wOF quantities to the PIV result, the wOF fields are subsampled to the PIV grid spacing using cubic interpolation. These are labelled as the 'wOF Downsampled'. The discrepancy between the wOF and PIV fields is represented by the absolute difference.

B.1 Instantaneous example

B.1.1 Velocity magnitude |U|

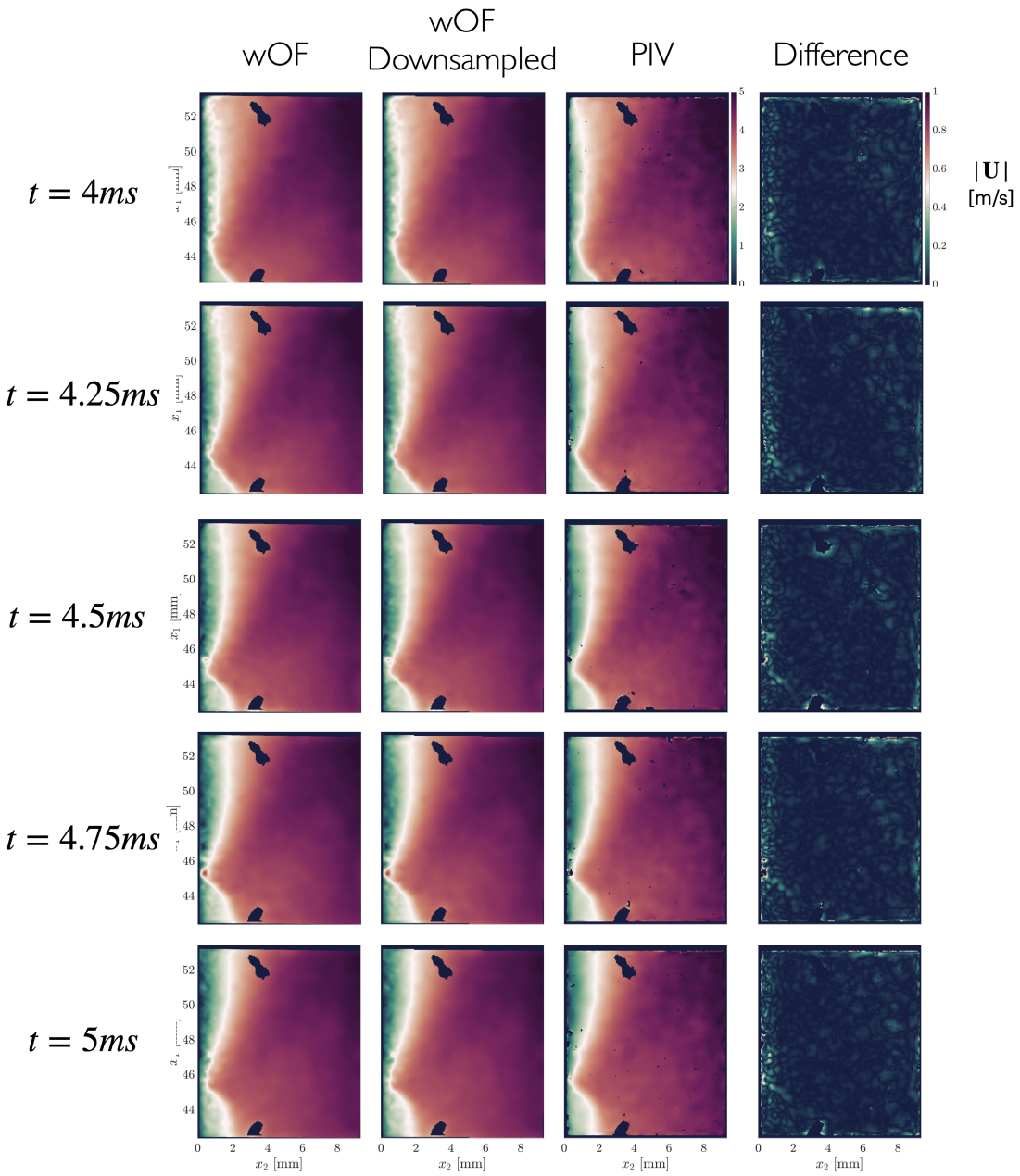

Figure B.1

B.1.2 Swirling strength Λ_{ci}

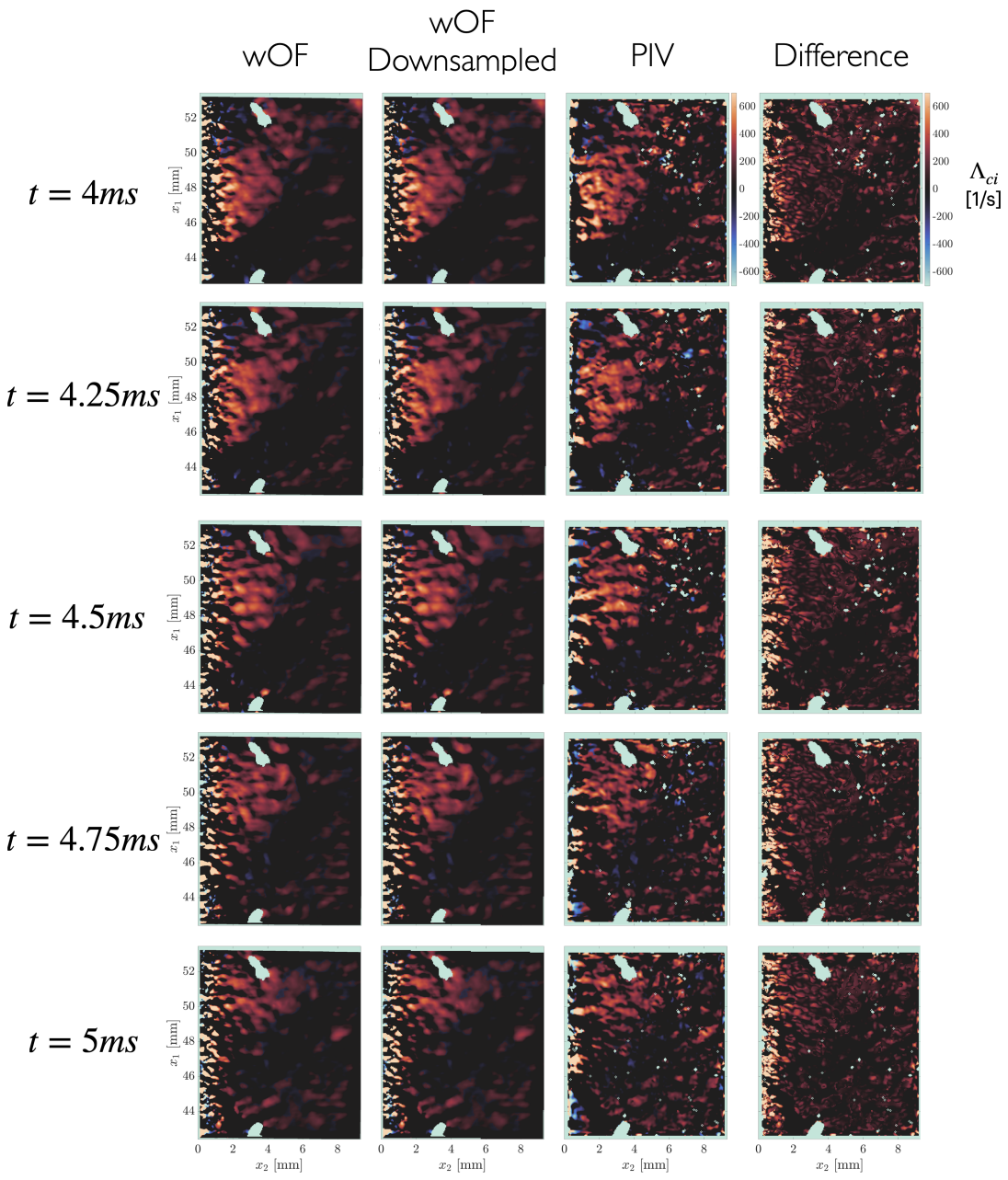

Figure B.2

B.2 Conditioned fields

Results of the $1\times1\text{mm}^2$ highlight are shown.

B.2.1 Instantaneous strain S^*

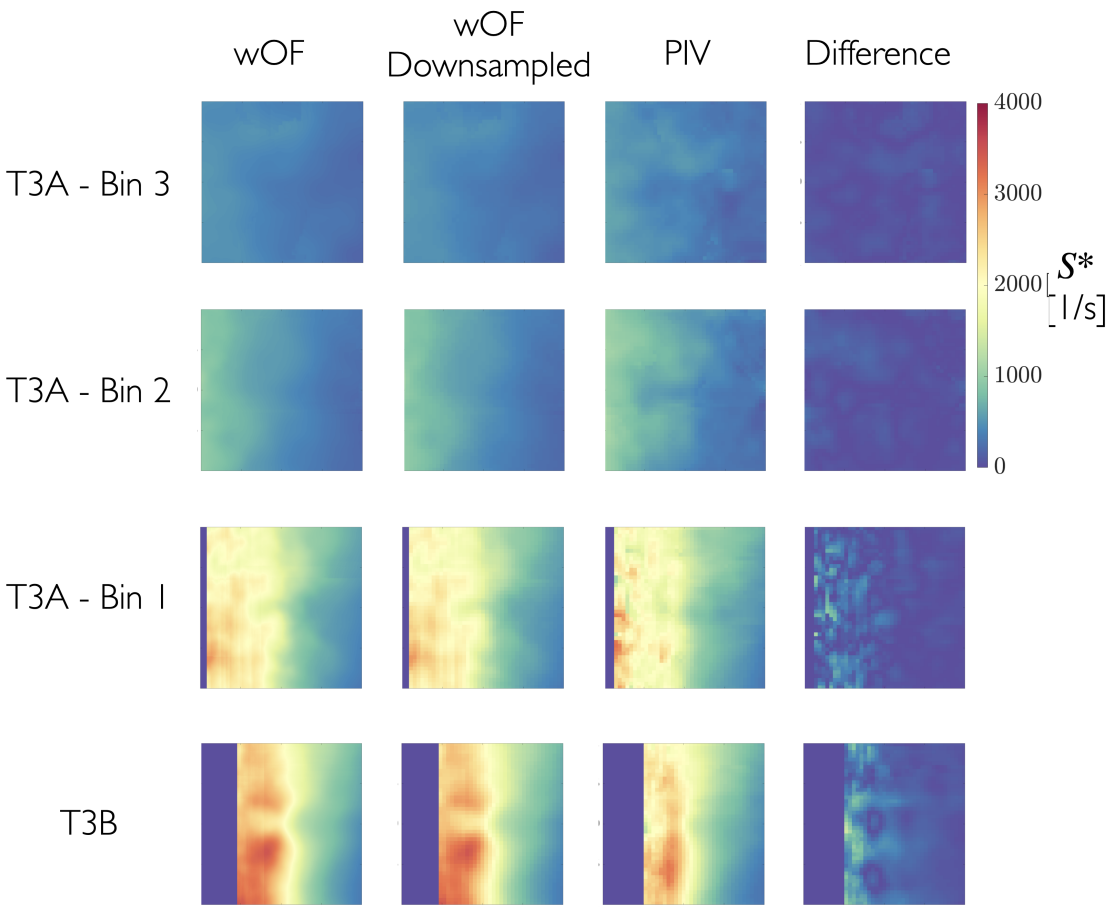

Figure B.3

B.2.2 Fluctuating strain s^*

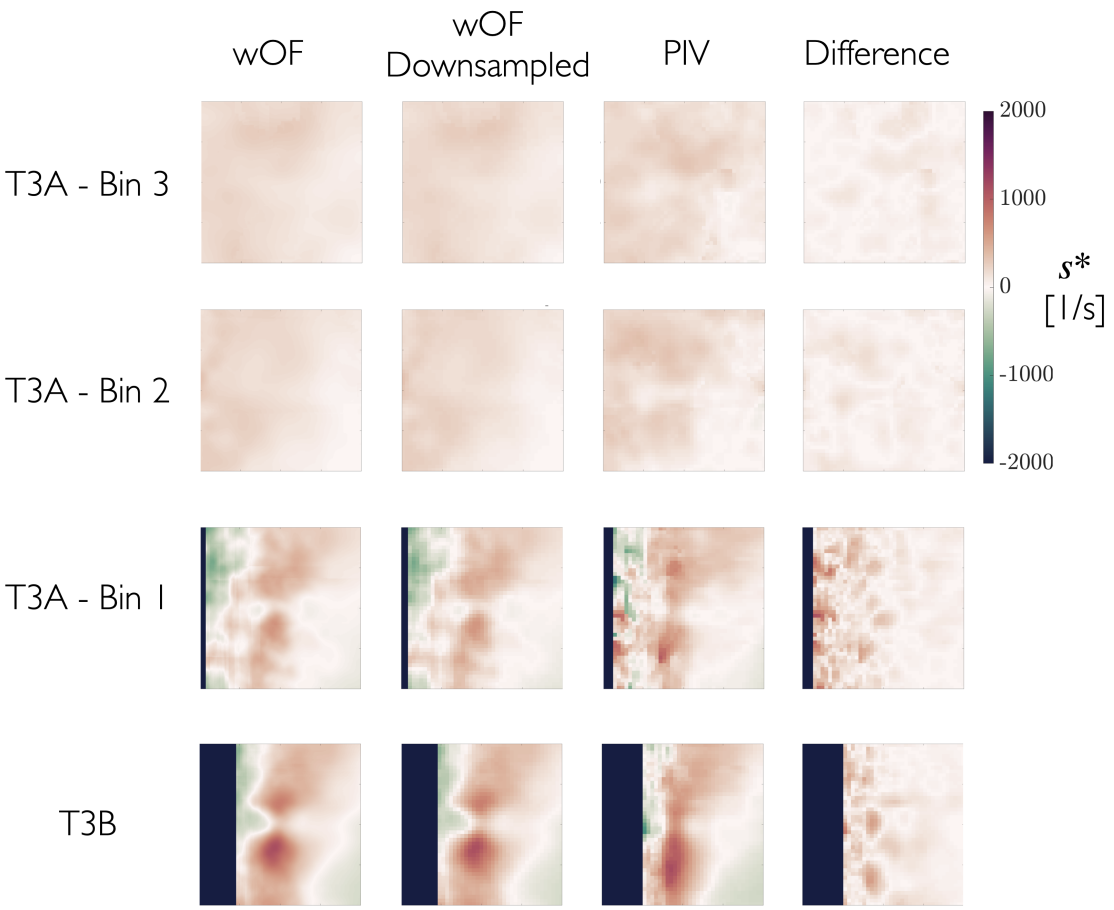

Figure B.4

B.2.3 Fluctuating vorticity ω^*

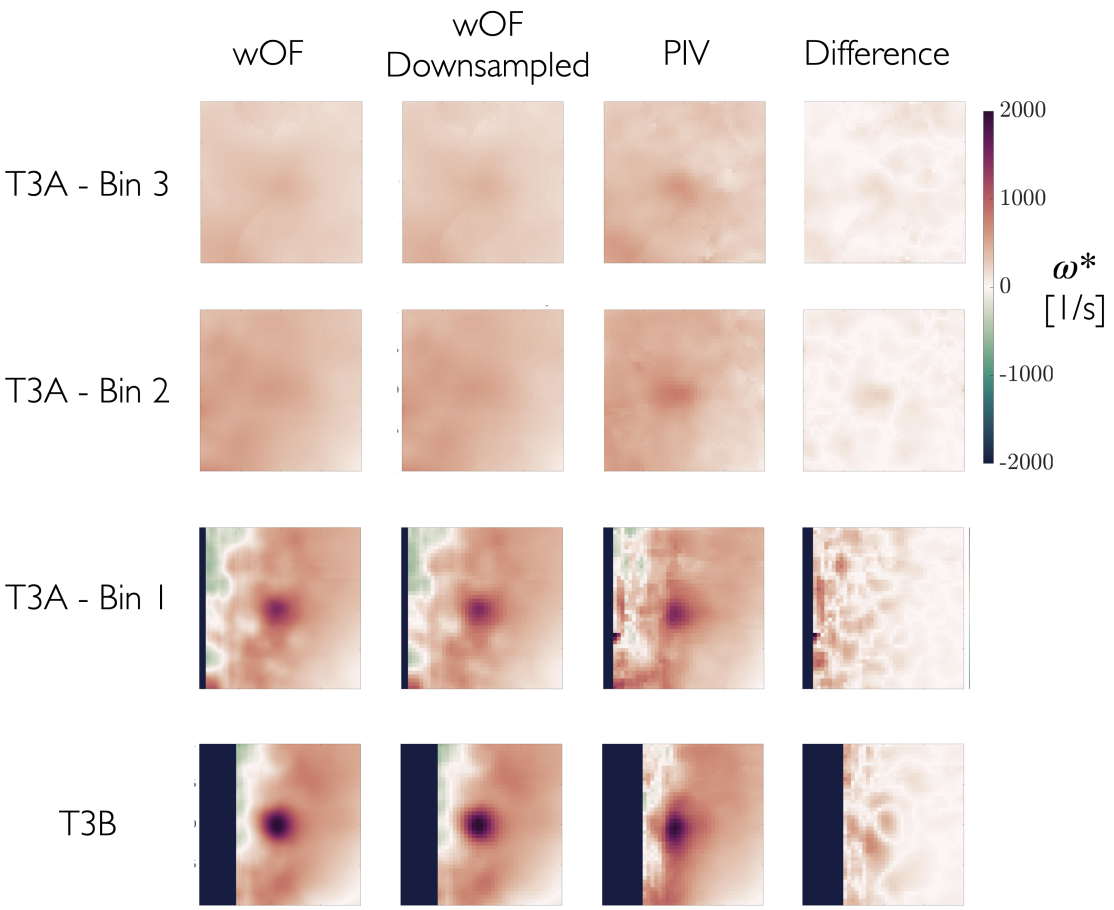

Figure B.5

B.2.4 Swirling strength Λ^*_{ci}

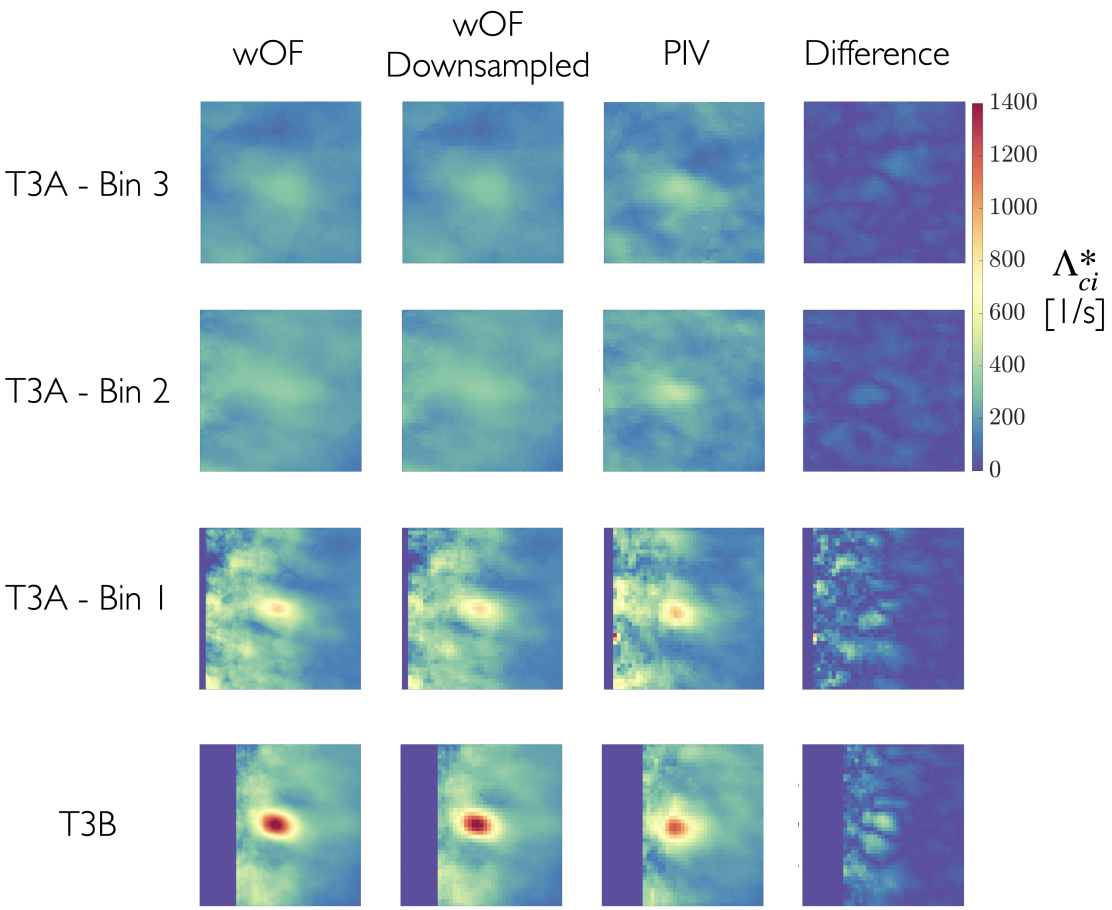

Figure B.6

B.3 Statistics of vortex kinematic properties

B.3.1 Instantaneous strain of vortices

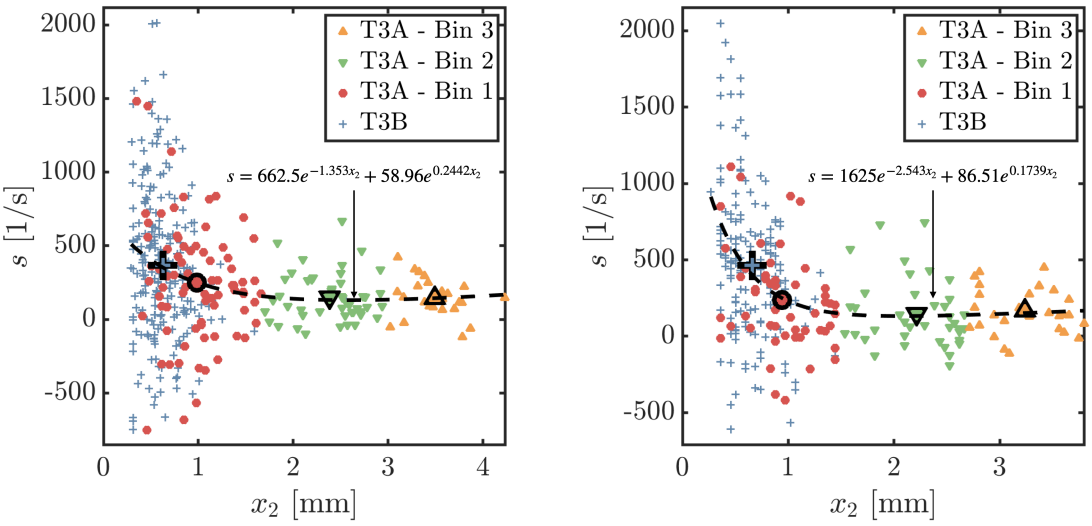

(a) wOF from Chapter 5. (b) PIV

Figure B.7

B.3.2 Fluctuating strain of vortices

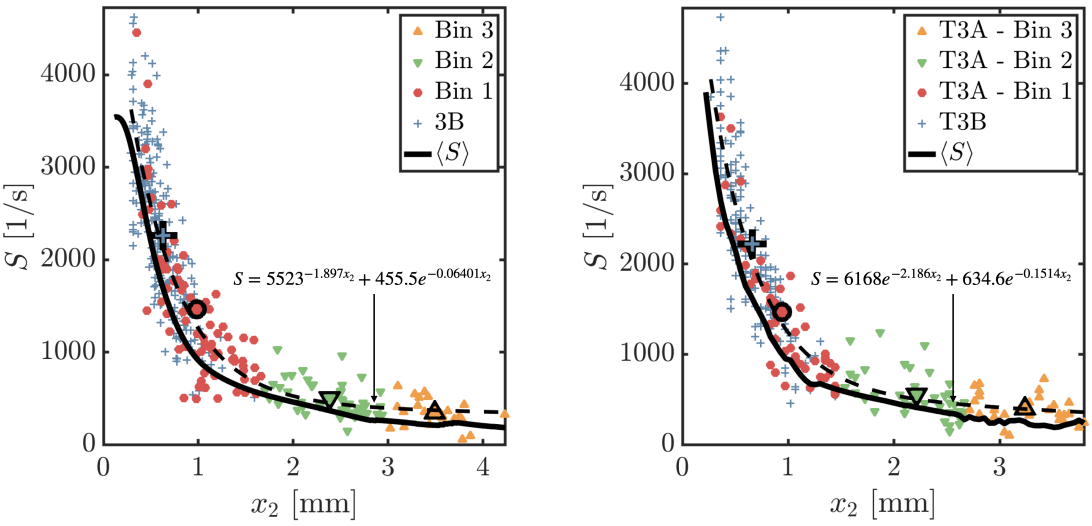

(a) wOF from Chapter 5. (b) PIV

Figure B.8

B.3.3 Fluctuating vorticity of vortices

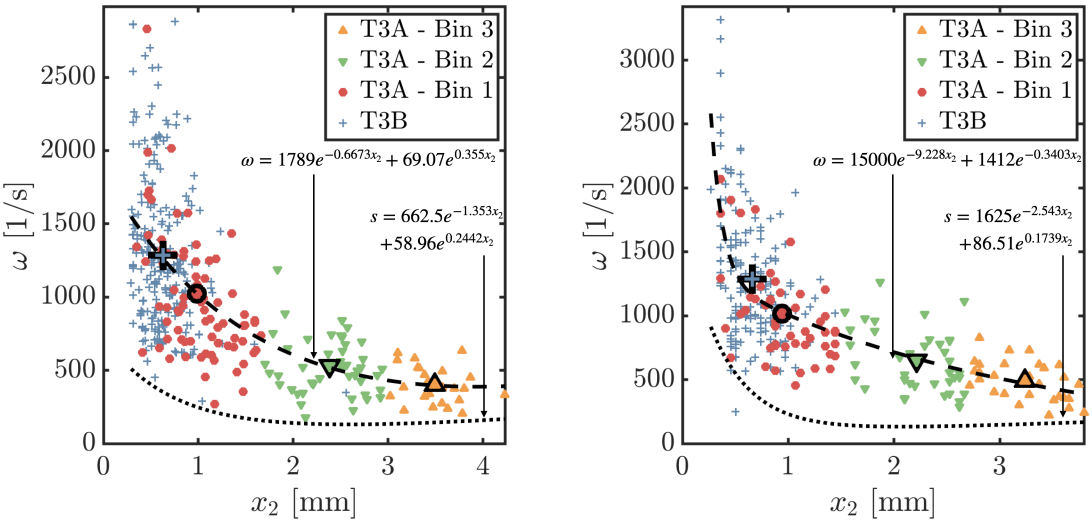

(a) wOF from Chapter 5 (b) PIV

Figure B.9

B.3.4 Swirling strength of vortices

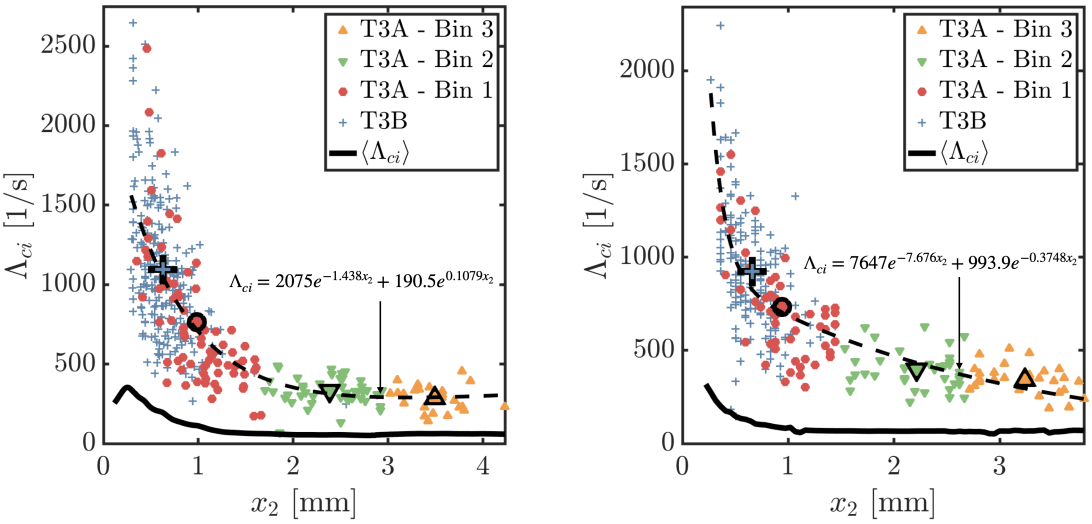

(a) wOF from Chapter 5 (b) PIV

Figure B.10

B.4 Vortex transport mechanism

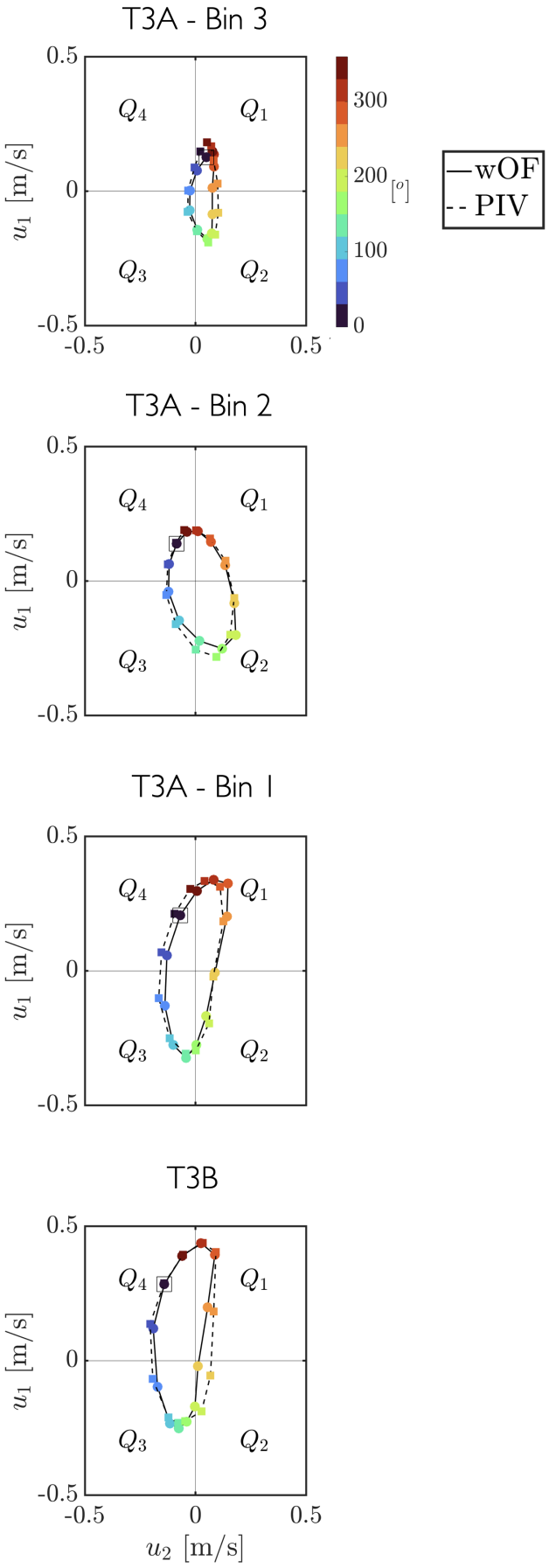

Figure B.11